DIPLOMARBEIT

Understanding Muon Detection Efficiencies for Quarkonium Polarization Measurements at the Compact Muon Solenoid

Ausgeführt am

Institut für Hochenergiephysik (HEPHY)
der Österreichische Akademie der Wissenschaften (ÖAW)

Unter der Anleitung von

Univ. Prof. Dipl.Ing. Dr. CHRISTIAN FABJAN & Dr. JOSEF STRAUSS
& Dipl.Ing. Dr. HERMINE WÖHRI

Durch

ILSE KRÄTSCHMER

März 2012

Abstract

The polarization of quarkonium states which are quark-antiquark pairs ($b\bar{b}$, $c\bar{c}$) is a topic of special interest and has therefore already been measured several times in the past. The experimental results however were seemingly contradictory because not the full physical information was used. The CMS quarkonium polarization analysis determines the full angular distribution in three different reference frames as well as the frame-invariant parameter $\tilde{\lambda}$. An important input to this analysis are the detection efficiencies. A precise knowledge and good understanding of the efficiencies, in particular how they depend on kinematical parameters, is needed to extract the correct polarization.

The central issues of this thesis are the single muon detection efficiencies for low p_T dimuon triggers of 2011 extracted with the Tag and Probe method. Different reconstruction and trigger efficiencies are discussed and evaluated. To build the dimuon efficiencies from the single muon efficiencies, a correction factor, the so called ρ factor, is required. It can introduce artificial polarization if not accounted for correctly. Results for the ρ factor are also presented in this thesis.

Kurzbeschreibung

Die Polarisation sogenannter Quarkonium-Zustände, die aus einem Quark und seinem Antiquark ($b\bar{b}$, $c\bar{c}$) bestehen, sind von besonderem Interesse und wurden daher bereits in der Vergangenheit wiederholte Male gemessen. Die aus verschiedenen Experimenten gewonnenen Resultate widersprachen sich jedoch scheinbar, da in den Analysen nur die Verteilung des Polarwinkels verwendet wurde. Die CMS Quarkonium Polarisationsanalyse misst sowohl die gesamte Winkelverteilung des Quarkonium-Zerfalls in drei verschiedenen Referenzsystemen als auch einen vom Referenzsystem unabhängigen Parameter $\tilde{\lambda}$. Die Effizienzien sind ein zentraler Beitrag zu dieser Analyse, da ein profundes Wissen und gutes Verständnis der Effizienzen nötig ist, um die richtige Polarisation zu extrahieren.

Der größte Teil dieser Arbeit handelt von den Effizienzen zum Nachweis einzelner Myonen in Triggern mit einer niedrigen, transversalen Impulsschwelle. Verschiedene Rekonstruktions- und Triggereffizienzen werden diskutiert und evaluiert. Um aus den Effizienzen einzelner Myonen jene für Myonenpaare zu bilden, wird ein zusätzlicher Korrekturfaktor, der sogenannte ρ Faktor, benötigt. Dieser kann Resultate der Polarisationsanalyse verfälschen, falls er nicht richtig behandelt wird, und wird daher auch ausführlich in dieser Arbeit diskutiert.

Thanks to everyone who supported me and made this thesis possible!

'Are you Death?'
IT'S THE SCYTHE, ISN'T IT? PEOPLE ALWAYS NOTICE THE SCYTHE.
'I'm going to die?'
POSSIBLY.
'Possibly? You turn up when people are *possibly* going to die?'
OH YES, IT IS QUITE THE NEW THING. IT'S BECAUSE OF THE UNCERTAINTY PRINCIPLE.
'What's that?'
I'M NOT SURE.
'That's very helpful.'
I THINK IT MEANS PEOPLE MAY OR MAY NOT DIE. I HAVE TO SAY IT'S PLAYING HOB WITH MY SCHEDULE BUT I TRY TO KEEP UP WITH MODERN THOUGHT.

– Terry Pratchett, The fifth elephant

Contents

CHAPTER 1

Introduction

Ever since the discovery of the J/ψ in the '70s, physicists have been trying to measure the cross-sections and the polarization of quarkonium states. Quarkonia are quark-antiquark pairs of either *beauty*, b, or *charm* quarks, c. So far, experimental results on quarkonium polarization have been seemingly inconsistent with each other as well as contrary to results from calculations based on QCD inspired simple theoretical models. Furthermore, quarkonia cross-section measurements also are affected by the unknown polarization in that it constitutes the largest systematic uncertainty in these measurements.

Since 2010, the Large Hadron Collider (LHC) has been producing collisions suitable for physics analysis. It produces quarkonia at a very high rate and thus provides good conditions to study quarkonia. All four main experiments at the LHC try to measure properties of quarkonia, in particular the polarization.

In this thesis, the analysis strategy of the quarkonium polarization measurement conducted with the Compact Muon Solenoid (CMS), which is especially well suited for studies of quarkonia decaying into two muons, is presented. In particular, this thesis deals with the detection efficiencies which are a crucial input to the determination of the polarization. Unless correctly accounted for, the transverse momentum p_T and pseudo-rapidity η dependent shape of the single muon detection efficiencies as well as the one of the correction factor needed to build the dimuon efficiencies may introduce fake polarization that would bias the result of the measurement.

In Chapters 2 and 3, an introduction to the LHC and to the CMS experiment is given. In Chapter 4, quarkonium polarization and its importance also to other studies are discussed. Results, both past and present, are presented. A frame-invariant approach for the analysis is introduced which is also used for the CMS quarkonium polarization analysis. The strategy of the analysis is presented in Chapter 5. In Chapters 6 and 7, the most important input to the polarization studies is discussed: the detection efficiencies. First, the single muon detection

efficiencies extracted with the Tag and Probe (TnP) method in two different ways are shown. Single muon efficiencies cannot be translated directly into dimuon efficiencies. An additional correction factor, the ρ factor, is needed which is discussed in Chapter 7.

Chapter 6 is based on the CMS internal analysis note AN-11-417.

Please enjoy this thesis as much as I did while writing it!

CHAPTER 2

The Large Hadron Collider

The Large Hadron Collider (LHC) is the world's biggest and most powerful particle collider with a nominal center of mass collision energy $\sqrt{s} = 14$ TeV for proton-proton (pp) collisions. It is located at the European Organization for Nuclear Research, in French Organisation Européenne pour la Recherche Nucléaire (CERN), near Geneva, buried 45 to 170 m underneath the Swiss-French border. Due to economical considerations, it was built in the already existing tunnel of the dismantled Large Electron Positron collider (LEP) which has a circumference of 26.7 km. A twin-bore or *two-in-one* magnet design was implemented to be able to accelerate counter circulating proton beams in a close space and two separate superconducting rings. Apart from protons, the LHC also collides lead ions with a design $\sqrt{s} = 2.76$ TeV/nucleon [1].

The LHC is fed by an accelerator complex that is presented in Fig. 2.1. The protons are injected from the LInear ACcelerator (LINAC2) into the Proton Synchroton Booster (PSB) at an energy of 50 MeV, where they are further accelerated to 1.4 GeV before being transferred to the Proton Synchrotron (PS). Here, proton bunches are formed with the 50 ns (nominally 25 ns) spacings needed for the LHC. At an energy of 25 GeV, the protons are fed to the Super Proton Synchrotron (SPS) before they reach the LHC at an energy of 450 GeV. The injection of the proton bunches from the SPS into the LHC has to be done in a certain scheme since the beam structure is important for synchronization, calibrating data and beam dumping. The LHC further accelerates the proton bunches to currently 3.5 TeV (4 TeV in 2012), nominally 7 TeV and collides them in four interaction points [2].

Six experiments are installed at the LHC:

- A Large Ion Collider Experiment (ALICE)
- A Toroidal LHC ApparatuS (ATLAS)
- Compact Muon Solenoid (CMS)

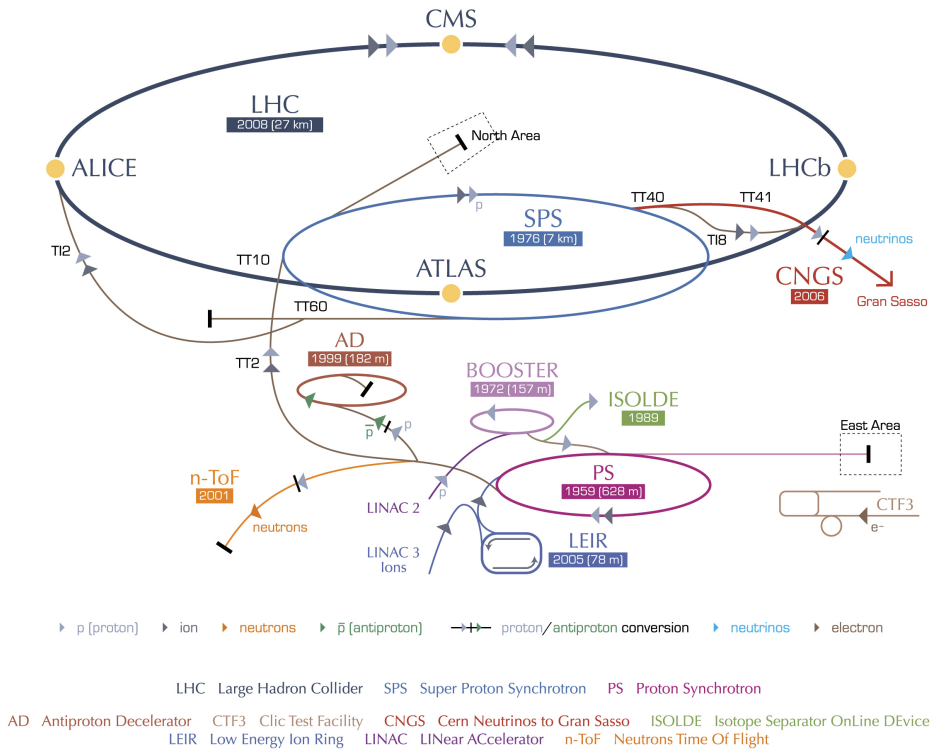

Figure 2.1: The CERN accelerator complex [3].

- Large Hadron Collider beauty experiment (LHC-b)
- TOTal Elastic and diffractive cross section Measurement (TOTEM)
- Large Hadron Collider forward experiment (LHC-f)

ALICE, ATLAS, CMS and LHC-b are located in four big caverns around the collision points (see Fig. 2.2) while TOTEM and LHC-f are installed near the CMS and ATLAS experiment, respectively.

CMS and ATLAS are high luminosity general purpose experiments. They investigate a large range of physics, from standard model precision measurements to searching for Higgs bosons and physics beyond the standard model such as SUperSYmmetry (SUSY), large extra dimensions and dark matter constituent particles. ALICE specializes on heavy ion collisions and studies matter in conditions similar to those just after the Big Bang. LHC-b tries to understand the asymmetry between matter and antimatter by studying the *beauty* quark, b. ALICE as well as LHC-b are low luminosity experiments in that they do not collect as many collision events as the general purpose experiments [4].

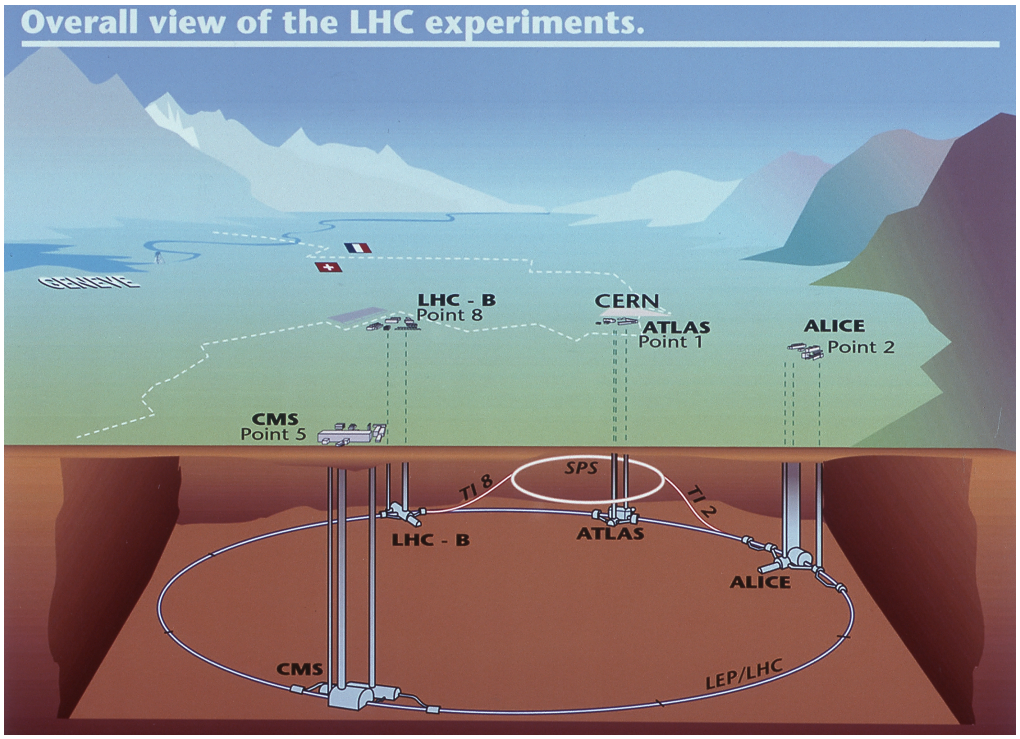

Figure 2.2: Overall view of the main LHC experiments: The four main experiments are spread out around the circumference of the LHC 45 to 170 m below the surface [5].

2.1 Physics at the LHC

Our current understanding of the universe is encapsulated in the Standard Model (SM) of particle physics which describes the fundamental particles and the forces between them. An overview of the particle content of the SM is given in Fig. 2.3. However, the model is incomplete and is only considered effective up to a scale of some TeV. The LHC was built to probe the SM and look for signs of physics beyond it. The main goals of the LHC are presented here.

For this thesis, the capabilities of the CMS detector are of particular interest. An in depth description of the wide range of physics analyses of the CMS detector can be found in the technical design report [6].

2.1.1 Search for the Higgs Boson

One of the biggest unanswered question within the scope of Standard model of particle physics is: Where does mass come from? The SM predicts the existence of a Higgs boson that would be the lowest excitation of the Higgs field which fills the whole space. Fermionic particles acquire mass by interacting with this field. The electroweak bosons, $W^{\pm}$ and Z, acquire their mass through the spon-

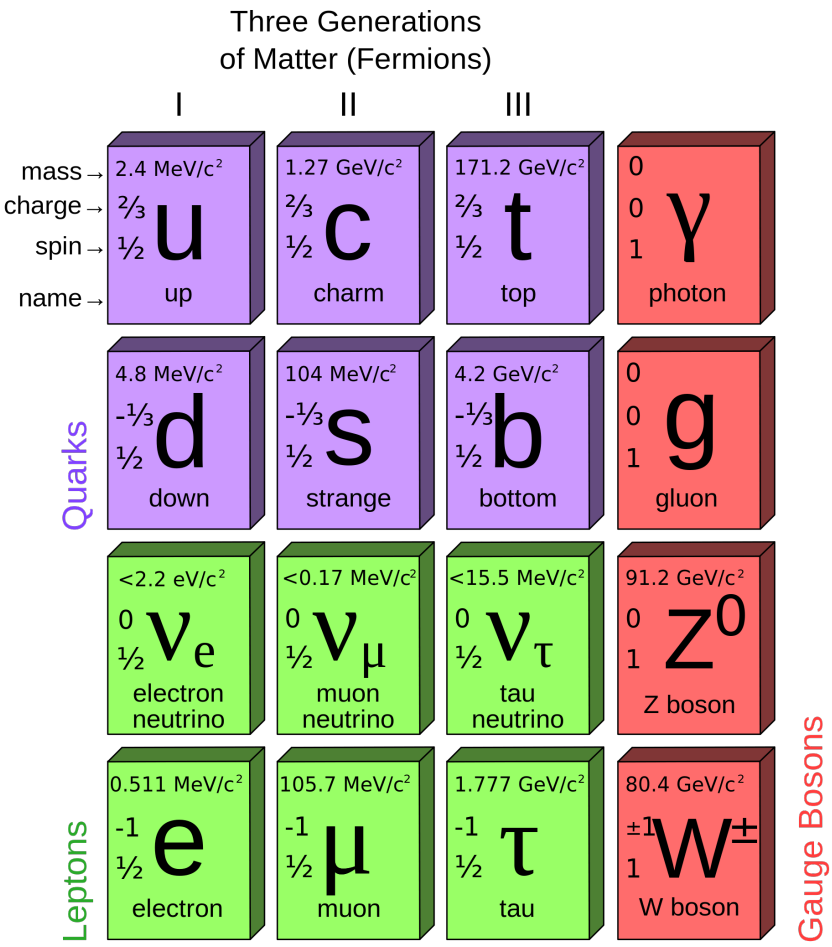

Figure 2.3: The fundamental particles in the Standard Model of particle physics: To the left, there are the three generations of fermions consisting of the quarks that build up heavy particles and the leptons. The gauge bosons which carry the forces between particles are listed on the right. The photon is the carrier of the electromagnetic force and applies to all charged fermions. The $W^{\pm}$ and Z^0 are the carriers of charged and neutral weak interactions respectively and apply to all fermions while the gluons are the carriers of the strong force which apply to quarks.

taneously breaking of the electroweak symmetry which is introduced in the SM by the Higgs mechanism [7, 8].

The SM fixes all properties of the Higgs boson except for its mass. Therefore, searches for the Higgs boson at the LHC have to cover the allowed mass range. Data collected in 2011 show no conclusive statement on the existence of the Higgs boson. However, CMS and ATLAS constrained the most likely mass region to 115 to 127 GeV/c^2 and 116 to 130 GeV/c^2, respectively [9].

2.1.2 Physics Beyond The Standard Model

Despite being a highly successful theory, the SM still leaves some questions unanswered, thus necessitating new models to amongst other things explain gravity, dark matter and dark energy, neutrino masses and matter-antimatter asymmetry of the universe. Apart from the direct searches for Beyond the Standard Model (BSM) physics, the SM will be probed precisely to indirectly find new physics. One precision measurement is the CP violating phase in the decay $B_s \rightarrow \mathrm{J}/\psi \ + \phi$. CP violation is expected to help in the understanding of the matter-antimatter asymmetry in our universe. LHC-b's recently published result for the B_s mixing phase is consistent with the SM, thus not yet revealing any new physics [10].

2.1.3 Search for Supersymmetry

SUperSYmmetry (SUSY) [11], a theory extending the SM, can stabilize the Higgs mass at the electroweak scale. There are indications that it will allow for the unification of the strong, the weak and the electromagnetic forces at very high energies. It is suggested by *grand unification* models which include gravity and predicts a supersymmetric partner for each of the known fundamental particles [12]. In a class of SUSY models, the Lightest Supersymmetric Particle (LSP) is stable and weakly interacting and can provide a dark matter constituent particle [13].

2.1.4 Dark Matter and Dark Energy

What is 96% of our universe made of? All that we can see in the universe like planets, stars and galaxies only account for 4% of it. Most of the universe is made out of invisible substances that can only be studied through their gravitational effects. Therefore, physicists are looking for particles responsible for the dark matter and dark energy. Dark matter makes up for about 22% of our universe while approximately 74% is dark energy (see Fig. 2.4). One possibility is that the dark matter is made out of the LSP which has yet to be discovered [14].

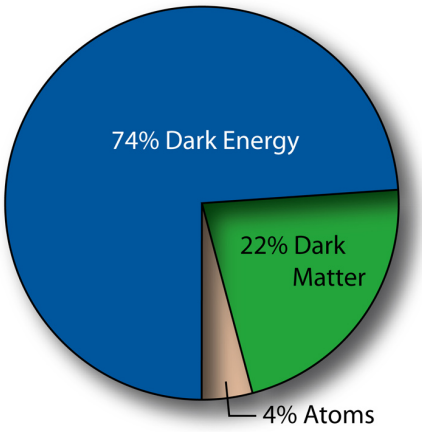

Figure 2.4: Only 4% of our universe is visible. Dark matter comprises about 22% of it while the rest ($\approx 74\%$) is composed of dark energy [15].

2.1.5 Matter-Antimatter Symmetry

During the Big Bang, the same amount of matter and antimatter has been produced. Somehow matter survived which poses some questions: Did antimatter and matter not completely annihilate after the Big Bang? Is there still antimatter somewhere in the universe? If not, what happened to it? Studying particles and their antiparticles will possibly provide some answers [16].

2.1.6 Quark-Gluon Plasma

In addition to the proton-proton collisions, the LHC also collides heavy ions which may provide a better understanding of the conditions of the early universe. The universe went through a stage where matter existed as a extremely hot, dense soup made of quarks and gluons – the Quark-Gluon Plasma (QGP). As the universe cooled, the quarks became confined into composite particles such as protons and neutrons. In the LHC, it is possible to reproduce QGP and thus be able to study basic properties of free quarks and the formation of ordinary matter [2].

One of the experimental signatures of the QGP, the suppression of high transverse momentum jets or so called jet quenching, was directly observed for the first time by ATLAS and CMS during the heavy ion runs in 2010 [17, 18].

2.1.7 Extra Dimensions

String theory suggests that at least another six spatial dimensions exist in addition to the three geometric dimensions and the time dimension. Somehow these extra dimensions are hidden from our senses. At sufficiently high energies, a win-

dow could open up and allow particles to move freely between the dimensions. This would manifest itself in the sudden disappearance of a particle into a hidden dimension or an unexpected appearance of a particle in an experiment [19].

CHAPTER 3

The Compact Muon Solenoid

The Compact Muon Solenoid (CMS) is a multipurpose particle physics experiment designed to study a wide range of physics topics. From the physics goals of the LHC outlined in Section 2.1, which largely coincide with those of CMS, the following design criteria have been established when CMS was conceived [13]:

- The detection of muons is of uttermost importance to CMS. Therefore, the requirements on the muon system are high: good muon identification and momentum resolution over a wide range of momenta and angles, good dimuon mass resolution of about 1% at 100 GeV/c^2 and the ability to unambiguously determine the charge of muons with a momentum below 1 TeV/c.
- The tracking system must measure charged tracks with good momentum resolution and reconstruction efficiency while achieving efficient triggering and offline tagging of τ's and b-jets that rely on precise determination of secondary vertices and thus require pixel detectors close to the interaction point.
- The Electromagnetic CALorimeter (ECAL) should cover a wide geometric range and have a good electromagnetic energy resolution as well as diphoton and dielectron mass resolution ($\approx$ 1% at 100 GeV/c^2). Furthermore, an efficient photon and lepton isolation at high luminosities is needed.
- The Hadron CALorimeter (HCAL) should supply a precise jet energy reconstruction to be able to calculate the missing transverse energy and a good dijet-mass resolution which requires a good coverage over a large geometric region with fine lateral segmentation.

The design of the particle detector reflects these requirements with emphasis on a good muon detection. The detector is 21.6 m long, 12 500 t heavy and has a diameter of 14.6 m. The key characteristic features are a 4 T field solenoid,

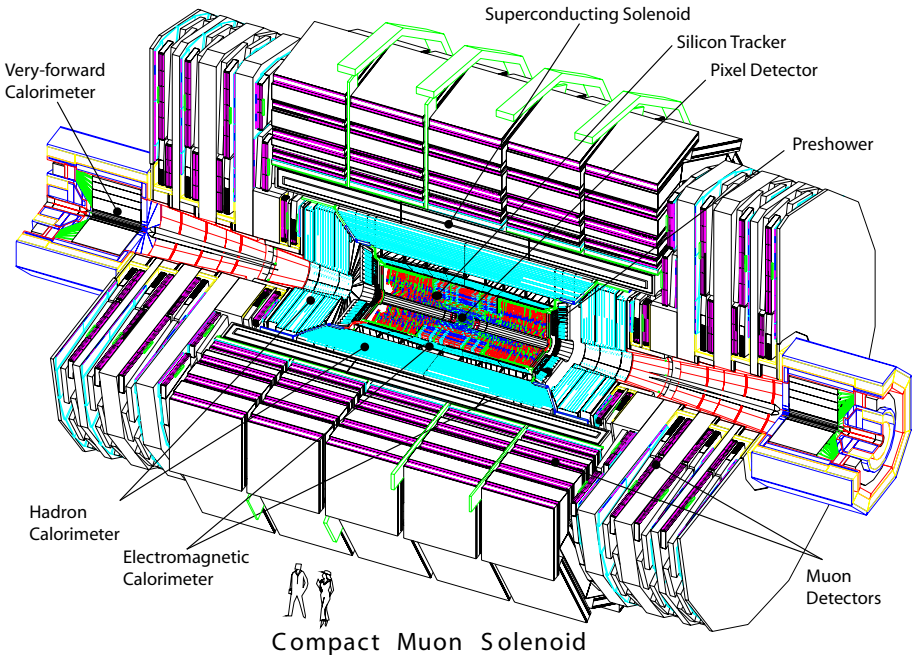

Figure 3.1: CMS detector layout: The pixel detector and silicon tracker form the innermost system, surrounded by the solenoid and calorimetry consisting of electromagnetic and hadron calorimeter. This is again enclosed by the outermost system, the muon stations [13].

a silicon-based inner tracking system and an electromagnetic calorimeter based on active scintillating crystals [13]. Figure 3.1 shows the overall layout of CMS. The particle tracker forms the innermost system, surrounded by the solenoid and calorimetry which is again enclosed by the outermost system, the muon stations. The individual detector components will be discussed in the following sections.

Figure 3.2 displays how different particles passing through a transverse slice of the CMS detector can be identified: Charged particles leave tracks in the inner detector. Electrons and photons are absorbed in the ECAL while hadrons are stopped in the HCAL. Neutral particles like photons do not have a matching charged track. Muons traverse the entire detector.

The coordinate system adopted by CMS has its origin in the nominal collision point. It is right-handed with the longitudinal direction z running along the beam direction towards the Jura mountains while the y-axis points vertically upwards and the x-axis radially inwards, towards the center of the LHC. The azimuthal angle ϕ is measured from the x-axis in the x-y-plane, the polar angle θ from the z-axis. Pseudo-rapidity η is defined as $\eta = -\ln\tan\left(\frac{\theta}{2}\right)$. The momentum and energy transverse to the beam direction, p_T and E_T, are calculated using the x and y components. Through the sum of transverse momentum and energy, the imbalance of the transverse energy denoted by the missing transverse energy

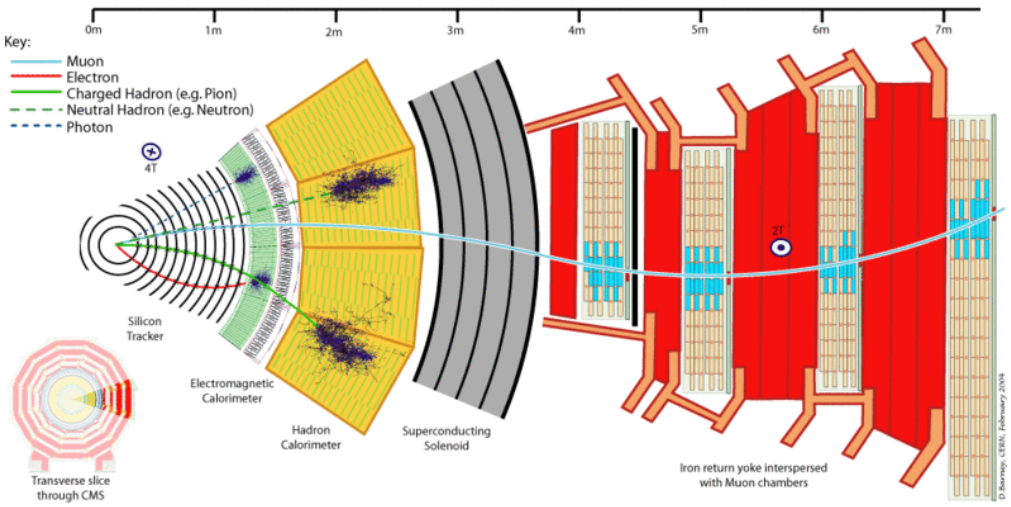

Figure 3.2: Particle identification: Charged particles leave tracks in the inner detector. Electrons and photons are absorbed in the ECAL. Hadrons are absorbed in the HCAL. Neutral particles are separated from charged ones by the absence of a matching charged track. Muons traverse the entire detector [20].

E_T^{miss} is derived [13].

In this thesis, the variable y denotes the rapidity of a particle with the mass m defined as

$$y = \ln \frac{\sqrt{m^2 + p_T^2 \cosh^2(\eta)} + p_T \sinh(\eta)}{\sqrt{m^2 + p_T^2}} \tag{3.1}$$

and not the y-axis.

3.1 Superconducting Magnet

The choice of the magnetic field configuration is a very important aspect of the detector design. A large bending power, i.e. a high magnetic field, is needed to achieve the required momentum resolution of $\frac{\Delta p}{p} \approx 10\%$ at p = 1 TeV/c which means that the sign of charged particles can be unambiguously determined up to a momentum of approximately 1 TeV/c. The high field forces the use of superconducting material, specifically a high purity aluminium stabilized Niobium-Titanium conductor. The conductor is wound in four layers in order to accommodate the high number of turns needed for generating a 4 T field. The coil is surrounded by a 10 000 t steel yoke to close the field lines. The main parameters of the solenoid are summarized in Table 3.1 [13].

Table 3.1: Parameters of the superconducting solenoid [13].

Central magnetic field	4 T
Inner diameter	5.9 m
Length	12.9 m
Cold mass	220 t
Number of turns	2169
Current	19.5 kA
Stored energy	2.7 GJ

3.2 Inner Tracking System

The inner tracking system is the innermost part of the CMS detector. It has a length of 5.8 m and a diameter of 2.6 m. At the LHC design luminosity (10^{34} cm^{-2} s^{-1}), about 1000 particles would travel through the tracker every 25 ns. This requires the tracker to have high granularity and a fast response to be able to provide a precise and efficient measurement of the trajectories of charged particles with a transverse momentum above 1 GeV/c. Moreover, precise reconstruction of secondary vertexes and impact parameters is needed for the identification of heavy flavours. The tracker in combination with the electromagnetic calorimeter and the muon system also has to identify muons and electrons [21].

To meet the requirements on granularity, speed and radiation hardness, the tracker is entirely silicon based. The tracker can be divided into three barrel regions by considering the charged particle flux at high luminosity. The full layout of the tracker is shown in Fig. 3.3.

1. Pixel detectors are used closest to the interaction point where the particle flux is highest (ca. 10^7 per second at $r \approx 10$ cm). They are placed in three layers at radii of 4.4, 7.3 and 10.2 cm. Their spatial resolution is about 10 μm in the transverse direction and about 20 μm in the longitudinal direction.

2. The intermediate region ($20 < r < 55$ cm) is called the Tracker Inner Barrel (TIB). The particle flux is low enough to be handled by four layers of silicon microstrip detectors. A cell size of 10 cm $\times$ 80 μm for the first two layers and 10 cm $\times$ 120 μm for the third and fourth layer is used. The resolution varies from 23 to 34 μm for the r-ϕ measurement and is about 230 μm in z.

3. Above a radius of 55 cm, the particle flux dropped sufficiently to use larger-pitched silicon microstrip detectors (25 cm $\times$ 183 μm and 25 cm $\times$122 μm) which are arranged in six layers. This so called Tracker Outer Barrel (TOB) extends to an outer radius of 116 cm. It has a resolution of $35 - 52$ μm in transverse and 530 μm in longitudinal direction.

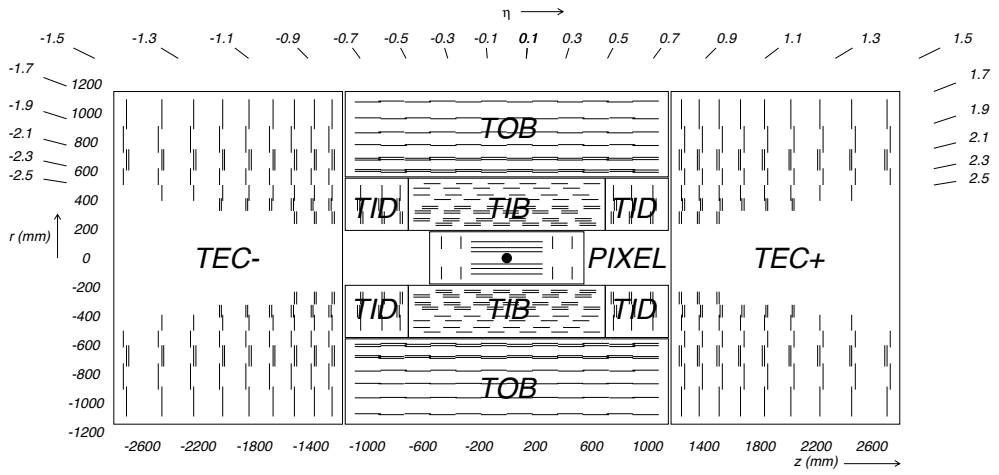

Figure 3.3: Layout of the CMS tracking system: The inner tracking system consists of silicon based subdetectors and covers an pseudo-rapidity range of up to 2.5. Each line represents a detector module [21].

The tracking system in the barrel is completed by two layers of pixel detectors and nine microstrip layers in each of the two endcaps, thus extending the acceptance up to $|\eta| < 2.5$. Since the TIB is shorter than the TOB to avoid shallow track crossing angles, three additional inner disks called Tracker Inner Disk (TID) have been placed in the transition region between the TIB and the Tracker EndCaps (TECs). The occupancy of the tracker is kept below 1% in the pixel detector and below 20% in the strip detectors to permit track reconstruction in this high density environment [13, 21].

3.3 Calorimeter

The calorimeter consists of two parts, the Electromagnetic CALorimeter (ECAL) and Hadron CALorimeter (HCAL), in order to provide a complete system for the measurement of electrons, photons and jets as well as E_T^{miss}.

3.3.1 Electromagnetic Calorimeter

One of the main criteria for the ECAL design was to be able to detect the decay of the postulated Higgs boson into two photons. This requires a good energy resolution and a high granularity provided by a homogeneous crystal calorimeter.

The ECAL is made out of 61 200 lead tungstate crystals in the barrel and 7 324 in each of the endcaps. It covers a pseudo-rapidity region up to $|\eta| < 3$. The chosen crystals are very fast, radiation hard, have a high density and fine granularity. They emit about 80% of the blue-green scintillation light in 25 ns, which is of

the same order of magnitude as the LHC bunch crossing time. The relatively low light output requires the use of photodetectors that have intrinsic gain and that can operate in high magnetic fields. Therefore, silicon Avalanche PhotoDiodes (APDs) are used in the barrel region while Vacuum PhotoTriodes (VPTs) are installed in the endcaps. A preshower detector is placed in front of the endcap crystal for Π^0 rejection [13, 21].

3.3.2 Hadron Calorimeter

The HCAL surrounding the ECAL is radially restricted by the outer radius of the ECAL (R = 1.77 m) and the inner extent of the superconducting solenoid (R = 2.7 m). This limits the total amount of material that can absorb the hadronic shower. To provide a good containment of all hadronic showers inside the calorimeter in spite of the spatial limits, the HCAL was designed to maximize the absorber material inside the magnet while minimizing the active medium. Centrally ($|\eta| < 1.26$), the shower containment is improved by an outer hadron calorimeter consisting of an array of scintillators which is placed outside the magnetic coil.

Brass was chosen as absorber material since the interaction length of particles in brass is reasonably short. The active medium is composed of plastic scintillator tiles read out by embedded WaveLength-Shifting (WLS) fibres.

The HCAL covering the pseudo-rapidity region $0 < |\eta| < 3$ is complemented by two forward calorimeter ($3 < |\eta| < 5$) located 11.2 m away from the interaction point. They are designed to measure energetic forward jets to increase the shower containment and to improve the measurement of the missing transverse energy [13, 21].

3.4 Muon System

As already the name of the detector implies, muon detection and thus the muon system play a central role in CMS. The layout of the muon system and the corresponding pseudo-rapidity regions are displayed in Fig. 3.4. Three different types of gaseous particle detectors, which were required to be inexpensive, robust and reliable, are used for the muon measurement. The shape of the magnet naturally gave rise to a cylindrical barrel region ($|\eta| < 1.2$) and two planar endcap regions ($1.2 < |\eta| < 2.4$). The magnetic field in the barrel is uniform and mostly contained in the steel yoke, the muon rate as well as the background induced by neutrons are low. Therefore, it is possible to use Drift Tubes (DTs). In the two endcaps, where the muon rate and the neutron induced background are high and also the magnetic field is high and non-uniform, Cathode Strip Chambers (CSCs) are installed. Resistive Plate Chambers (RPCs) are used additionally in both barrel and endcap regions to support the DTs and CSCs. The DTs and CSCs in combination with the RPCs provide two independent and complementary sources of information about muons [13].

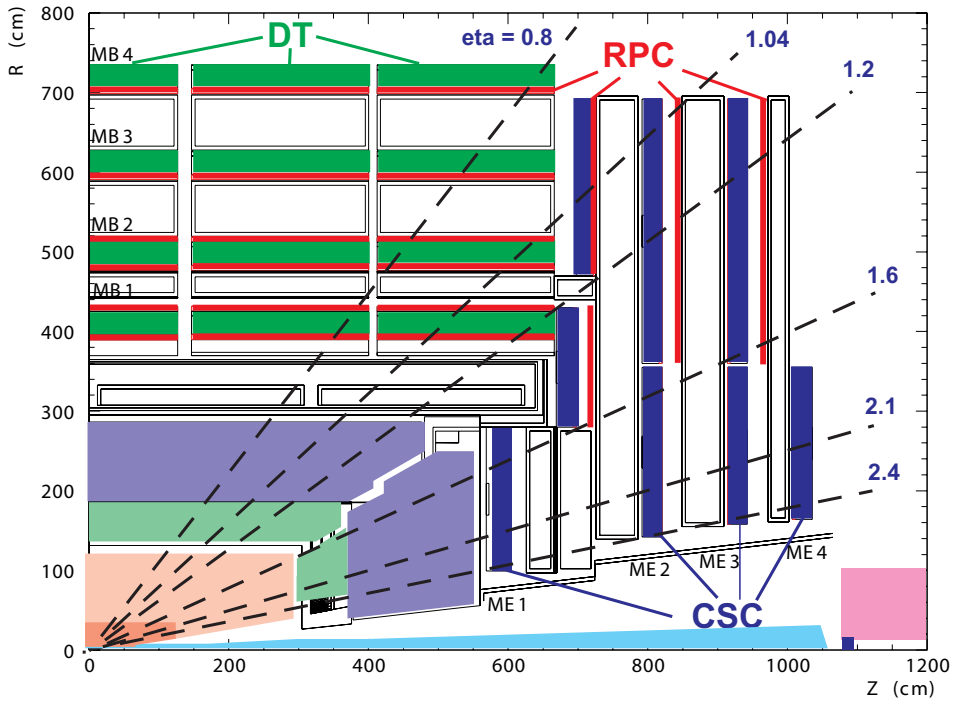

Figure 3.4: Layout of one quarter of the muon system [13].

Since the full pseudo-rapidity region ($|\eta| < 2.4$) is covered by muon detector elements without acceptance gaps, muon identification and reconstruction are ensured over a range corresponding to $10° < \theta < 170°$. They are however less efficient in regions around $|\eta| = 0.25$ and 0.8, corresponding to the regions between two barrel wheels, and $|\eta| = 1.2$ (the transition region between the DT and CSC systems), where there is no instrumentation [21].

The momentum of centrally produced muons is measured three times: in the inner tracker, after the coil and in the return flux. For low p_T muons, the best resolution is obtained by exclusively using the measurement in the silicon tracker while combining the measurements of the inner tracker and the muon detectors improves the resolution for high p_T muons [13].

3.4.1 Drift Tube Chambers

The 250 DTs are organized in four layers (labelled as Muon Barrel (MB) 1, MB2, MB3 and MB4 in Fig. 3.4) forming five wheels inside the magnet return yoke. In the first two layers, the DTs are sandwiched between two RPCs while each DT in the third and forth station is only coupled to one RPC. The redundancy in the first two stations allows the trigger algorithm to perform a reconstruction based on four layers, even for low p_T muon tracks which may stop before reaching the outer two stations. The chambers in each wheel are identical with the exception

of the wheels next to the central one. The ±1 wheels are by 40 cm shorter because the cryogenic chimneys are hosted in the sections covering the $|\eta|$ region around 0.25 [21, 13].

Muons entering the gaseous DT chambers ionize gas molecules along their path. The electrons and ions drift maximally 2 cm to the electrodes. Taking into account the drifting time of the ions, the coordinates of the muons can be reconstructed with a resolution of approximately 100 μm in position and 1 mrad in the radial direction. A high p_T muon in the barrel region can produce up to 44 measured points while crossing up to six RPCs and four DTs. A good muon track can be reconstructed using the hits in the subdetectors [13].

3.4.2 Cathode Strip Chambers

CSCs are multiwire proportional chambers which can operate at high rates and in large non-uniform magnetic fields. They have a trapezoidal shape and are arranged in rings overlapping in ϕ (except the third ring of the first endcap disk) to avoid gaps in the muon acceptance. In total, 468 CSCs are installed in four layers perpendicular to the beam axis in the two endcap regions. The resolution is typically about 200 μm in position and of the order of 10 mrad in the radial direction.

Up to $|\eta| = 1.6$, the CSCs are supported by RPCs to improve the time resolution and achieve a good p_T resolution. In the range where the endcap and barrel overlap ($0.9 < |\eta| < 1.2$), muons are detected by both systems – the DTs as well as the CSCs in combination with the RPCs [13, 21].

3.4.3 Resistive Plate Chambers

RPCs are gaseous parallel-plate detectors operated in avalanche mode to ensure good operation at high rates. They provide a fast response with a very good time, but coarser position resolution than CSCs and DTs. They can therefore identify unambiguously the correct bunch crossing to which a muon track is associated. They also help to resolve ambiguities in the measurement of muon tracks [21].

3.5 Trigger System

At the LHC design luminosity, approximately 20 proton-proton collisions occur simultaneously every 25 ns, leading to an interaction rate of 1 GHz (10^9 interactions/s). Since it is impossible to store this large amount of data, they have to be reduced drastically by about a factor of 10^6, down to an interaction rate of 1 kHz. This is achieved by a trigger system selecting physically interesting events. The data reduction is done with the help of trigger algorithms in two subsequent steps, the hardware-based Level 1 (L1) followed by the High Level Trigger (HLT) [13].

3.5.1 Level 1 Trigger

The completely hardware based L1 trigger uses Field Programmable Gate Arrays (FPGAs), Application Specific Integrated Circuits (ASICs), Programmable Logic Devices (PLDs) and Look-Up Tables (LUTs) to reach a fast decision whether to keep or reject an event. The total time for the L1 trigger to take a decision is 3.2 μs including the transition time, leaving less than 1 μs for actual calculations. During this time, the detector data has to be held in buffers.

The L1 trigger uses coarsely segmented data from the calorimeters and the muon systems. Figure 3.5 shows the architecture of the L1 trigger. It is divided into local, regional and global components. The local trigger or Trigger Primitive Generators (TPGs) exploits the energy deposits in the calorimeters and the hit patterns in the muon chambers as a first step towards the selection of interesting events. The regional triggers combine the information from the local triggers and determine ranks and sort the trigger objects. The ranks are based on energy or momentum and the quality which reflects the level of confidence attributed to the L1 parameter measurements. This information is respectively sent to the Global Calorimeter Trigger and the Global Muon Trigger (GMT) which determine the highest-rank calorimeter and muon objects to transfer to the Global Trigger (GT). The GT is the entity that takes the decision to reject an event or to accept it for further evaluation by the HLT. The data rate is reduced to 100 kHz after the L1 trigger.

Since the work presented in this thesis focuses on quarkonia decaying into two muons, a more detailed explanation of the muon trigger is needed: The local DT and CSC systems provide independent and complementary information in form of muon hit patterns and track segments to the L1 trigger. The regional muon triggers or Track Finders (TFs) identify the muon candidates by extrapolating from one track segment in one muon station to another station with a pre-calculated trajectory originating at the vertex. They also determine their transverse momenta and quality to sort them by rank. The DT and CSC TFs each deliver up to four muon candidates with the highest p_T and the best quality to the GMT. In addition, the RPCs also send four plus four track candidates based on the regional hit patterns. All chambers also provide the bunch crossing from which an event originates.

The GMT combines the information from the three subsystems consisting of the muon candidate's p_T, charge, η, ϕ and quality. The DT and CSC candidates are matched to the ones from the RPCs based on the proximity of the candidates in the (η, ϕ)-space. The kinematic parameters of matched candidates are merged, thus achieving an improved momentum resolution and efficiency.

Unmatched candidates are suppressed based on their quality and η. The GMT contains a logic to cancel duplication of muons and reject ghost tracks – i.e. a single muon reported by both the DT and CSC triggers, but which is otherwise unmatched – especially in the overlap region between the barrel and the endcaps.

After the matching, muons candidates are extrapolated through the calorimeter

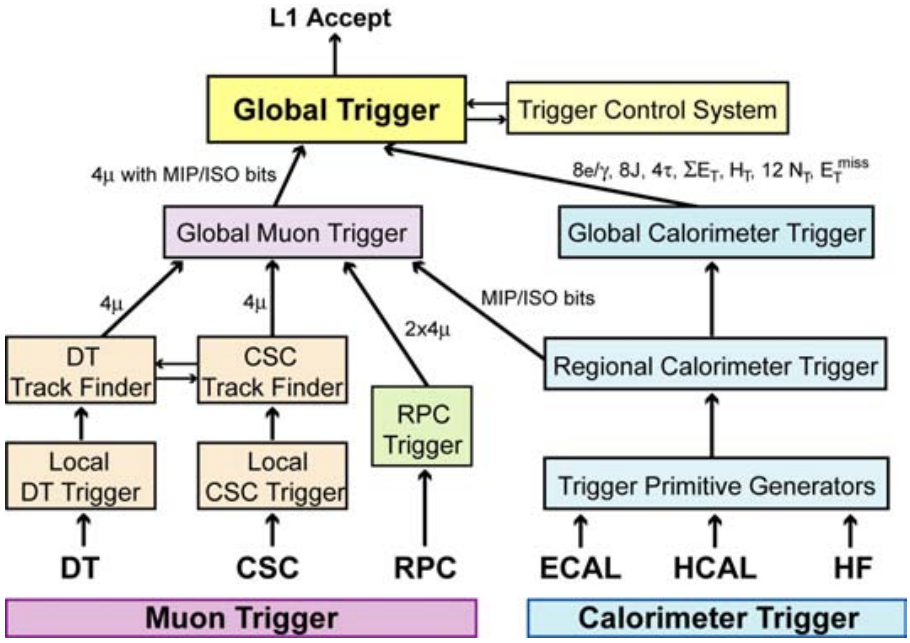

Figure 3.5: Architecture of the L1 trigger: Multiple data streams from subdetectors are combined in a multi level hierarichical trigger to determine if an event is accepted for further study [21].

regions to the vertex to get the corresponding calorimeter information about isolation and minimum ionizing particles. Then, they are sorted by quality, transverse momentum and rank. The four best muon candidates are sent to the GT which takes the final decision of rejecting or accepting an event [13, 21].

3.5.2 High Level Trigger

The software based HLT comes into effect after an event has been accepted by the L1 trigger. The data from the buffer is transferred to the front-end readout buffers and then to one of the about one thousand commercial processors running the HLT software code. The HLT has access to the complete read-out data of the events selected by the L1 trigger. However, only objects and regions that are actually needed are reconstructed to be able to reject an event as soon as possible. For muons, for example, first only the information of the muon system is used and then in a second step combined with the information from the tracker. This partial reconstruction leads to the notion of two different virtual trigger levels: Level 2 (L2) and Level 3 (L3). All levels of the HLT combined are required to reduce the data rate by a factor of 10^3 from 100 kHz to about 100 Hz.

In the following subsections, only the HLT muon reconstruction will be discussed as it is the most important subsystem for the work presented in this thesis.

Level 2 Trigger

The starting point for a highly efficient and reliable muon reconstruction are the L1 seeds which define a region of interest where a muon candidate with its corresponding track position, momentum and direction was found by the L1 trigger. The subsequent standalone muon reconstruction only uses information from the muon detectors, i.e. DTs, CSCs and RPCs. The RPCs, in particular, complement the tracking chambers in the overlap region of the barrel and endcaps where the geometric coverage is problematic.

The standalone muon reconstruction is seeded by the L1 candidate muon at the innermost chambers of the muon system. Using the seed's parameters, it searches for more muon hits along a predicted trajectory, working from the innermost to the outermost muon chambers. At each step, the track position, momentum and direction are updated with the newly found information. Hits far away from the trajectory, which are mostly due to showering, delta rays and pair production, are rejected by a cut on χ^2 of the hit and the track. Then the whole process is repeated in reverse, working from the outermost to the innermost muon chamber, and the track is extrapolated to the nominal interaction point [13].

Level 3 Trigger

The global or L3 muon reconstruction extends the existings extrapolated muon trajectories from L2 to also include hits from the silicon inner tracker. The silicon layers compatible with the muon trajectories define the regions of interests, which have a strong impact on the reconstruction efficiency, fake rate and CPU reconstruction time. Well measured muons are reconstructed faster and more efficient than poorly measured ones.

In a region of interest, regional seeds are built from pairs of reconstructed hits that are coming from two different tracker layers. Starting from the innermost layer, each seed is transformed into a set of trajectories which is propagated to the next tracker layer until the outermost tracker layer is reached. The trajectory information is updated with the compatible measurements found at each step. After having built trajectories, a cleaning based on the number of hits and the χ^2 of the track fit is applied to resolve ambiguities between multiple trajectories that may result from a single seed. In a final step, the reconstructed tracks are fitted once more, this time without a beam-spot constraint, using the hits in the muon chambers as well as ones in the silicon tracker (global fit). A second cleaning based on a χ^2 cut is applied to select the final global muon candidates [13].

At this level, some filters, mainly p_T thresholds, rapidity limitations and impact parameter cuts, are applied [22].

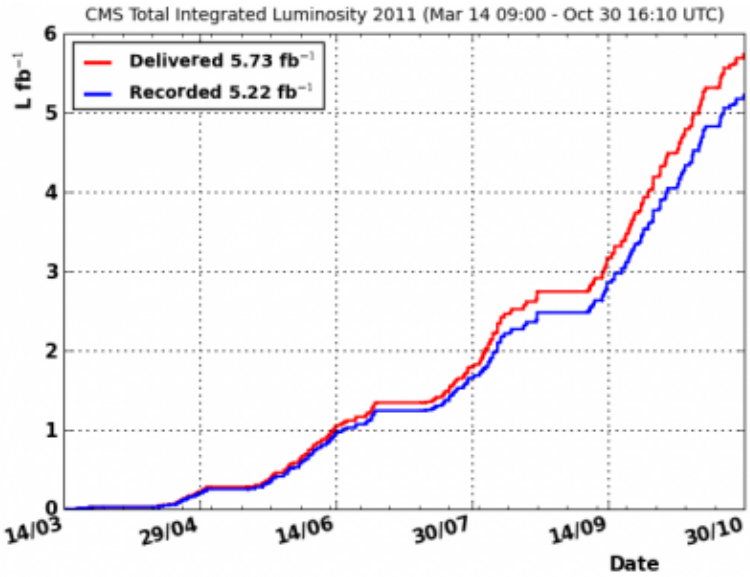

Figure 3.6: The graph shows the integrated luminosity delivered by the LHC (red) and collected by CMS (blue) in the 2011 pp collision run [23].

3.6 CMS Detector Performance

The performance of CMS in 2011 was outstanding. It recorded 5.22 fb^{-1} of the 5.73 fb^{-1} of data which the LHC delivered during proton-proton collisions with a center of mass energy of 7 TeV (see Fig. 3.6). In total, the LHC provided excellent 1 364 hours of stable beams in 2011 with an instantaneous luminosity of up to 3.55×10^{33} Hz/cm^2. This peak value was reached on 26th October 2011 [23].

In comparison, the total integrated luminosity delivered by the LHC in 2010 was 47.03 pb^{-1} whereof CMS recorded 43.17 pb^{-1} [24]. In 2012, an operation of the LHC at $\sqrt{s} = 8$ TeV is foreseen which could give even more than 15 fb^{-1} [25].

CHAPTER 4

Quarkonium Polarization

4.1 Quarkonia

In 1974, a new particle, named J, was discovered by a research group led by Samuel Ting at Brookhaven National Laboratory (BNL) [26] while almost at the same time, another group headed by Burton Richter found the Ψ at the Stanford Linear Accelerator Complex (SLAC) [27]. Both groups independently discovered the same particle, now called J/ψ, consisting of a charm quark and its antiquark with a mass resonance at 3.1 GeV/c^2 (see Fig. 4.1). The J/ψ was the first direct experimental sign of a charm quark and opened up a whole new field in particle physics – quarkonium physics.

Quarkonia are bound states of a heavy quark and its antiquark and exist as colorless, uncharged mesons. In general, all $c\bar{c}$ (charmonium) and $b\bar{b}$ (bottomonium) states are called quarkonia. The corresponding $t\bar{t}$ state does not exist. Because of its high mass, the top quark decays through the electroweak interaction before a bound state can form.

Quarkonia are characterized by the spin S, the angular momentum L and the total angular momentum $J = S + L$ and are referred to as J^{PC} where P is the parity $P = -1^{L+1}$ and C is the charge conjugation $C = -1^{L+S}$. They can also be written in the spectroscopic notation $n^{2S+1}L_J$ where n is the principal quantum number. The properties of the mesons that are most relevant to this thesis are summarized in Table 4.1.

Figure 4.2 exhibits the charmonium and bottomonium spectra. Also shown are decays of higher states to the 1S ground states. A large fraction of the J/ψ's produced in hadron-hadron collisions originate from the decay of heavier charmonium states. Together with the directly produced J/ψ's, these feed-down contributions form the so called prompt component of the J/ψ decay. At low p_T, about 67% of the prompt J/ψ's are directly produced while about $8.1 \pm 0.3\%$ come from the Ψ' and $25 \pm 5\%$ from the χ_c states [29].

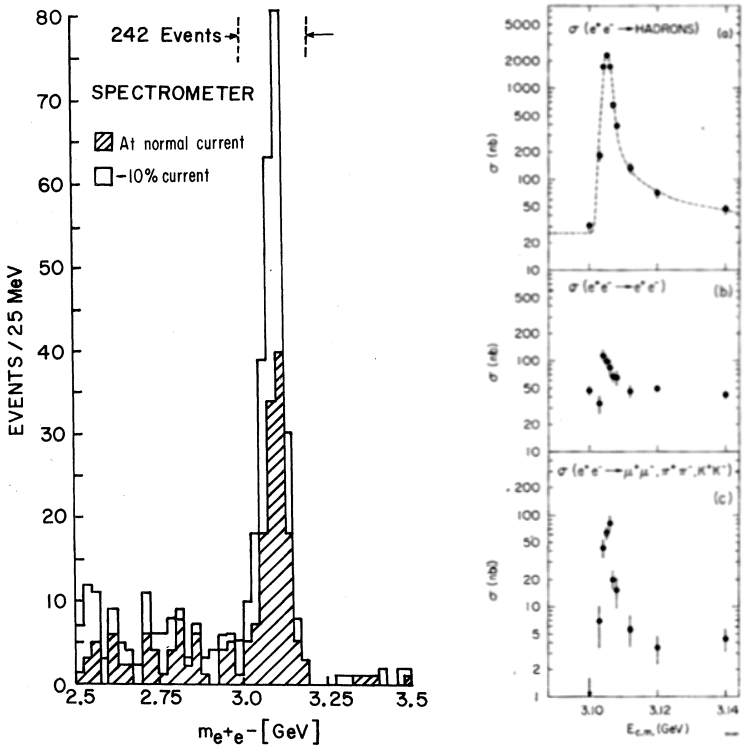

(a) Mass spectrum (b) Cross-section vs energy

Figure 4.1: The first observation of the J/ψ: (a) Mass spectrum showing the existence of J/ψ obtained at the BNL in p + Be collisions [26]. (b) Cross-section versus energy measured in e^+e^- collisions at SLAC for multi-hadron final states (top), e^+e^- final states (middle) and $\mu^+\mu^-, \pi^+\pi^-$ and K^+K^- final states (bottom), showing a resonance at the energy of 3.1 GeV/c^2 [27].

Additionally, there are decays from b hadrons: B^+, B_s, B^0 and Λ_b. J/ψ's originating from these decays can be identified easily since the b hadrons decay to J/ψ's after lifetimes of the order of 10^{-12} s and hence can be tagged through the displaced secondary vertex. Therefore, this contribution is called the non-prompt component. For the bottomonium, there is no delayed production mechanism.

The $\psi(2S)$ and $\Upsilon(3S)$ states are particularly interesting for the polarization measurement since they do not have feed-down contributions from heavier states. The polarization of these higher χ states can be very different to the one of the directly produced J/ψ's because of their different parity and angular momentum properties in comparison to the directly produced J/ψ or Υ. They also originate from different partonic processes [30].

The leptonic decay mode of J/ψ has a branching ratio of about 5.9% for the J/$\psi \to \mu^+\mu^-$ as well as the J/$\psi \to e^+e^-$ channel. For $\Upsilon(1S)$, the corresponding

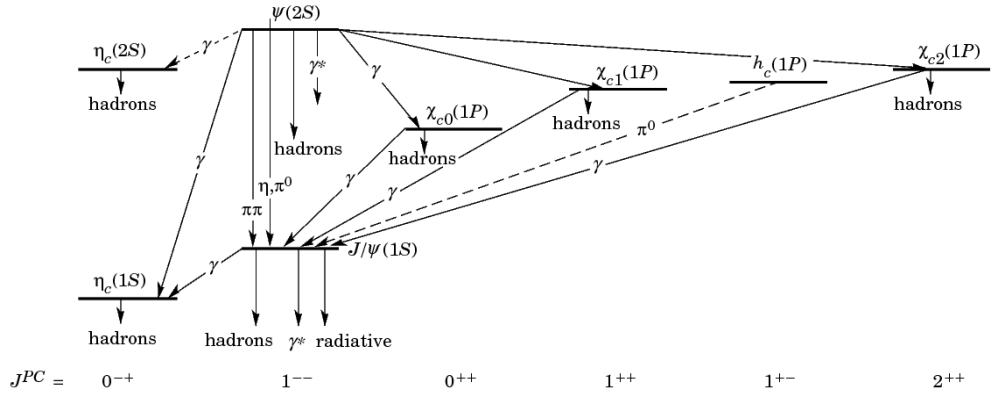

(a) Charmonium spectrum

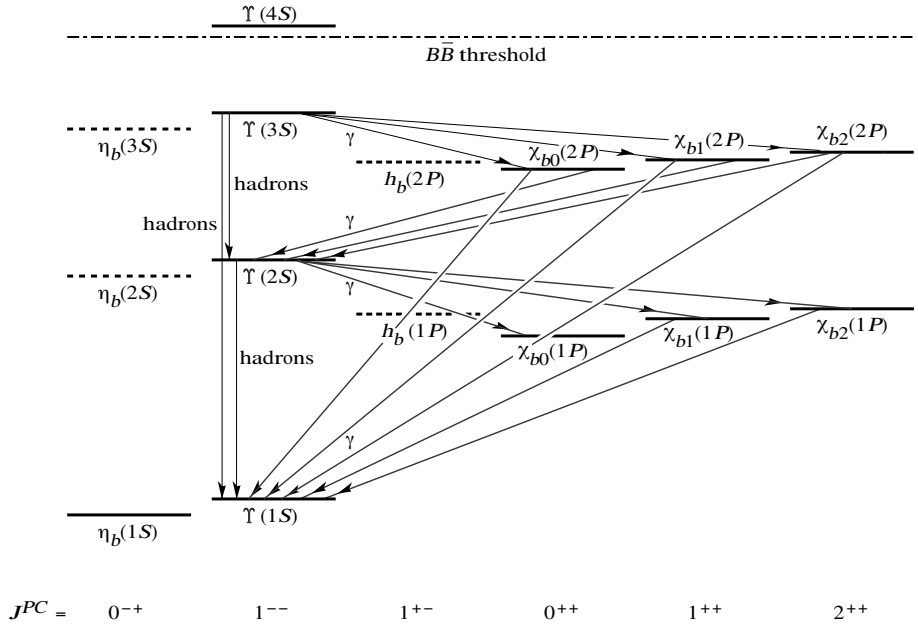

(b) Bottomonium spectrum

Figure 4.2: Quarkonium spectra: (a) Charmonium spectrum and decay modes, (b) bottomonium spectrum and decay modes. Heavier states are higher up in the diagram [28].

Table 4.1: Properties of quarkonium mesons [28].

Meson	J^{PC}	$n^{2S+1}L_J$	**Mass [MeV]**	**Full Width**
J/ψ	1^{--}	1^3S_1	$3\ 096.916 \pm 0.011$	92.9 ± 2.8 keV
χ_{c0}	0^{++}	1^3P_0	$3\ 414.75 \pm 0.31$	10.3 ± 0.6 MeV
χ_{c1}	1^{++}	1^3P_1	$3\ 510.66 \pm 0.07$	0.86 ± 0.05 MeV
χ_{c2}	2^{++}	1^3P_2	$3\ 556.20 \pm 0.09$	1.97 ± 0.11 MeV
$\Psi(2S)$	1^{--}	2^3S_1	$3\ 686.09 \pm 0.04$	304 ± 9 keV
$\Upsilon(1S)$	1^{--}	1^3S_1	$9\ 460.30 \pm 0.26$	54.02 ± 1.25 keV
$\chi_{b0}(1P)$	0^{++}	1^3P_0	$9\ 859.44 \pm 0.42 \pm 0.31$	-
$\chi_{b1}(1P)$	1^{++}	1^3P_1	$9\ 892.78 \pm 0.26 \pm 0.31$	-
$\chi_{b2}(1P)$	2^{++}	1^3P_2	$9\ 912.21 \pm 0.26 \pm 0.31$	-
$\Upsilon(2S)$	1^{--}	2^3S_1	$10\ 023.26 \pm 0.31$	31.98 ± 2.63 keV
$\chi_{b0}(2P)$	0^{++}	2^3P_0	$10\ 232.50 \pm 0.40 \pm 0.50$	-
$\chi_{b1}(2P)$	1^{++}	2^3P_1	$10\ 255.46 \pm 0.22 \pm 0.50$	-
$\chi_{b2}(2P)$	2^{++}	2^3P_2	$10\ 268.5 \pm 0.22 \pm 0.50$	-
$\Upsilon(3S)$	1^{--}	3^3S_1	$10\ 355.20 \pm 0.50$	20.32 ± 1.85keV

branching ratios are 2.4% for the dielectron decay and 2.5% for the dimuon decay [28]. The CMS quarkonium polarization study focuses on the decay into dimuons since CMS was designed for precise muon detection.

4.2 Quarkonium Polarization

Vector quarkonia ($J^{PC} = 1^{--}$) can be produced in one of three possible eigenstates of the angular momentum component J_z ($J_z = -1, 0, +1$) along a characteristic quantization axis or in a certain mixture of these three. They can decay electromagnetically into two leptons which represents the cleanest way to get the polarization and the production yield of a quarkonium. The term polarization refers to the average angular momentum state measured by studying the decay distribution with respect to a certain reference frame. When the decay distribution is spherically symmetric, the particle is unpolarized while it is called polarized when the distribution shows anisotropy. These preferred *spin alignments* are due to angular momentum conservation and basic symmetries of the electromagnetic and strong interactions. Particles with spin projection $J_z = \pm 1$ are called transversely and particles with $J_z = 0$ longitudinally polarized [31].

Different elementary processes displayed in Fig. 4.3 give rise to different types of polarization. Vector quarkonia can be produced in e^+e^- annihilation via an intermediate photon as shown in Fig. 4.3a. Due to helicity and angular momentum conservation applied in the limit of vanishing mass, they have the angular momentum component $J_z = \pm 1$ along the direction of the colliding leptons (corresponding to the z-axis of the Collins-Soper (CS) frame which is introduced later on in this chapter). The annihilating electron and positron must have opposite helicities since the intermediate photon has zero helicity. Their momenta in the

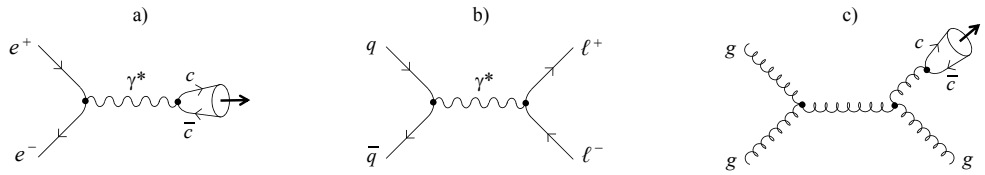

Figure 4.3: Example of leading order diagrams of production processes giving rise to observable polarization: (a) quarkonium production in e^+e^- annihilation via an intermediate photon, (b) Drell-Yan lepton pair production in quark-antiquark annihilation, (c) quarkonium production through gluon fragmentation [31].

laboratory are opposite, thus leading to a parallel spin of the two leptons and, because of angular momentum conservation, to the angular momentum component $J_z = \pm 1$ of the produced quarkonium [31].

Figure 4.3b shows the production of Drell-Yan lepton pairs in quark-antiquark annihilation. The same reasoning applies here. The annihilating quark-antiquark pair, in the limit of vanishing mass, must have opposite helicities leading to the angular momentum component $J_z = \pm 1$ of the produced lepton pair along the beam direction (CS axis) [31].

At very high p_T, the dominant production process of quarkonia is gluon fragmentation where a high energy gluon is split into a quarkonium state and other partons (see Fig. 4.3c) [32]. The fragmenting gluon is believed to have helicity ± 1 and pass it on to the resulting state, which is predicted to be dominated by the color-octet state $c\bar{c}[^3S_1^{(8)}]$ in Non Relativistic (NR) Quantum ChromoDynamics (QCD). During the non-perturbative transition from the color-octet state to the color neutral physical quarkonium state via gluon emission, the helicity properties are transferred. Therefore, the observed quarkonium has the angular momentum component $J_z = \pm 1$, this time along its own flight direction (corresponding to the z-axis of the Helicity (HX) frame).

The polarization is always measured with respect to a certain reference frame and depends on the choice of it. Popular choices are the Helicity (HX) and the Collins-Soper (CS) frames – representing two extreme opposite and physically interesting cases and differing by a rotation of up to 90° – and the Gottfried-Jackson (GJ) frame.

The two colliding beams as seen from the quarkonium rest frame form the production plane. The y-axis is taken as perpendicular to the production plane. The quantization axis z is chosen in the production plane according to conventions, meaning that all the possible definitions of reference frames differ only by a rotation around the y-axis. The polar angle θ is defined as the angle between the direction of one of the decay products, conventionally the positive lepton, and the chosen z-axis while the azimuthal angle ϕ is measured with respect to the production plane. Figure 4.4 illustrates the coordinate system.

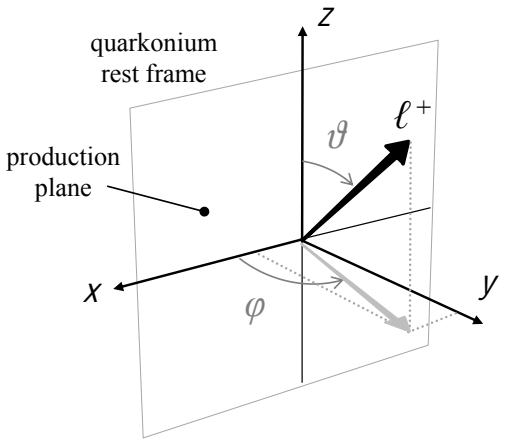

Figure 4.4: The coordinate system for the measurement of the angular decay distribution in the quarkonium rest frame [31].

Figure 4.5 shows the definitions of the z-axis of the HX, CS and GJ frames. The z-axis of the HX frame coincides with the momentum of the quarkonium as it is seen in the center of mass system of the colliding beams. The CS axis is defined as the bisector of the angle between one beam and the opposite momentum direction of the other beam. It is approximately along the direction of the colliding beams seen in the center of mass system. The GJ axis is along the direction of the momentum of one of the two beams.

Additionally to the CS and HX frames, the CMS quarkonia polarization analysis also considers the Perpendicular Helicity (PX) frame where the z-axis is perpendicular to the CS axis. The PX frame exhibits a simple shape of the acceptance and efficiency coverage which reflects most directly limitations in the muon acceptance [33].

The angular decay distribution in its most general form can be written as:

$$\begin{aligned}\mathcal{W}(\cos\theta,\phi) \;\propto\; & \frac{1}{(3+\lambda_\theta)}(1+\lambda_\theta\cos^2\theta+\lambda_\phi\sin^2\theta\cos 2\phi+ \\ & + \lambda_{\theta\phi}\sin 2\theta\cos\phi+\lambda_\phi^{\perp}\sin^2\theta\sin 2\phi+\lambda_{\theta\phi}^{\perp}\sin 2\theta\sin\phi+ \\ & + 2A_\theta\cos\theta+2A_\phi\sin\theta\cos\phi+2A_\phi^{\perp}\sin\theta\sin\phi) \qquad (4.1)\end{aligned}$$

where λ_θ, λ_ϕ and $\lambda_{\theta\phi}$ are the polarization parameters containing information about the average angular momentum composition and A_θ and A_ϕ are parity-asymmetry parameters expressing the parity properties of the decay [34]. Only parity-conserving processes ($\phi \to \phi+\pi$ and $\theta \to \theta+\pi$) are considered, resulting in the parameters A_θ, A_ϕ and $A_\phi^{\perp}$ to be equal to 0. The invariance under parity transformation leads to the symmetry by reflection about the production plane ($\phi \to -\phi$) which makes the terms $\sin^2\theta\sin 2\phi$ and $\sin 2\theta\sin\phi$ unobservable because they vanish on average.

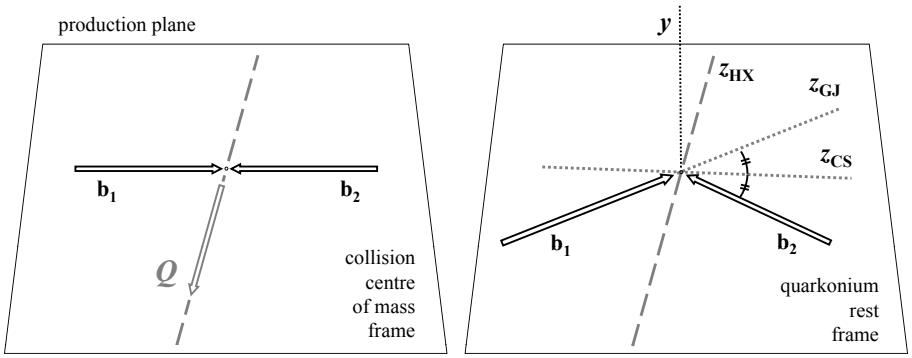

Figure 4.5: Definition of the quantization axis z in the CS, HX and GJ frame with respect to the directions of the quarkonium ($\mathcal{Q}$) and the colliding beams (b1, b2) [31].

This results into the most general observable average angular decay distribution:

$$\mathcal{W}(\cos\theta,\phi) \propto \frac{1}{(3+\lambda_\theta)}(1+\lambda_\theta\cos^2\theta+\lambda_\phi\sin^2\theta\cos 2\phi+\lambda_{\theta\phi}\sin 2\theta\cos\phi) \quad (4.2)$$

If the polarization parameters $\lambda_\theta, \lambda_\phi$ and $\lambda_{\theta\phi}$ are non-zero, the decay distribution is anisotropic, meaning that the quarkonium is polarized [31].

In the past, experiments only used one of the three polarization parameter, namely λ_θ, to measure the polarization. They also used different reference frames which made it difficult to interpret the results which all seem to contradict each other. Figure 4.6 shows the results of the Experiment 866 (E866) at Fermilab [35], the Collider Detector at Fermilab (CDF) [36] and the HERA-B experiment (Hadron Elektron Ring Anlage) in Hamburg [37] for the J/ψ polarization. E866 found a small transverse polarization ($\lambda_\theta \approx 0.1$) in the CS frame without any obvious dependence on the transverse momentum. HERA-B determined a longitudinal polarization, which increases with decreasing p_T, in the same frame and same p_T range. CDF, however, measured the polarization in the HX frame and obtained a slightly longitudinal polarization that increases with p_T for run I. It also determined the polarization of the J/ψ in a second run, this time measuring a transverse polarization, strongly depending on p_T (see Fig. 4.7) [38].

Not only do the experiments disagree, but also the theoretical models seem to fail to describe the experiments as displayed in Fig. 4.8. There are (at least) two different theoretical approaches for quarkonium polarization:

- **Color Singlet Model (CSM):** The CSM assumes that quarkonia are produced as pure color-singlet states, thus ignoring all long distance effects that could come from color-octet states. The quarkonia are determined by the original quantum number of the initial $q\bar{q}$ state. The Next to Leading

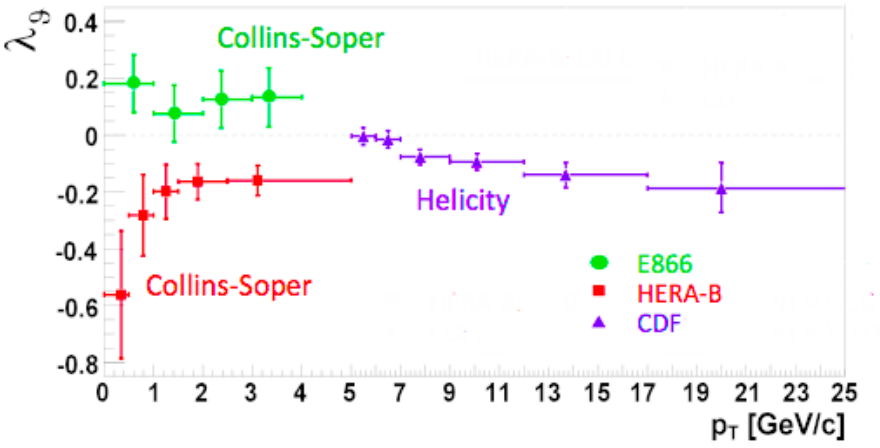

Figure 4.6: Polarization parameter λ_θ as a function of p_T measured by E866, HERA-B and CDF in the CS or the HX frame [39].

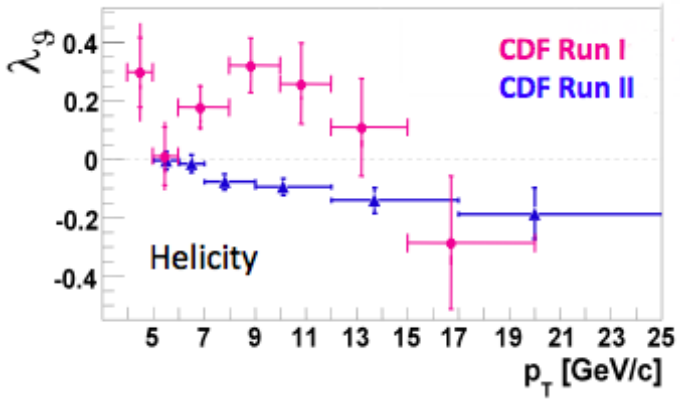

Figure 4.7: CDF run I and run II results for the J/ψ polarization measurement as a function of p_T in the HX frame [40].

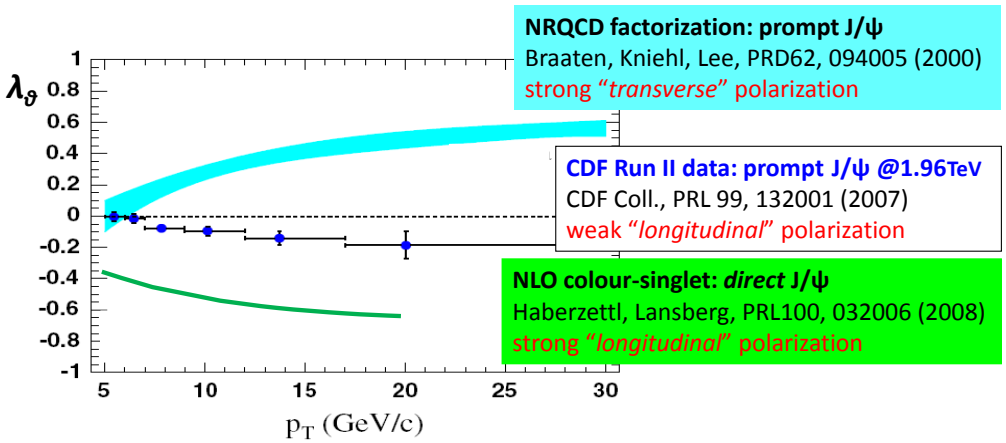

Figure 4.8: CDF run I data results in comparison to the NRQCD and the NLO CSM predictions [36].

Order (NLO) calcualtions of the CSM predict the polarization of prompt J/ψ's to be longitudinal in the HX frame [41].

- **Non Relativistic QCD factorization:** Quarkonia are produced as colored quark pairs. Color-octet terms are expected to dominate at large p_T in hadron colliders [42]. The polarization of directly produced J/ψ's is predicted to be transverse in the HX frame.

The seemingly contradictory results from experiment and theory makes the quarkonium polarization measurement a very interesting analysis, but they also show that a new more consistent approach using the full physical information is needed.

4.3 A Frame-Invariant Formalism

A new framework for polarization measurements was proposed in Ref. [43], enabling unambiguous and straightforward comparisons between different experimental results.

First of all, the full decay angular distribution, i.e. all three polarization parameters, has to be measured instead of just one parameter since the extraction of only one parameter allows for ambiguous interpretations. As Fig. 4.9 shows, the determination of λ_θ alone does not allow to distinguish between a longitudinal (doughnut-shaped) or transverse (peanut-shaped) angular distribution. Therefore, the full angular distribution must be extracted. This should be done in at least two reference frames since the observed polarization strongly depends on the chosen frame as is also illustrated in Fig. 4.9. At mid-rapidity, the HX and CS frames are orthogonal to each other which makes them a good minimal set of polarization frames.

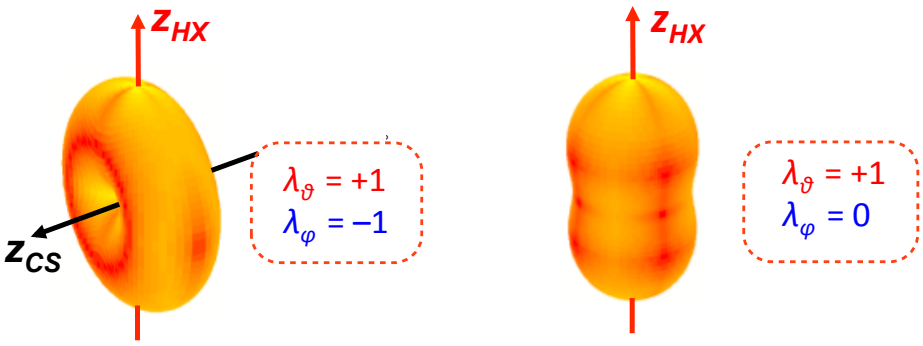

Figure 4.9: Extracting only one polarization parameter in one reference frame leads to ambiguous polarization scenarios.

The seemingly contradictory J/ψ results presented in the previous section 4.2 can be consistently described when the same reference frame is chosen. The CS frame, i.e. along the direction of the colliding partons, was assumed to be the most suitable axis system [39]. Fig. 4.10 shows that the J/ψ's that were directly produced in E866, HERA-B and CDF, could have been longitudinally polarized at low momentum and transversely polarized at high momentum in the CS frame.

Another reason for performing the analysis in more than one reference frame is that the J/ψ acquires its polarization with respect to a *natural* polarization axis which is a priori unknown. The orientation of the polar axis of the chosen frame with respect to this *natural* axis changes from event to event, resulting into a superposition of many equally shaped, but rotated distributions. The average angular distribution is thus smeared to a more spherically symmetric shape [39]. To find the frame closest to the *natural* frame, one needs to determine the smallest $\lambda_{\theta\phi}$ value of the chosen reference frames [44].

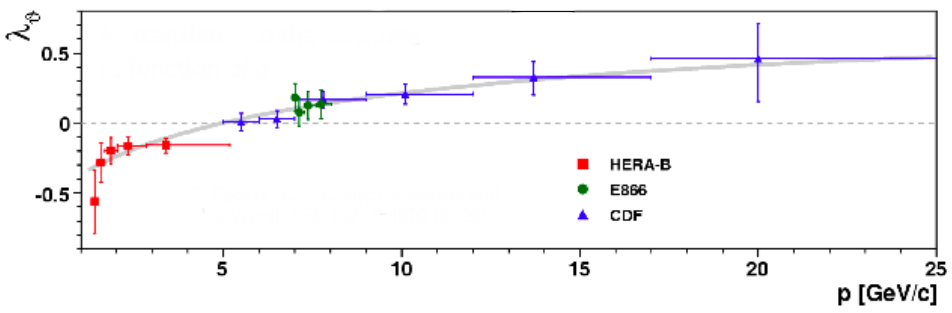

Figure 4.10: λ_θ as a function of p in the CS frame calculated with data from E866, HERA-B and CDF run I. The previously contradictory results are now consistent [39].

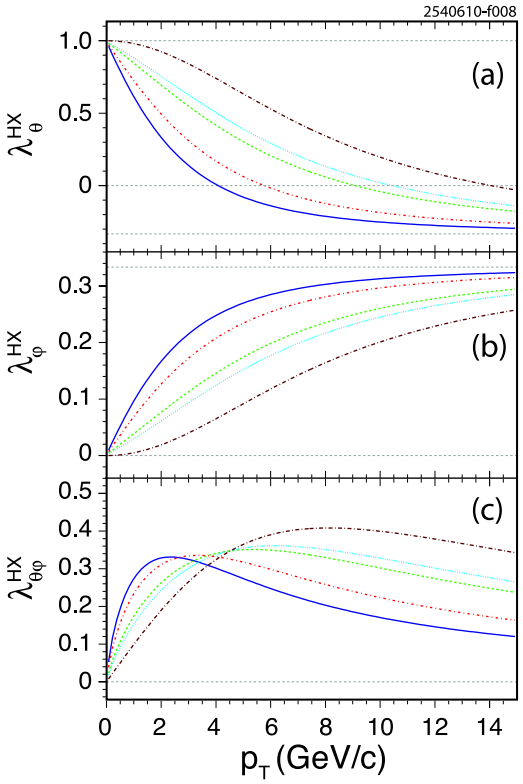

Figure 4.11: Polarization parameters (a) λ_θ, (b) λ_ϕ and (c) $\lambda_{\theta\phi}$ for the $\Upsilon(1S)$ angular distribution as a function of p_T for a fully transverse polarization $\lambda_\theta = +1$ in the CS frame translated to the HX frame. The curves correspond to different rapidity intervals: $|y| < 0.6$ (CDF, blue line), $|y| < 0.9$ (ALICE, e^+e^- channel, dashed red line), $|y| < 1.8$ (D0, dashed green line), $|y| < 2.5$ (ATLAS and CMS, dashed turquois line), $2 < |y| < 5$ (LHC-b, dashed brown line). For simplicity, the events were generated flat in y [31].

Moreover, kinematic averages as for example over the full rapidity range should be avoided since the polarization depends on the kinematics. Figure 4.11 shows how a fully transverse polarization in the CS frame translates to different p_T dependences of the polarization in different rapidity ranges in the HX frame. Experiments measure the average angular distribution of events accepted by the detector, trigger and analysis cuts in the probed phase space window. Two experiments may find different polarization even though they cover the same kinematic range because their acceptance shapes are different. This can be solved by presenting the results in narrow (p_T, y) intervals [43].

Furthermore, frame-invariant parameters can be calculated from the full angular decay distribution as a consequence of its rotational invariance. These parameters facilitate the comparison between experiments and can, when evaluated in

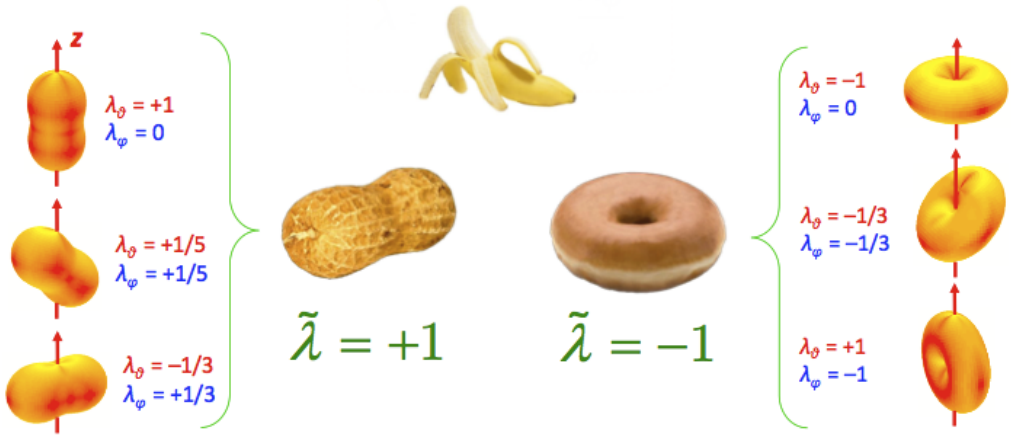

Figure 4.12: The frame-invariant parameter $\tilde{\lambda}$ characterizes the shape of the angular distribution and helps unambiguously determining the polarization. $\tilde{\lambda} = -1$ corresponds to a fully longitudinal polarization and a doughnut-shaped distribution while $\tilde{\lambda} = +1$ indicates a fully transverse polarization and a peanut-shaped distribution. A banana-shaped distribution is not a possible polarization scenario.

different frames, further be used as self-consistency check which can demonstrate unaccounted systematic effects or biases like not well subtracted background or badly described detector acceptances [43].

One of the frame-invariant parameters is defined as

$$\tilde{\lambda} = \frac{\lambda_\theta + 3\lambda_\phi}{1 - \lambda_\phi} \tag{4.3}$$

with λ_θ and λ_ϕ evaluated in the same chosen reference frame.

It characterizes the shape of the decay distribution which is frame-invariant as can be seen in Fig. 4.12. A fully longitudinal polarization is indicated by $\tilde{\lambda} = -1$ while the fully transverse polarization has $\tilde{\lambda} = +1$.

The rotational invariance also imposes constraints on the polarization parameters. Since λ_θ never exceeds 1, the absolute parameters of the other two parameters, λ_ϕ and $\lambda_{\theta\phi}$, are also limited to 1 or below. The frame-independent inequalities deduced from the rotational invariance also show that $|\lambda_\phi| \leq 0.5$ for $\lambda_\theta = 0$ and that $|\lambda_\phi|$ vanishes for $\lambda_\theta \to -1$. Figure 4.13 exhibits the allowed regions for the decay angular parameters. A more detailed description can be found in [31].

This frame-invariant formalism allows not only to facilitate the comparison between experiments and theoretical calculations, but it also provides a self-consistency check while minimizing the dependence of the measured result on the experimental acceptance. Moreover, it is independent of any assumptions on theoretical quarkonium production or polarization models.

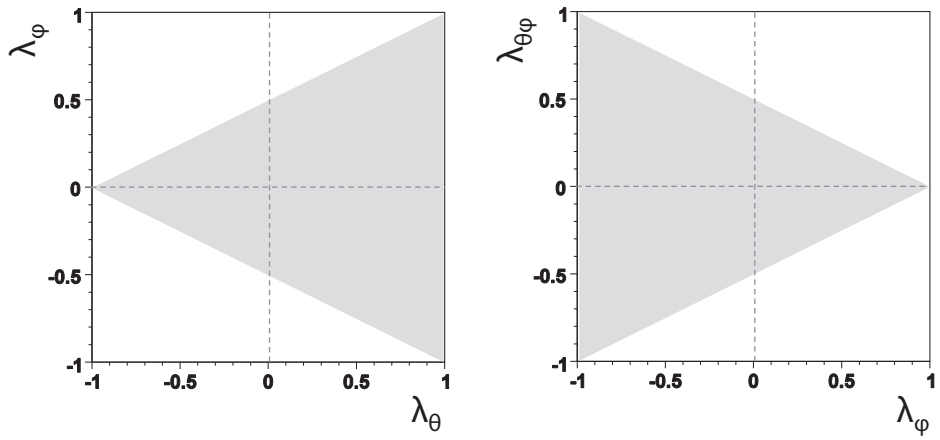

Figure 4.13: Allowed regions (grey) for the polarization parameters [31].

4.4 Recent Results

Recent quarkonium polarization measurements made use of this frame-invariant approach. CDF redid its analysis with data from run II and determined the full angular decay distribution of the $\Upsilon(nS)$ states decaying to $\mu^+\mu^-$ in the CS as well as the HX frame [45]. The consistency was checked by also calculating the frame-invariant parameter $\tilde{\lambda}$. Figure 4.14 shows the results of $\tilde{\lambda}$ for the $\Upsilon(1S)$, $\Upsilon(2S)$ and $\Upsilon(3S)$. This is the first published study where the complete three-dimensional angular decay distribution of all the $\Upsilon(nS)$ states was measured. The polarization for all the states is consistent with zero.

CDF also found that there is a significant difference between the polarization parameters of the signal and the backgrounds, making a good background subtraction even more important.

The new result which is different from the one obtained by the previous CDF run II analysis is consistent with the CDF run I measurement (see Fig. 4.15).

The ALICE experiment recently measured the polar and azimuthal angle distributions of the J/ψ decaying into two muons in the CS and the HX frame [47]. Due to the limited statistics, the polarization parameters could not be extracted at the same time. Therefore, λ_θ was determined first, integrating over λ_ϕ, and then λ_ϕ was obtained. The frame-invariant parameter $\tilde{\lambda}$ was used to impose constraints on the fit to extract the parameters.

The results presented in Fig. 4.16 show that the polarization parameters λ_θ and λ_ϕ are consistent with zero, except λ_θ in the HX frame which exhibits some longitudinal polarization at low p_T, however vanishing with increasing p_T.

The polarization obtained by CDF and ALICE which is consistent with zero is surprising and very interesting because the angular distribution of J^{--} states is never intrinsically isotropic [31]. Only a lucky superposition of quarkonia

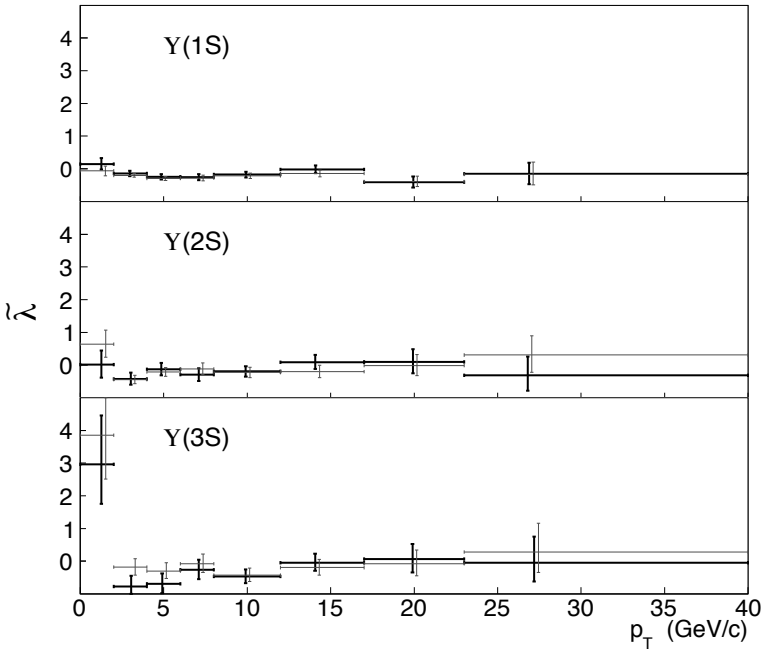

Figure 4.14: $\tilde{\lambda}$ as a function of p_T for the $\Upsilon(1S)$ (top), the $\Upsilon(2S)$ (middle) and the $\Upsilon(3S)$ state (bottom), measured in CDF run II [45].

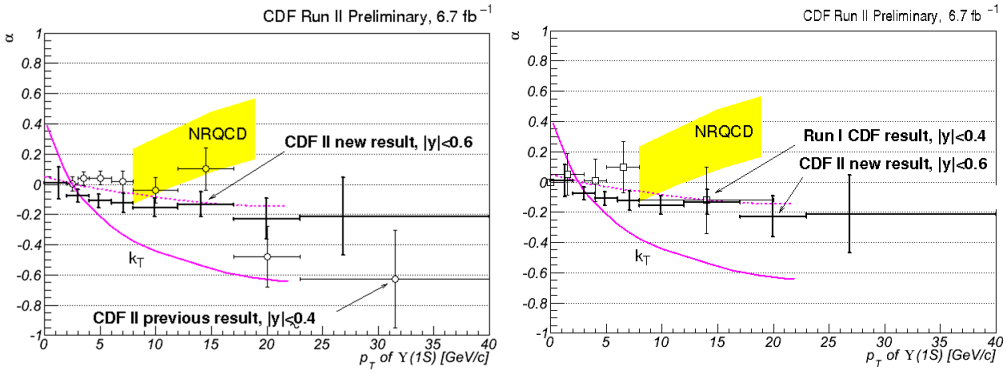

Figure 4.15: The polarization parameter $\alpha \equiv \lambda_\theta$ in the HX frame obtained by the new CDF run II result (solid black crosses) in comparison to the old run II (left, hollow points) and the run I measurement (right, hollow points). Also the NRQCD (yellow shaded area) and the CSM predictions (pink line) are displayed [46].

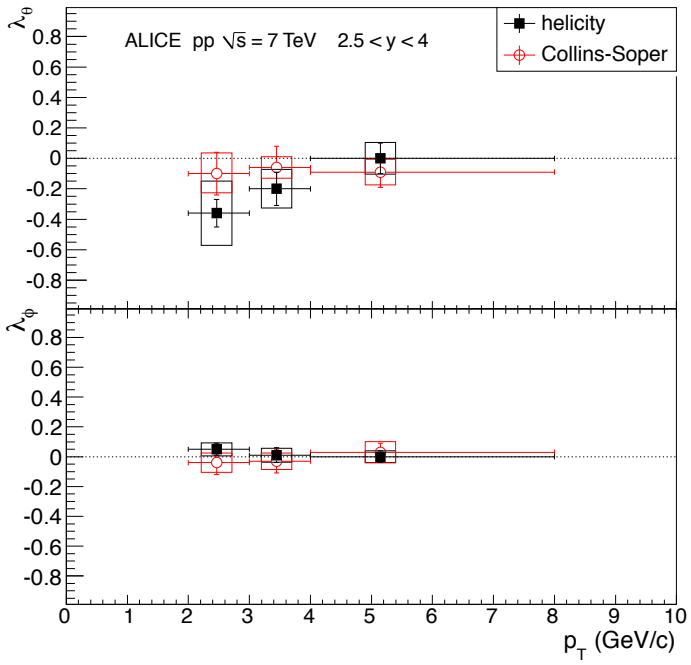

Figure 4.16: λ_θ (top) and λ_ϕ (bottom) as a function of p_T for the J/ψ measured in the CS and HX frame. The error bars show the statistical errors while the boxes represent the systematic uncertainties [47].

production from more than just one spin state could result in a cancellation of all three polarization parameters.

When a quarkonium comes from a J = 0 state, the vanishing of all polarization parameters is observed, however not at all momenta [48]. The pre-quarkonium state transforms into a quarkonium state by the emission of a gluon. This process is identical to the radiative χ_{c0} decay ($\chi_{c0} \to \mathrm{J}/\psi + \gamma$). In the χ_{c0} rest frame, the J/ψ is fully transversely polarized with respect to the photon direction. However, it becomes totally unpolarized in the collision center of mass frame when forgetting the existence of the photon. At low momentum ($p \lesssim M(\mathrm{J}/\psi)$), the polarization observed in the HX frame goes from fully transverse to zero. It would in principle be possible to see that the J/ψ is actually polarized, even if the average decay distribution at higher momentum is isotropic, by separating the two photon polarization states ($J_z = +1, J_z = -1$). The transition from the χ_{c0} leads to unpolarized J/ψ's in the collision center of mass frame because it is the sum of two subprocesses:

1. $\chi_{c0} \to \mathrm{J}/\psi + \gamma(+1)$
2. $\chi_{c0} \to \mathrm{J}/\psi + \gamma(-1)$

The J/ψ decay distribution of these two subprocesses are anisotropic and of opposite sign, resulting in an isotropic sum.

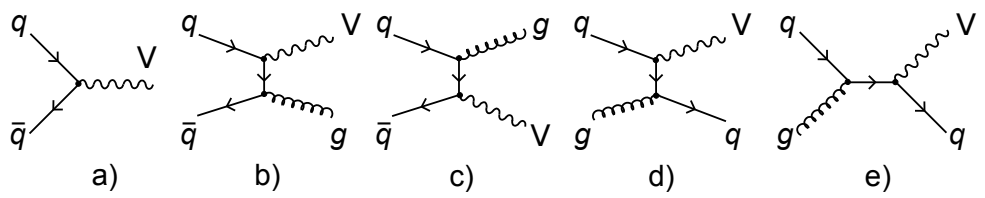

Figure 4.17: Leading order $\mathcal{O}(\alpha_S^0)$ and $\mathcal{O}(\alpha_S^1)$ QCD correction processes for V = Z, γ^*, W production: All processes give rise to transverse dilepton polarizations, but along different quantization axis: (a) CS, (b, c, d) GJ and (e) HX [34].

Therefore, the observation of unpolarized quarkonia is very interesting and would also rule out the CSM where final states cannot be produced by non-perturbative effects like a transition from a J = 0 state [48].

4.5 Importance of the Polarization Measurement

The polarization analysis is not only interesting for quarkonia, but also for other systems. A few examples are discussed in the following:

- **Understanding still unexplained production mechanisms:** The polarization represents the biggest uncertainty (about 20%) in the study of quarkonium production cross section. Experimental results for the cross-sections may be biased because they were assuming the wrong polarization or relying on the wrong theoretical model. The polarization analysis will also help to check the importance of formation of the quark-antiquark bound state which is a long-distance effect.

- **Identifying processes:** As already outlined in Section 4.2, different production processes give rise to different polarization. Therefore, the polarization can be used to identify the underlying processes. It can also help to characterize signal and background processes and estimate their relative contributions in the distribution of events.

- **Testing QCD calculations:** The Lam-Tung relation [49] that accounts for Drell-Yan production in perturbative QCD is a special case of a frame-independent quantity:

$$\lambda_\theta + 4\lambda_\phi = 1 \tag{4.4}$$

  It is not only a consequence of rotation invariance, but also of helicity conservation. The latter leads to a fully transverse polarization of all contributing processes, even if with respect to different reference frames. Figure 4.17

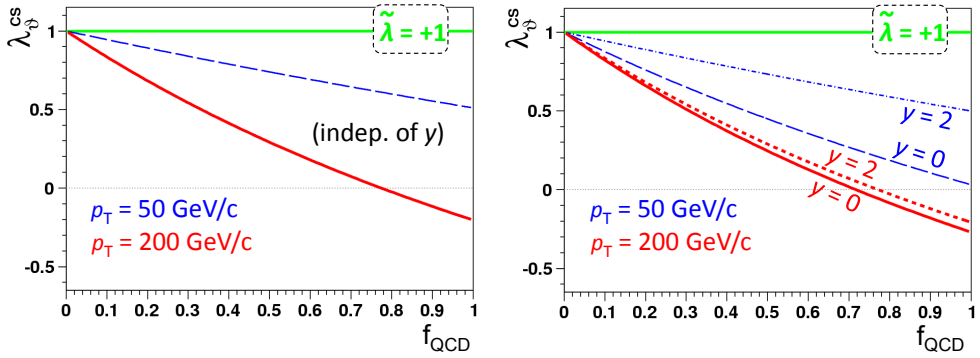

Figure 4.18: $\tilde{\lambda}_{CS}$ of the W decay as a function of the relative contribution of leading order QCD corrections for different p_T and y values. The contributions are either assumed to be dominated by the quark-antiquark diagrams (left) or by the quark-gluon diagrams (right). Only the latter are rapidity-dependent [50].

shows the leading order $\mathcal{O}(\alpha_S^0)$ and $\mathcal{O}(\alpha_S^1)$ QCD correction processes contributing to the direct Z, γ^* and W production. The process described in Fig. 4.17a gives rise to a fully transversely polarized lepton pair with respect to the CS frame, while the ones in Fig. 4.17b, c and d are transversely polarized with respect to the GJ frame and in Fig. 4.17e with respect to the HX frame. Measuring the frame-independent variable $\tilde{\lambda}$ will therefore always give the value $+1$. The polar anisotropy λ_θ however helps disentangling the contributions from the quark-antiquark and quark-gluon processes.

λ_θ observed in the CS frame is maximal only at $p_T = 0$. With increasing p_T, the observed polarization is reduced because the relative contributions of the transverse polarization in the other reference frames. This p_T dependence is displayed in Fig. 4.18. In the case of the quark-antiquark diagrams being the dominant contribution to the leading order QCD corrections, λ_θ^{CS} is rapidity-independent while in case of a dominance of quark-gluon processes the polar anisotropy depends on the rapidity [34].

An accurate rapidity-dependent measurement of λ_θ^{CS} at not too high p_T can therefore test if QCD corrections are dominated by quark-antiquark or by quark-gluon diagrams.

- **Measuring parity violation:** The parity-violating terms in Eqn. 4.1 can be transformed into a rotation-invariant quantity:

$$\begin{aligned} \mathcal{A} &= \frac{4}{3+\lambda_\theta}\sqrt{A_\theta^2 + A_\phi^2 + A_\phi^{\perp 2}} \\ &= \frac{4}{3}\sqrt{\mathcal{A}_{\cos\theta}^2 + \mathcal{A}_{\cos\phi}^2 + \mathcal{A}_{\sin\phi}^{\perp 2}} \end{aligned} \tag{4.5}$$

where $\mathcal{A}_{\cos\theta}, \mathcal{A}_{\cos\phi}$ and $\mathcal{A}_{\sin\phi}^{\perp}$ represent the azimuthal and polar *projections* of the asymmetry. The asymmetry $\mathcal{A}_{\cos\theta}$ is the so called forward-backward

asymmetry $\mathcal{A}_{FB}$ and is usually studied experimentally in the direct Z, γ^* and W production in the CS frame.

$\mathcal{A}$ represents the magnitude of the maximal observable parity-violating asymmetry, i.e. of the net asymmetry that is measured along the polarization axis that maximizes the asymmetry.

The determination of the frame-independent variable $\mathcal{A}$ improves the significance of the measured parity-violating effect. It is not affected by a non-optimal frame choice, independent of extrinsic kinematics and can be checked in different reference frames [34].

- **Constraining Standard Model couplings:** One example is the weak mixing or Weinberg angle which can be constrained as a result of the parity violation measurement from Z, γ^* decays [50].

- **Probing Quark-Gluon Plasma formation:** At sufficiently high temperatures, the binding of heavy quarks will be impossible and the so called QGP is formed instead. It is a gas of free quarks and gluons in which the interactions can be described by perturbative QCD only.

  Usually, the feed-down contribution from χ_c states to the J/ψ production is around 30%, leaving about 70% directly produced J/ψ's and J/ψ's from feed-down from $\Psi(2S)$ decays. The feed-down from χ_c decays smears the polarization since χ_c states have different angular momentum and parity properties. As the χ_c and $\Psi(2S)$ mesons dissolve in the QGP, the polarization will change. Assuming that the J/ψ is transversely polarized ($\lambda_\theta \approx 0.7$) at high p_T, the polarization parameter λ_θ is predicted to increase from approximately 0.7 to around 1 at high values of p_T. The determination of the polarization thus provides an effective tool to detect the QGP formation in heavy ion collisions [50, 51].

4.6 Quarkonium Polarization In Brief

The polarization of vector quarkonia describes the average angular momentum state measured by studying the decay distribution with respect to a certain reference frame. Most popular choices are the Helicity, Collins-Soper and Gottfried-Jackson frames.

The most general observable average angular decay distribution can be written as:

$$W(\cos\theta, \phi) \propto \frac{1}{(3+\lambda_\theta)}(1 + \lambda_\theta \cos^2\theta + \lambda_\phi \sin^2\theta \cos 2\phi + \lambda_{\theta\phi} \sin 2\theta \cos\phi) \quad (4.6)$$

where λ_θ, λ_ϕ and $\lambda_{\theta\phi}$ are the polarization parameters.

To avoid ambiguous results as were presented in the past, a few rules should be followed:

- The full angular decay distribution, i.e. all polarization parameters, should be measured.
- This should be done in at least two different reference frames.
- A frame-invariant parameter should be used to facilitate the comparison between experiments, but also as a self-consistency check. It helps demonstrating unaccounted systematic effects or biases like not well subtracted background or badly described detector acceptances.

Moreover, feed-down contributions have to be carefully considered since the higher states have different angular momentum and parity properties and thus different polarization.

ALICE and CDF recently observed unpolarized quarkonium polarization which is a surprising result since the angular distribution of J^{--} states is never intrinsically isotropic. All polarization parameters may however cancel when the quarkonium is produced by a non-perturbative transition from a J = 0 state. The resulting isotropic distribution should not persist at all momenta, at low momentum an anisotropy should be observed.

The polarization analysis is not only an interesting measurement in its own right, but it will also help in some other aspects such as the precise determination of the quarkonium cross-section, the identification of production processes, the measurement of parity violation, testing QCD calculations or probing the formation of QGP.

CHAPTER 5

CMS Quarkonium Polarization Analysis

The measurement of the quarkonium polarization is a sensitive and complex problem. Therefore, a very careful approach is needed. The CMS quarkonium polarization analysis extracts the full set of angular distribution parameters λ_θ, λ_ϕ and $\lambda_{\theta\phi}$ as well as the invariant parameter $\tilde{\lambda}$ for dimuons resulting from the decays of S-wave quarkonia in the CS, HX and PX reference frames. It uses a minimal set of assumptions. The only input needed are the muon detection efficiencies which are determined with the Tag and Probe (TnP) method using real data in combination with a correction factor for the detector induced dimuon correlations. The TnP method is discussed in more detail in Chapter 6. No assumptions on any theoretical model are made.

The method is based on an unbinned likelihood approach. The background is subtracted on an event-to-event basis before the polarization parameters are determined. The method does not rely on any fitting or minimization algorithm and thus is simple, robust and fast [33].

The basic inputs for the determination of the polarization parameters are:

1. The muon four-vectors of the selected events.
2. The detection efficiencies: This input is very important since it is the only input that can change the extracted polarization. Already a small change in the efficiencies can alter the extracted polarization parameters drastically. Only the shape of the efficiencies, not the absolute value, is of interest since polarization is a measurement of the angular correlations.
3. The previously determined level of background.
4. The background distribution which is provided as a function of p_T, y, M, $\cos\theta$ and ϕ, where M is the invariant mass of the dimuon. Under the assumption

that the background shape under the signal peak can be obtained through interpolation between the two sidebands of the invariant mass spectrum, the background is fixed using the sideband region. Since the amount of the selected events does not allow a five-dimensional histogram, the product of the $(\cos\theta, \phi)$ and (p_T, y, M) histograms is provided.

The first step towards the extraction of the polarization parameters is the background subtraction. A fraction of events having the same $(p_T, y, M, \cos\theta, \phi)$ distribution as the background model are removed from the data sample. This is done on an event-by-event basis. After background subtraction, fiducial cuts may be applied on the data sample which, by definition, now only consists of signal events. Since the dimuon is only accepted if both muons are in the kinematic regions defined by the cuts on single muons (see Section 6.2), no acceptance correction has to be taken into account. The dimuon event is either accepted or rejected.

The likelihood $\mathcal{L}$ is built using unbinned data. It is a function of six variables:

$$\mathcal{L}(\vec{p_1}, \vec{p_2}) = \mathcal{W}(\cos\theta, \phi|\vec{\lambda})\varepsilon(\vec{p_1}, \vec{p_2}) \tag{5.1}$$

where $\vec{p_1}$ and $\vec{p_2}$ are the three-momenta of the two muons and $\mathcal{W}(\cos\theta, \phi|\vec{\lambda})$ is the assumed dimuon angular distribution defined in Equation 4.2.

The correction of the muon efficiencies are applied per event. The efficiency $\varepsilon_{\mu\mu}$ is defined as

$$\varepsilon_{\mu\mu}(\cos\theta, \phi, p_T, |y|) = \varepsilon_{\mu 1}(p_T, |\eta|) \cdot \varepsilon_{\mu 2}(p_T, |\eta|) \cdot \varepsilon_{Vtx}(\cos\theta, \phi) \cdot \rho(\cos\theta, \phi, p_T, |y|) \tag{5.2}$$

where $\varepsilon_{\mu 1}$ and $\varepsilon_{\mu 2}$ are the single muon efficiencies obtained through the TnP method as a function of the single muon's p_T and η, $\varepsilon_{Vtx}(\cos\theta, \phi)$ is the efficiency of the dimuon vertexing module as a function of the dimuon's $\cos\theta$ and ϕ and ρ is the correlation between the two muons as a function of the dimuon's p_T, $|y|$, $\cos\theta$ and ϕ. Chapter 6 discusses the efficiencies in detail.

The normalization of the likelihood cannot be performed directly on the events since they are not unpolarized. Therefore, events are generated with Monte Carlo (MC) according to the efficiency and acceptance corrected p_T, y and M distributions derived from the data events. The decay distributions of the dimuons are generated uniformly to be able to integrate uniformly over $\cos\theta$ and ϕ.

To draw samples from the likelihood function, the Metropolis-Hastings algorithm [52] based on the concept of importance sampling is used: New sets of parameters are extracted according to a given probability distribution. They are accepted or rejected depending on the likelihood ratio of the given extraction with respect to the previous one.

The multi-dimensional distributions of the accepted parameters are filled into an output file from which the posterior Probability Density Function (PDF) of the angular parameters can be read. More details about the method used to extract the angular polarization parameters can be found in [33].

5.1 Determination of the Dimuon Efficiency

The CMS quarkonium polarization analysis uses the single muon trigger efficiencies obtained through the TnP method using real data. These are calculated in two ways:

- Factorized single muon efficiencies
- Inclusive single muon efficiencies

To evaluate which of the two approaches is the better method and has the wider range of applicability, the single muon MC TnP efficiencies of both methods are compared with the true MC single muon efficiencies. Since only the shape and not the absolute value of the efficiencies is important, the better method is the one giving the flatter ratio $\varepsilon_{\mathrm{MC}}^{\mathrm{TnP}}/\varepsilon_{\mathrm{MC}}^{\mathrm{Truth}}$ over wider ranges of the single muon's p_T and $|\eta|$. The ratio also allows to determine the minimum p_T value where the two methods are applicable.

After selecting the better TnP model, the TnP efficiencies using real data must be parametrized since they show statistical fluctuations.

Details of the two approaches, the determination of the single muon efficiencies and the results are presented in Chapter 6.

The dimuon efficiency does not correspond to the product of the single muon efficiency of the first and the second muon. Therefore, correlations between the two muons, called the ρ factor, have to be taken into account. This factor is discussed in more detail in Chapter 7.

5.2 Determination of Systematic Uncertainties

Several systematic uncertainties of the polarization parameters have to be established:

1. **Systematic uncertainty from the fitting framework and the background subtraction:** The uncertainty from the fitting framework and the background subtraction is obtained with the help of MC studies using the same event populations and background fractions as in the data and different generated polarizations for signal and background. Realistic background polarizations, as suggested by the data, are checked in particular.
2. **Systematic uncertainty from the background model:** To check the assumption on the background, the polarization in the sidebands as well as in the signal window with a lifetime cut to reduce the background is measured. If the test confirms the background model, its uncertainties will be tested by changing the relative importance of the left and right sidebands and by altering the invariant mass window of the signal region.

3. **Systematic uncertainty from the efficiencies:** To determine the systematic uncertainty due to the chosen TnP model, the difference between polarization measurement using the MC truth efficiencies and the ones from the chosen TnP method are evaluated. The systematic error introduced by the parametrization of the efficiency curves is tested by varying the parametrized efficiencies by $\pm 1\sigma$. The systematic uncertainty due to the ρ factor determination is obtained through applying and not applying the ρ factor during the extraction of the polarization. The error assigned is half of the difference between the two measurements.

   The following tests are entirely based on data: Single muon efficiencies from different run periods are evaluated and compared. Also results with and without applying the efficiency of the dimuon vertexing module are evaluated. The change in polarization when removing critical kinematic regions, for example $0.2 < |\eta| < 0.3$, is looked at.

The tests mentioned above as well as the ratio $\varepsilon_{\mathrm{MC}}^{\mathrm{TnP}}/\varepsilon_{\mathrm{MC}}^{\mathrm{Truth}}$ will determine a safe kinematic region where the uncertainties are reasonably small for the final measurements.

5.3 CMS Quarkonium Polarization Analysis In Brief

All polarization parameters as well as the frame-invariant parameter $\tilde{\lambda}$ are extracted in the Helicity, the Collins-Soper and the Perpendicular Helicity frames. An unbinned likelihood approach is used. A background subtraction is performed prior to the determination of the polarization parameters on an event-to-event basis using the full event kinematics. The polarization parameters are sampled with the help of a Metropolis-Hastings algorithm. The method to measure the angular decay distribution is not a fitting algorithm and does not rely on any theoretical assumptions. It is thus a fast, simple and robust algorithm.

The efficiencies are the most important input to the framework and can drastically alter the polarization measurement if not determined correctly. Two approaches for the calculation of the efficiencies, both using the Tag and Probe method, are tested and compared in terms of their applicability over wider ranges in p_T, but also their similarity to the shape of the true MC efficiencies. The better approach is used for the final analysis.

Systematic uncertainties concerning the determination of efficiencies, the fitting framework, the background model and the background subtraction have to be evaluated.

CHAPTER 6

Tag and Probe Efficiencies

Tag and Probe (TnP) is a standard method to extract data-driven efficiencies. It uses a known dilepton resonance like J/ψ or Z to select particles. For the CMS quarkonium polarization analysis, dimuons in the J/ψ mass window ($2.8 < M(\mathrm{J}/\psi) < 3.4$ GeV/c^2) are chosen in the following way: One muon satisfying all muon requirements – called *tag* – is paired with another muon with looser selection criteria (*probe*). The selection of the tag and probe muon pair is such that their combined mass is consistent with the invariant mass of the J/ψ. Background is subtracted through fitting since it can be shown that the background exhibits a significantly lower efficiency than the signal. The efficiency is defined as the number of probes passing the selection criteria N_{pass} divided by the total number of probes N_{all} [53]:

$$\varepsilon = \frac{N_{pass}}{N_{all}} = \frac{N_{pass}}{N_{pass} + N_{fail}} \tag{6.1}$$

where N_{fail} is the number of probes failing to pass the selection criteria.

In a first step, the tag and probe muon pairs are selected with the TnP producer – for more details see Ref. [54]. If there is more than one possible probe for a tag, an arbitration can be chosen. The standard value for the fitter scripts used to extract the efficiencies presented in this chapter is *OneProbe* where only one possible probe for a tag is accepted. In case of the efficiency of the trigger dimuon vertexing module, the arbitration *OnePair* is applied instead so that the pair becomes the probe and can be studied in an unbiased way.

Secondly, the TnP analyzer is used on the dataset filled by the TnP producer to obtain the efficiencies through fitting with a defined Probability Density Function (PDF). A Crystal Ball function consisting of a Gaussian function and asymmetric tails for the signal peak and an exponential function for the background tail was chosen. The mass distribution of the tag once combined with the passing and once with the failing probes are fitted simultaneously while keeping the efficiency as a free fitting parameter [55].

In order not to bias the measurement, one has to be very careful about the selection criteria. The efficiency of the probed muon should not in any way be biased by the presence of the second muon. The correlations between the two muons induced by the detector or trigger system can not be reproduced by the TnP single muon efficiencies. These correlations, also called the ρ factor, have to be studied with other methods, but have to be taken into account in the calculation of the dimuon efficiency. More details are presented in Section 7.

To avoid inherent biases, the tag by default matches only opposite signed probes to avoid that the tag is also the probe and the efficiency of the tag passing the probe criteria is measured [53].

Furthermore, special efficiency triggers were developed to study the single muon efficiency. The low p_T single muon triggers were highly prescaled in 2011, i.e. only a fraction of events was recorded, and thus not suitable for the extraction of the data-driven single muon efficiencies since the amount of J/ψ's collected with these triggers is not big enough. The special efficiency triggers are *dimuon* triggers with one part (leg) being a muon and the other leg being either a silicon track or a L2 muon: `HLT_MuX_TrackY_Jpsi` or `HLT_MuX_L2MuY_Jpsi`. The `HLT_MuX_TrackY_Jpsi` trigger is rather impure since the second leg being a silicon track is no guarantee for becoming a second muon.

The total single muon efficiency $\varepsilon_{tot}(\mu)$ can be factorized into five sequential ones:

$$\varepsilon_{tot}(\mu) = \varepsilon_{Track}(\mu) \cdot \varepsilon_{MuonID}(\mu) \cdot \varepsilon_{MuonQual}(\mu) \cdot \varepsilon_{L1\cdot L2}(\mu) \cdot \varepsilon_{L3}(\mu) \qquad (6.2)$$

where

1. $\varepsilon_{Track}(\mu)$ is the offline muon tracking efficiency in the silicon tracker,
2. $\varepsilon_{MuonID}(\mu)$ is the offline reconstruction efficiency in the muon chambers with respect to a silicon track,
3. $\varepsilon_{MuonQual}(\mu)$ is the efficiency of the muon quality cuts with respect to an offline reconstructed muon with no quality cuts,
4. $\varepsilon_{L1\cdot L2}(\mu)$ is the combined L1 $\cdot$ L2 trigger efficiency with respect to an offline reconstructed muon with quality cuts specified in the previous efficiency and
5. $\varepsilon_{L3}(\mu)$ is the L3 trigger efficiency with respect to all the previous efficiencies.

The offline muon tracking efficiency was studied extensively by the MUON Physics Object Group (POG), a group within CMS dealing with muon reconstruction and related issues, and was thus not determined here. The efficiency is evaluated to be $(99 \pm 1)\%$ [56].

The muon reconstruction and the L1·L2 efficiencies are studied in an unbiased way with the help of the efficiency trigger `HLT_MuX_TrackY_Jpsi` while `HLT_MuX_L2MuY_Jpsi` allows the unbiased evaluation of the muon quality and the L3 trigger efficiency.

Table 6.1: Datasets used for the TnP studies.

Data set	Trigger menu	Run range
Run2011A-May10ReReco-v1	5E32	160404 – 163869
Run2011A-PromptReco-v4	1E33+1.4E33	165082 – 167915
Run2011A-PromptReco-v5	2E33	170720 – 172618
Run2011A-PromptReco-v6	2E33+3E33	172620 – 173696

6.1 Used Datasets

The data collected with trigger of the B-Physics group are stored in the *MuOnia* Primary Dataset (PD). The following efficiency triggers exist in the PD: `HLT_Mu5_Track2_Jpsi`, `HLT_Mu7_Track7_Jpsi` and `HLT_Mu5_L2Mu2_Jpsi`.

`HTL_Mu5_Track2_Jpsi` as well as `HLT_Mu7_Track7_Jpsi` are made for studying the same efficiencies, but cover a different p_T region with $p_T > 2$ or 7 GeV/c. `HLT_Mu5_Track2_Jpsi` has a higher prescale, but covers a p_T region where the efficiencies have not yet reached their saturation value.

The TnP studies presented in this chapter are based on the run periods summarized in Table 6.1. The data collected during the 5E32 run period was only used for the studies of muon reconstruction and muon quality efficiency because the trigger settings changed several times during this period. From the 1E33 menu onwards, only minor changes were made in the L1 settings which should not or only marginally affect the trigger efficiency [57].

There are only two changes worth mentioning:

1. After the run 175971, the GMT changed assignment of the muon candidates' p_T value. In case that the muon system in the barrel as well as the one in the endcaps measured the muon candidate at the same time, the lowest p_T value was sent to the Global Trigger, which was changed to now give the p_T value based on a preprogrammed rank instead [57].

2. The L1 seed was changed from `L1_DoubleMu0` for the run period 165088 – 172868 to `L1_DoubleMu0_HighQ` from run 173236 onwards to reduce the trigger rate.

The L2 trigger settings were not changed throughout the whole data taking period in 2011. The L3 reconstruction settings were only altered once during the 5E33 menu. The transverse momentum was taken from the measurement in the tracker only from run 178380 onwards, while before it was obtained through the global fit.

All changes in the trigger settings are summarized in Table 6.2.

The TnP skims of the `May10ReReco` and `PromptReco` data sets were produced using the following data certification files for declaring certified run periods and luminosity sections:

Table 6.2: Trigger changes and their corresponding run ranges.

Trigger level	Run range	Feature
L1	165088 – 172868	L1_DoubleMu0 seed
L1	173236 – 175970	L1_DoubleMu0_HighQ seed
L1	> 175971	changed p_T assignment of GMT
L3	165088 – 178379	measurement of p_T from the global fit
L3	> 178380	measurement of p_T from tracker only

- `Cert_160404-163869_7TeV_May10ReReco_Collisions11_JSON_MuonPhys_v3`
- `Cert_160404-180252_7TeV_PromptReco_Collisions11_JSON_MuonPhys`

6.1.1 Monte Carlo Sample

Apart from data-driven efficiencies, also Monte Carlo (MC) samples were produced and processed with TnP. A private MC was produced with the L1 and HLT trigger menu settings really used during the 1E33, 1.4E33, 2E33 and 3E33 menus covering the *runA* data taking period of 2011 neglecting the initial 200 pb^{-1} collected with the 5E32 trigger menu. The simulation used dedicated code that works as a J/ψ gun that feeds events to the full CMS detector simulation. The events were produced with flat p_T ($3 < p_T(\mu\mu) < 50$ GeV/c) and y ($|y(\mu\mu)| < 1.3$) distributions. Since the single muons are highly correlated with the dimuon's kinematics, the limitation in the rapidity of the dimuon is also reflected in the rapidity of the single muons. Thus, the simulation does not contain any single muon events beyond $|\eta| \gtrsim 1.4$.

The concrete setup of the MC simulation can be found in Appendix A.

6.2 Selection of Tag and Probe Muons

In order to select events faithfully representing the physics data analysis sample, fiducial cuts on the tag as well as the probe were applied. Originally, three different sets of muon cuts were used which were obtained on the basis of a MC simulation requesting the single muon reconstruction efficiency to be above a certain value.

1. ***Global50* cuts**
   A reconstruction efficiency of at least 50% on a global muon is required. The right side of Fig. 6.1 indicates the region where this criterion is fulfilled.

$$
\begin{aligned}
|\eta| < 1.1 : &\qquad p_{\mathrm{T,min}} = 4.6 \rightarrow 4.0 \text{ GeV}/c \\
1.1 < |\eta| < 1.4 : &\qquad p_{\mathrm{T,min}} = 4.0 \rightarrow 2.75 \text{ GeV}/c \\
1.4 < |\eta| < 2.4 : &\qquad p_{\mathrm{T,min}} = 2.75 \rightarrow 2 \text{ GeV}/c
\end{aligned}
$$

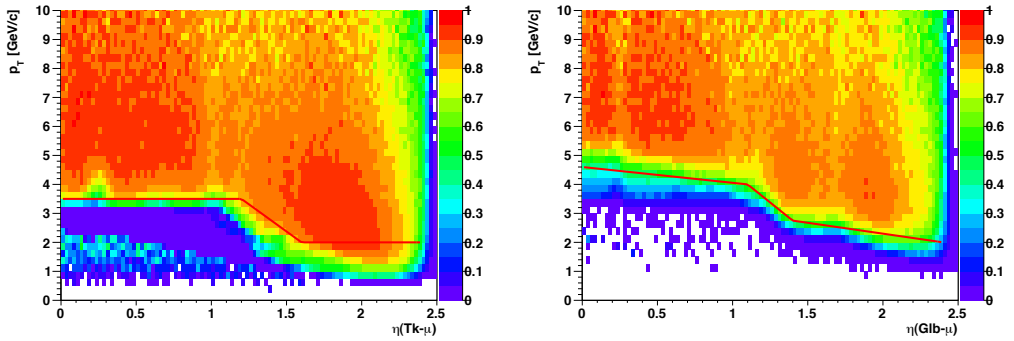

Figure 6.1: MC based reconstruction efficiency with (left) and without requiring the tracker muon also to be a global muon (right). The red lines indicate the *tracker50* (left) and *global50* cuts (right).

The efficiencies were studied in 2D using the following bins which reflect the above p_T and $|\eta|$ borders:

- $p_T = 2, 2.75, 3.5, 4.5, 5.5, 7, 10, 15, 50$ GeV/c
- $|\eta| = 0, 0.2, 0.3, 0.6, 0.8, 1.2, 1.6, 2.1, 2.4$

2. ***Tracker50* cuts**
   The reconstruction efficiency of tracker muons has to be at least 50% as is indicated by the red line on the left side of Fig. 6.1.

$$\begin{aligned} |\eta| < 1.2: &\quad p_{\mathrm{T,min}} = 3.5 \text{ GeV}/c \\ 1.2 < |\eta| < 1.6: &\quad p_{\mathrm{T,min}} = 3.5 \rightarrow 2.0 \text{ GeV}/c \\ 1.6 < |\eta| < 2.4: &\quad p_{\mathrm{T,min}} = 2 \text{ GeV}/c \end{aligned}$$

   The binning was adjusted to the shifted borders:

   - $p_T = 2, 2.5, 3, 3.5, 4, 4.5, 5, 5.5, 6, 7, 8, 10, 15, 20, 100$ GeV/c
   - $|\eta| = 0, 0.2, 0.3, 0.6, 0.8, 1.2, 1.6, 2.1, 2.4$

3. ***Tracker80* cuts**
   The *tracker80* cuts are a tighter version of the *tracker50* cuts and ensure a reconstruction efficiency of at least 80%.

$$\begin{aligned} |\eta| < 1.2: &\quad p_{\mathrm{T,min}} = 3.8 \text{ GeV}/c \\ 1.2 < |\eta| < 1.6: &\quad p_{\mathrm{T,min}} = 3.8 \rightarrow 2.0 \text{ GeV}/c \\ 1.6 < |\eta| < 2.4: &\quad p_{\mathrm{T,min}} = 2 \text{ GeV}/c \end{aligned}$$

   Finer bins in $|\eta|$ were introduced while the binning in p_T stayed the same:

   - $p_T = 2, 2.5, 3, 3.5, 4, 4.5, 5, 5.5, 6, 7, 8, 10, 15, 20, 100$ GeV/c
   - $|\eta| = 0, 0.2, 0.3, 0.6, 0.8, 1, 1.2, 1.4, 1.6, 2.1, 2.4$

In the following sections, efficiencies using the *tracker80* cuts are shown since they are defined as the default efficiencies of the CMS polarization studies. Some studies were only conducted with *global50* or *tracker50* cuts. The results of these studies remain valid for the *tracker80* cuts. The full sets of efficiencies using the *tracker50* and *global50* cuts can be found in Refs. [58] and [59]. Ref. [60] shows additional studies performed with slightly altered definitions of the muon reconstruction and the muon quality efficiency with respect to the definitions given in the following sections.

6.3 Offline Muon Reconstruction Efficiency

The offline muon reconstruction efficiency, also referred to as muon identification efficiency, is the probability of finding an offline muon track in the muon chambers given that a muon track was found in the silicon tracker. The tags are HLT muons matched to the `Mu5` leg of the `HLT_Mu5_Track2_Jpsi` trigger path. The probes are offline tracks from the collection `generalTracks` which are matched to the second leg of the efficiency trigger path.

Passing probes are

- arbitrated tracker muons or
- global muons which are also arbitrated tracker muons, have more than 10 hits in the muon station included in the global muon track fit (`globalTrack.hitPattern.numberOfValidMuonHits` > 0) and a reduced global fit-χ^2 smaller than 20.

The criteria of the passing probes are shortly referred to as *BMuons*.

Since no quality requirements can be applied at this stage, the background in failing and all probes is not negligible as shown in Fig. 6.2. Due to the high background and the small signal in the failing probes, it is difficult to extract reliable TnP efficiencies based on data. The MC simulation consists of signal only and describes the data-driven efficiencies quite well, given the large uncertainties. Figures 6.3 and 6.4 exhibit the p_T and $|\eta|$ differential muon reconstruction efficiencies, respectively, obtained with data as well as MC. The data-driven efficiencies typically vary between 80 and 100% due to the high background while the efficiencies obtained with MC show a clear trend, flattening out at around 8 GeV/c at a value close to 100%.

The somewhat lower efficiencies for the bin $0.2 < |\eta| < 0.3$ seen in the MC simulation are likely due to the fact that this pseudo-rapidity interval corresponds to the partly non-instrumented region between the central and the ± 1 wheels of the muon barrel detectors as displayed in Fig. 3.4. This inefficiency is more pronounced at low p_T where tracker or global muons typically only reach the first muon station and are easily lost in the gap between the central and ± 1 wheels.

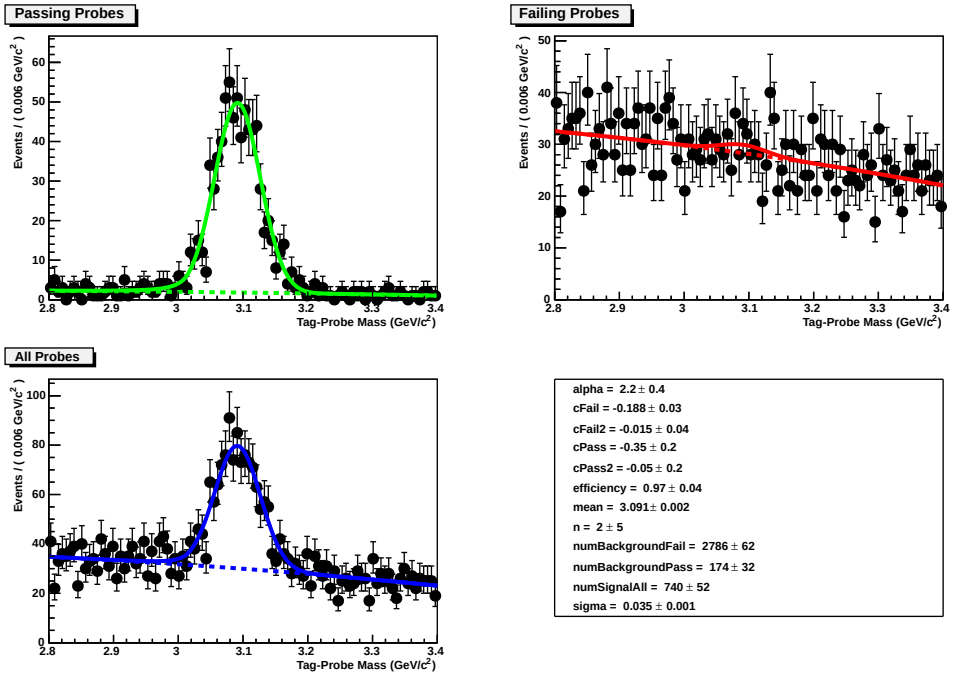

Figure 6.2: Example of the fitted mass distributions of passing, failing and all probes in case of the muon reconstruction efficiency for $1.2 < |\eta| < 1.4$ and $4.0 < p_T < 4.5$ GeV/c.

The studies of the offline muon reconstruction were conducted for all muon pairs, meaning seagull as well as cowboy dimuons. Dimuons are called seagulls (cowboys) if they are emitted such that the magnetic field bends them away from each other (towards each other). The efficiencies for seagulls and cowboys were also studied separately, but did not show any differences. This is due to the fact that only arbitrated tracker muons or global muons that are also arbitrated tracker muons were considered which are subjected to different reconstruction algorithms and thus not affected by the inefficiencies seen for L1, L2 and standalone muons. Therefore, the muon reconstruction efficiency as well as the efficiency of the muon quality cuts were obtained on the basis of all pairs.

6.4 Efficiency of the Muon Tracking Quality Cuts

The efficiency of the muon tracking quality cuts measures the probability that an offline reconstructed muon passes certain quality cuts. The tags are again HLT muons matched to the `Mu5` leg of the `HLT_Mu5_L2Mu2_Jpsi` trigger path while the probes, which are passing probes from the previous step, are matched to the `L2Mu2` leg.
Passing probes have to satisfy the following tracking related quality cuts, also referred to as *BMuQual*:

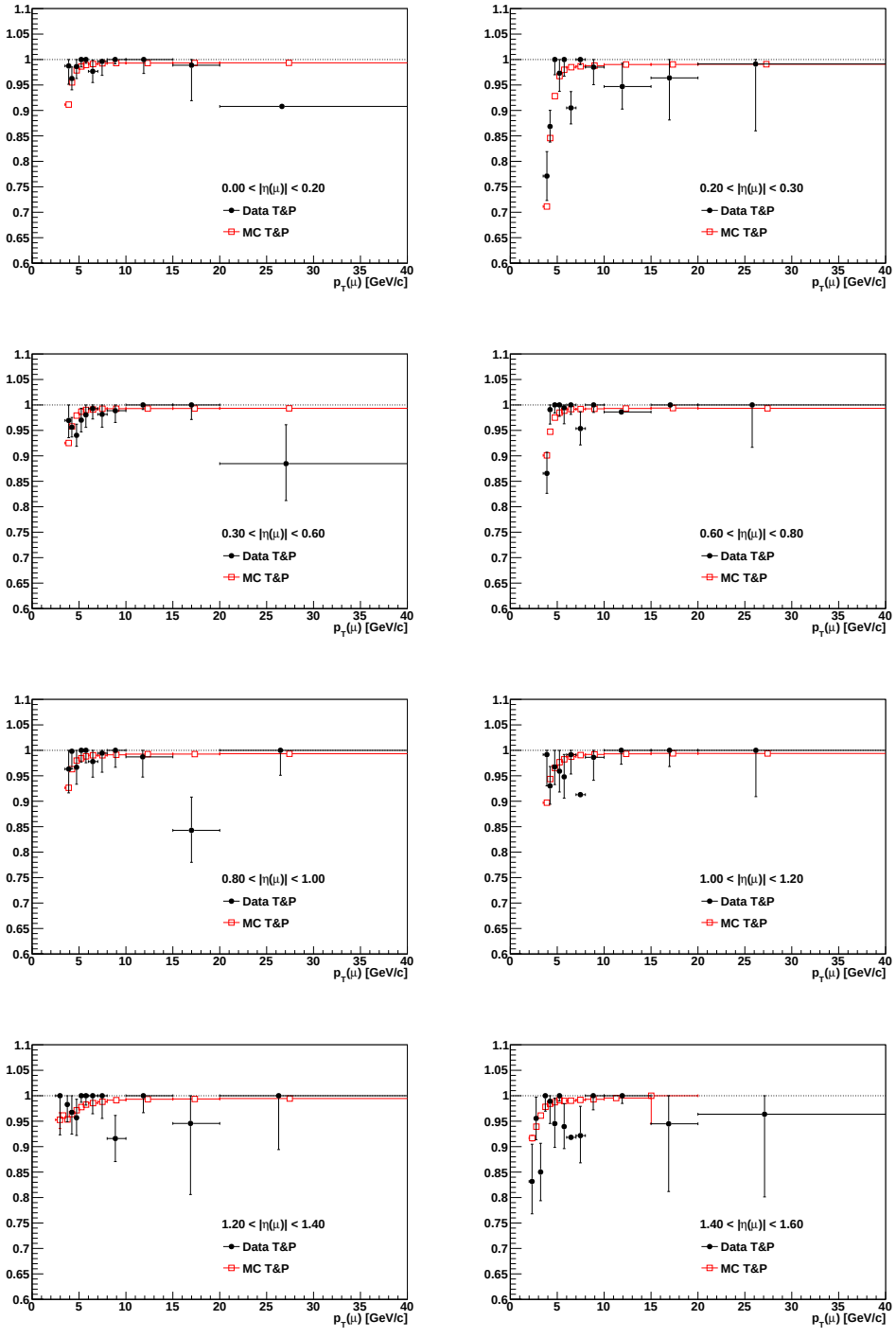

Figure 6.3: Muon reconstruction efficiency as a function of p_T in various slices of $|\eta|$, using the *tracker80* muon cuts (160404 – 173692).

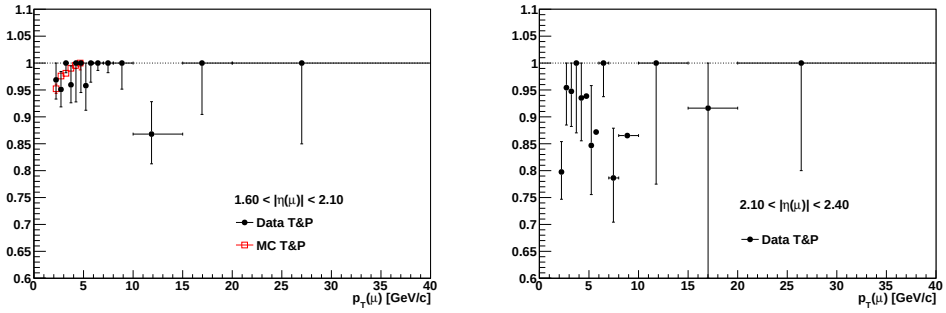

Figure 6.3: p_T dependence of the muon reconstruction efficiency (cont.).

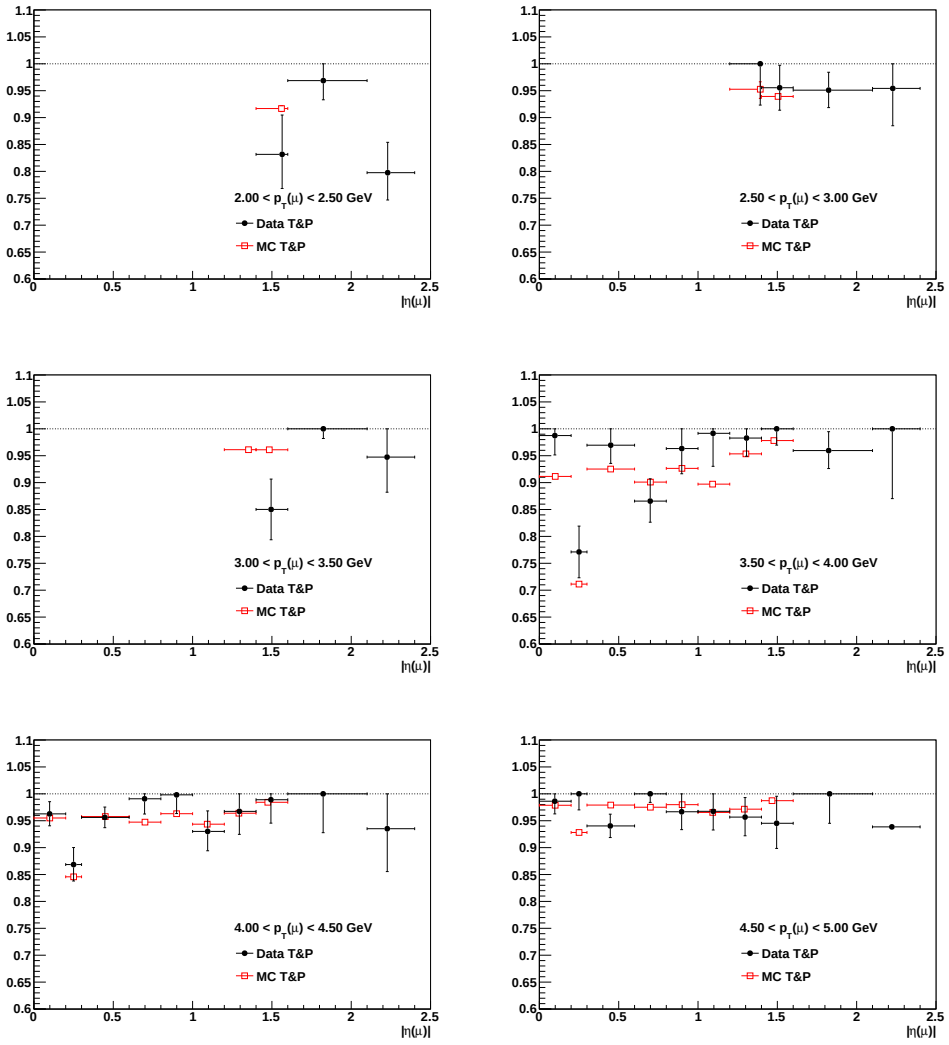

Figure 6.4: Muon reconstruction efficiency as a function of $|\eta|$ in various slices of p_T, using the *tracker80* muon cuts (160404 – 173692).

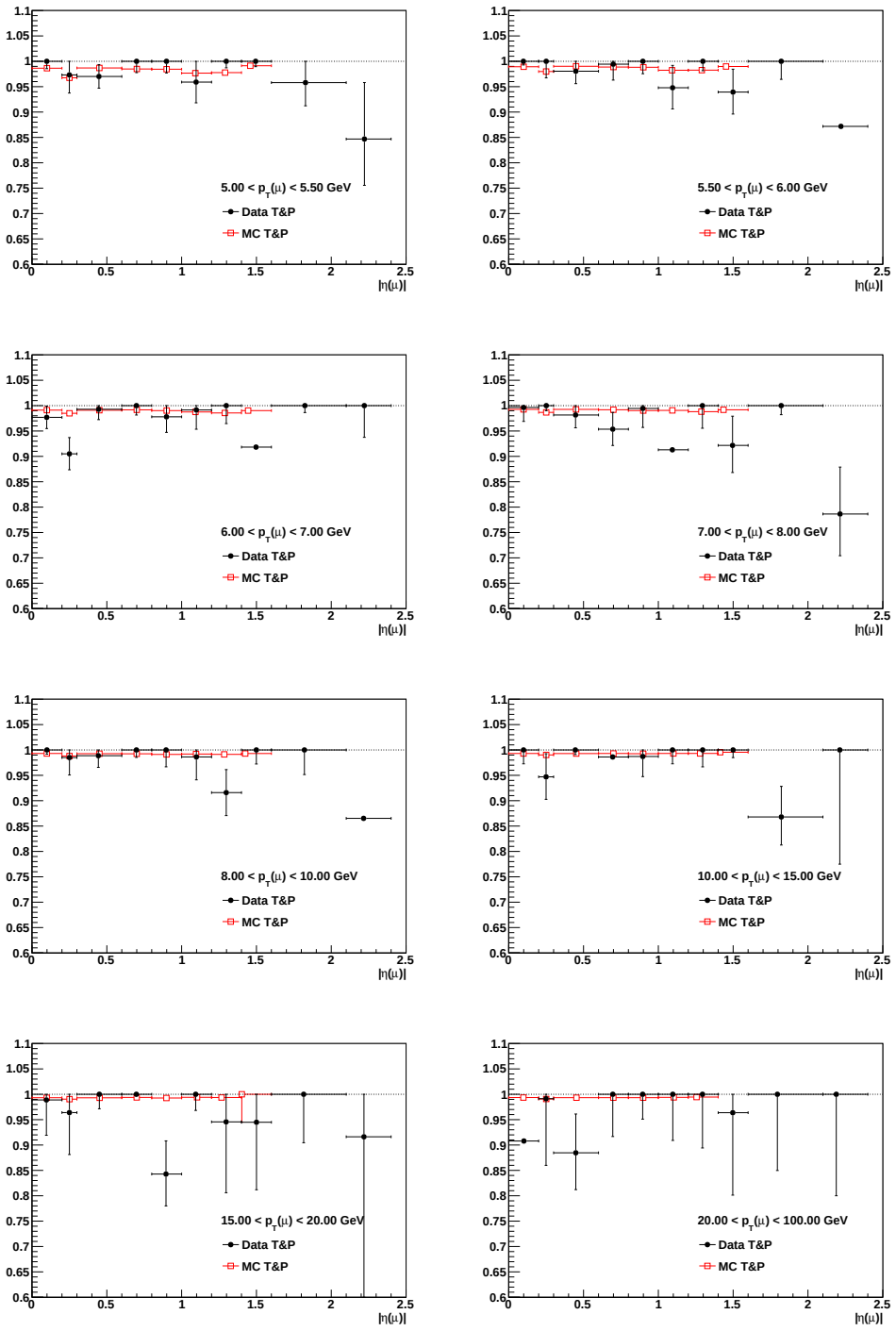

Figure 6.4: $|\eta|$ dependence of the muon reconstruction efficiency (cont.).

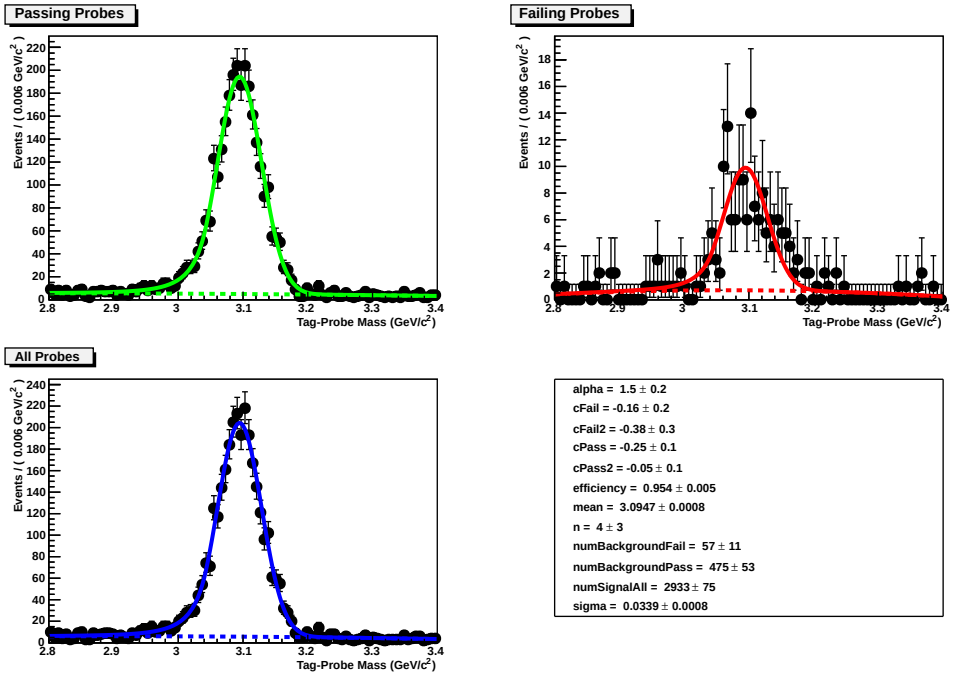

Figure 6.5: Example of the fitted mass distributions of passing, failing and all probes in case of the efficiency of the muon quality cuts for $1.0 < |\eta| < 1.2$ and $7 < p_T < 8$ GeV/c.

- The number of valid hits in the silicon tracker has to be larger than 10.
- The fit of the track has to have a reduced χ^2 below 1.8.
- More than one pixel layer has to measure the muon track.
- The track from the silicon tracker can be matched with at least one muon segment (in any station) in both x and y direction within a 3σ window (`TMOneStationTight`).
- The transverse and longitudinal impact parameter cuts with respect to the primary vertex are quite loose ($|dB| < 3$ cm, $|dz| < 30$ cm).

These cuts are widely used in quarkonium related analyses.

The 2D studies of the efficiencies are displayed in Figs. 6.6 and 6.7. They show a slight $|\eta|$ dependence and only a mild p_T turn-on behavior. The efficiencies are typically between 93 and 98%, flattening out at around 10 GeV/c. The background in the passing, failing and all probes are quite small as can be seen in Fig. 6.5. The analyzed data sample is large enough to obtain small statistical uncertainties. The data-driven efficiencies are accurately described by the MC TnP efficiencies.

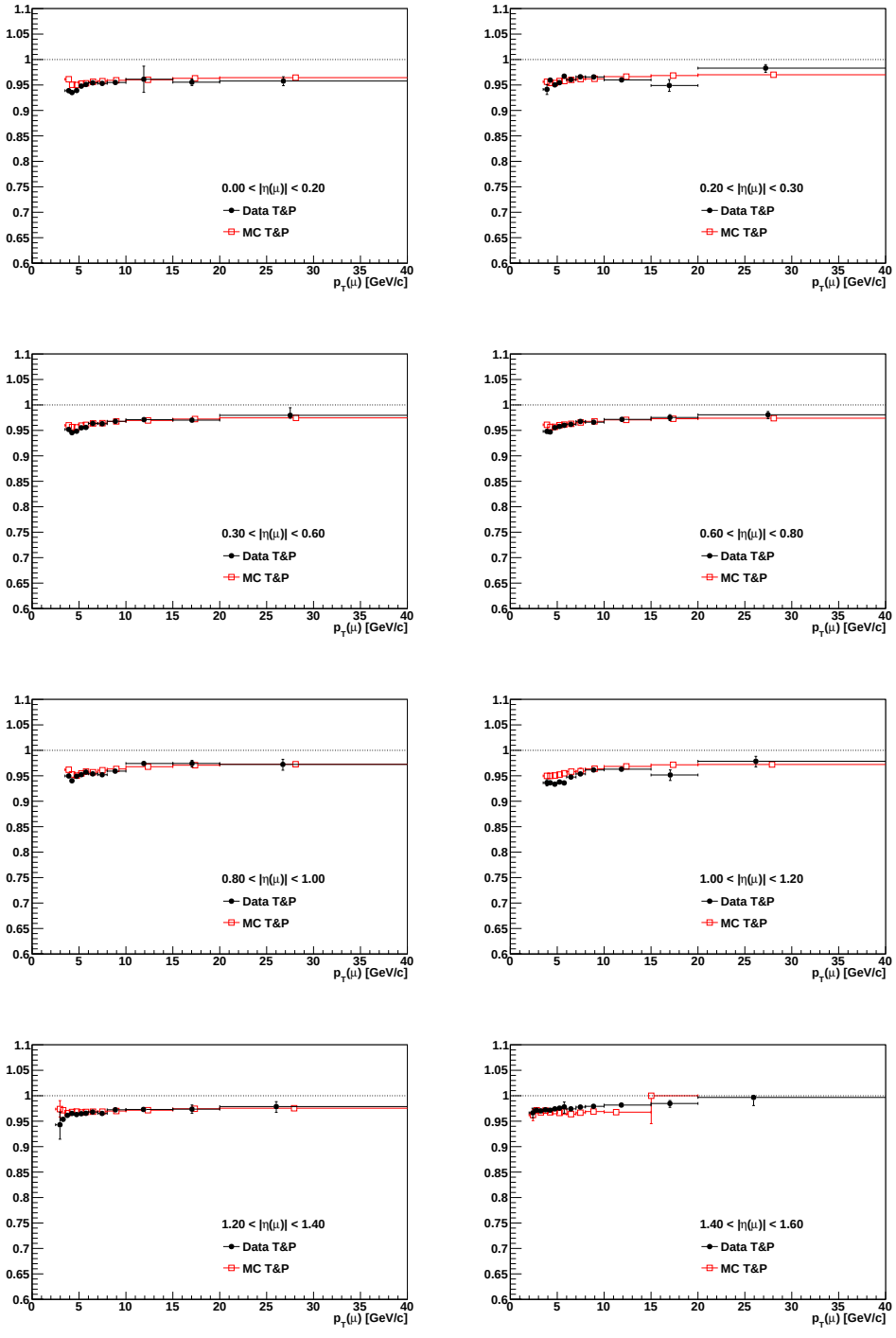

Figure 6.6: Efficiency of the muon quality cuts as a function of p_T in various slices of $|\eta|$, using the *tracker80* muon cuts (160404 – 173692).

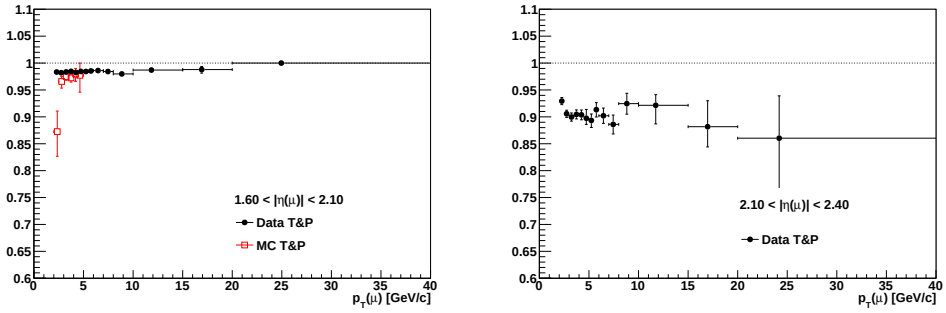

Figure 6.6: p_T dependence of the muon quality efficiency (cont.).

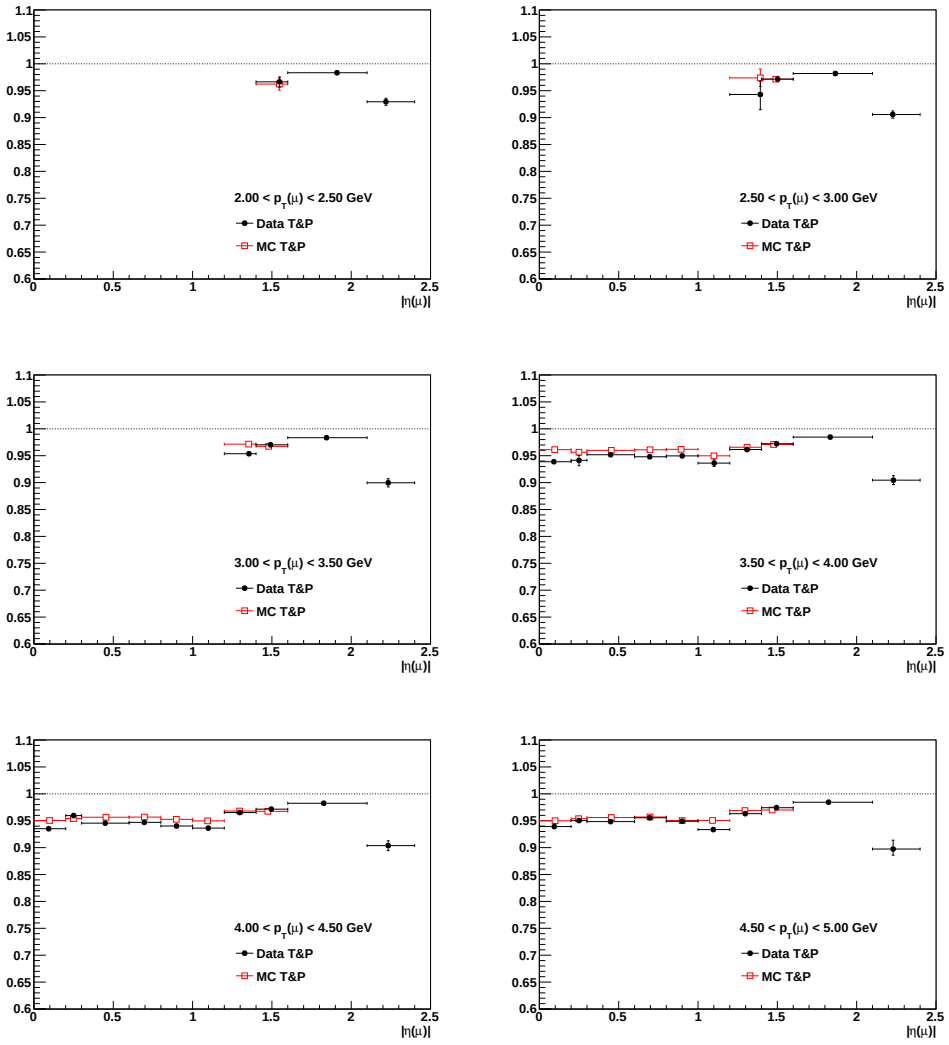

Figure 6.7: Efficiency of the muon quality cuts as a function of $|\eta|$ in various slices of p_T, using the *tracker80* muon cuts (160404 – 173692).

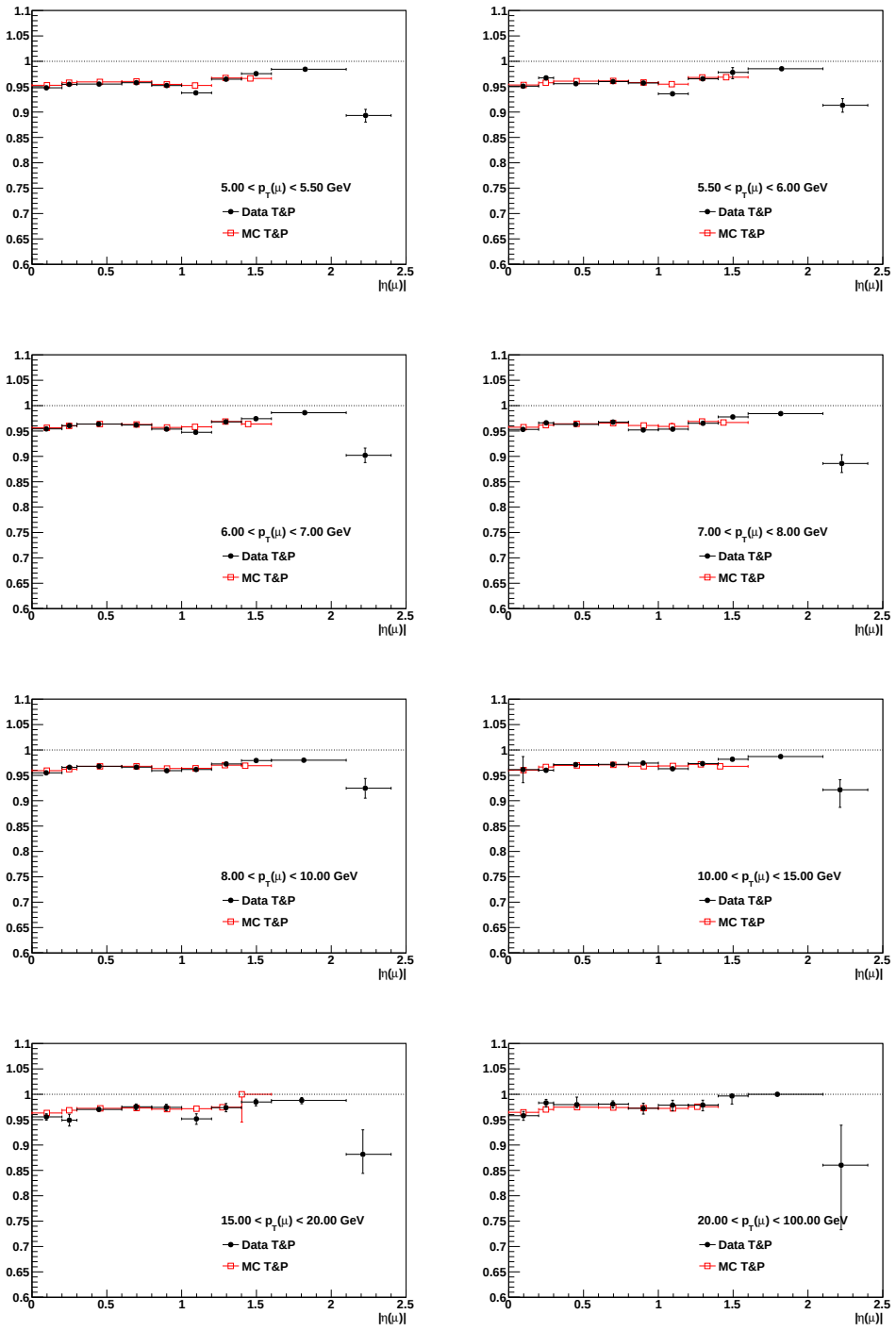

Figure 6.7: $|\eta|$ dependence of the muon quality efficiency (cont.).

6.5 Dimuon Trigger Inefficiencies for *Close-by* Muons

In the past, a single real muon accompanied by a *ghost* track lead to a large fraction of fake events in dimuon triggered samples. Therefore, a ghost busting veto was implemented by the CSC L1 trigger group which rejects muons that are too close in space. Unfortunately, this veto also discards high p_T J/ψ's that may form two almost collinear muons. Also cowboy dimuons from J/ψ's are most likely to be rejected by the ghost busting veto algorithm since the muons have a high probability of crossing each other at a certain radius from the interaction point where the trigger logic is situated. The L2 trigger contains a similar rejection algorithm. If two potential trigger muons, after having survived the L1 trigger veto, have one or more hits (currently even invalid hits) in common, only one is chosen, thus eliminating cowboy dimuons and high p_T J/ψ's.

To determine the inefficiencies induced at L1 and L2 for *close-by* muons, two separate studies for L1 and for L2 have been performed. The tags for the L1 as well as L2 trigger efficiency are matched to the `Mu5` leg of the `HLT_Mu5_Track2_Jpsi` trigger path. The probes for the L1 trigger efficiency need to fulfill the *BMuQual* criteria and match the `Track2` leg of the efficiency trigger path. Passing probes also have to pass the L1 filter used by all the quarkonium triggers, `hltDimuonL1-Filtered0`. The passing probes from the L1 trigger efficiency then become probes for the exclusive L2 trigger efficiency, i.e. the L2 trigger efficiency studied with respect to L1. Passing probes are required to pass the L2 filter of the quarkonium triggers, `hltDimuonL2PreFiltered0`.

Figure 6.8 shows the L1, L2 and combined L1·L2 trigger efficiency for cowboys and seagulls as functions of the probe muon's $|\eta|$ and p_T. At mid-rapidity the efficiencies are very similar, while they became rather different at forward rapidities as can be seen from the left hand side of Fig. 6.8. Starting from $|\eta| = 1.4$ – the p_T dependence of the efficiencies in the bin $1.4 < |\eta| < 2.1$ is depicted in the right hand side of Fig. 6.8 –, the seagull dimuons are more efficient than the cowboy dimuons. The effect seems to be less pronounced at L1.

Special attention should be given to the $|\eta|$ region between 0.2 and 0.3 which corresponds to the partly non-instrumented gap between the central and ± 1 muon wheels. Figure 6.9 shows the L1 and L2 trigger efficiencies for this region. This time, there seems to be a rather significant inefficiency of cowboy dimuons at L1, which is not seen for the L2 trigger efficiency.

Further studies concerning the distance between the two muons were conducted. The distance was characterized by the separation between the tag and probe muons expressed as $\Delta R = \sqrt{\Delta\eta^2 + \Delta\phi^2}$, the angular difference between the two muons $\Delta\phi$ as well as the physical distance. All three variables were measured at the second muon station. The corresponding data-driven and MC based efficiencies were studied for a probe p_T smaller and larger than 6 GeV/c and for different pseudo-rapidity regions. Figure 6.10 displays the L1 trigger efficiency as a function of ΔR for cowboys and seagulls, while Fig. 6.11 shows the corresponding efficiencies for the exclusive L2 trigger efficiency. Up to $|\eta| = 1.2$,

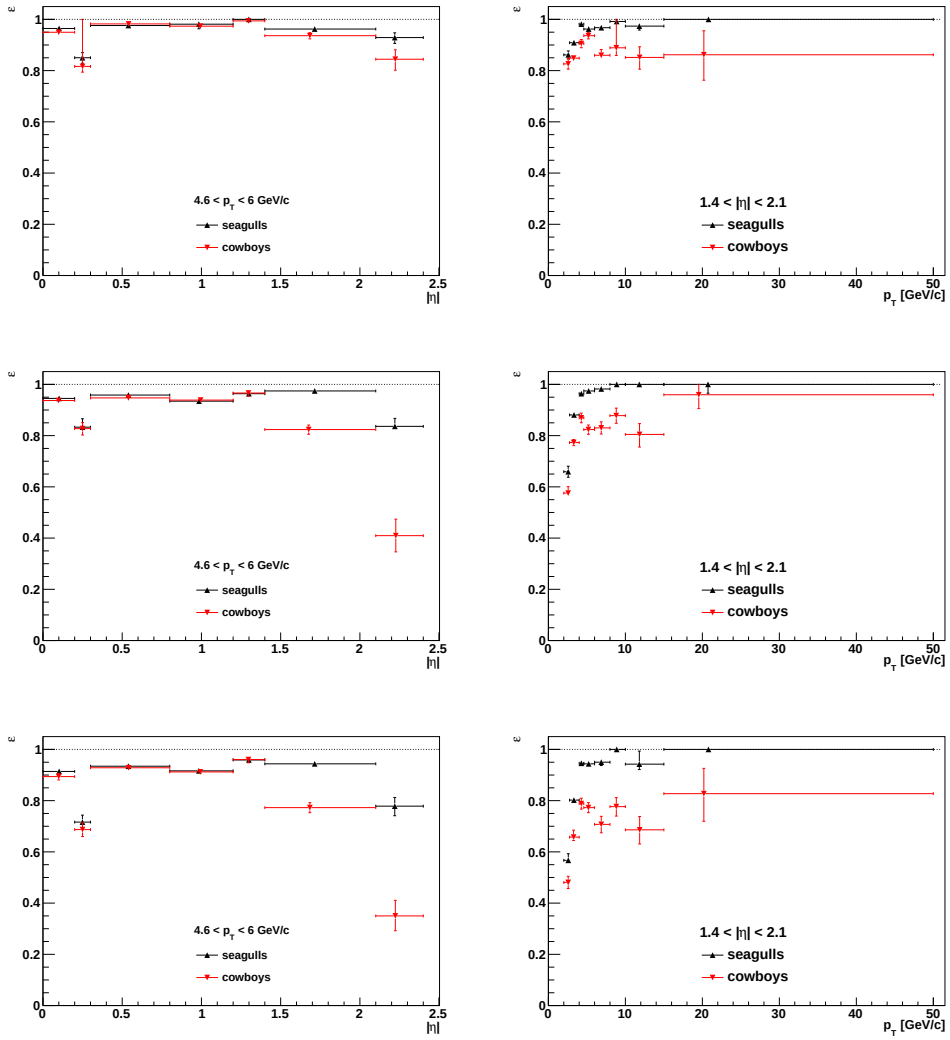

Figure 6.8: L1 (top), L2 (middle) and L1·L2 trigger efficiency (bottom) for cowboy (red) and seagull (black) dimuons as a function of $|\eta|$ (left) and p_T (right), using the *global50* muon cuts.

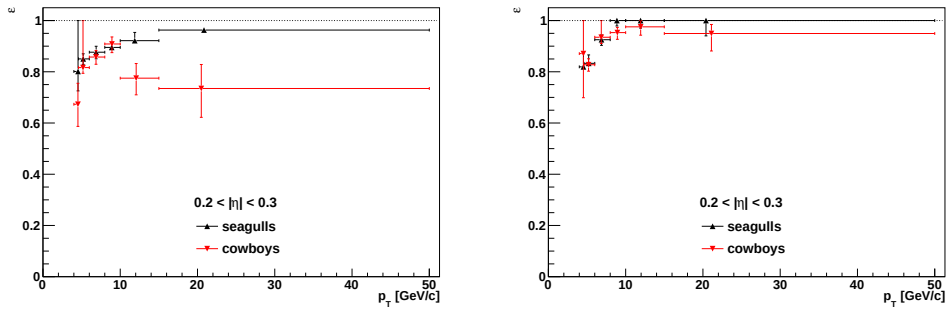

Figure 6.9: L1 (left) and L2 trigger efficiency (right) for cowboy (red) and seagull (black) dimuons as a function of p_T for $0.2 < |\eta| < 0.3$, using the *global50* muon cuts.

the efficiencies of the two dimuon types are similar. Above $|\eta| = 1.2$, the cowboys seem to develop an inefficiency for small separations. The inefficiencies are more pronounced for the L2 trigger efficiency. While the L1 trigger efficiency does not exhibit any deviations for cowboy dimuons in the bin $1.2 < |\eta| < 1.6$, $p_T < 6$ GeV/c, the corresponding L2 trigger efficiency for cowboys drops by up to 50% for a ΔR value below 0.5.

The decrease of efficiencies at large ΔR for $p_T < 6$ GeV/c, is most likely due to a hidden p_T dependence: Large ΔR, meaning a large opening angle between the two muons, is characteristic for low p_T J/ψ's which in general have a lower trigger efficiency.

Figure 6.12 displays the L1 trigger efficiency as a function of $\Delta\phi$. Fig. 6.13 shows the corresponding L2 trigger efficiencies. At mid-rapidity, cowboy dimuons have a natural separation in $\Delta\phi$ and do not suffer from inefficiencies. At more forward rapidities, inefficiencies for cowboys start developing. For $p_T > 6$ GeV/c, already the $|\eta|$ region between 0.8 and 1.2 seems to have inefficiencies at L1 for cowboys. This is not reproduced by the L2 trigger efficiency indicating that the inefficiencies are stronger for the L1 trigger efficiency. In general however, they are again more pronounced for the exclusive L2 trigger efficiency.

Figures 6.14 and 6.15 exhibit the L1 and exclusive L2 trigger efficiency as a function of the physical distance measured between the two muons at the second muon station. The results do not add any new information, they show the same inefficiencies for cowboys as the previous figures. However, they illustrate very well that inefficiencies are observed up to a separation of around 150 cm.

These studies were obtained using the *global50* muon cuts. The results are valid for the other two sets of cuts as well and are the reason for discarding cowboy dimuons from the studies of the trigger efficiencies. After run 170249, cowboys were automatically rejected by the trigger.

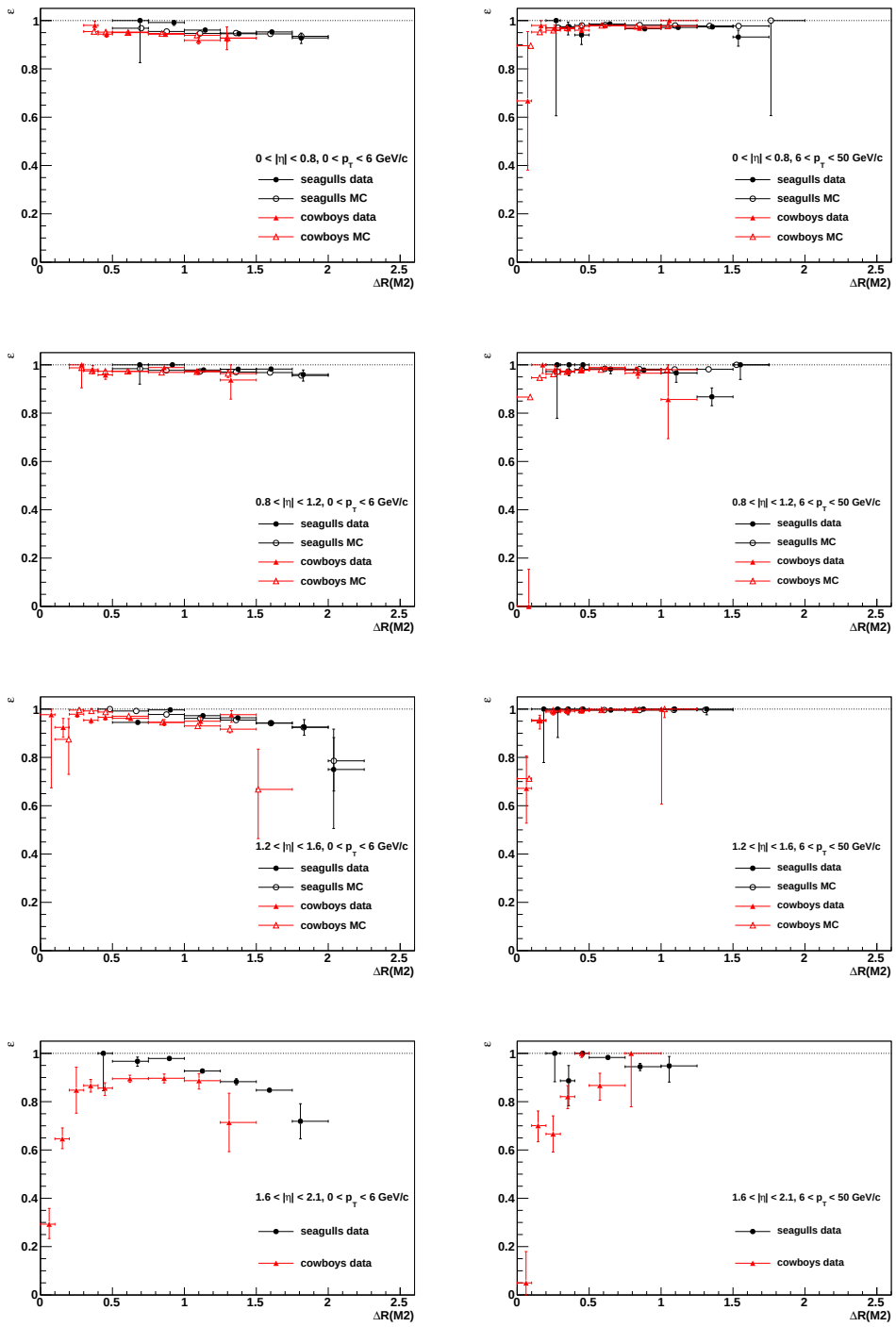

Figure 6.10: L1 trigger efficiency as a function of ΔR, extrapolated to the 2nd muon station, using the *global50* muon cuts. Left: For $p_T <$ 6 GeV/c. Right: For $p_T >$ 6 GeV/c. The rows from top to bottom show different pseudo-rapidity ranges.

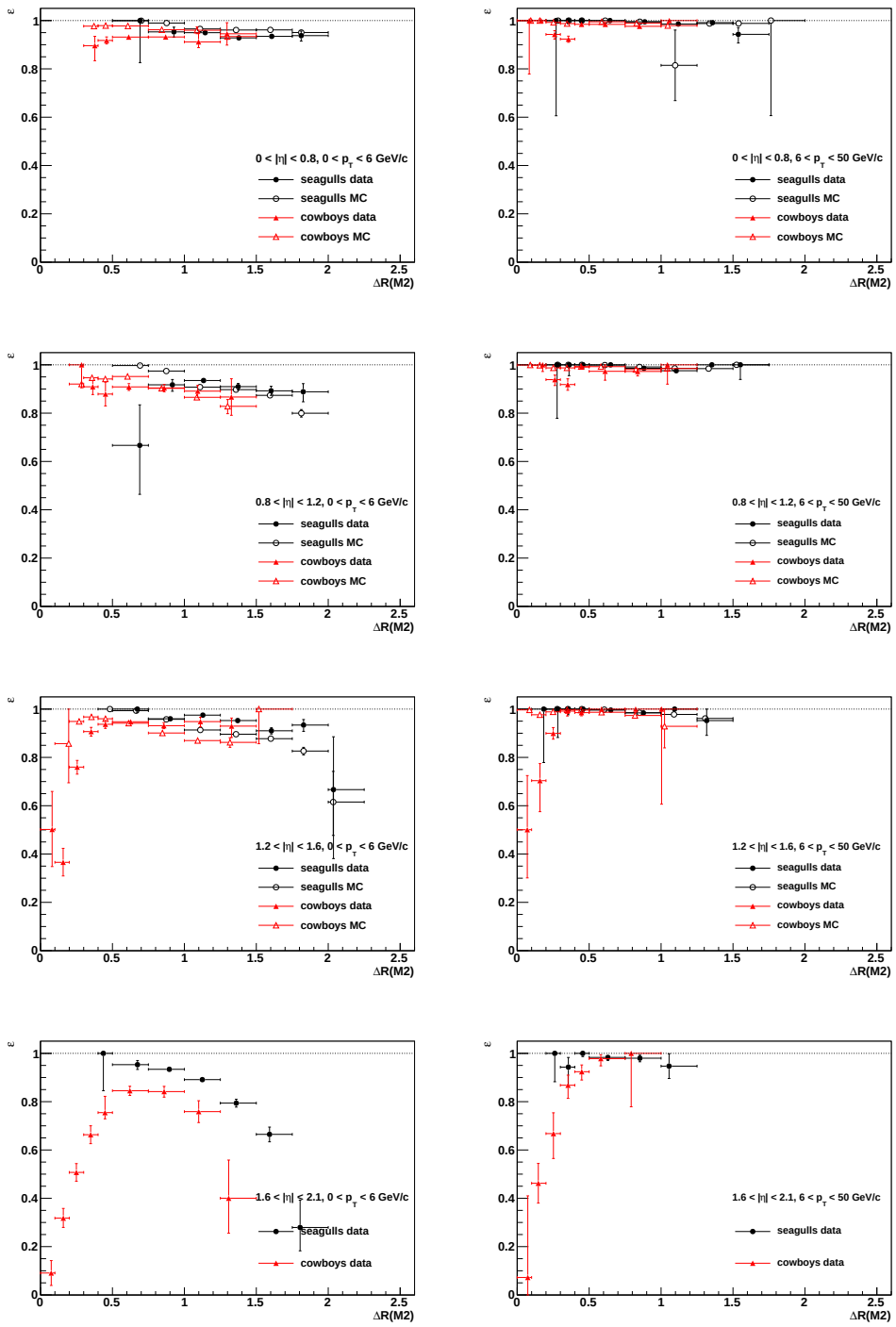

Figure 6.11: Exclusive L2 trigger efficiency as a function of ΔR, extrapolated to the 2nd muon station, using the *global50* muon cuts. Left: For $p_T < 6$ GeV/c. Right: For $p_T > 6$ GeV/c. The rows from top to bottom show different pseudo-rapidity ranges.

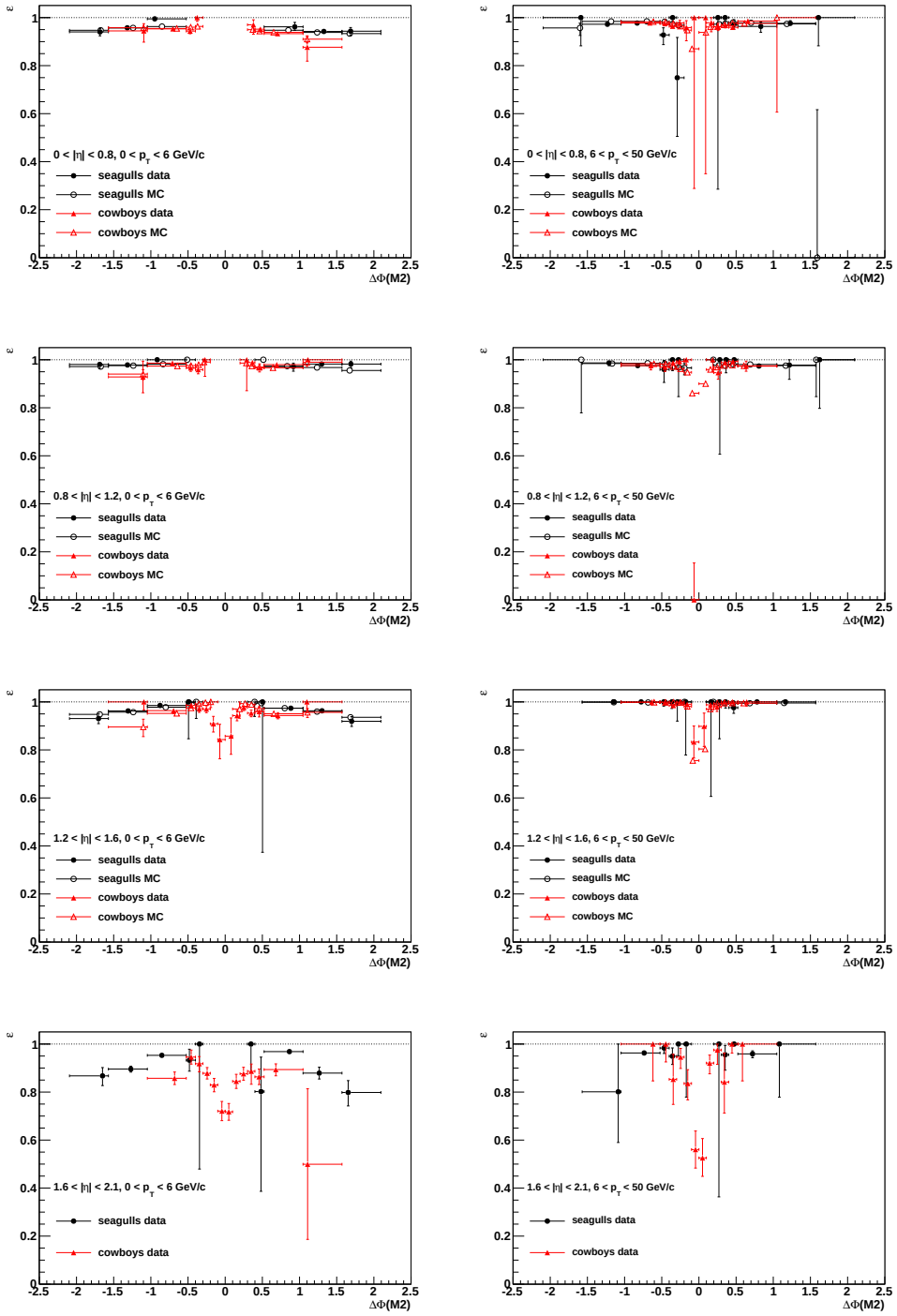

Figure 6.12: L1 trigger efficiency as a function of $\Delta\phi$, extrapolated to the 2nd muon station, using the *global50* muon cuts. Left: For $p_T <$ 6 GeV/c. Right: For $p_T >$ 6 GeV/c. The rows from top to bottom show different pseudo-rapidity ranges.

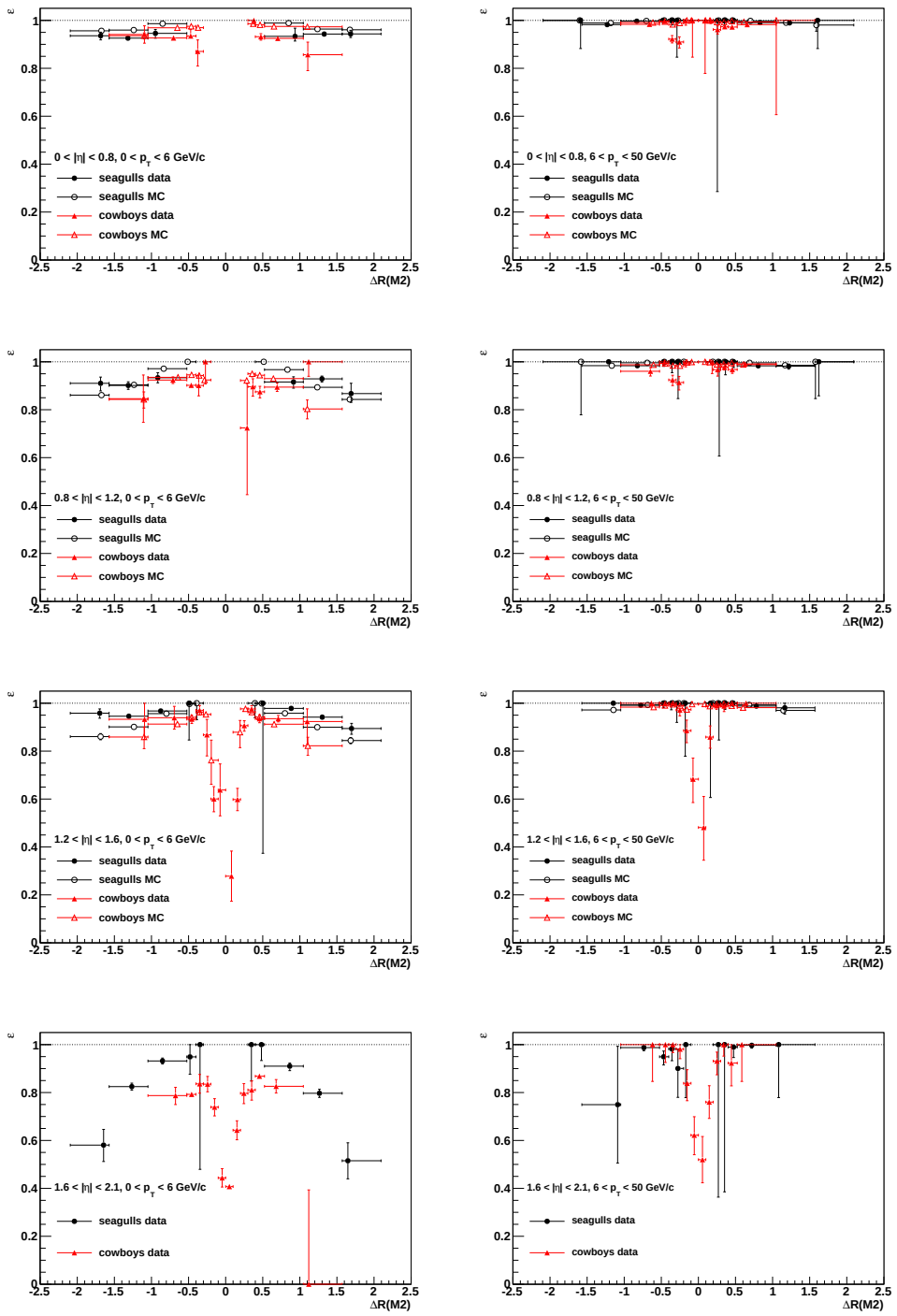

Figure 6.13: Exclusive L2 trigger efficiency as a function of $\Delta\phi$, extrapolated to the 2nd muon station, using the *global50* muon cuts. Left: For $p_T < 6$ GeV/c. Right: For $p_T > 6$ GeV/c. The rows from top to bottom show different pseudo-rapidity ranges.

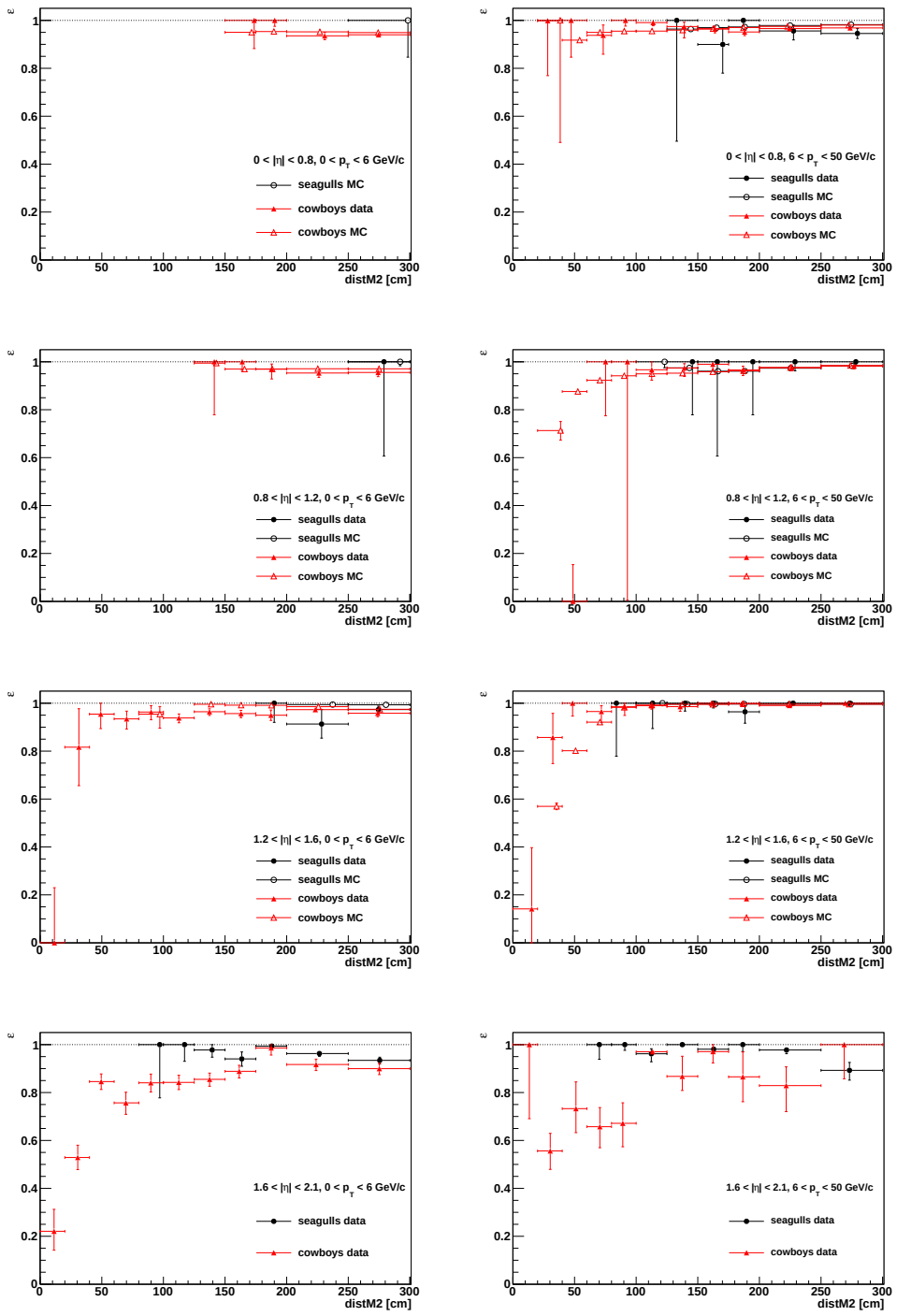

Figure 6.14: L1 trigger efficiency as a function of the distance between the two muons, measured at the 2nd muon station, using the *global50* muon cuts. Left: For $p_T < 6$ GeV/c. Right: For $p_T > 6$ GeV/c. The rows from top to bottom show different pseudo-rapidity ranges.

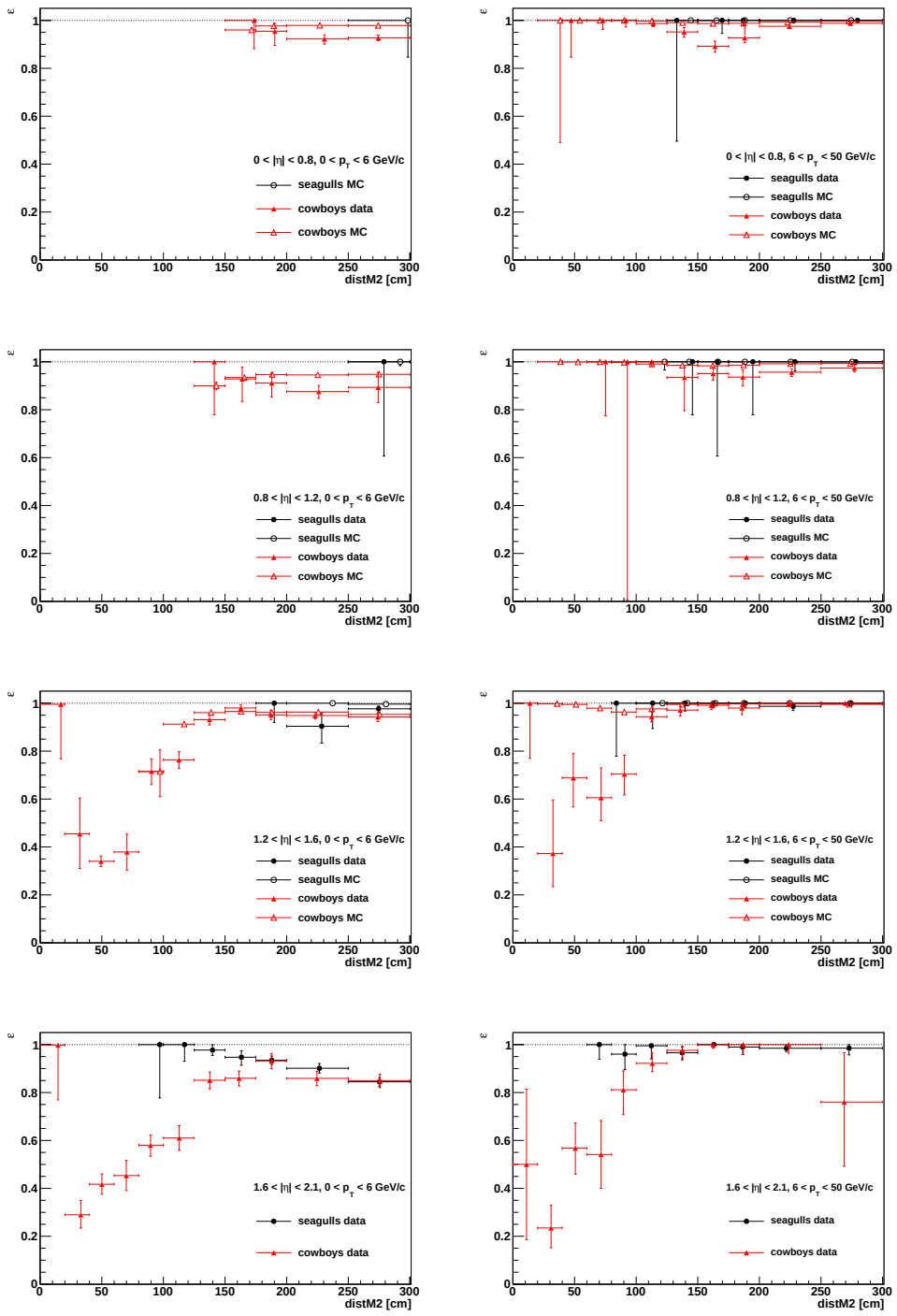

Figure 6.15: Exclusive L2 trigger efficiency as a function of the distance between the two muons, measured at the 2nd muon station, using the *global50* muon cuts. Left: For $p_T < 6$ GeV/c. Right: For $p_T > 6$ GeV/c. The rows from top to bottom show different pseudo-rapidity ranges.

6.6 L1·L2 Trigger Efficiency

The L1·L2 trigger efficiency uses the `HLT_Mu5_Track2_Jpsi` trigger path in which the tags are matched to `Mu5` leg and the probes to the online track, `Track2`. Moreover, the probes have to satisfy the *BMuQual* criteria. Passing probes are requested to pass the L2 filter used by all the dimuon triggers in the *MuOnia* PD, `hltDimuonL2PreFiltered0`. No bias is introduced in the extraction of efficiencies due to the usage of the efficiency trigger path which is a *single* muon trigger. The quality criteria of single muon triggers are in general stricter than the ones of dimuon triggers, meaning that if a tag and probe pair is inefficient, it is not because the tag is inefficient, given that a matching to a dimuon trigger filter is requested.

As outlined in Section 6.1, there were two significant changes in the L1 trigger setting leading to separate studies of the run ranges 165088 – 172868, 173236 – 175970 and > 175971. The efficiencies for the first run period, where the `L1_DoubleMu0` seed was used, can be seen p_T differentially in Fig. 6.16 and $|\eta|$ differentially in Fig. 6.17. The efficiency begins to flatten out in $|\eta|$ (apart from the bins 0.2 – 0.3 and 0.8 – 1) for the bin $8 < p_T < 10$ GeV/c, indicating that the plateau value is reached below 10 GeV/c. The drop in efficiency for $0.2 < |\eta| < 0.3$ has its origin in the partly non-instrumented region between the central and ±1 muon wheel, where muons fail to fire the trigger. Comparing the p_T turn-on curves, one will also find that the bin $0.8 < |\eta| < 1.0$ shows somewhat lower efficiencies because this $|\eta|$ region corresponds to a gap between the DTs and the CSCs. The inefficiency is more pronounced for the bin $0.2 < |\eta| < 0.3$ because the ±1 wheels are shorter than the others due to the cryogenic chimneys.

The MC based efficiencies describe the data-driven ones quite well. In this context, one should also keep in mind that the MC simulation was generated flat in p_T. This simplification is justified given that the efficiencies are obtained in fine bins of $|\eta|$ and p_T.

Starting with run 173236, the L1 seed was changed from the `L1_DoubleMu0` seed to the `L1_DoubleMu0_HighQ` seed. The signal efficiency was expected to be similar while the trigger rate was reduced significantly. The L1 seed change concerned certain classes of unconfirmed CSC candidates which means that the L1·L2 efficiency is only expected to change above $|\eta| = 1.2$ [57].

Efficiency triggers during the second run period (173236 – 175970) using the `L1_DoubleMu0_HighQ` seed were highly prescaled, even though most physics triggers were collected during this period. Therefore, there is not sufficient statistics to extract accurate data-driven efficiencies. The statistical uncertainties are relatively large, but the data-driven efficiencies are compatible with the efficiencies using the `L1_DoubleMu0` seed within statistical errors as can be seen in Fig. 6.18. Looking at Fig. 6.19, the trend of the data-driven L1·L2 efficiencies of the second run period seem to be reproduced by the MC TnP efficiencies within the uncertainties.

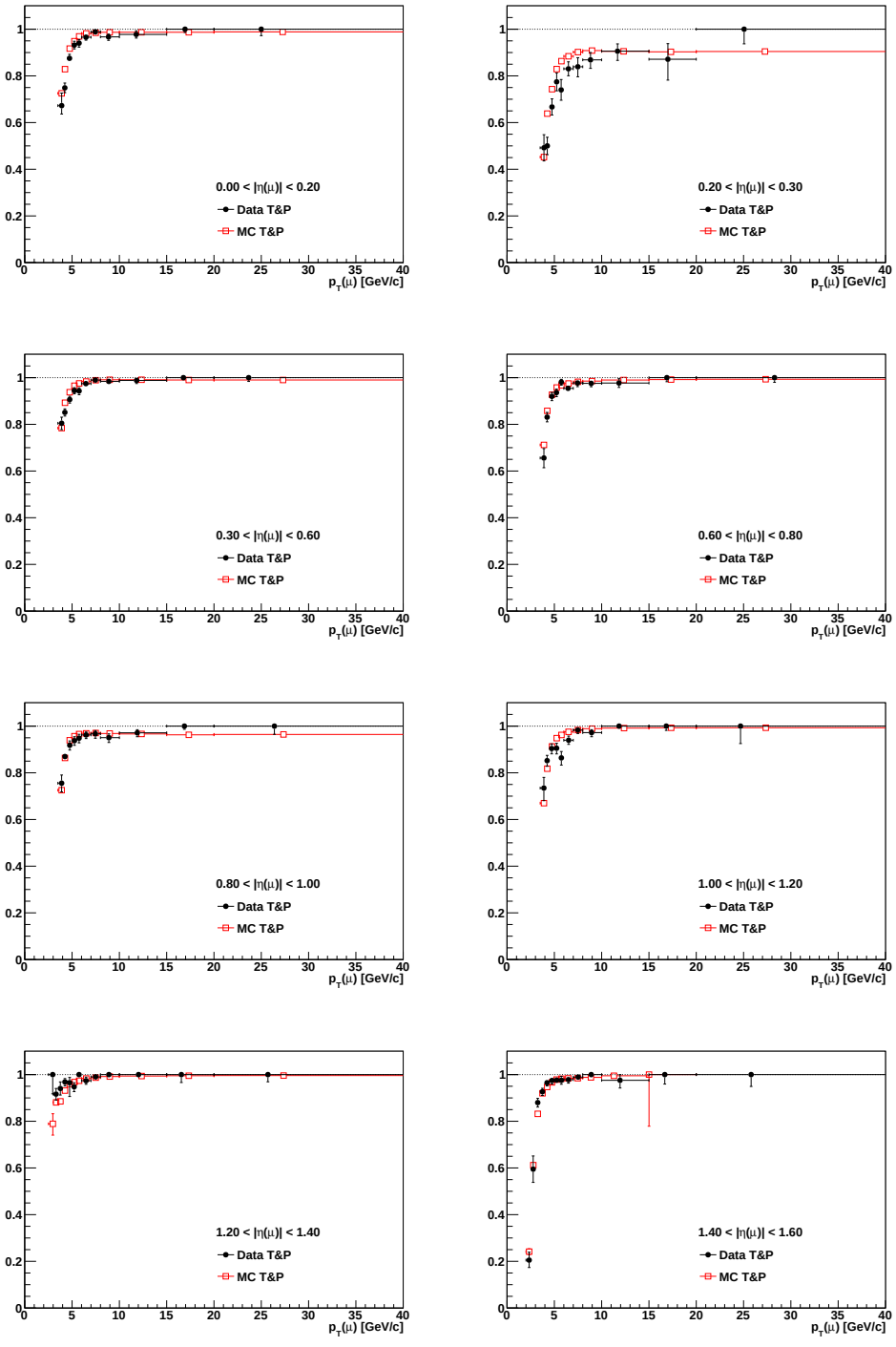

Figure 6.16: L1·L2 trigger efficiency as a function of p_T in various slices of $|\eta|$, using the *tracker80* muon cuts (165088 – 172868).

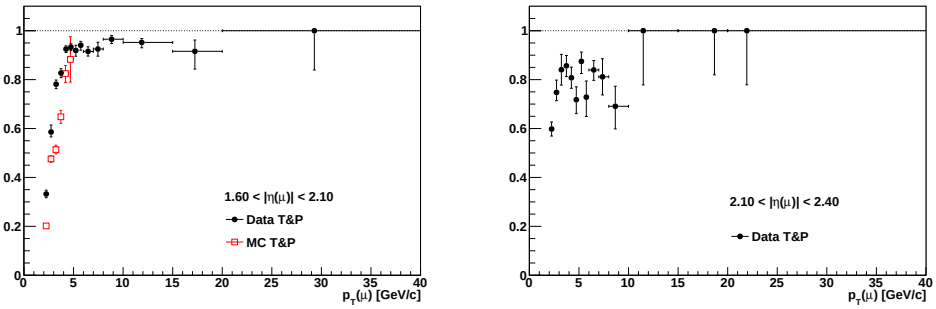

Figure 6.16: p_T dependence of the L1·L2 trigger efficiency (cont.).

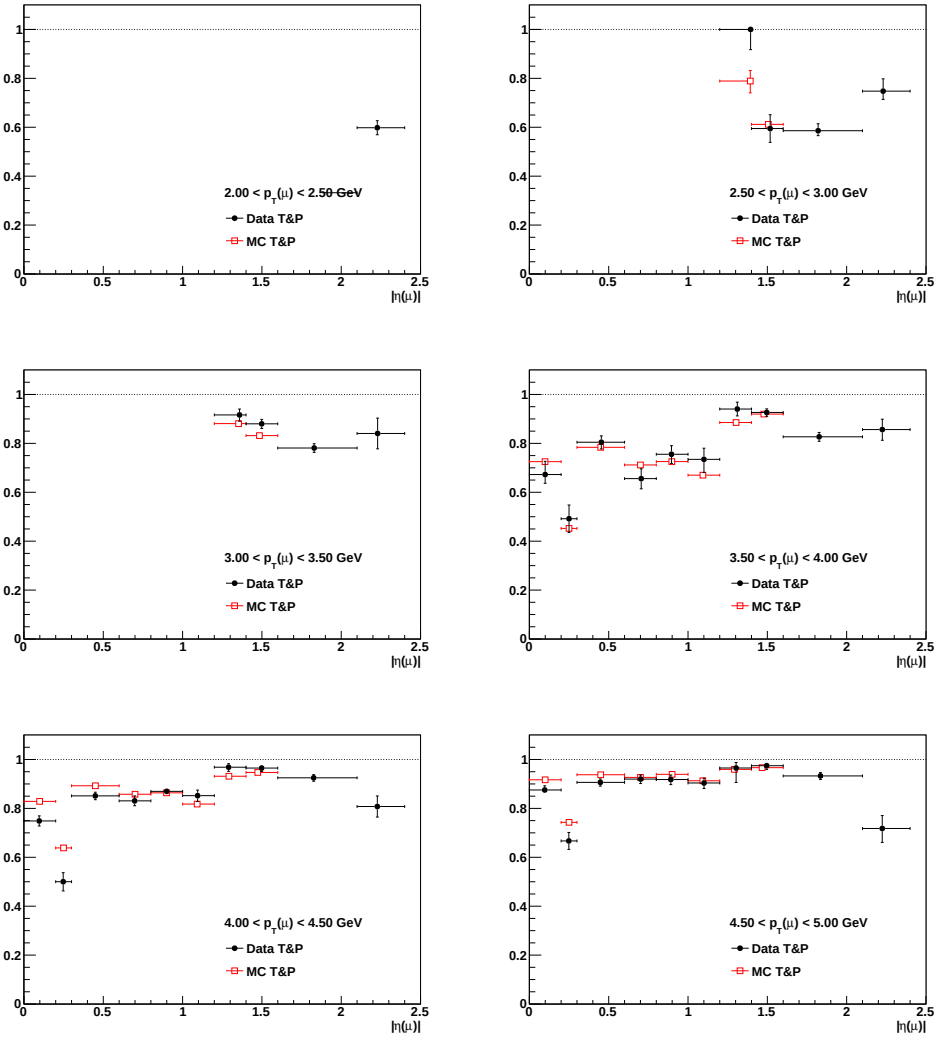

Figure 6.17: L1·L2 trigger efficiency as a function of $|\eta|$ in various slices of p_T, using the *tracker80* muon cuts (165088 – 172868).

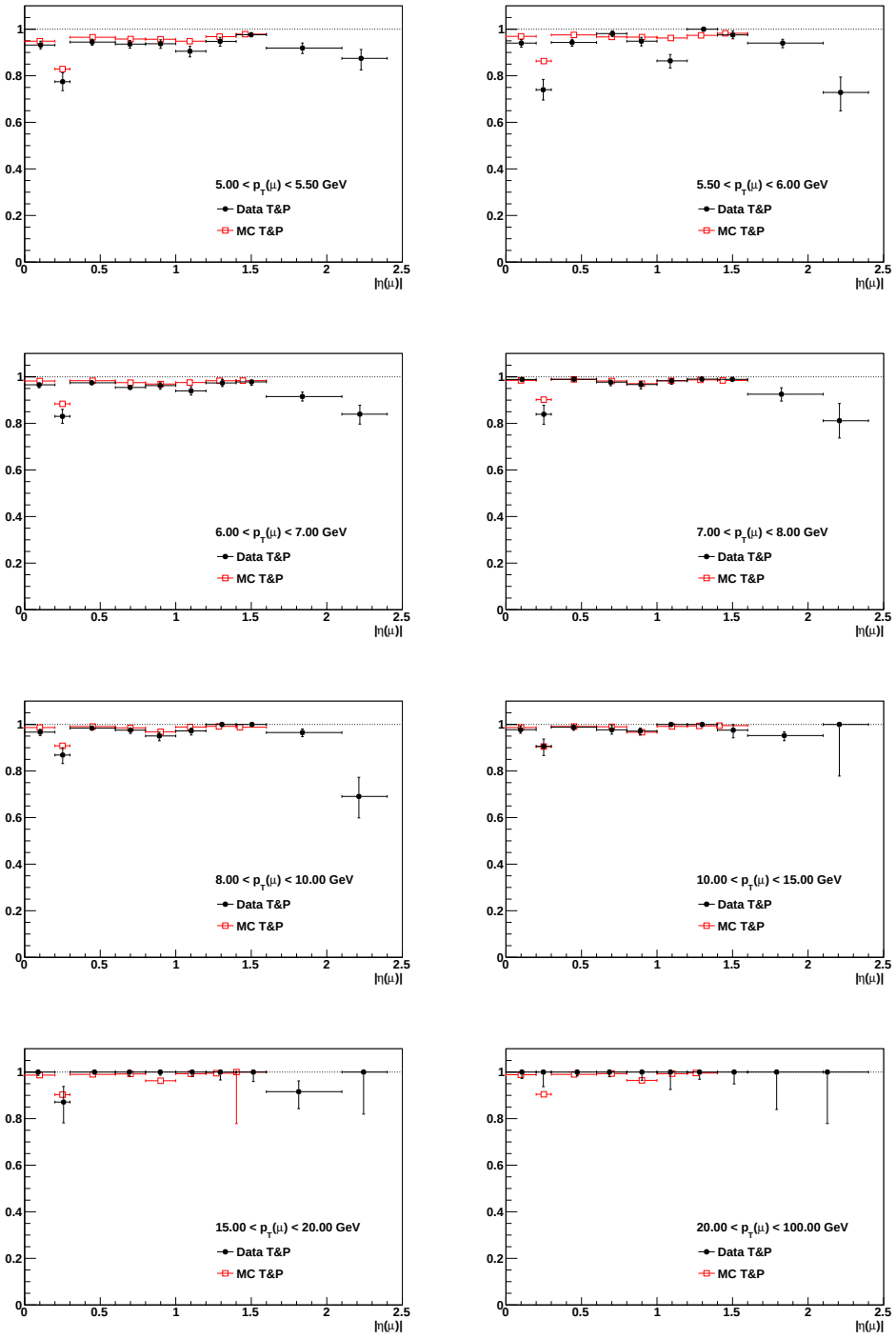

Figure 6.17: $|\eta|$ dependence of the L1·L2 trigger efficiency (cont.).

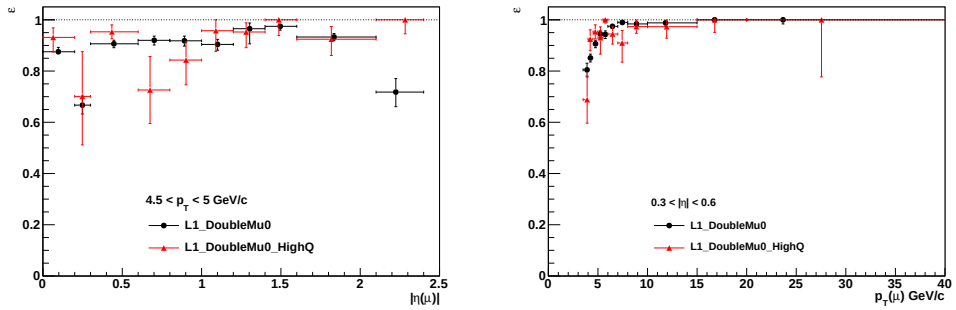

Figure 6.18: Comparison of the L1·L2 trigger efficiency during the first (165088 – 172868) and the second run period (173236 – 175970) as a function of $|\eta|$ (left) and p_T (right), using the *tracker80* muon cuts.

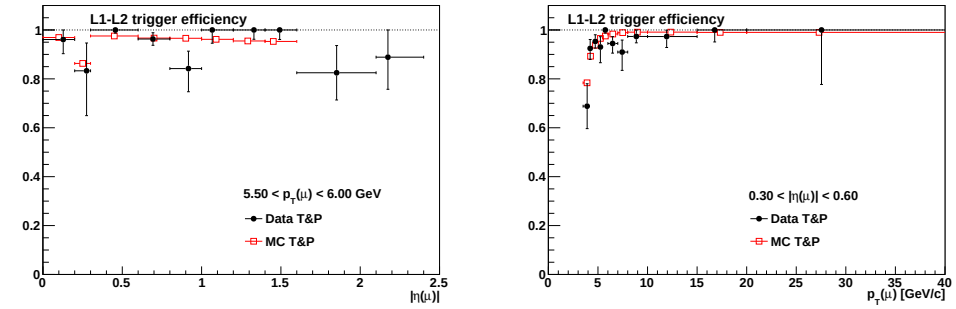

Figure 6.19: L1·L2 trigger efficiency using the `L1_DoubleMu0_HighQ` seed as a function of $|\eta|$ (left) and p_T (right), using the *tracker80* muon cuts (173236 – 175970).

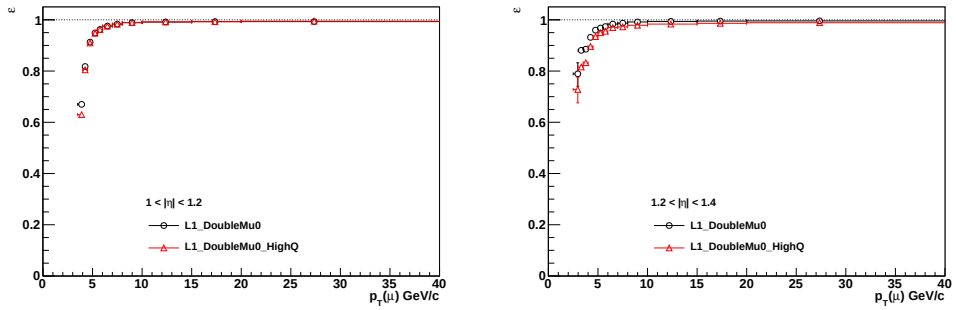

Figure 6.20: Comparison of the MC based L1·L2 trigger efficiency using the `L1_DoubleMu0` seed and the `L1_DoubleMu0_HighQ` seed as a function of p_T for $1.0 < |\eta| < 1.2$ (left) and $1.2 < |\eta| < 1.4$ (right). *Tracker80* muon cuts were used.

The MC comparisons for the two run periods displayed in Fig. 6.20 do not show any deviations up to $|\eta| = 1.2$ as is expected. Above $|\eta| = 1.2$, the efficiencies using the `L1_DoubleMu0_HighQ` seed are slightly lower, an effect which is more pronounced at lower p_T.

The efficiencies of the third run period (> 175970), after the GMT assignment has changed, compared to the first period of data taking are displayed in Figs. 6.21 and 6.22. Only data-driven efficiencies are shown. The efficiencies of the third run period have a larger statistical uncertainty, but seem to agree quite well with the ones from the first run period. Both show similar behavior. No clear trends can be seen.

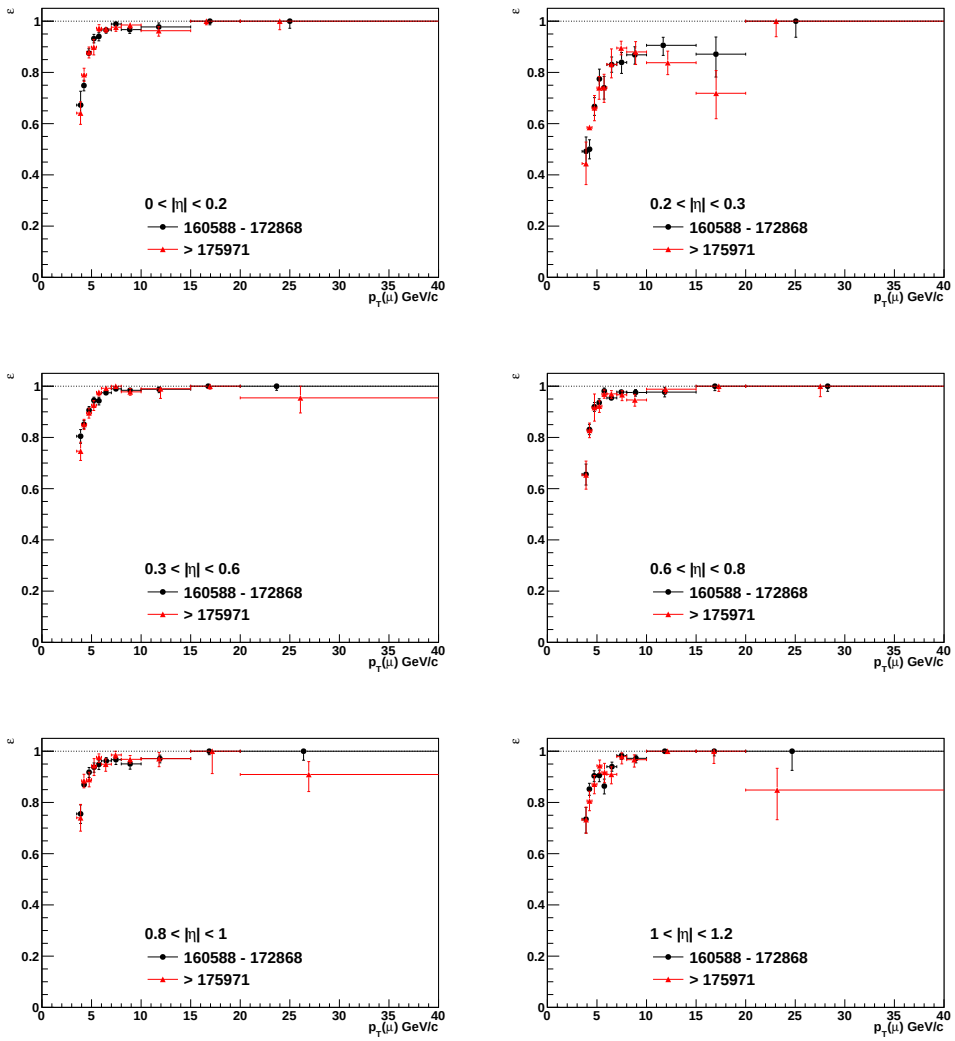

Figure 6.21: p_T dependence of the L1·L2 trigger efficiency during the first (165088 – 172868) and the third run period (> 175971) as a function of p_T in various slices of $|\eta|$, using the *tracker80* muon cuts.

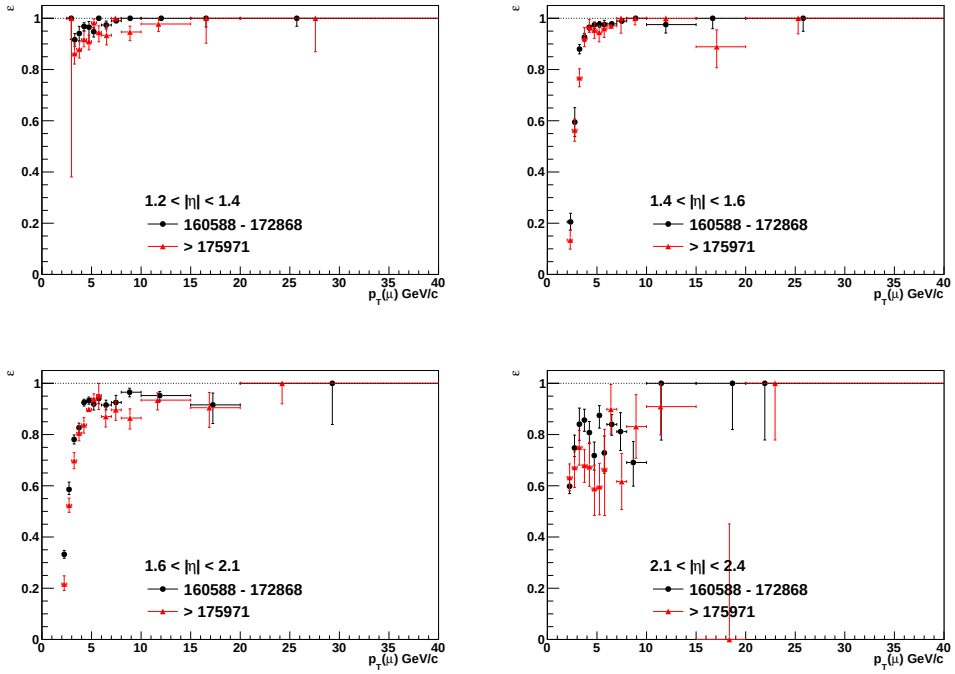

Figure 6.21: p_T dependence of the L1·L2 trigger efficiency (cont.).

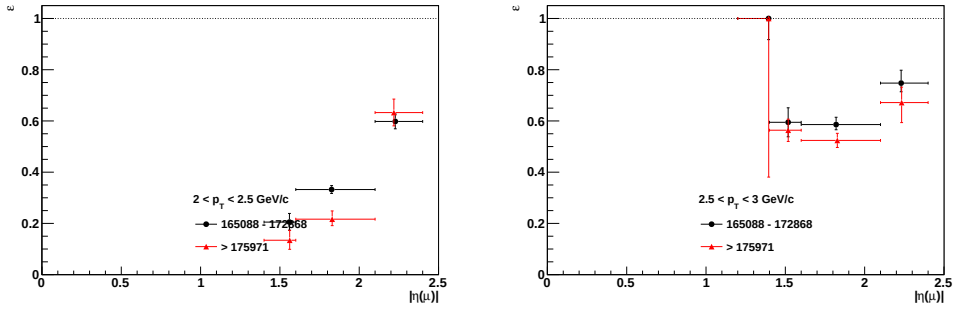

Figure 6.22: Comparison of the L1·L2 trigger efficiency during the first (165088 – 172868) and the third run period (> 175971) as a function of $|\eta|$ in various slices of p_T, using the *tracker80* muon cuts.

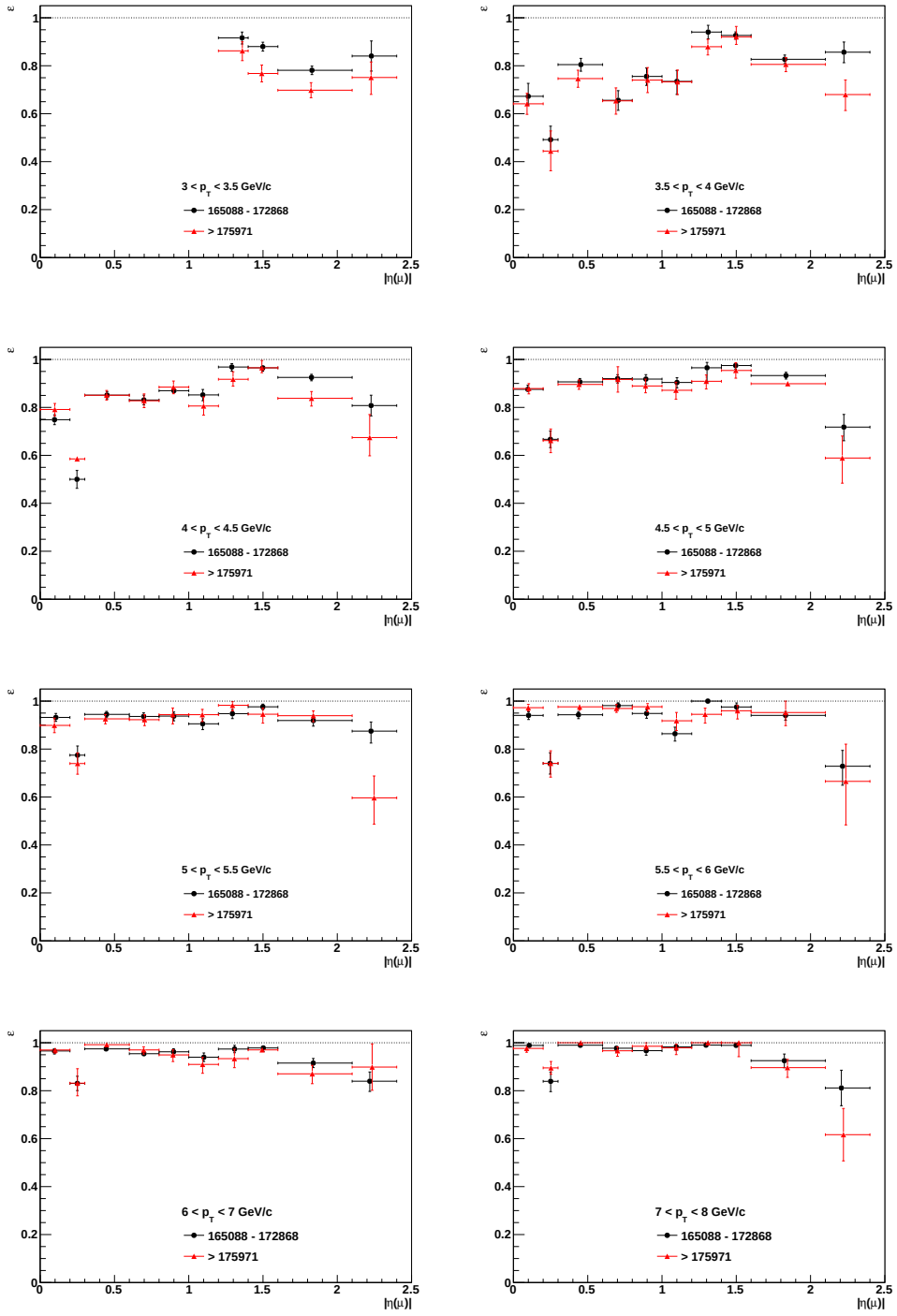

Figure 6.22: $|\eta|$ dependence of the L1·L2 trigger efficiency (cont.).

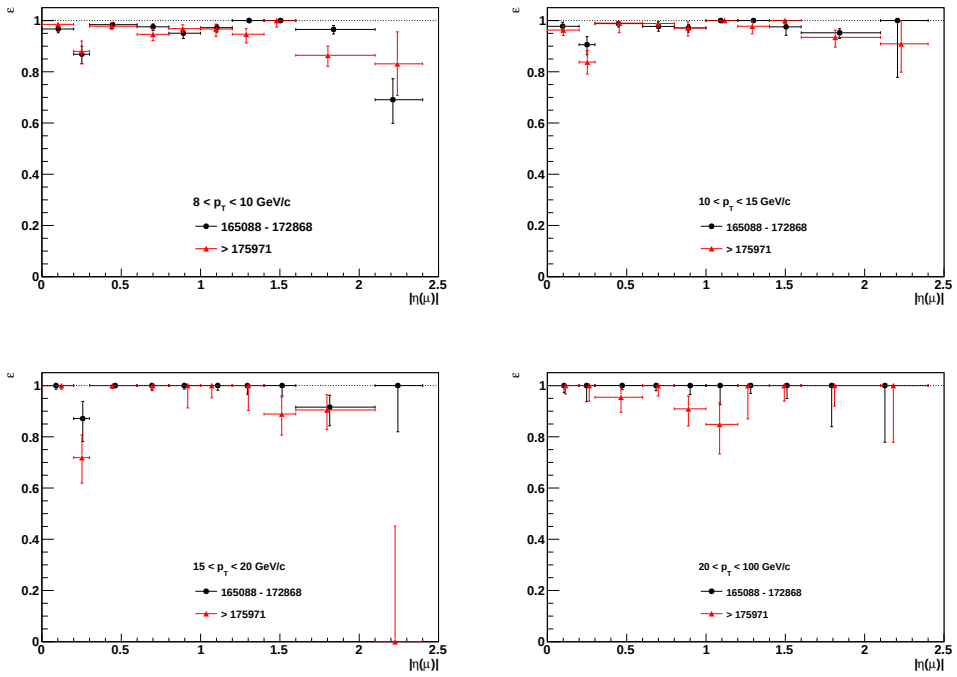

Figure 6.22: $|\eta|$ dependence of the L1·L2 trigger efficiency (cont.).

6.7 L3 Trigger Efficiency

The L3 trigger efficiency gives the probability of a L2 muon passing the L3 filters. In order to be able to measure the full p_T and $|\eta|$ range unaffected by prescale factors, the L3 trigger efficiencies presented here correspond to the intrinsic trigger efficiencies of L3 muons and are not measured with respect to a certain L3 filter. This means that cuts used in specific L3 filters are not accounted for. The effect of those cuts, like the Distance of Closest Approach (DCA) cut which is part of almost all L3 filter used in the *MuOnia* dataset, have to be measured in an independent way.

The tags are as usual HLT muons matched to `Mu5` leg of the `HLT_Mu5_L2Mu2_Jpsi` trigger path. The probes are matched to the `L2Mu2` leg, thus have to pass the corresponding L2 filter (`hltMu5L2Mu2JpsiTrackMassFiltered`) and must also pass the *BMuQual* criteria. The passing probes are requested to be contained in the collection `hltL3MuonCandidate` and have a $p_T > 2$ GeV/c.

The L3 trigger efficiencies studied in 2D can be found in Figs. 6.23 and 6.24 where the cowboys were discarded due to the inefficiencies on L2. For a transverse momentum up to 5.5 GeV/c, the L3 trigger efficiencies exhibit a $|\eta|$ dependence. Afterwards 100% efficiency is measured, meaning that the plateau value is reached around $p_T \gtrsim 5.5$ GeV/c. The turn-on curve is steeper than for the L1·L2

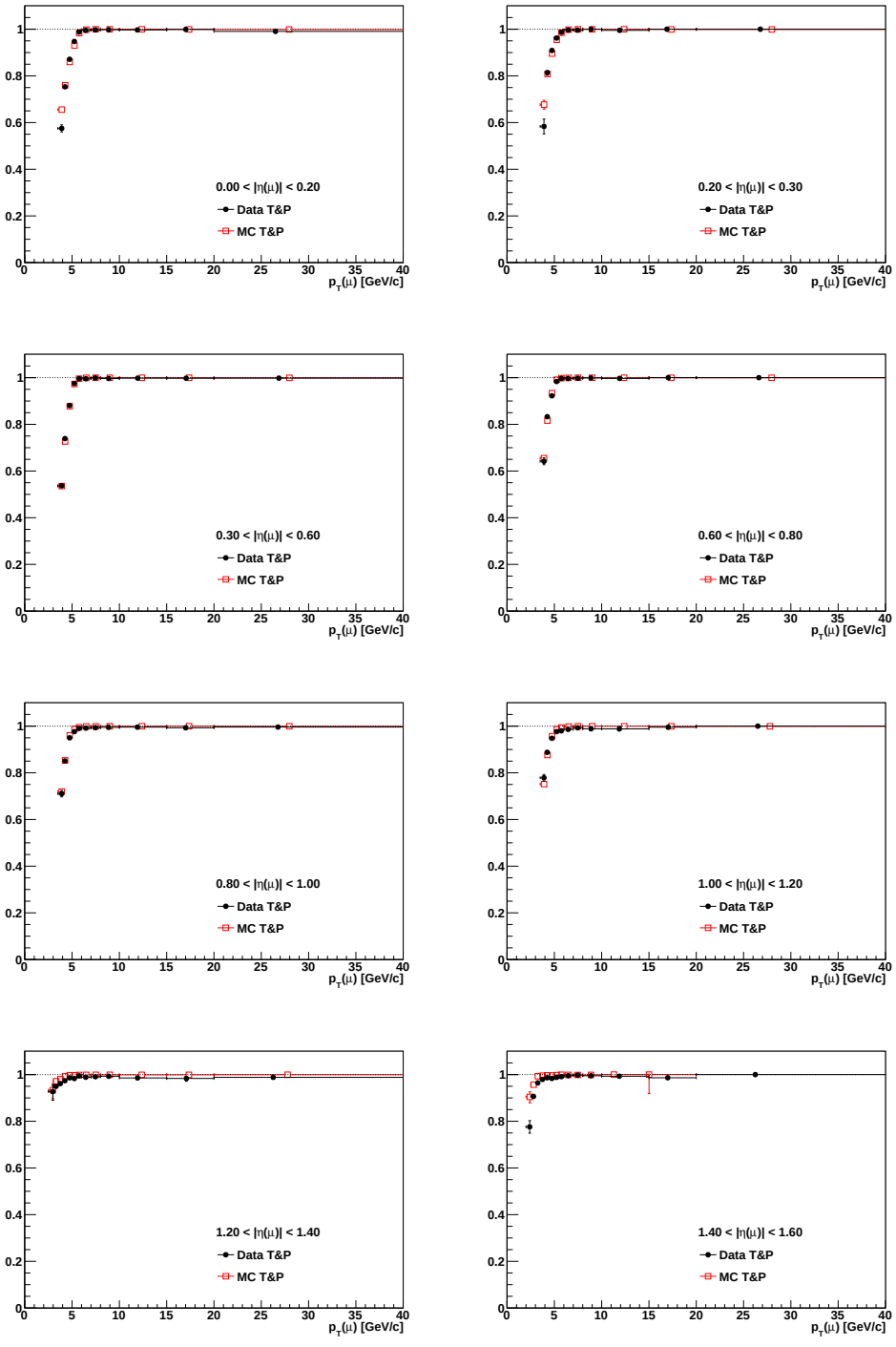

Figure 6.23: L3 trigger efficiency as a function of p_T in various slices of $|\eta|$, using the *tracker80* muon cuts (165088 – 178379).

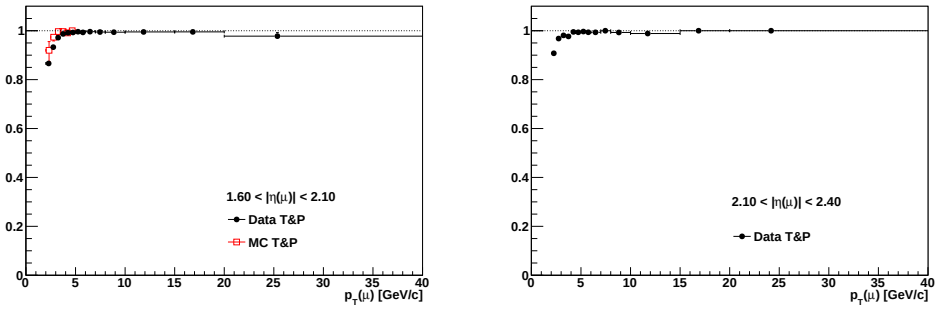

Figure 6.23: p_T dependence of the L3 trigger efficiency (cont.).

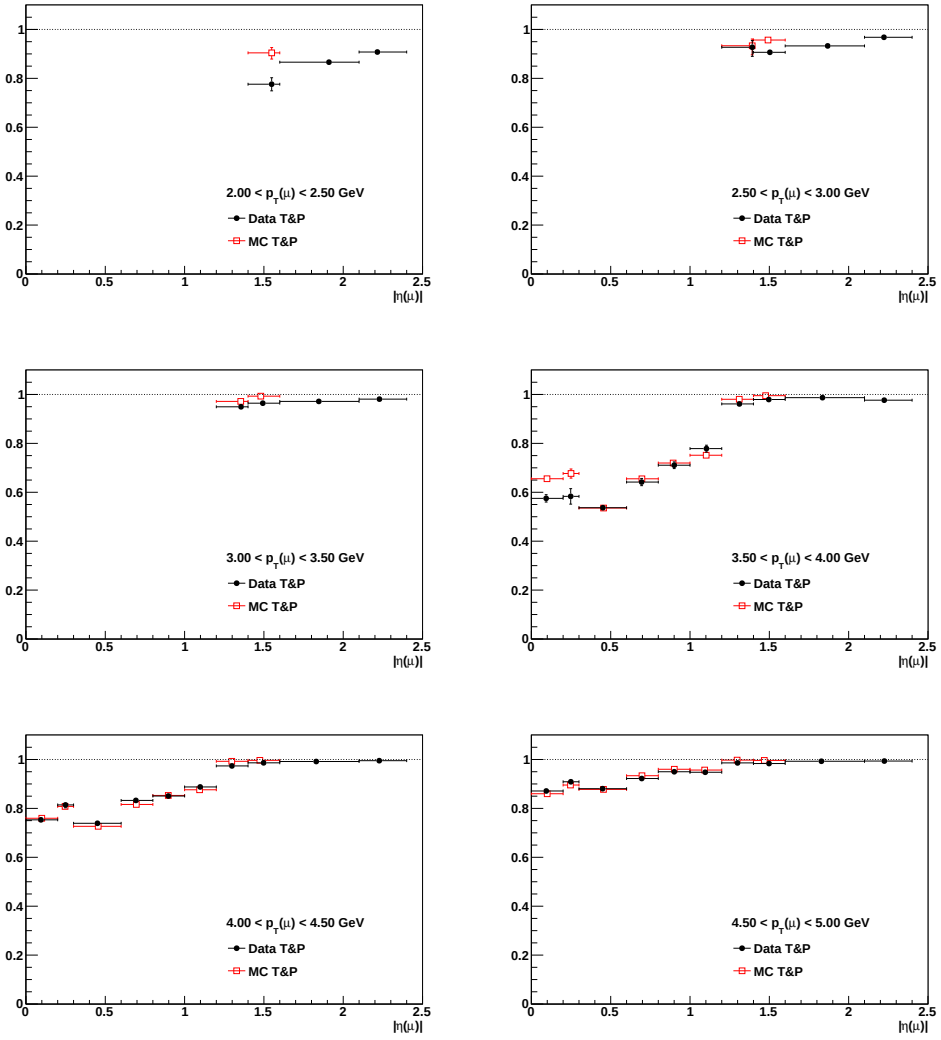

Figure 6.24: L3 trigger efficiency as a function of $|\eta|$ in various slices of p_T, using the *tracker80* muon cuts (165088 – 178379).

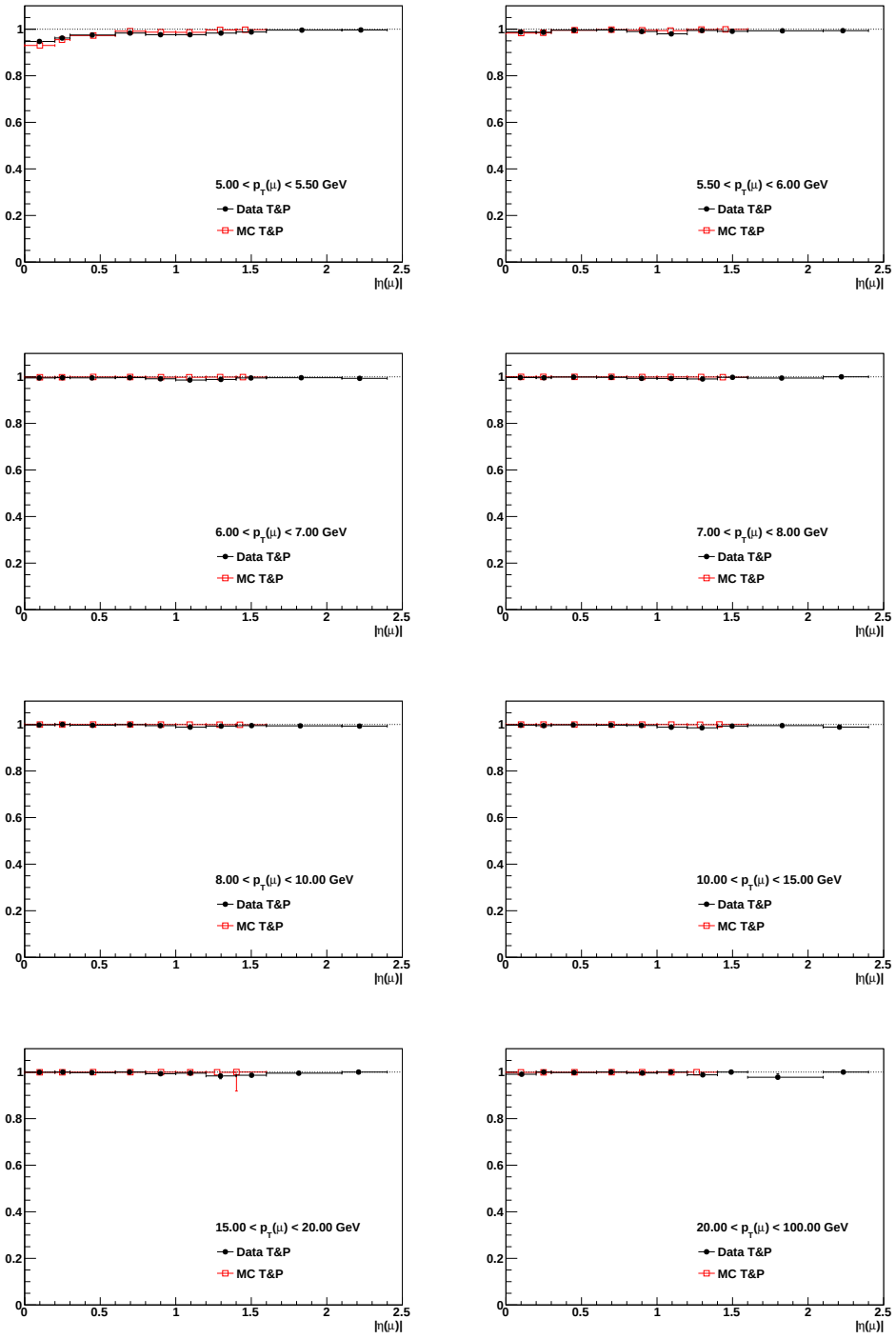

Figure 6.24: $|\eta|$ dependence of the L3 trigger efficiency (cont.).

trigger efficiencies. The data-driven efficiencies have a small statistical error and are accurately reproduced by the MC TnP efficiencies.

As explained in Section 6.2, the p_T assignment of the L3 muons changed in run 178380 which is why the run period 165088 – 178379 and the one from 178380 onwards are considered separately. Figs. 6.25 and 6.26 show the comparison of the data-driven efficiencies of these run periods differentially in p_T and $|\eta|$ for small slices of $|\eta|$ and p_T, respectively. The efficiencies show similar behavior. No striking differences or clear trends can be seen.

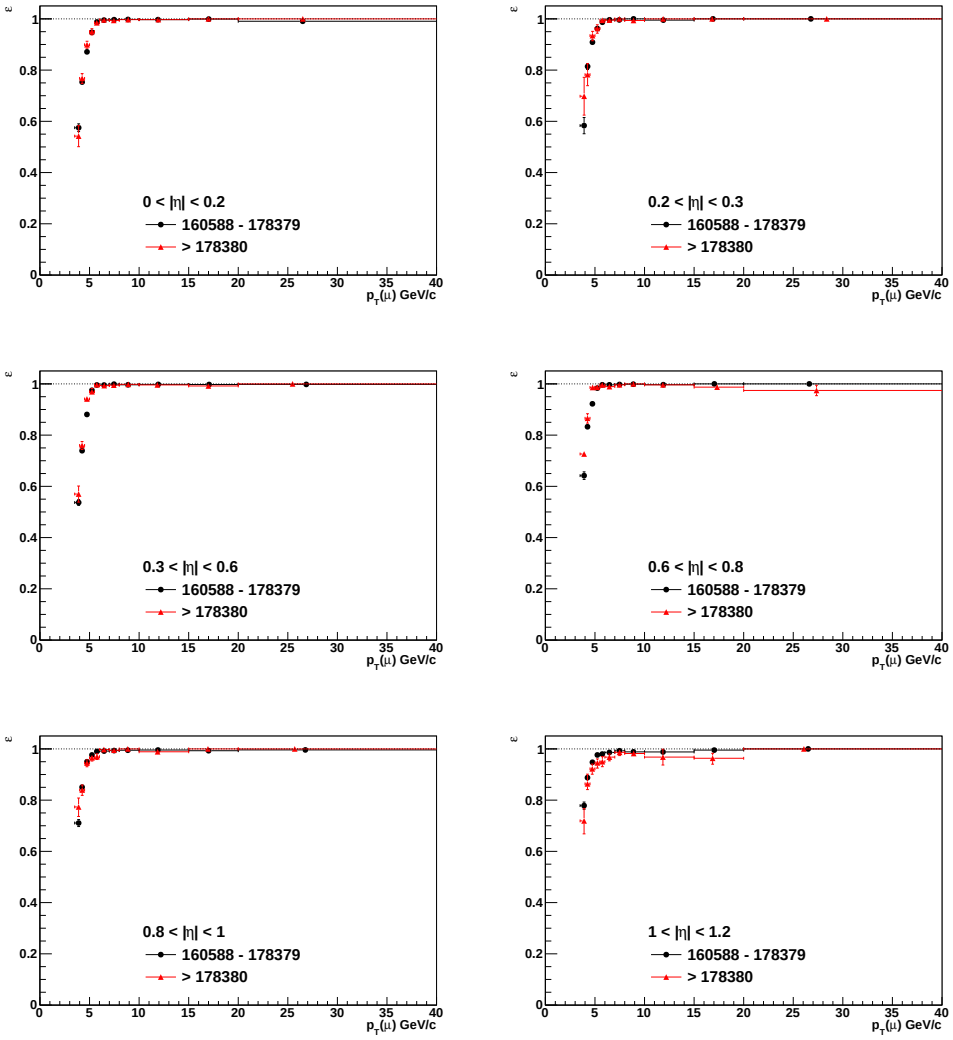

Figure 6.25: Comparison of the L3 trigger efficiency during the two different run periods as a function of p_T in various slices of $|\eta|$, using the *tracker80* muon cuts.

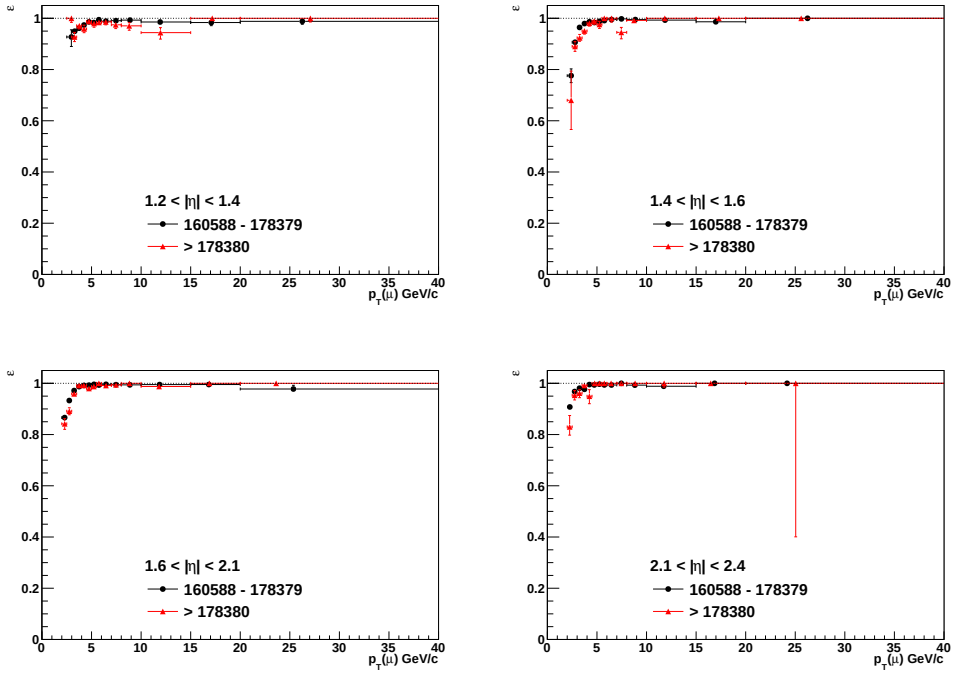

Figure 6.25: p_T dependence of the L3 trigger efficiency (cont.).

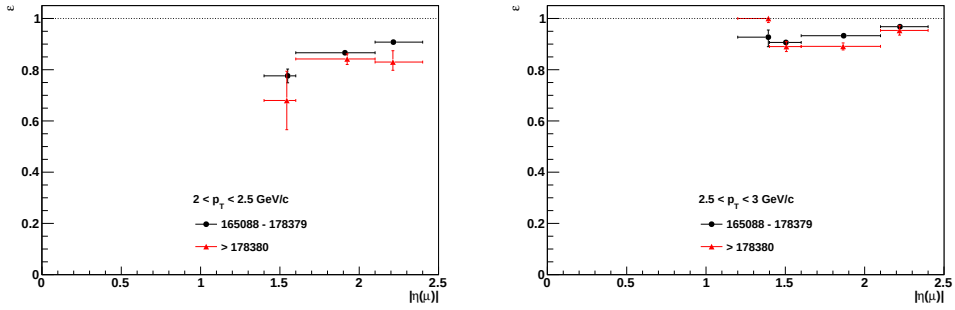

Figure 6.26: Comparison of the L3 trigger efficiency during the two different run periods as a function of $|\eta|$ in various slices of p_T, using the *tracker80* muon cuts.

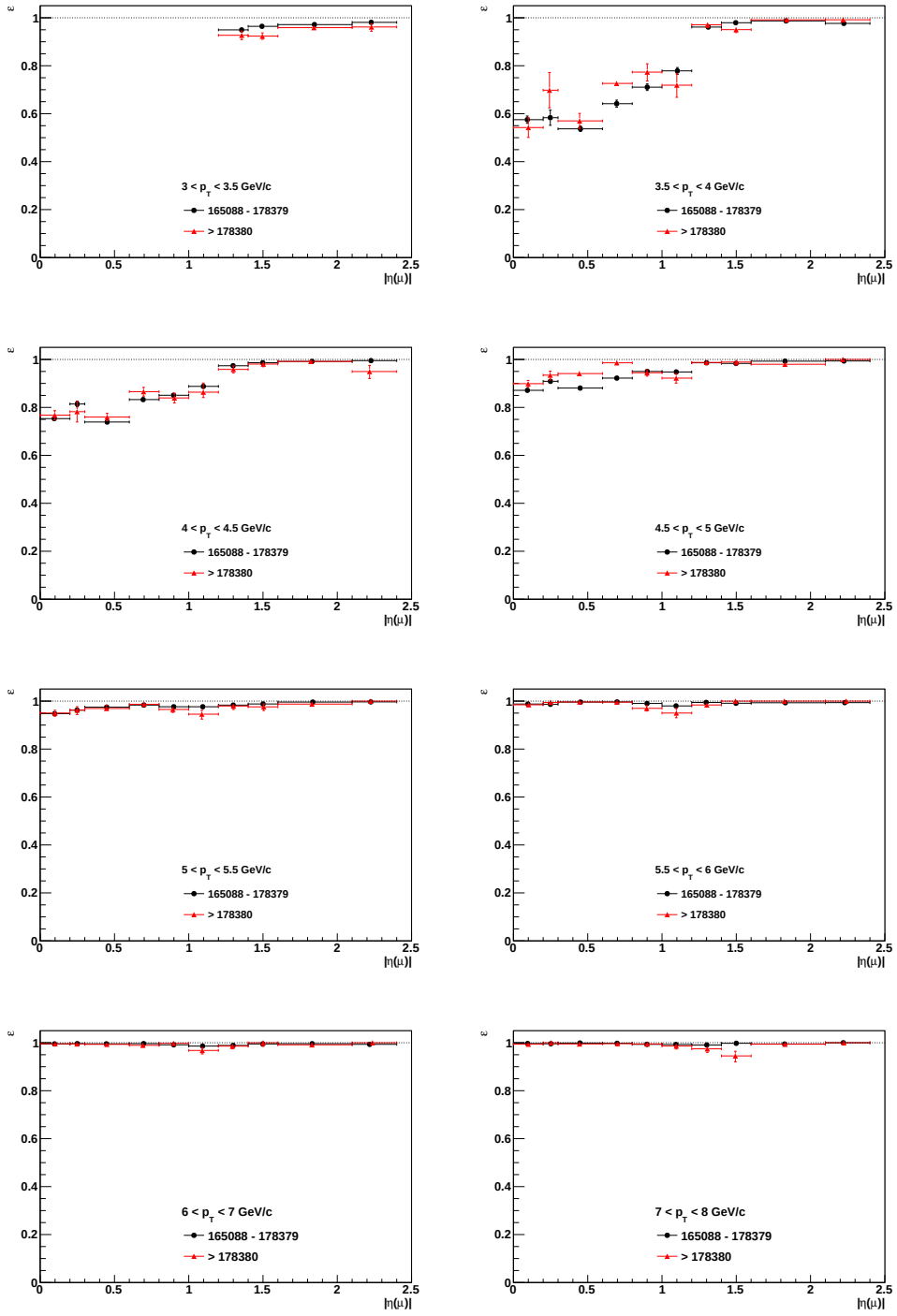

Figure 6.26: $|\eta|$ dependence of the L3 trigger efficiency (cont.).

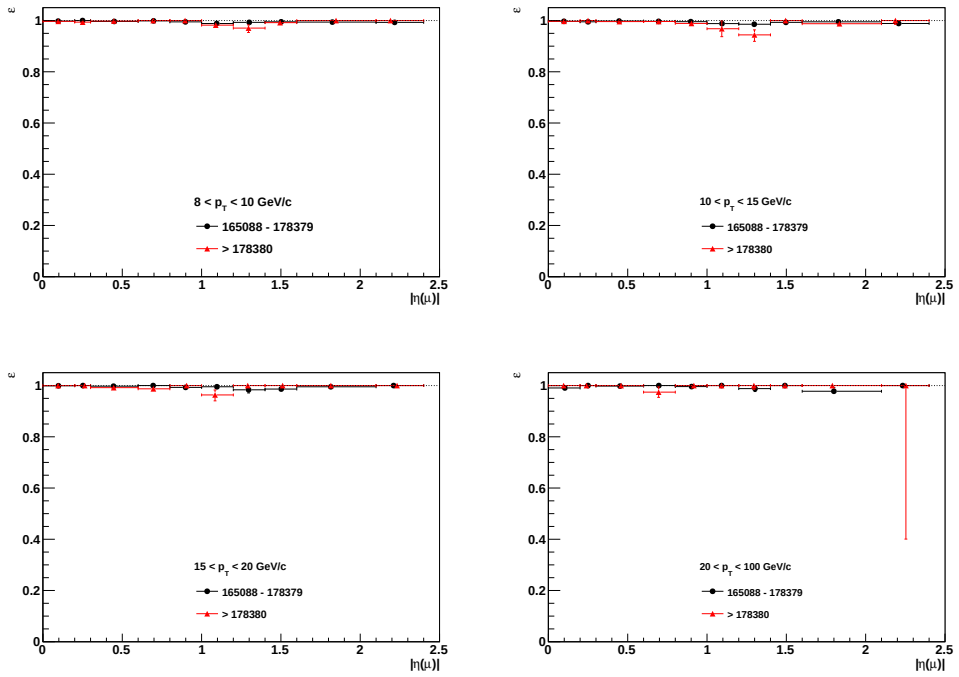

Figure 6.26: $|\eta|$ dependence of the L3 trigger efficiency (cont.).

6.8 Factorized Single Muon Detection Efficiencies

The overall single muon detection efficiency or factorized efficiency results from the individual components of the single muon efficiencies as

$$\varepsilon_{tot}(\mu) = \varepsilon_{Track}(\mu) \cdot \varepsilon_{MuonID}(\mu) \cdot \varepsilon_{MuonQual}(\mu) \cdot \varepsilon_{L1 \cdot L2}(\mu) \cdot \varepsilon_{L3}(\mu) \qquad (6.3)$$

The tracking efficiency is evaluated to be $(99 \pm 1)\%$. The error is obtained through error propagation, assuming that the individual efficiencies are fully uncorrelated. Figures 6.27 and 6.27 depict the factorized efficiency as functions of $|\eta|$ and p_T. The variations in the data-driven efficiencies are mostly due to the high background in the failing probes of the muon reconstruction efficiency as is explained in Section 6.3. Therefore, the product calculated with the MC based muon reconstruction efficiency together with the data-driven trigger efficiency and efficiency of the muon quality cuts are used for the polarization studies. This is feasible since the MC muon reconstruction efficiencies reproduce the data-driven ones within the uncertainties.

Since all the individual single muon efficiencies are reasonably described by the corresponding MC based efficiencies, also the overall comparison is in rather good agreement. Both data as well as MC based efficiencies show a p_T turn-on curve saturating at the maximum efficiency of around 95% for a p_T below 10 GeV/c.

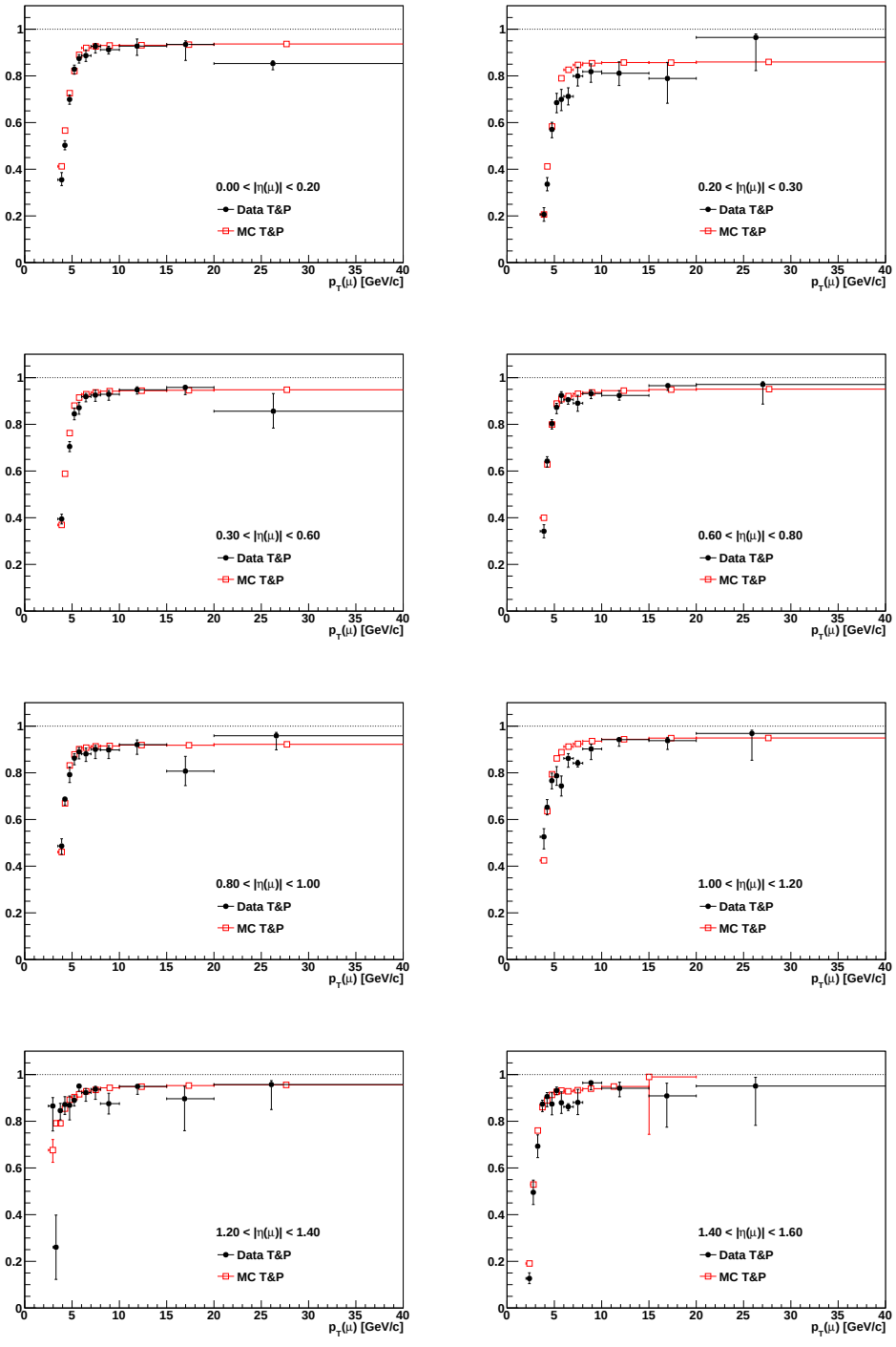

Figure 6.27: Factorized single muon efficiency as a function of p_T in various slices of $|\eta|$, using the *tracker80* muon cuts.

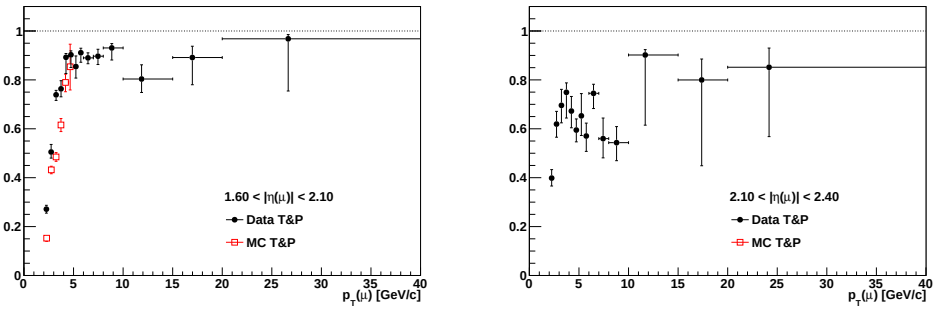

Figure 6.27: p_T dependence of the factorized efficiency (cont.).

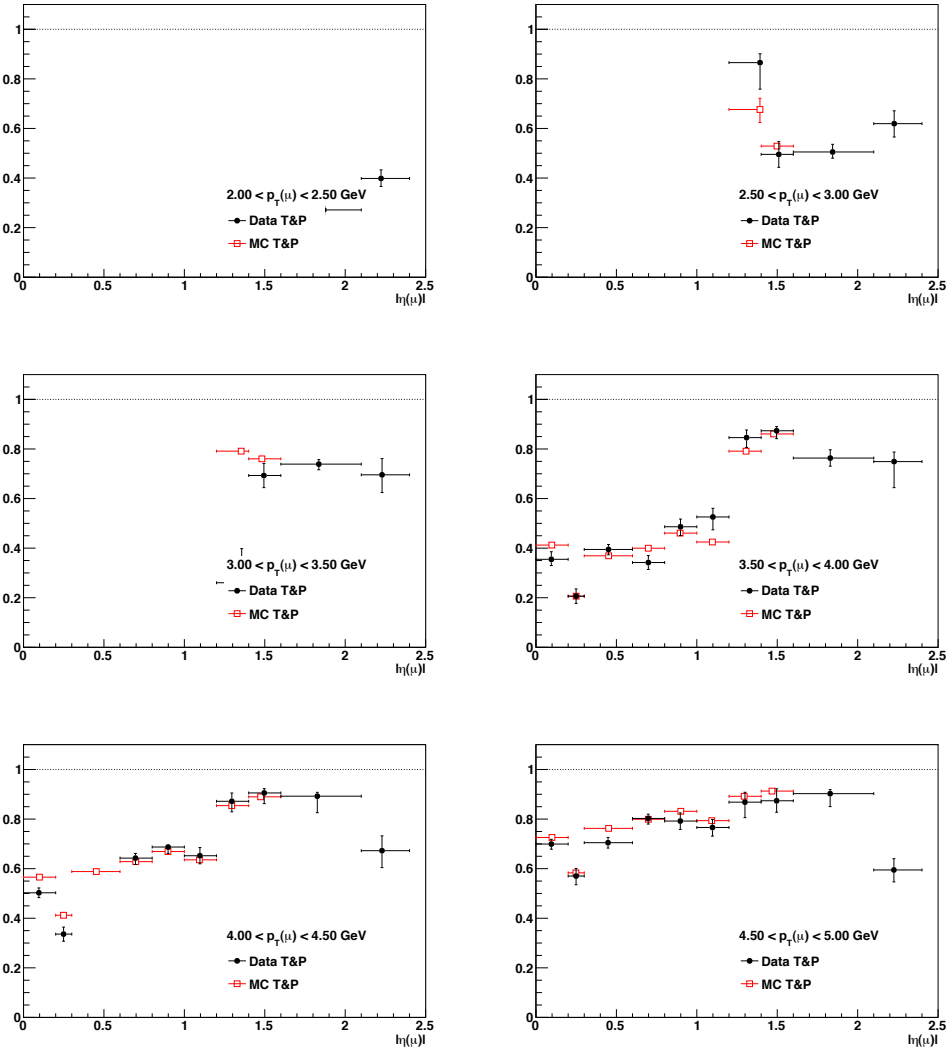

Figure 6.27: Factorized single muon efficiency as a function of $|\eta|$ in various slices of p_T, using the *tracker80* muon cuts.

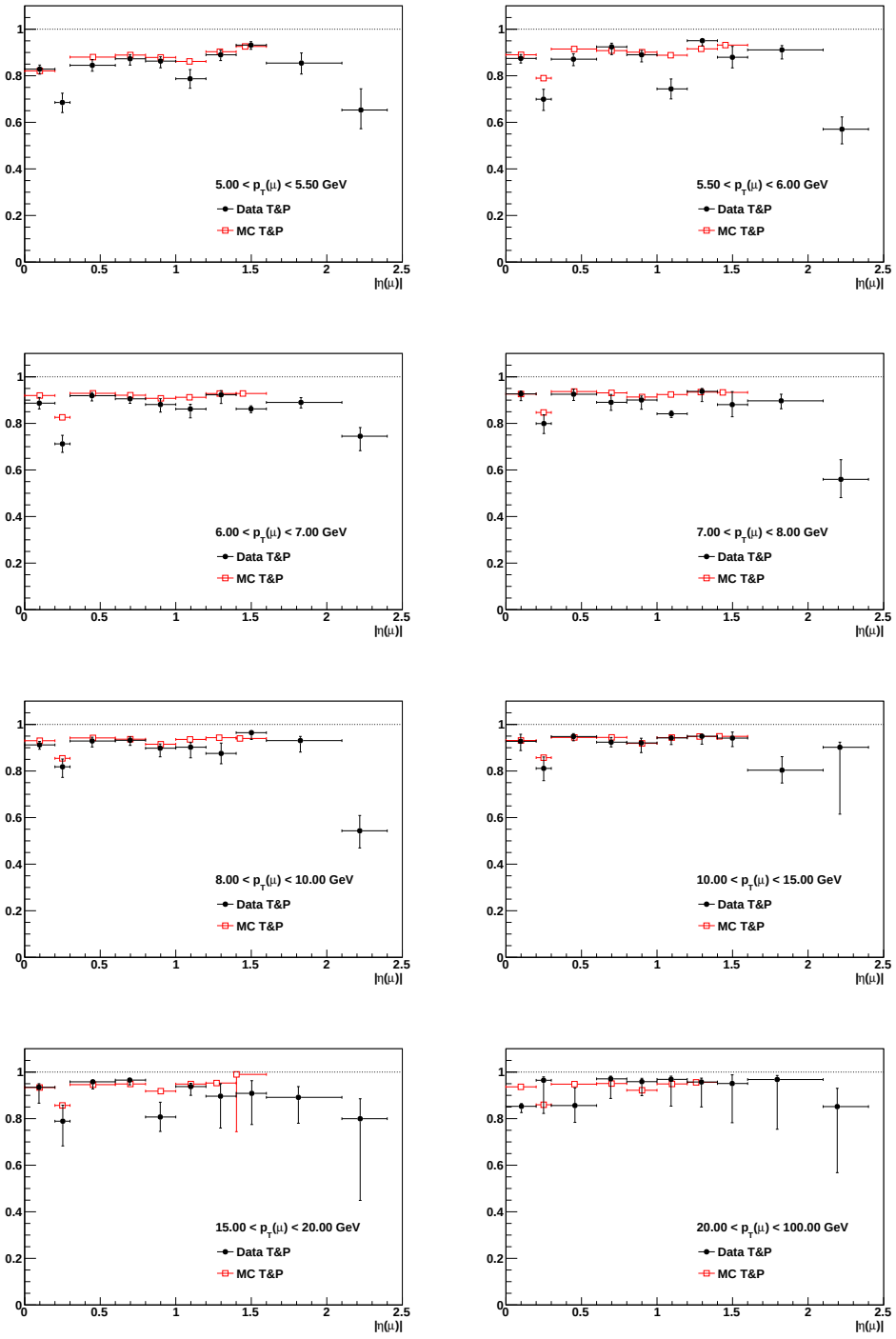

Figure 6.27: $|\eta|$ dependence of the factorized efficiency (cont.).

6.9 Inclusive Single Muon Efficiency

The total single muon efficiency can not only be obtained through the factorization into the individual single muon efficiencies, but can also be studied on its own without factorization. The `HLT_Mu5_Track2_Jpsi` efficiency trigger is used where the tag is again matched to the `Mu5` leg while the probe is matched to `Track2`. The passing probes have to pass the *BMuQual* criteria as well as the L3 trigger condition, i.e. be a L3 muon candidate with $p_T > 2$ GeV/c, to reproduce the factorized efficiency. This means that the combination of the muon reconstruction, the L1·L2, L3 trigger efficiency as well as the efficiency of the muon quality cuts are studied all at once with respect to an offline track. To avoid any inefficiencies related to the *close-by* cowboy dimuons, only seagulls are taken into account.

Figure 6.28 depicts the inclusive efficiency p_T differentially for various slices in p_T while Fig. 6.29 shows the corresponding $|\eta|$ differential efficiencies for various slices of $|\eta|$. The variation of the data-driven efficiencies is again due to the high background in the failing probes as already discussed for the muon reconstruction efficiency in Section 6.3. An example for the fitting of the mass distributions can be seen in Fig. 6.30. Given the large uncertainties, the MC describes the data rather accurately.

The two methods of extracting the overall single muon efficiency, the factorized and the inclusive approach, are equivalent, given that the individual single muon efficiencies were obtained with respect to the previous efficiency, i.e. without any bias. The comparison between the two approaches is discussed in detail in the next section.

6.10 Validation of the Single Muon Efficiencies

In order to validate the single muon efficiencies, a sample with true dimuons was generated using a special muon pair gun. The positive muon is simulated with *fixed* kinematical configurations ($\eta = \pm 1$, $p_T = 40$ GeV/c, $\phi = 10°$) while the negative muon is generated *freely* with a uniform p_T ($2 < p_T < 100$ GeV/c), η ($-2.4 < \eta < 2.4$) and ϕ distribution. The sign of η of the *fixed* muon is always opposite of the one of the *free* muon. Therefore, the muons are measured in different detector elements and do not suffer from the dimuon trigger inefficiencies of *close-by* muons. Moreover, the kinematics of the *fixed* muon are chosen in a way that its efficiency is constant and close to 100%. The *free* muon is ergo not biased by the presence of the second *fixed* muon.

Since the resulting dimuon mass does not have the one of the J/ψ anymore, but instead is arbitrary, the trigger simulation is done without any dimuon mass constraints while the rest of the trigger menu is identical to the trigger settings used in the 1E33 to the 3E33 menu. After the full detector simulation, the *free* muon is matched to a HLT muon passing the last filter in the dimuon triggers

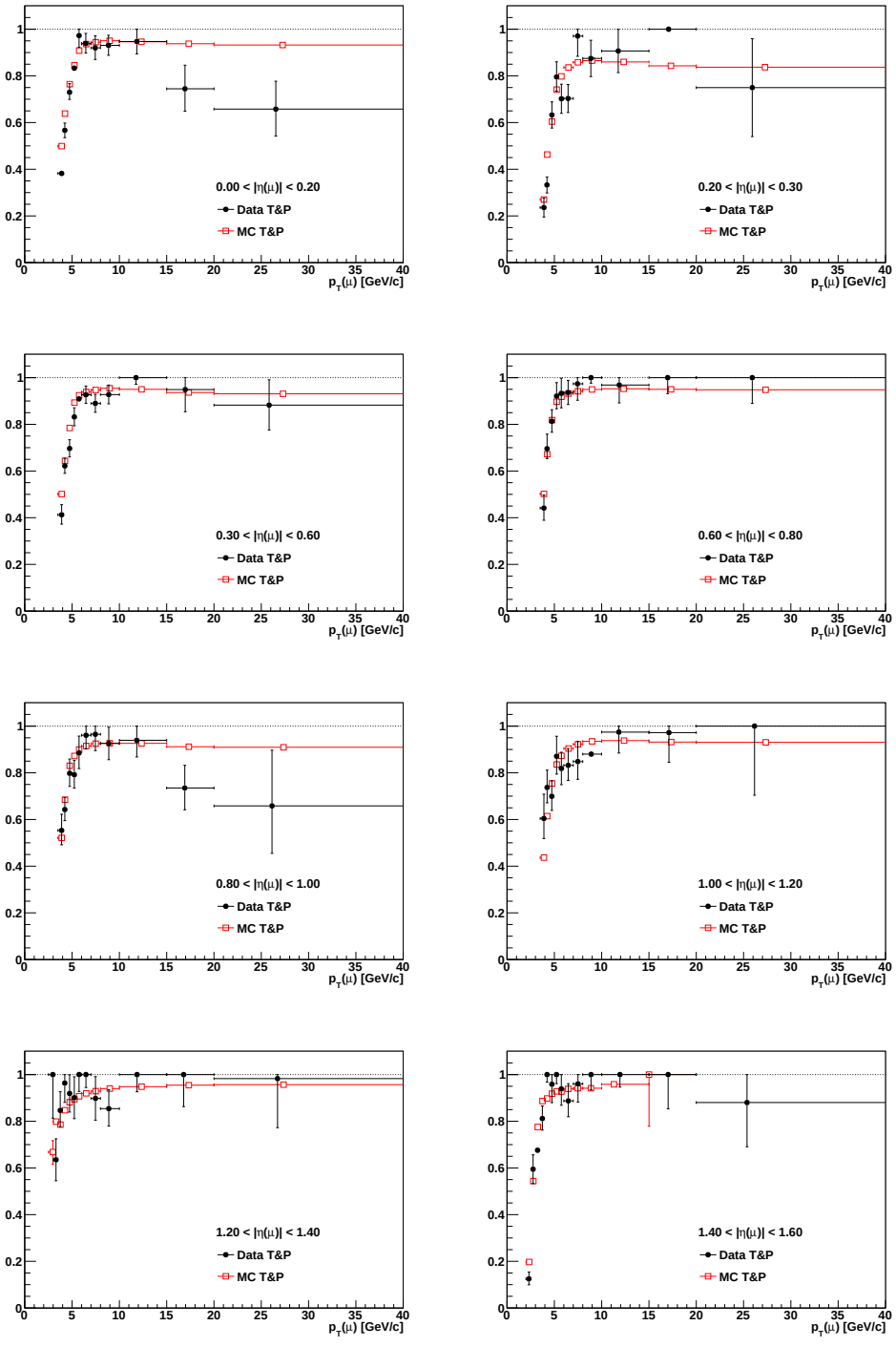

Figure 6.28: Inclusive efficiency as a function of p_T in various slices of $|\eta|$, using the *tracker80* muon cuts (165088 – 173692).

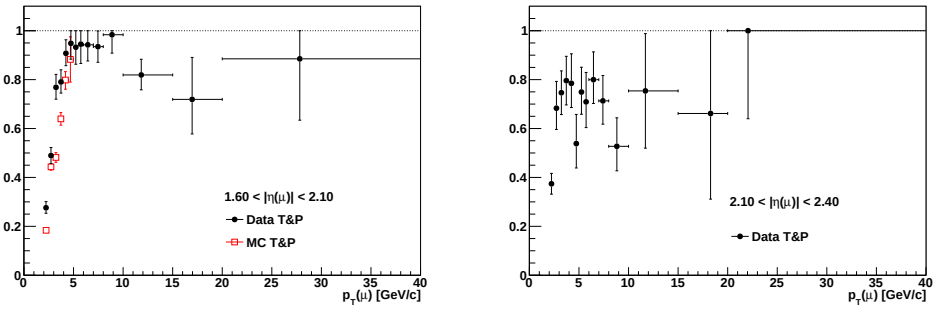

Figure 6.28: p_T dependence of the inclusive efficiency (cont.).

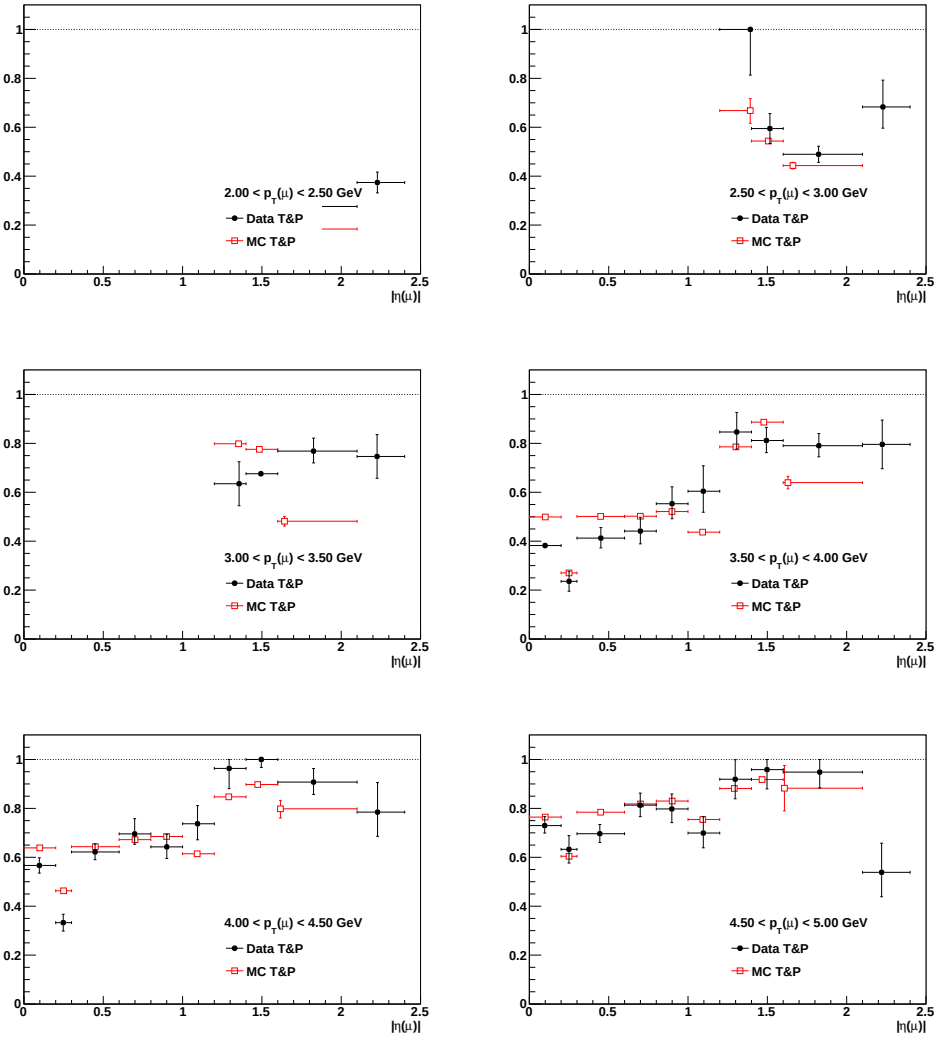

Figure 6.29: Inclusive efficiency as a function of $|\eta|$ in various slices of p_T, using the *tracker80* muon cuts (165088 – 173692).

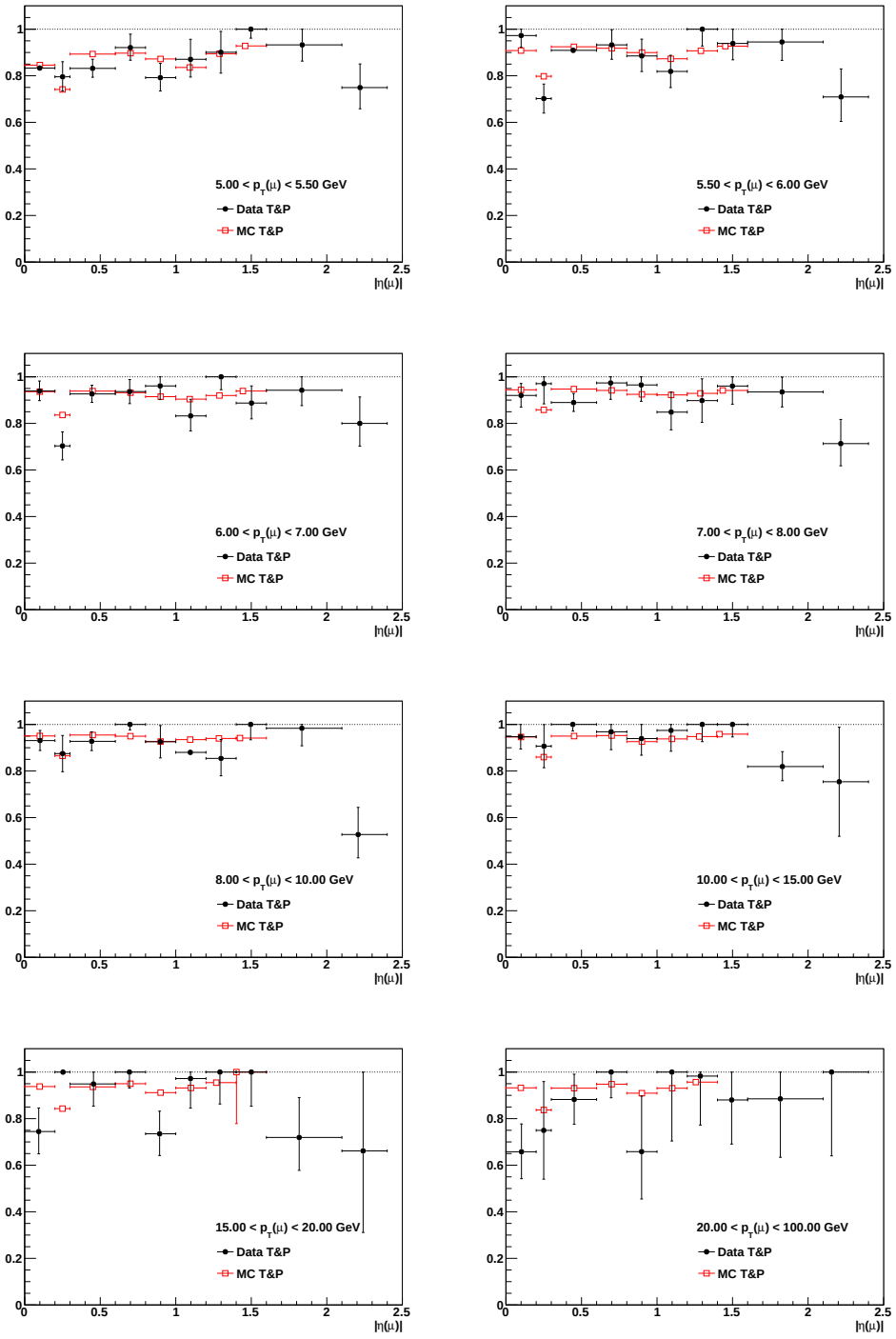

Figure 6.29: $|\eta|$ dependence of the inclusive efficiency (cont.).

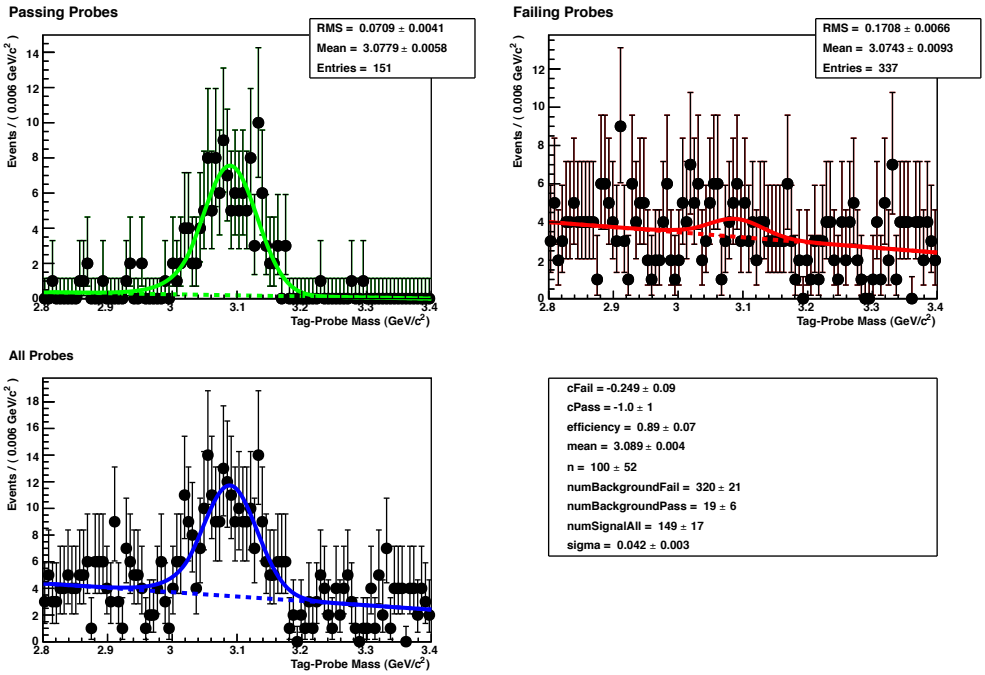

Figure 6.30: Example of the fitted mass distributions of passing, failing and all probes in case of the inclusive efficiency for $1.4 < |\eta| < 1.6$ and $6 < p_T < 7$ GeV/c.

Table 6.3: Trigger versions used in the CMS quarkonia polarization studies, their trigger menu, run range and prescale factor PS.

Trigger	Trigger menu	Run range	PS
HLT_Dimuon10_Jpsi_Barrel_v1	1E33	165088 – 166967	1
	1.4E33	167039 – 167043	
HLT_Dimuon10_Jpsi_Barrel_v2	1E33	166346	1
HLT_Dimuon10_Jpsi_Barrel_v3	1.4E33	167078 – 167913	2
HLT_Dimuon10_Jpsi_Barrel_v5	2E33	170249 – 172868	1
HLT_Dimuon10_Jpsi_Barrel_v6	3E33	173236 – 178421	1
HLT_Dimuon10_Jpsi_Barrel_v9	5E33	178421 – 180252	1
HLT_Dimuon13_Jpsi_Barrel_v1	3E33	173236 – 178421	1
HLT_Dimuon13_Jpsi_Barrel_v4	5E33	178421 – 180252	1
HLT_Dimuon5_Upsilon_Barrel_v1	1E33	165088 – 166967	1
	1.4E33	167039 – 167043	
HLT_Dimuon5_Upsilon_Barrel_v2	1E33	166346	1
HLT_Dimuon5_Upsilon_Barrel_v3	1.4E33	167078 – 167913	1
HLT_Dimuon5_Upsilon_Barrel_v5	2E33	170249 – 172868	1
HLT_Dimuon7_Upsilon_Barrel_v1	3E33	173236 – 178421	1
HLT_Dimuon7_Upsilon_Barrel_v4	5E33	178421 – 180252	1
HLT_Dimuon9_Upsilon_Barrel_v1	3E33	173236 – 178421	1
HLT_Dimuon9_Upsilon_Barrel_v4	5E33	178421 – 180252	1

employed in the CMS polarization analysis, namely `HLT_DimuonX_Jpsi_Barrel` in case of the J/ψ and `HLT_DimuonX_Upsilon_Barrel` in the case of the Υ. The term `Barrel` refers to a dimuon rapidity cut of $|y| < 1.25$ while the `X` in the trigger name gives the value for the cut on the minimal transverse momentum. The different trigger versions, their trigger menu, run range and prescale factor are listed in Table 6.3.

The MC truth efficiency is defined as the number of reconstructed dimuon events divided by all generated events. Figure 6.31 exhibits the single muon MC truth efficiencies in comparison with the MC based factorized efficiencies and the MC based inclusive efficiencies as a function of p_T. The plots are cut at $p_T = 20$ GeV/c to be able to better scrutinize the differences in the turn-on region. The factorized and inclusive efficiencies are very similar and rather close to the MC truth efficiency, thus validating the TnP framework. The MC truth efficiencies seem to describe both of the two TnP approaches up to $|\eta| < 1.0$ very well. The discrepancies above are most likely due to the restriction of the MC simulation to $|y(\mu\mu)| < 1.3$. This good agreement of the p_T dependence of the different efficiencies makes it difficult to evaluate the better TnP method by looking at the turn-on curves. Therefore, the ratio between the MC truth efficiencies and the MC based factorized efficiencies and the MC based inclusive efficiencies, respectively, is built. Figure 6.32 shows the results.

Looking closely at the ratio, the product of the single muon efficiencies seems to give the flatter ratio over wider ranges of p_T which means that it would be the better choice of efficiency approach in terms of shape.

The ratio $\varepsilon_{\mathrm{MC}}^{\mathrm{TnP}}/\varepsilon_{\mathrm{MC}}^{\mathrm{Truth}}$ also gives information about the p_T region over which the single muon efficiencies are applicable. Assuming that the error bars of the ratio are larger in the problematic $0.2 < |\eta| < 0.3$ bin than in the other bins, the minimum p_T could be set to 4.5 GeV/c in all bins under study except in the $1.4 < |\eta| < 1.6$ bin where the p_T cut can even be at 3.5 GeV/c.

6.11 Efficiency of the Trigger Dimuon Vertexing Module

The dimuon vertexing module is the last L3 filter used in all the quarkonium physics trigger of the *MuOnia* PD, in case of the `HLT_Dimuon10_Jpsi_Barrel` trigger path under study it is `hltVertexmumuFilterJpsiBarrel`. In order to determine its efficiency, a slightly different procedure has to be adopted since not a single muon, but a dimuon efficiency is probed. The TnP skim needs to be prepared with the arbitration option *OnePair* as explained in Section 6. In this way, the pair becomes the probe.

The efficiency is measured with respect to two muons coming from the collection `hltL3MuonCandidate`, having $p_T > 2$ GeV/c and passing the *BMuQual* criteria. Moreover, the dimuon's p_T is required to be larger than 10 GeV/c, the dimuon's $|y|$ below 1.2 and the DCA below 4.8 mm. Only seagull dimuons are taken into account.

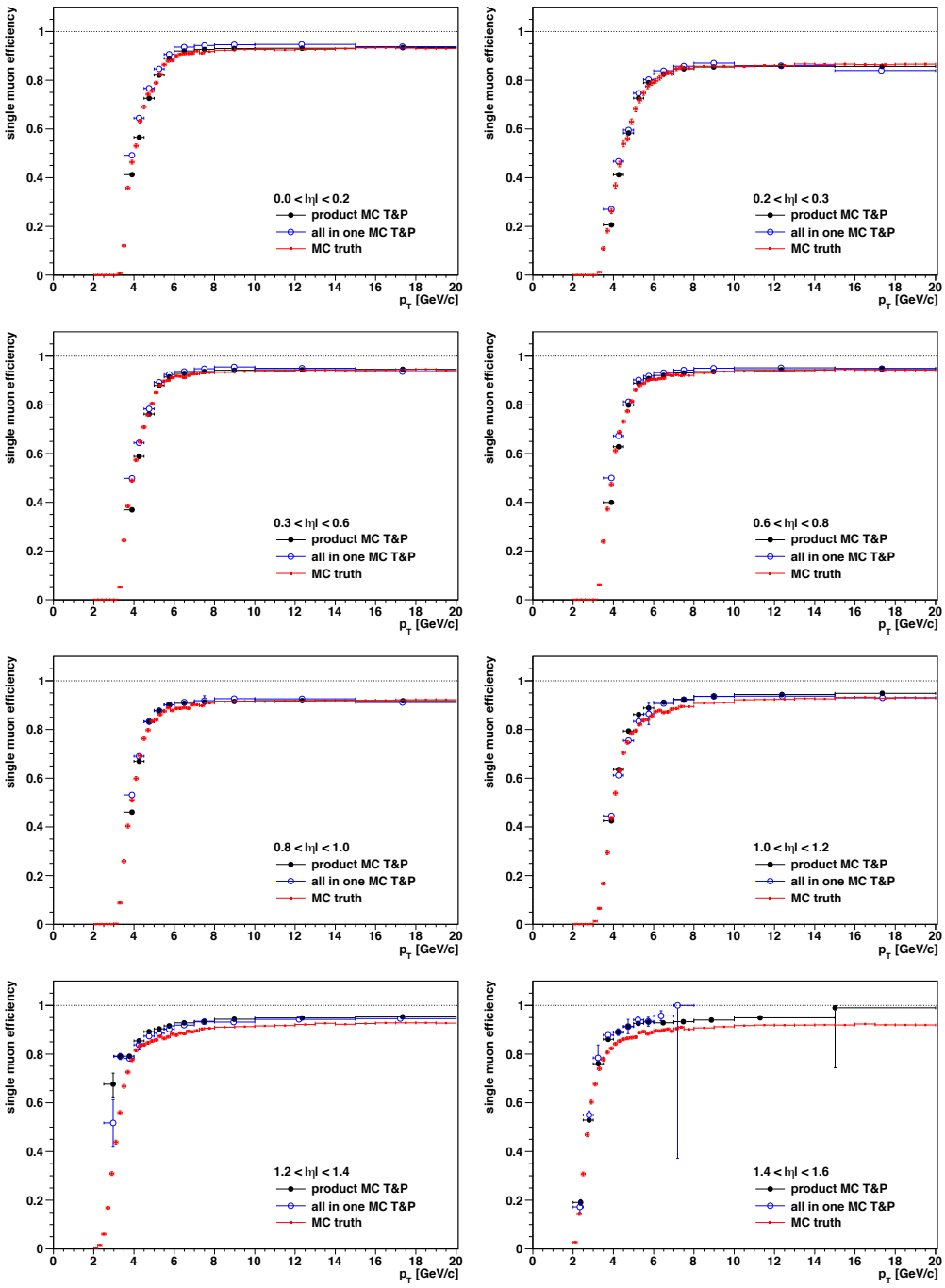

Figure 6.31: Comparison of the p_T dependence of the MC truth efficiency to the factorized and the inclusive efficiencies, using the *tracker80* muon cuts.

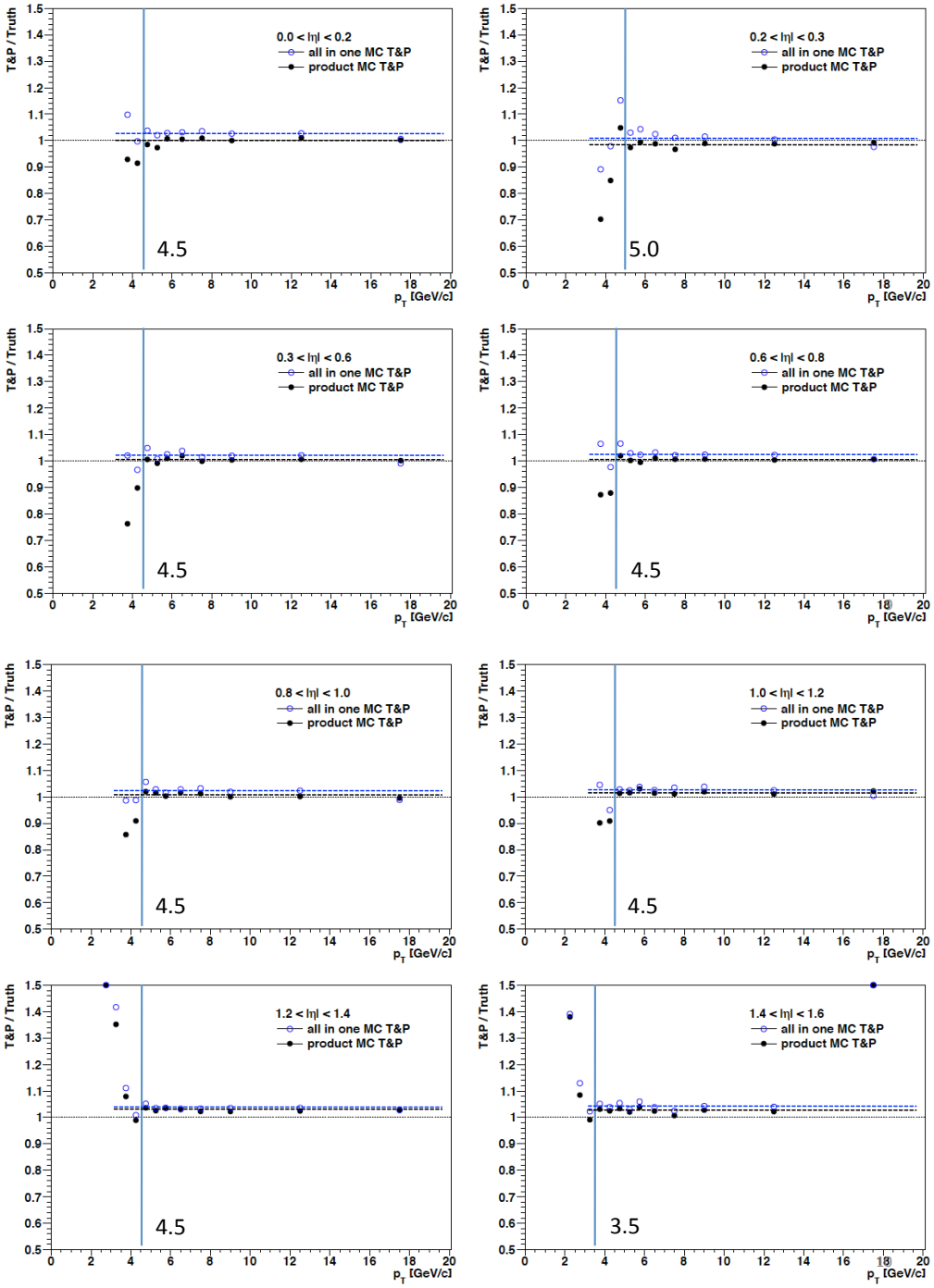

Figure 6.32: Ratio $\varepsilon_{\mathrm{MC}}^{\mathrm{TnP}}/\varepsilon_{\mathrm{MC}}^{\mathrm{Truth}}$ with MC TnP being either the factorized efficiency (black) or the inclusive efficiency (blue): The ratios are fitted with a flat line. The vertical line indicates the lowest p_T value where the efficiencies are still applicable.

Like this, the efficiency of the trigger dimuon vertexing module corresponds to the intrinsic efficiency of the dimuon vertexing algorithm and the effect of the cut on the vertex probability which is part of the dimuon vertexing filter. It requests the dimuon secondary vertex to have a fit χ^2 probability larger than 0.5%.

Since the polarization is extracted in terms of $\cos\theta$ and ϕ, the studies of the dimuon vertexing efficiency are conducted in bins of $\cos\theta$ and ϕ of the three reference frames:

- $\cos\theta = -1, -0.75, -0.5, -0.25, 0, 0.25, 0.5, 0.75, 1$
- $\phi = -180, -135, -112.5, -90, -77.5, -45, 0, 45, 77.5, 90, 112.5, 135, 180$

Only the results obtained in the CS frame are shown here. The efficiency of the dimuon vertexing module extracted in other reference frames can be found in Ref. [59]. However, the conclusions that are drawn here are valid for all reference frames. Figures 6.33 and 6.34 exhibit the efficiencies as functions of $\cos\theta_{CS}$ and ϕ_{CS}. The discrepancy between the data and the MC simulation is not yet understood and has to be studied in more detail. The shapes of the data-driven and MC based efficiencies, which are the crucial ingredient for the polarization studies, are very similar apart from the regions of low acceptance where the data-driven efficiency shows large uncertainties. The efficiencies are relatively flat in $\cos\theta_{CS}$ and ϕ_{CS}. This suggests that the effect on the polarization of the dimuon vertexing efficiency will be small and more importantly will not introduce any fake polarization.

6.12 Summary of Results on Tag and Probe Efficiency

Two methods of extracting the total single muon detection efficiency with the Tag and Probe method are used:

1. **Factorized efficiencies:** The total single muon efficiency is broken into five individual parts: muon tracking, muon reconstruction, muon quality, L1·L2 and L3 trigger efficiency. It is studied in a way that the five parts fully factorize.
2. **Inclusive efficiencies:** The total single muon efficiency is studied all at once.

The trigger efficiencies at L1 and L2 show inefficiencies for certain dimuon topologies (cowboy dimuons) which led to the rejection of the cowboys for the L1·L2 and L3 trigger efficiencies as well as the inclusive efficiencies.

Furthermore, the efficiency of the dimuon vertexing module which is the last L3 filter in all 2011 quarkonium triggers is studied. Since this filter is applied on a dimuon, a special TnP skim with the *OnePair* arbitration was produced.

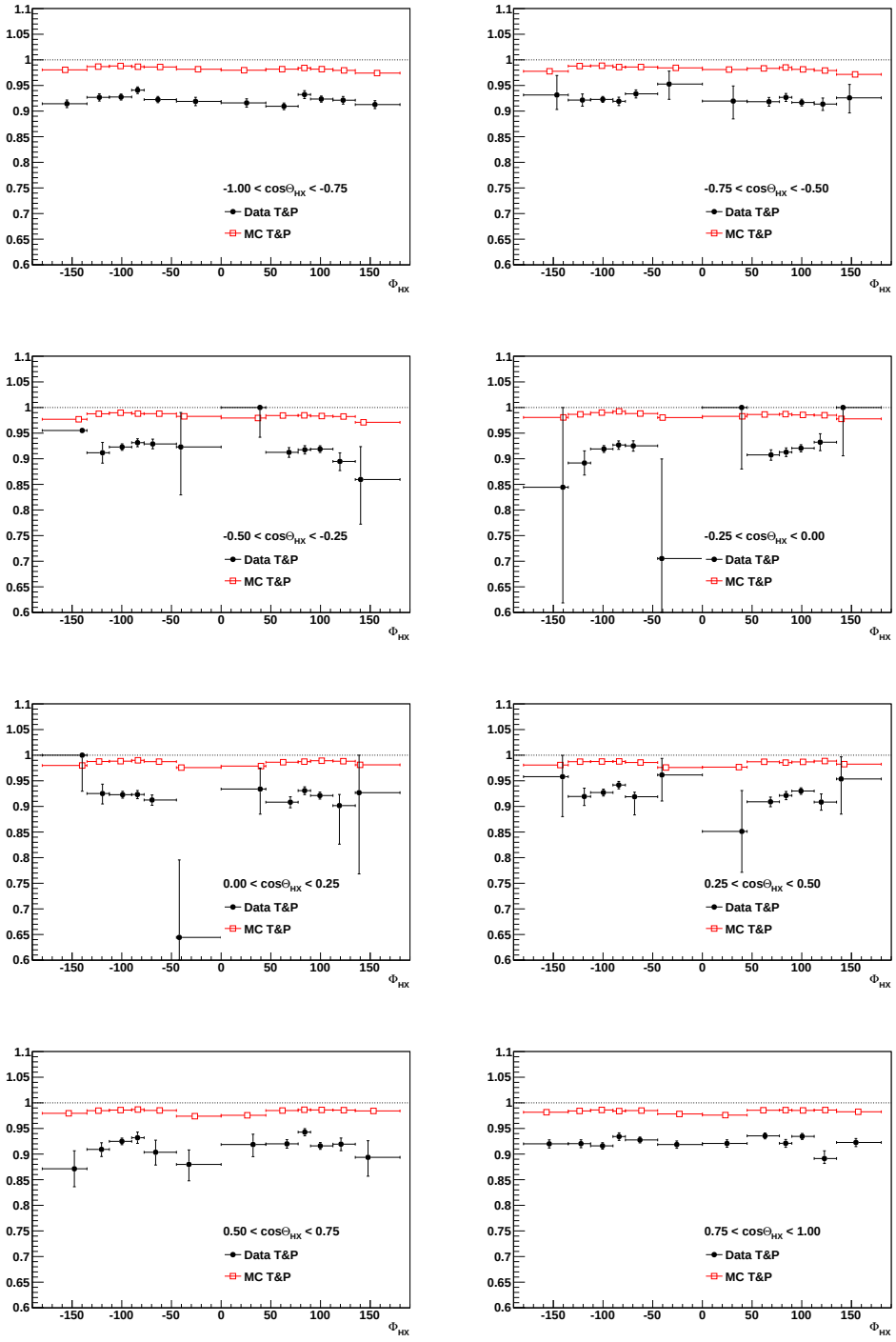

Figure 6.33: Efficiency of the dimuon vertexing module as a function of ϕ_{CS} in various slices of $\cos\theta_{CS}$, using the *tracker80* muon cuts (165088 – 178380).

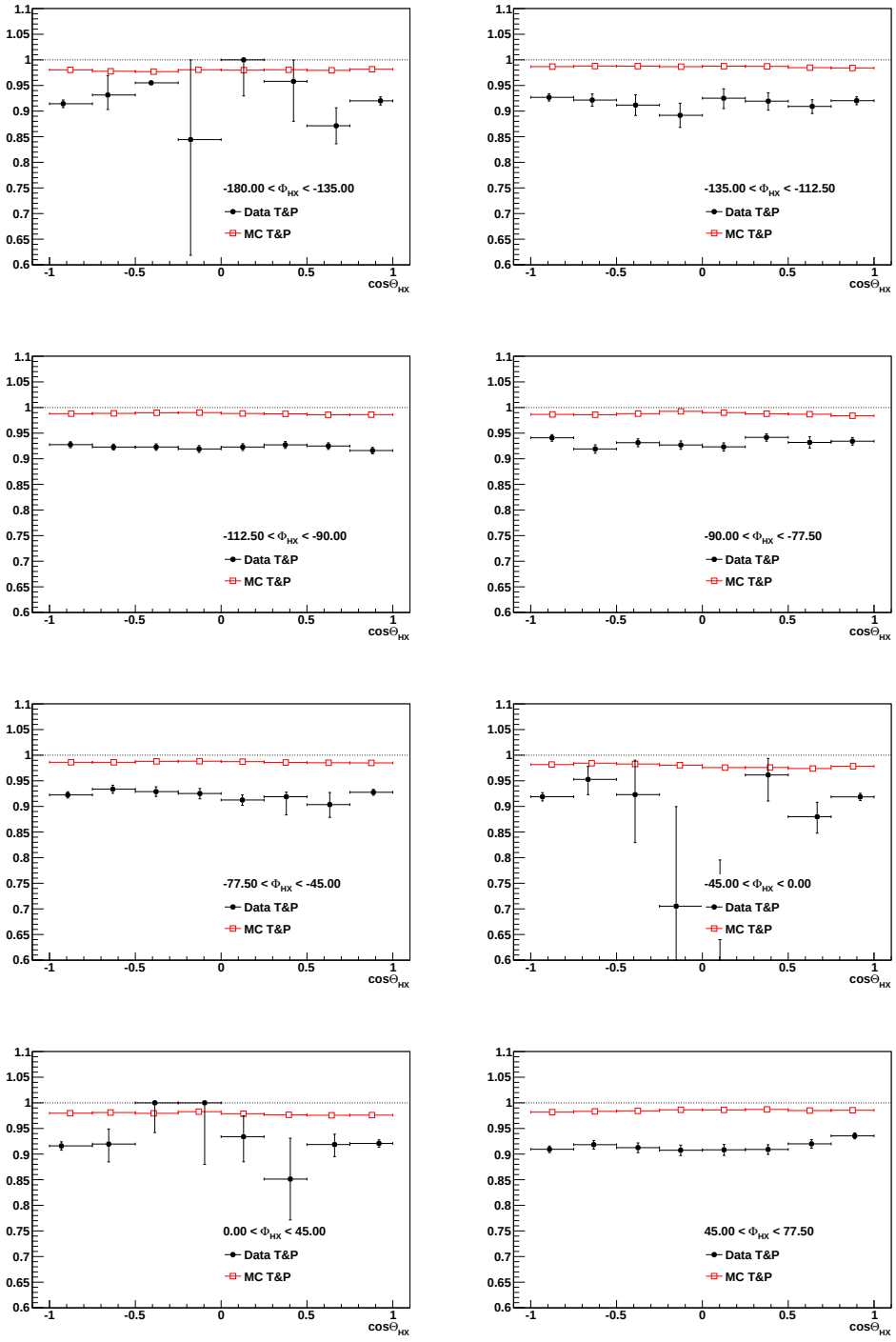

Figure 6.34: Efficiency of the dimuon vertexing module as a function of $\cos\theta_{CS}$ in various slices of ϕ_{CS}, using the *tracker80* muon cuts (165088 – 178380).

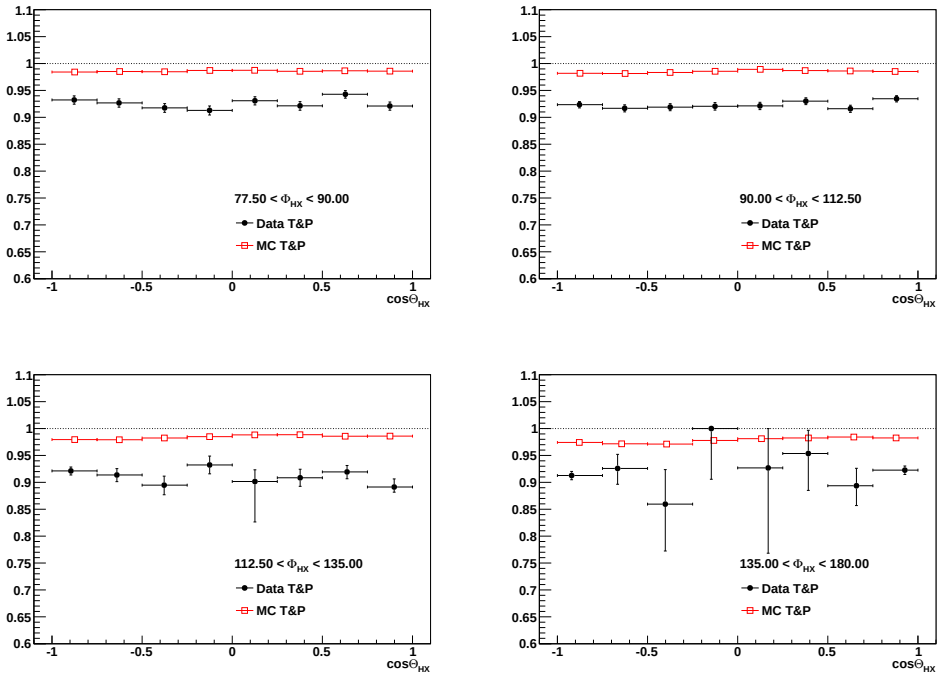

Figure 6.34: $\cos\theta_{CS}$ dependence (continued).

All efficiencies are compared to MC based TnP studies. A private MC simulation with realistic L1 and HLT reconstruction settings as well as trigger menu settings (1E33 – 3E33) was generated flat in p_T and η. The data-MC comparisons are in general in rather good agreement. Only the efficiency of the dimuon vertexing module exhibits a discrepancy between data and MC in terms of absolute values. The shapes, however, which are crucial for the polarization studies are similar and such that they will not introduce any fake polarization.

To validate the single muon efficiencies and to find the better TnP approach, a MC truth sample was produced using a special muon pair gun. Looking at the p_T turn-on curves, the MC truth efficiencies agree with both MC TnP approaches quite well. Therefore, the ratio $\varepsilon_{\mathrm{MC}}^{\mathrm{TnP}}/\varepsilon_{\mathrm{MC}}^{\mathrm{Truth}}$ is built, showing that the factorized efficiencies are slightly flatter over wider ranges in p_T.

The ratio also gives information about the range of applicability of the TnP efficiencies. The cuts on the minimum p_T according to this study should be set to 4.5 GeV/c in all $|\eta|$ bins except the $1.4 < |\eta| < 1.6$ bin where it can even be set to 3.5 GeV/c.

CHAPTER 7

Dimuon Efficiency and ρ Factor

The dimuon efficiency is not a simple product of the total single muon detection efficiencies of the two muons. For instance, it must also account for correlations induced on the two muons in those cases where the detector is insensitive to the presence of a muon pair. The dimuon efficiency can be written as

$$\varepsilon_{\mu\mu}(\cos\theta, \phi, p_T, |y|) = \varepsilon^{tot}_{\mu 1}(p_T, |\eta|) \cdot \varepsilon^{tot}_{\mu 2}(p_T, |\eta|) \cdot \rho(\cos\theta, \phi, p_T, |y|) \qquad (7.1)$$

where $\varepsilon^{tot}_{\mu 1}(p_T, |\eta|)$ and $\varepsilon^{tot}_{\mu 2}(p_T, |\eta|)$ represent the total single muon detection efficiencies of the two muons and $\rho(\cos\theta, \phi, p_T, |y|)$ is a correction factor.

Several factors contribute to the ρ factor:

1. **Intrinsic detector induced correlations:** The intrinsic correlations are mainly related to the trigger which rejects pairs that are too close to each other. As outlined in Section 6.5, this trigger requirement rejects ghost tracks that could lead to a fake dimuon trigger signal and mainly concerns cowboy dimuons or high p_T J/ψ's whose single muons are highly boosted such that they are almost collinear.

2. **Finite bin size of the single muon TnP efficiencies:** This effect can be reduced by setting points of the efficiency curves at the center of gravity and then parametrizing the p_T turn-on curves.

3. **Different populations of relative momentum components:** The influence of the different populations of the relative momentum components p_x, p_y and p_z of the tag and the probe muon in the TnP analysis and the physics data analysis was seen in data taken in 2010, using different efficiency triggered samples. Figure 7.1 shows that the efficiency obtained with the trigger path `HLT_Mu3_Track3_Jpsi` is always slightly above the

one calculated with `HLT_Mu5_Track0_Jpsi`. In data taken in 2011, this systematic effect is washed out by the limited statistical precision as shown in Fig. 7.2. Such effects need to be considered when applying the muon efficiencies studied from the J/ψ to correct Υ related muons, which is feasible as the efficiencies of the J/ψ and the Υ are the same to the first order.

4. **Underlying dependence on the polarization scenario:** Given that the polarization is unknown, the relative momenta of the two muons are different in data and MC. The effects on the efficiencies are similar to the ones showing in the previous point. The dependence on the polarization scenario is automatically remedied by using data based TnP efficiencies.

The ρ factor is defined as ratio between the MC truth dimuon efficiency $\varepsilon_{\mu\mu}^{\text{MC truth}}$

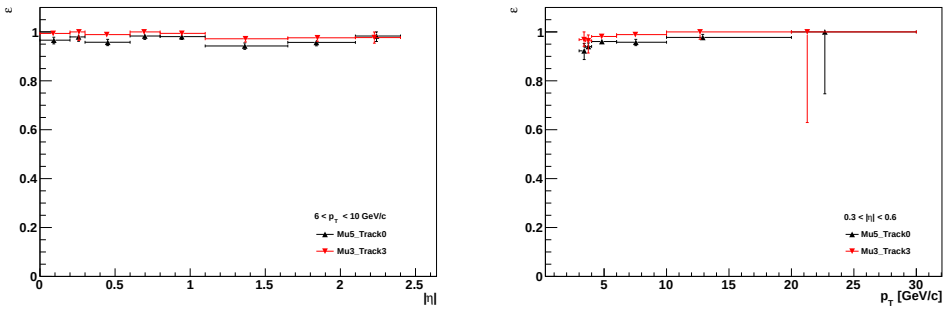

Figure 7.1: Comparison of the L1·L2 efficiencies showing 2010 data and using the trigger path `HLT_Mu5_Track0_Jpsi` (black) and the `HLT_Mu3_Track3_Jpsi` trigger path (red) as a function of $|\eta|$ for the bin $6 < p_T < 10$ GeV/c (left) and as a function of p_T for $0.3 < |\eta| < 0.6$.

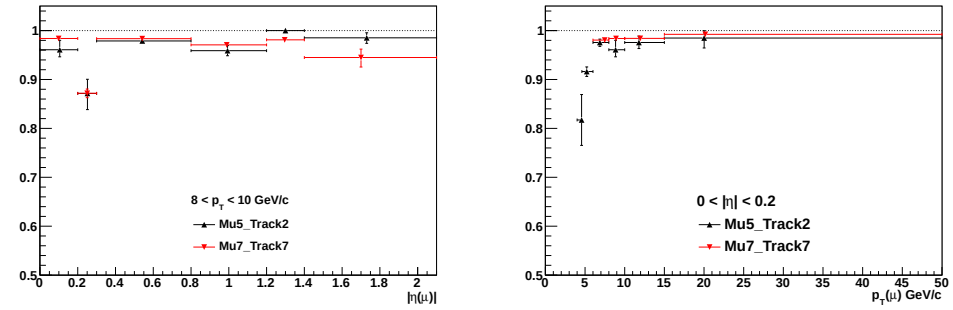

Figure 7.2: Comparison of the L1·L2 efficiencies showing 2011 data and using the default trigger path `HLT_Mu5_Track2_Jpsi` (black) and the `HLT_Mu7_Track7_Jpsi` trigger path (red) as a function of $|\eta|$ for the bin $8 < p_T < 10$ GeV/c (left) and as a function of p_T for $0.0 < |\eta| < 0.2$. *Global50* muon cuts are applied.

and the product of the total single muon detection efficiencies of the two muons.

$$\rho = \frac{\varepsilon_{\mu\mu}^{\mathrm{MCTruth}}}{\varepsilon_{\mu 1}^{\mathrm{MCTnP}} \cdot \varepsilon_{\mu 2}^{\mathrm{MCTnP}}} \tag{7.2}$$

The ρ factor is particularly important for the polarization analysis since this analysis consists of measuring the correlations between the two muons. If the detector induced ρ factor is not accounted for correctly, it can introduce an artificial polarization.

7.1 Calculation of the ρ Factor

The dimuon efficiencies for the calculation of the ρ factor for the J/ψ and the Υ efficiencies were generated using a dedicated code that works as a J/ψ and a Υ gun that feeds events to the full CMS detector simulation. J/ψ and $\Upsilon(1S)$ events were produced with flat y and p_T distributions. Additional events were simulated in the low p_T region to properly map out the turn-on curve. No spin alignment was assumed.

The single muon efficiencies for the determination of the ρ factor are taken from the MC truth efficiency measurement. This accounts exclusively for the detector induced correlations. The finite bin size of single muon TnP efficiencies as well as the underlying dependence on the polarization scenario are remedied as discussed above. The effect of the different populations of the relative momenta is incorporated in the polarization studied through the assignment of a systematic uncertainty. The final analysis will use parametrized data-driven efficiencies.

The single muon distributions of the J/ψ and $\Upsilon(1S)$ events are corrected with the measured MC based single muon efficiencies. The MC TnP dimuon efficiency $\varepsilon_{\mu 1}^{\mathrm{MCTnP}} \cdot \varepsilon_{\mu 2}^{\mathrm{MCTnP}}$ is built by dividing the number of events firing the considered dimuon trigger path by all the events in the considered kinematical region.

The ρ factor is extracted binned in $\cos\theta$ and ϕ in three different reference frames – the HX, the CS and the PX frames. Only the HX frame results as a function of $\cos\theta$ are discussed here. The results as a function of ϕ and the ones in the other two reference frames can be found either in Appendix C or in Ref. [61]. Figure 7.3 exhibits the ρ factor for the $\Upsilon(1S)$ as a function of $\cos\theta_{\mathrm{HX}}$ while Fig. 7.4 displays the corresponding factor for the J/ψ. To get a rough idea about the possible influence of the ρ factor on the polarization results, the ρ factors are fitted to a curve with the functional form $f(\cos\theta) \propto (1 + \lambda_{\mathrm{eff}} \cdot \cos\theta)$ where the effective λ parameter is used as a free fit parameter.

Comparing the different $p_T(\mu\mu)$ bins in Fig. 7.3, one can see that the coverage in $\cos\theta$ gets better with higher dimuon p_T. The ρ factor of the $\Upsilon(1S)$ is relatively flat over all dimuon p_T and y bins. This means that this factor does not introduce artificial polarization for the $\Upsilon(1S)$ state. The magnitude of the polarization

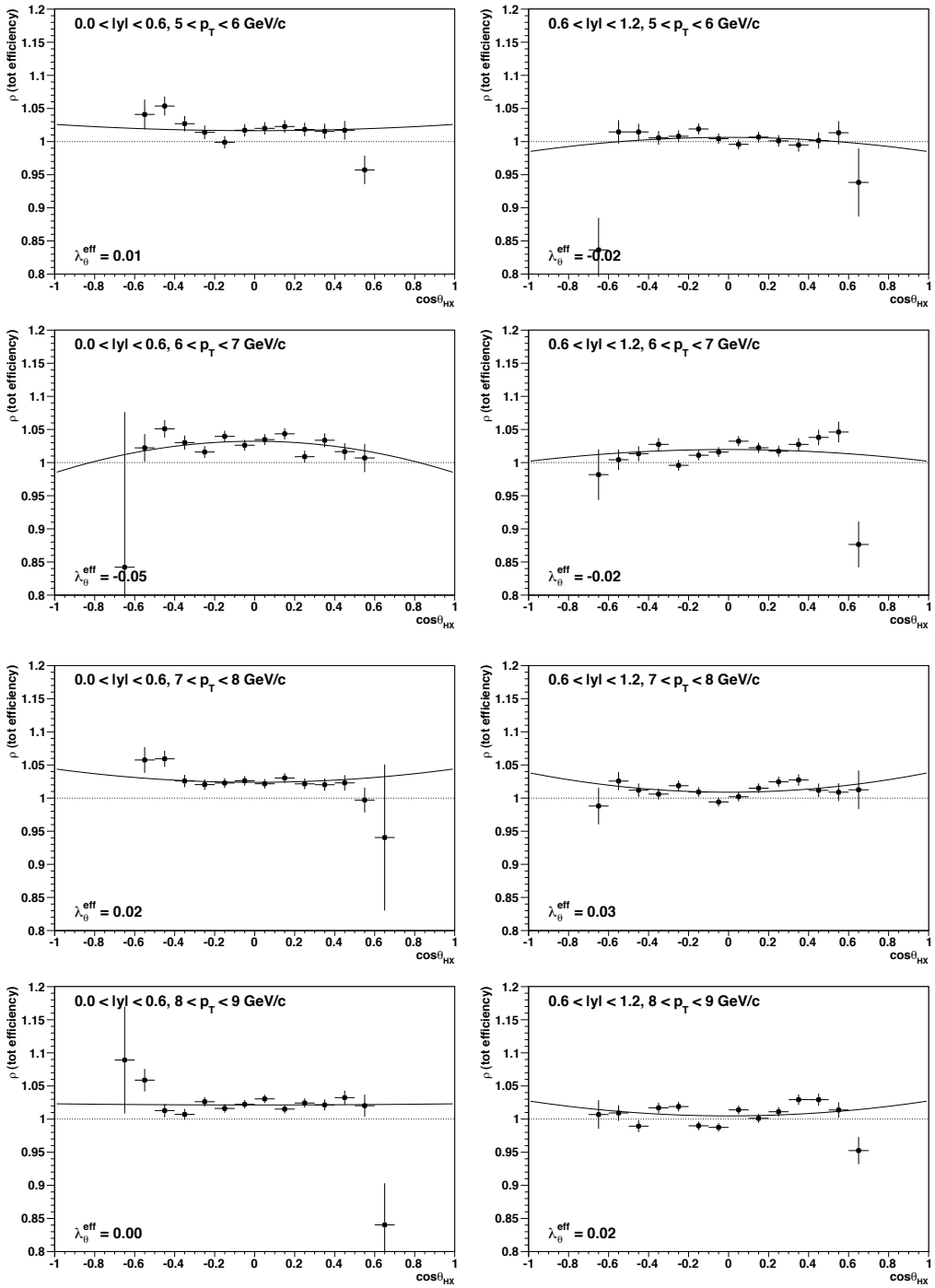

Figure 7.3: ρ factor for the $\Upsilon(1S)$ as a function of $\cos\theta$, calculated in the HX frame using the `HLT_Dimuon5_Upsilon_Barrel` trigger path. The left panel shows the ρ factor at mid-rapidity ($|y| < 0.6$), the right side at $0.6 < |y| < 1.2$.

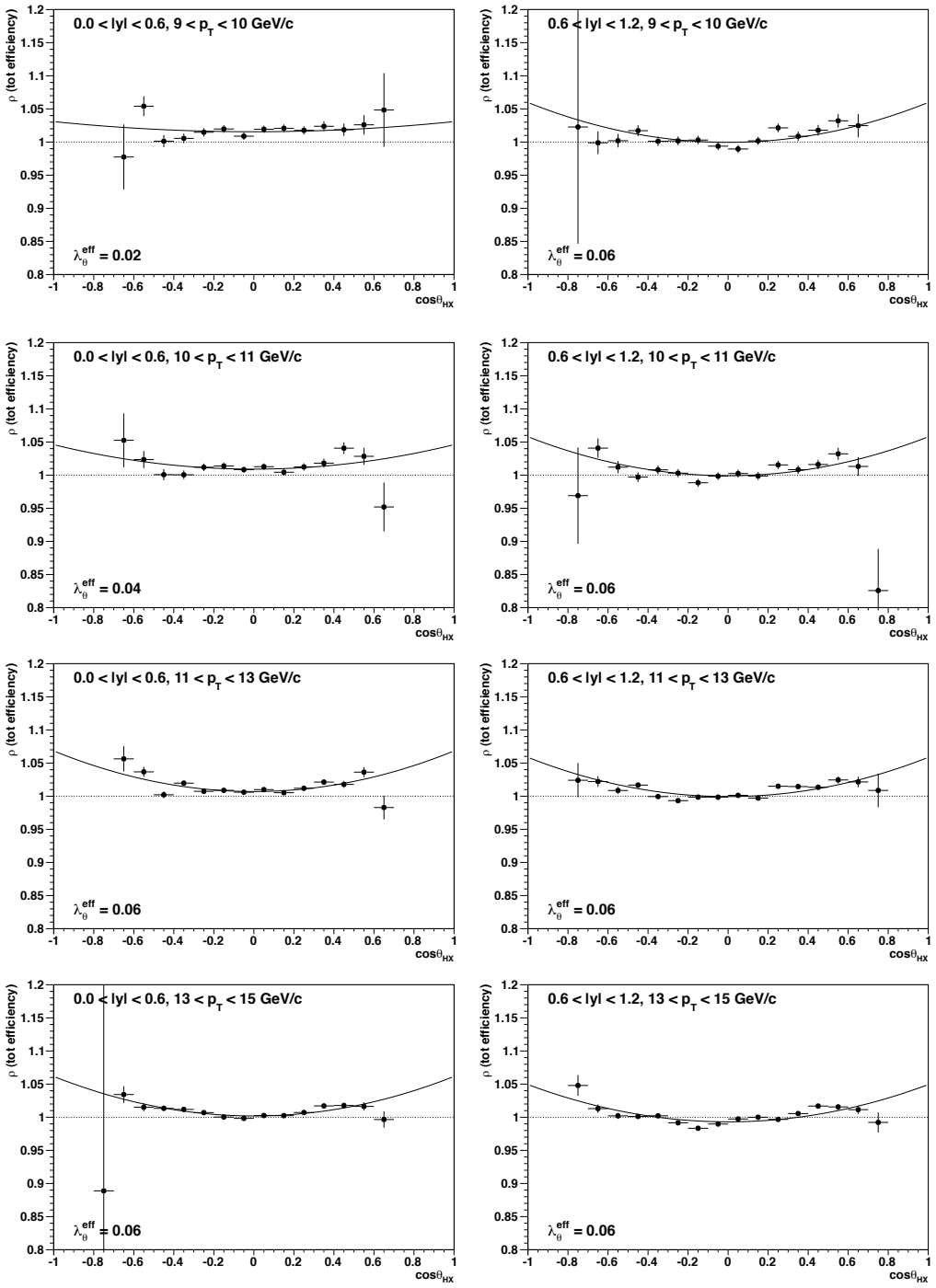

Figure 7.3: ρ factor for $\Upsilon(1S)$ (cont.).

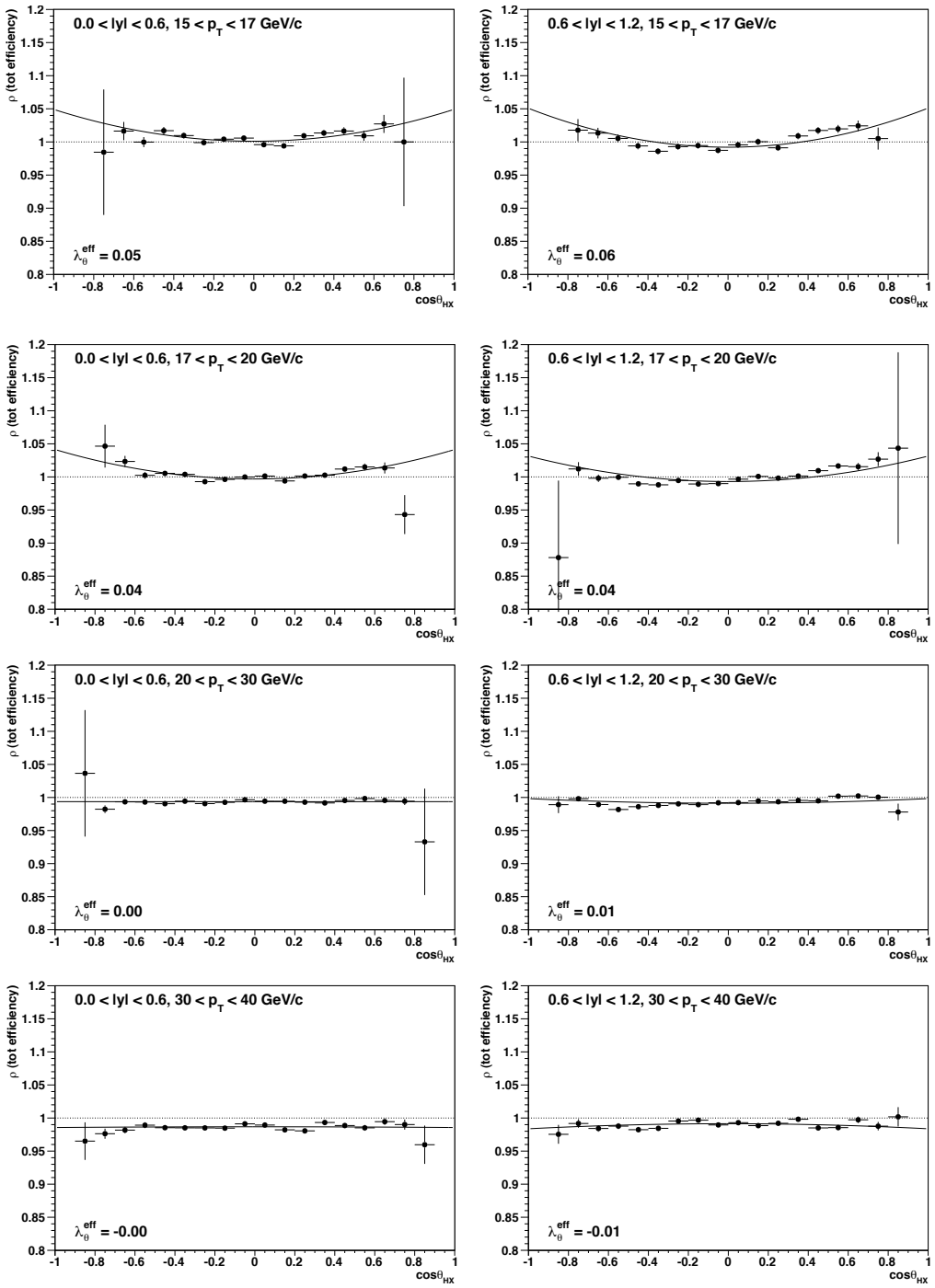

Figure 7.3: $\cos\theta_{HX}$ dependence of the ρ factor for $\Upsilon(1S)$ (cont.).

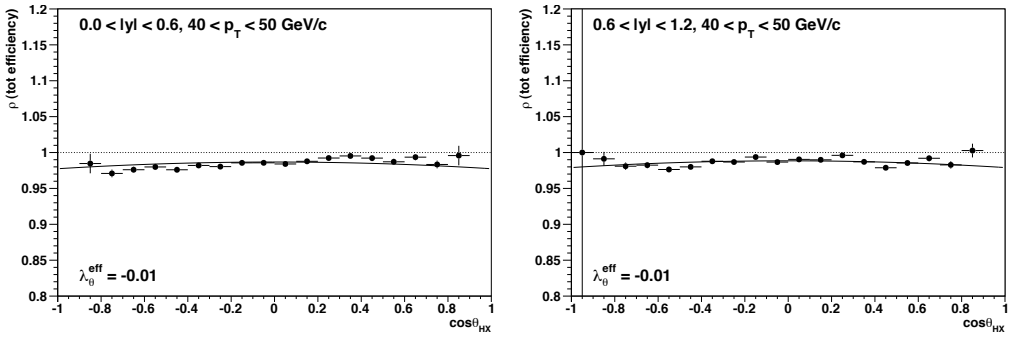

Figure 7.3: $\cos\theta_{HX}$ dependence of the ρ factor for $\Upsilon(1S)$ (cont.).

introduced by the ρ factor can be judged by the effective $\tilde{\lambda}$ value shown in the figures.

The J/ψ, on the other hand, exhibits a non-flat ρ factor above a dimuon p_T of 30 GeV/c. The higher the p_T, the stronger the effect of the dimuon correlations get. The deviation from uniformity is partly due to the intrinsic detector induced correlations. As discussed before, trigger algorithms reject high p_T J/ψ's decaying into two almost collinear muons. This effect at high p_T needs to be taken into account properly in order not to introduce fake transverse polarization in the high p_T bins.

7.2 Dimuon Efficiencies In Brief

As seen earlier in this chapter, the dimuon efficiencies can be written as

$$\varepsilon_{\mu\mu}(\cos\theta, \phi, p_T, |y|) = \varepsilon^{tot}_{\mu 1}(p_T, |\eta|) \cdot \varepsilon^{tot}_{\mu 2}(p_T, |\eta|) \cdot \rho(\cos\theta, \phi, p_T, |y|) \qquad (7.3)$$

where $\varepsilon^{tot}_{\mu 1}(p_T, |\eta|)$ and $\varepsilon^{tot}_{\mu 2}(p_T, |\eta|)$ represent the total single muon detection efficiency for the first and the second muon, respectively, and $\rho(\cos\theta, \phi, p_T, |y|)$ is a correction factor which is defined as ratio between the MC truth dimuon efficiency and the total single muon detection efficiencies of the two muons.

The ρ factor does not only correct for dimuon correlations, but also absorbs effects from finite bin sizes and different populations of the relative momentum components p_x, p_y and p_z of the tag and the probe muon in the TnP analysis and the physics data analysis. Furthermore, a simpler analysis without a rho factor accounting for these factors could introduce a artificial polarization in the final analysis.

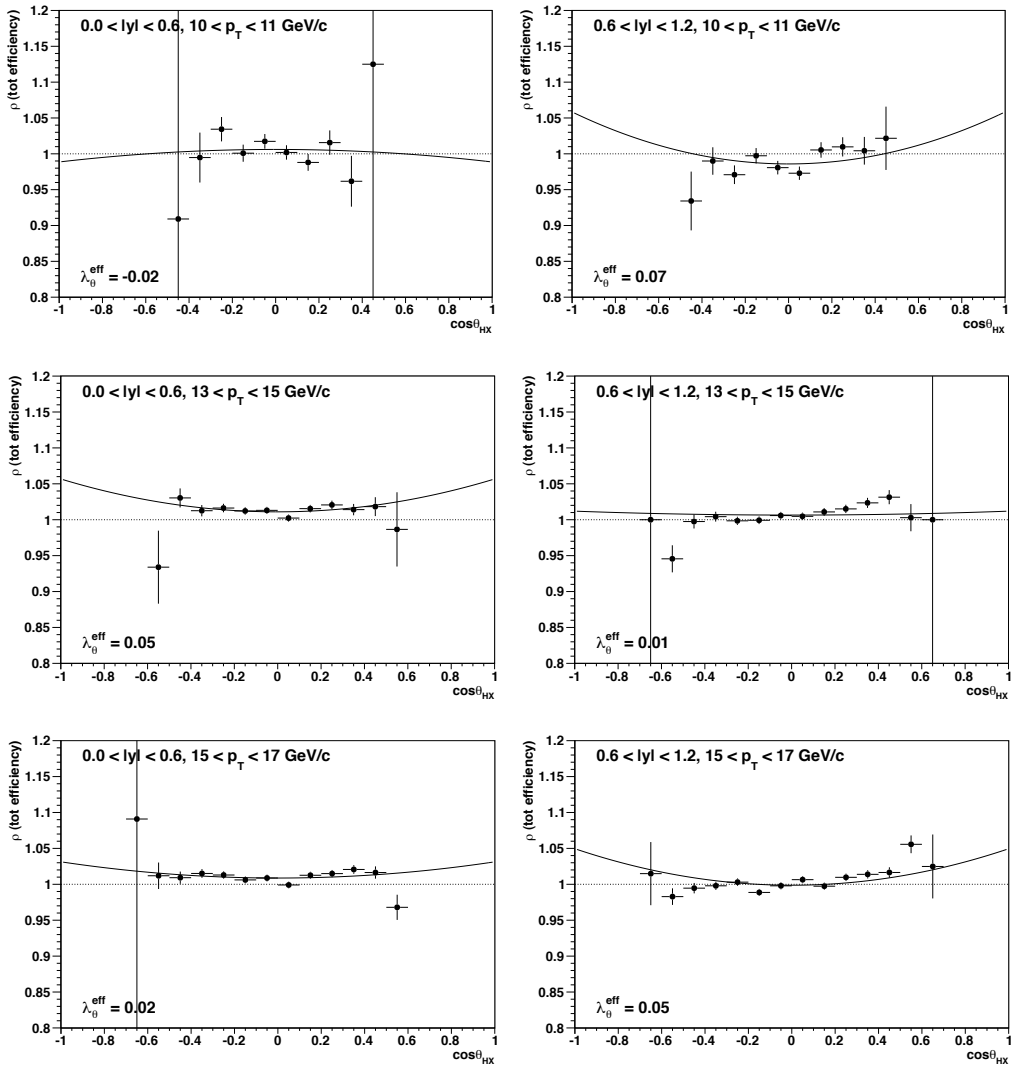

Figure 7.4: ρ factor for the J/ψ as a function of $\cos\theta$, calculated in the HX frame using the `HLT_Dimuon10_Jpsi_Barrel` trigger path. The left panel shows the ρ factor at mid-rapidity ($|y| < 0.6$), the right side at $0.6 < |y| < 1.2$.

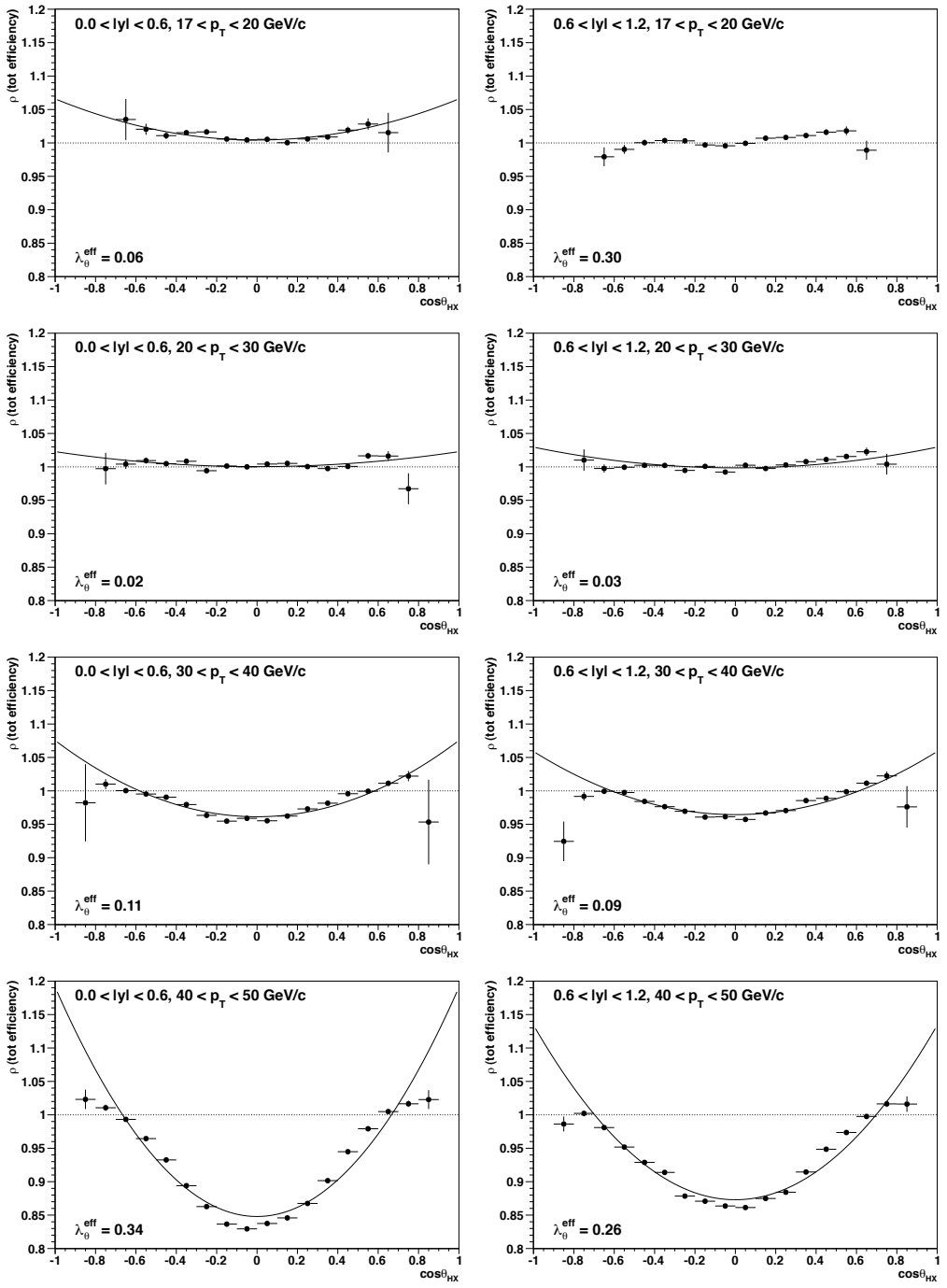

Figure 7.4: $\cos\theta_{HX}$ dependence of the ρ factor for J/ψ (cont.).

CHAPTER 8

Summary and Conclusions

The quarkonium polarization measurement requires a complex analysis which depends in a very sensitive way on small changes in the parameters. Many years of both experimental and theoretical work resulted in seemingly contradictory experimental results. In order to resolve the issues where only one of the three parameters characterizing the average angular decay distribution was extracted, a formalism with a frame invariant parameter has been developed [31, 43]. Thus, in order to get a complete picture of the polarization the following items must be considered:

- The full angular decay distribution in at least two reference frames should be measured to avoid ambiguous interpretations.
- The determination of the polarization parameters in different reference frames is also important to find the *natural* polarization axis with respect to which the quarkonium state is polarized.
- A frame-invariant parameter should be calculated not only to test the self-consistency of the measurement, but also to facilitate the comparisons between different experiments.

Using this formalism, CDF [45] and ALICE [47] recently published new results on the polarization of the $\Upsilon(nS)$ and the J/ψ. These analyses determined that the polarization of the particles is consistent with being uniform which is surprising since quarkonia should intrinsically be polarized. A non-perturbative transition from a J = 0 state offers an explanation to the unpolarized J/ψ's and Υ's. However, the angular decay distribution would then not be consistent with zero for all momenta. This transition also excludes the Color Singlet Model that does not include any non-perturbative terms.

One of the most important inputs to the polarization analysis are the detection efficiencies. The polarization depends strongly on the shape of the efficiencies and

not the absolute values since the polarization is the measurement of the shape of the decay angular distribution. Extensive studies on the single muon detection efficiencies using TnP methods were performed. Two different approaches are used:

1. **Factorized efficiencies:** The total single muon detection efficiency is broken into five individual parts (offline muon tracking, offline muon reconstruction, muon quality, L1·L2 and L3 trigger efficiency) and studied in a way that these individual efficiencies fully factorize.
2. **Inclusive efficiencies:** The total single muon efficiency is studied in one go.

The trigger efficiencies at Level 1 and Level 2 show inefficiencies for cowboy dimuons which led to the rejection of the cowboys for the L1·L2 and L3 trigger efficiencies as well as the inclusive efficiencies.

Both the factorized as well as the inclusive efficiency TnP approaches give similar results for data and the MC simulation. To further validate and evaluate the efficiencies from the two approaches, also a MC truth sample was prepared using a special muon pair gun. To find which TnP efficiencies better describe the MC truth efficiencies over a wider range of p_T, the ratios of the MC truth divided by the MC TnP efficiencies are built. The factorized efficiencies seem to give the flatter ratio over wider ranges of p_T. However, more studies have to be conducted before reaching the final decision about which efficiencies to use for the CMS polarization analysis.

Additionally, a study of the efficiency of the dimuon vertexing module which is the last L3 filter in all 2011 quarkonium triggers was made. Since this filter is applied on dimuons, a special TnP skim with the *OnePair* arbitration was produced. The resulting data-driven efficiencies deviate from the MC based ones. However, both exhibit similar, rather flat shapes which will not introduce any artificial polarization.

Correlations between the two muons have to be taken into account when building the dimuon efficiencies from the single muon efficiencies. The corresponding correction factor ρ does not only include these correlations, but also absorbs effects coming from the finite bin size of the efficiencies and the different event populations in the TnP analysis and the physics data analysis.

The shape of the single muon efficiencies as well as the ρ factor can introduce artificial polarization if not known precisely and not accounted for correctly. Therefore, having a good control over low p_T muons and understanding the efficiencies, in particular in the low p_T region, are of crucial importance to the polarization studies.

At the time of writing, the CMS results on quarkonium polarization, for which the work presented in this thesis is a valuable input, is in the process of being approved. The results will help to further understand the production mechanisms of the quarkonia. Polarization analyses may also allow to amongst other things test

QCD calculations [34], probe QGP formation [51], constrain SM couplings [50] and measure parity violation [34].

In the 2011 run, the collisions at the LHC produced quarkonia states in large amounts at higher momenta than in any previous collider. With this data we soon expect to shed light into the complicated formation processes of quarkonia production and thus test QCD in both the perturbative and non-perturbative regimes.

Appendices

APPENDIX A

Settings for the Private MC Simulation

The MC simulation was set up in `CMSSW_4_2_9_HLT1_hltpatch1` with the global tag `START42_V14A::All`. The following packages were additionally checked out:

- `V00-00-00-00 Configuration/AlCa`
- `V04-01-12 Configuration/EventContent`
- `V01-02-00 Configuration/HLT`
- `V02-24-02 FastSimulation/Configuration`
- `V00-04-01 FastSimulation/Muons`
- `V12-02-00 HLTrigger/Configuration`
- `V00-10-01 HLTrigger/Egamma`
- `V03-08-07 HLTrigger/HLTanalyzers`
- `V00-04-01 HLTrigger/JetMET`
- `V02-11-11 HLTrigger/Muon`

In order to use the L1 trigger settings really applied during the 1E33 to the 3E33 menu [62], some lines of code were added to the simulation configuration file to overwrite the L1 trigger settings of the L1 trigger menu loaded through the global tag:

```
process.GlobalTag.toGet.append(
    cms.PSet(
        record  = cms.string( 'L1MuGMTParametersRcd' ),
```

```
        tag     = cms.string( 'L1MuGMTParameters_synctf_10_mc' ),
        label   = cms.untracked.string( '' ),
        connect = cms.untracked.string('frontier://FrontierProd/CMS_COND_31X_L1T')
    ))
process.GlobalTag.toGet.append(
    cms.PSet(
        record  = cms.string( 'L1MuDTTFParametersRcd' ),
        tag     = cms.string( 'L1MuDTTFParameters_dttf11_TSC_09_17_col_mc' ),
        label   = cms.untracked.string( '' ),
        connect = cms.untracked.string('frontier://FrontierProd/CMS_COND_31X_L1T')
        ))
process.GlobalTag.toGet.append(
    cms.PSet(
        record  = cms.string( 'L1MuCSCTFConfigurationRcd' ),
        tag     = cms.string( 'L1MuCSCTFConfiguration_90511_mc' ),
        label   = cms.untracked.string( '' ),
        connect = cms.untracked.string('frontier://FrontierProd/CMS_COND_31X_L1T')
        ))
process.GlobalTag.toGet.append(
    cms.PSet(
        record  = cms.string( 'L1RPCBxOrConfigRcd' ),
        tag     = cms.string( 'L1RPCBxOrConfig_LHC7_1EX_mc' ),
        label   = cms.untracked.string( '' ),
        connect = cms.untracked.string('frontier://FrontierProd/CMS_COND_31X_L1T')
        ))
process.GlobalTag.toGet.append(
    cms.PSet(
        record  = cms.string( 'L1RPCConeDefinitionRcd' ),
        tag     = cms.string( 'L1RPCConeDefinition_LHC7_1EX_mc' ),
        label   = cms.untracked.string( '' ),
        connect = cms.untracked.string('frontier://FrontierProd/CMS_COND_31X_L1T')
        ))
process.GlobalTag.toGet.append(
    cms.PSet(
        record  = cms.string( 'L1RPCConfigRcd' ),
        tag     = cms.string( 'L1RPCConfig_LHC7_1EX_mc' ),
        label   = cms.untracked.string( '' ),
        connect = cms.untracked.string('frontier://FrontierProd/CMS_COND_31X_L1T')
        ))
process.GlobalTag.toGet.append(
    cms.PSet(
        record  = cms.string( 'L1RPCHsbConfigRcd' ),
        tag     = cms.string( 'L1RPCHsbConfig_LHC7_1EX_mc' ),
        label   = cms.untracked.string( '' ),
        connect = cms.untracked.string('frontier://FrontierProd/CMS_COND_31X_L1T')
        )
    )
```

An HLT menu, containing all the J/ψ trigger paths that were running during the 1E33 up to the 3E33 menu, was set up, also including the different L1 seeds.

APPENDIX B

Numerical Values of the Factorized Efficiencies

The numerical values of the individual single muon efficiencies and the product of the single muon efficiency using the *tracker80* cuts can be found in Table B.1. The corresponding MC efficiencies are listed in Table B.2. As explained in Section 6.1.1, the MC simulation was limited to $|y(\mu\mu)| < 1.3$. Therefore, the single muon efficiencies cannot be calculated for $|\eta| \gtrsim 1.6$.

The values reported in the second column $\langle p_T \rangle$ give the center of gravity of the individual efficiencies.

Table B.1: Data-driven single muon efficiencies applying *tracker80* cuts: The muon reconstruction and muon quality efficiency use the run range 160404 - 173692, the L1·L2 efficiency 185088 - 173692 and the L3 efficiency 165088 - 178379.

	p_T [GeV/c]	$\langle p_T \rangle$ [GeV/c]	$\varepsilon_{\text{MuonID}}$ [%]	$\varepsilon_{\text{MuonQual}}$ [%]	$\varepsilon_{L1\cdot L2}$ [%]	ε_{L3} [%]	ε_{μ} [%]
$\lvert\eta\rvert < 0.2$	3.5–4.00	3.90,3.90,3.90,3.90	$98.7^{+1.3}_{-3.6}$	$93.9^{+0.5}_{-0.5}$	$67.3^{+5.4}_{-3.6}$	$57.5^{+1.5}_{-1.5}$	$35.5^{+3.1}_{-2.5}$
	4.0–4.5	4.23,4.25,4.23,4.26	$96.3^{+2.3}_{-2.2}$	$93.5^{+0.3}_{-0.3}$	$74.9^{+2.1}_{-2.1}$	$75.3^{+0.7}_{-0.8}$	$50.3^{+2.0}_{-2.0}$
	4.5–5.0	4.73,4.74,4.73,4.74	$98.6^{+1.4}_{-2.4}$	$93.9^{+0.3}_{-0.3}$	$87.5^{+1.7}_{-1.1}$	$87.1^{+0.6}_{-0.6}$	$69.9^{+1.9}_{-2.1}$
	5.0–5.5	5.23,5.24,5.24,5.24	$100.0^{+0.0}_{-1.5}$	$94.8^{+0.3}_{-0.3}$	$93.2^{+1.6}_{-1.6}$	$94.7^{+0.4}_{-0.5}$	$82.9^{+1.8}_{-2.1}$
	5.5–6.0	5.74,5.74,5.74,5.74	$100.0^{+0.0}_{-0.7}$	$95.1^{+0.3}_{-0.3}$	$94.0^{+1.5}_{-1.7}$	$98.8^{+0.2}_{-0.3}$	$87.4^{+1.7}_{-2.0}$
	6.0–7.0	6.46,6.46,6.47,6.46	$97.7^{+2.2}_{-2.2}$	$95.4^{+0.3}_{-0.3}$	$96.6^{+1.1}_{-1.3}$	$99.5^{+0.1}_{-0.1}$	$88.7^{+2.4}_{-2.5}$
	7.0–8.0	7.46,7.47,7.46,7.48	$99.6^{+0.4}_{-2.7}$	$95.3^{+0.3}_{-0.3}$	$98.9^{+0.7}_{-1.0}$	$99.7^{+0.1}_{-0.1}$	$92.7^{+1.2}_{-2.9}$
	8.0–10.0	8.85,8.87,8.85,8.88	$100.0^{+0.0}_{-0.8}$	$95.5^{+0.3}_{-0.3}$	$96.7^{+1.2}_{-1.5}$	$99.8^{+0.1}_{-0.1}$	$91.2^{+1.5}_{-1.9}$
	10.0–15.0	11.90,11.90,11.78,11.90	$100.0^{+0.0}_{-2.7}$	$96.1^{+2.6}_{-2.6}$	$97.8^{+1.6}_{-1.6}$	$99.7^{+0.1}_{-0.1}$	$92.7^{+3.0}_{-4.0}$
	15.0–20.0	16.99,17.04,16.94,17.02	$98.9^{+1.1}_{-7.0}$	$95.5^{+0.6}_{-0.7}$	$100.0^{+0.0}_{-1.4}$	$99.9^{+0.1}_{-0.3}$	$93.5^{+1.5}_{-6.8}$
	20.0–100.0	26.63,26.78,25.00,26.50	$90.8^{+0.0}_{-0.0}$	$95.8^{+0.8}_{-0.9}$	$100.0^{+0.0}_{-2.8}$	$99.1^{+0.3}_{-0.4}$	$85.3^{+1.2}_{-2.7}$
$0.2 < \lvert\eta\rvert < 0.3$	3.5–4.0	3.90,3.91,3.90,3.90	$77.1^{+4.8}_{-4.8}$	$94.1^{+0.9}_{-1.0}$	$49.2^{+5.6}_{-5.6}$	$58.3^{+3.2}_{-3.2}$	$20.6^{+2.9}_{-2.9}$
	4.0–4.5	4.23,4.25,4.25,4.26	$86.9^{+3.2}_{-3.1}$	$96.0^{+0.4}_{-0.5}$	$50.0^{+3.7}_{-3.8}$	$81.4^{+1.2}_{-1.2}$	$33.6^{+2.8}_{-2.9}$
	4.5–5.0	4.74,4.75,4.75,4.75	$100.0^{+0.0}_{-3.0}$	$95.0^{+0.5}_{-0.5}$	$66.7^{+3.5}_{-3.5}$	$90.9^{+0.9}_{-0.9}$	$57.0^{+3.1}_{-3.5}$
	5.0–5.5	5.24,5.24,5.24,5.24	$97.3^{+2.7}_{-3.6}$	$95.5^{+0.5}_{-0.5}$	$77.4^{+3.8}_{-3.8}$	$96.2^{+0.6}_{-0.7}$	$68.5^{+4.0}_{-4.3}$
	5.5–6.0	5.74,5.74,5.72,5.75	$100.0^{+0.0}_{-3.3}$	$96.7^{+0.4}_{-0.5}$	$74.0^{+4.4}_{-4.4}$	$98.7^{+0.0}_{-0.0}$	$69.9^{+4.3}_{-4.8}$
	6.0–7.0	6.46,6.46,6.49,6.47	$90.5^{+3.2}_{-3.1}$	$96.1^{+0.4}_{-0.4}$	$83.0^{+3.0}_{-3.0}$	$99.6^{+0.2}_{-0.2}$	$71.2^{+3.7}_{-3.6}$
	7.0–8.0	7.46,7.46,7.48,7.45	$100.0^{+0.0}_{-1.0}$	$96.6^{+0.4}_{-0.5}$	$83.9^{+3.9}_{-4.3}$	$99.6^{+0.2}_{-0.2}$	$79.9^{+3.8}_{-4.3}$
	8.0–10.0	8.87,8.88,8.82,8.89	$98.5^{+1.5}_{-3.4}$	$96.6^{+0.4}_{-0.4}$	$86.9^{+3.2}_{-3.6}$	$100.0^{+0.0}_{-0.0}$	$81.8^{+3.3}_{-4.6}$
	10.0–15.0	11.93,11.86,11.68,11.90	$94.7^{+4.6}_{-4.4}$	$96.0^{+0.5}_{-0.5}$	$90.6^{+3.1}_{-3.9}$	$99.5^{+0.2}_{-0.3}$	$81.1^{+4.9}_{-5.3}$
	15.0–20.0	16.96,16.94,17.00,16.90	$96.4^{+3.6}_{-8.3}$	$94.9^{+1.2}_{-1.2}$	$87.1^{+6.7}_{-8.9}$	$100.0^{+0.0}_{-0.1}$	$78.9^{+6.9}_{-10.6}$
	20.0–100.0	26.15,27.21,25.06,26.77	$99.1^{+0.9}_{-13.1}$	$98.3^{+0.7}_{-0.8}$	$100.0^{+0.0}_{-6.3}$	$100.0^{+0.0}_{-0.9}$	$96.5^{+1.5}_{-14.2}$

Continued on next page

Continued from previous page

$0.3 < \|\eta\| < 0.6$	3.5–4.0	3.90,3.90,3.90,3.90	$97.0^{+3.0}_{-3.4}$	$95.2^{+0.3}_{-0.3}$	$80.5^{+2.6}_{-2.7}$	$53.7^{+1.1}_{-1.1}$	$39.5^{+2.0}_{-2.1}$
	4.0–4.5	4.23,4.24,4.24,4.25	$95.6^{+1.9}_{-1.9}$	$94.6^{+0.2}_{-0.2}$	$85.1^{+1.5}_{-1.6}$	$73.9^{+0.6}_{-0.6}$	$56.3^{+1.7}_{-1.7}$
	4.5–5.0	4.74,4.74,4.75,4.74	$94.0^{+2.2}_{-2.2}$	$94.8^{+0.2}_{-0.2}$	$90.6^{+1.4}_{-1.5}$	$88.1^{+0.5}_{-0.5}$	$70.5^{+2.1}_{-2.2}$
	5.0–5.5	5.24,5.24,5.24,5.24	$97.0^{+2.3}_{-2.3}$	$95.5^{+0.2}_{-0.3}$	$94.5^{+1.2}_{-1.4}$	$97.5^{+0.2}_{-0.3}$	$84.5^{+2.5}_{-2.5}$
	5.5–6.0	5.73,5.74,5.74,5.74	$98.0^{+2.0}_{-2.5}$	$95.6^{+0.3}_{-0.3}$	$94.3^{+1.4}_{-1.6}$	$99.6^{+0.1}_{-0.1}$	$87.1^{+2.3}_{-2.8}$
	6.0–7.0	6.46,6.47,6.46,6.46	$99.3^{+0.7}_{-2.0}$	$96.4^{+0.2}_{-0.2}$	$97.4^{+0.8}_{-0.8}$	$99.5^{+0.1}_{-0.1}$	$91.9^{+1.4}_{-2.2}$
	7.0–8.0	7.46,7.47,7.46,7.46	$98.2^{+1.8}_{-2.5}$	$96.3^{+0.3}_{-0.3}$	$99.0^{+0.8}_{-0.8}$	$99.9^{+0.1}_{-0.1}$	$92.5^{+2.1}_{-2.7}$
	8.0–10.0	8.87,8.88,8.89,8.88	$98.9^{+1.1}_{-2.3}$	$96.8^{+0.2}_{-0.2}$	$98.4^{+0.8}_{-1.0}$	$99.6^{+0.1}_{-0.1}$	$92.9^{+1.6}_{-2.6}$
	10.0–15.0	11.82,11.93,11.82,11.93	$100.0^{+0.0}_{-0.9}$	$97.1^{+0.2}_{-0.2}$	$98.8^{+0.8}_{-1.3}$	$99.8^{+0.1}_{-0.1}$	$94.8^{+1.3}_{-1.8}$
	15.0–20.0	16.98,17.04,16.77,17.06	$100.0^{+0.0}_{-2.9}$	$97.0^{+0.5}_{-0.5}$	$100.0^{+0.0}_{-0.9}$	$99.8^{+0.1}_{-0.1}$	$95.8^{+1.1}_{-3.1}$
	20.0–100.0	27.06,27.51,23.67,26.86	$88.5^{+7.6}_{-7.3}$	$98.0^{+1.5}_{-0.6}$	$100.0^{+0.0}_{-1.6}$	$99.8^{+0.1}_{-0.1}$	$85.6^{+7.6}_{-7.2}$
$0.6 < \|\eta\| < 0.8$	3.5–4.0	3.90,3.90,3.90,3.90	$86.6^{+4.1}_{-3.9}$	$94.8^{+0.5}_{-0.5}$	$65.6^{+4.0}_{-4.2}$	$64.2^{+1.5}_{-1.5}$	$34.2^{+2.8}_{-2.8}$
	4.0–4.5	4.23,4.25,4.24,4.25	$99.1^{+0.9}_{-2.8}$	$94.7^{+0.3}_{-0.3}$	$83.1^{+2.0}_{-2.0}$	$83.3^{+0.7}_{-0.7}$	$64.3^{+1.9}_{-2.6}$
	4.5–5.0	4.74,4.74,4.74,4.74	$100.0^{+0.0}_{-1.6}$	$95.5^{+0.3}_{-0.3}$	$92.0^{+1.7}_{-1.8}$	$92.2^{+0.5}_{-0.5}$	$80.3^{+1.7}_{-2.3}$
	5.0–5.5	5.23,5.24,5.22,5.24	$100.0^{+0.0}_{-2.2}$	$95.8^{+0.3}_{-0.3}$	$93.6^{+1.5}_{-1.7}$	$98.3^{+0.3}_{-0.3}$	$87.3^{+1.7}_{-2.7}$
	5.5–6.0	5.73,5.74,5.74,5.74	$99.4^{+0.6}_{-3.1}$	$96.0^{+0.3}_{-0.3}$	$98.1^{+1.2}_{-1.3}$	$99.6^{+0.2}_{-0.2}$	$92.4^{+1.6}_{-3.3}$
	6.0–7.0	6.45,6.46,6.45,6.46	$100.0^{+0.0}_{-1.8}$	$96.2^{+0.3}_{-0.3}$	$95.4^{+0.0}_{-0.0}$	$99.6^{+0.1}_{-0.1}$	$90.6^{+1.0}_{-1.9}$
	7.0–8.0	7.47,7.47,7.45,7.47	$95.4^{+3.3}_{-3.2}$	$96.8^{+0.3}_{-0.3}$	$97.7^{+1.1}_{-1.6}$	$99.8^{+0.1}_{-0.2}$	$89.1^{+3.4}_{-3.5}$
	8.0–10.0	8.88,8.88,8.89,8.87	$100.0^{+0.0}_{-1.5}$	$96.6^{+0.3}_{-0.3}$	$97.6^{+1.1}_{-1.4}$	$99.9^{+0.1}_{-0.1}$	$93.2^{+1.5}_{-2.2}$
	10.0–15.0	11.84,11.89,11.83,11.89	$98.6^{+0.0}_{-0.0}$	$97.2^{+0.3}_{-0.3}$	$97.7^{+1.9}_{-1.9}$	$99.7^{+0.1}_{-0.1}$	$92.4^{+2.0}_{-2.0}$
	15.0–20.0	17.05,17.01,16.89,17.04	$100.0^{+0.0}_{-0.0}$	$97.5^{+0.6}_{-0.6}$	$100.0^{+0.0}_{-1.7}$	$100.0^{+0.0}_{-0.0}$	$96.6^{+1.1}_{-2.0}$
	20.0–100.0	25.78,27.47,28.27,26.62	$100.0^{+0.0}_{-8.3}$	$98.1^{+0.6}_{-0.8}$	$100.0^{+0.0}_{-2.0}$	$100.0^{+0.0}_{-0.0}$	$97.1^{+1.2}_{-8.4}$

Continued on next page

Continued from previous page

$0.8 < \|\eta\| < 1.0$	3.5–4.0	3.90,3.90,3.90,3.90	$96.3^{+3.7}_{-4.7}$	$95.0^{+0.5}_{-0.5}$	$75.5^{+3.5}_{-3.7}$	$71.1^{+1.4}_{-1.4}$	$48.6^{+3.1}_{-3.5}$
	4.0–4.5	4.23,4.24,4.25,4.25	$99.8^{+0.2}_{-3.5}$	$94.0^{+0.3}_{-0.3}$	$87.0^{+0.0}_{-0.0}$	$85.1^{+0.7}_{-0.7}$	$68.7^{+0.9}_{-2.6}$
	4.5–5.0	4.74,4.74,4.75,4.74	$96.7^{+3.3}_{-3.3}$	$94.9^{+0.3}_{-0.3}$	$91.8^{+1.8}_{-2.1}$	$95.0^{+0.4}_{-0.5}$	$79.2^{+3.3}_{-3.4}$
	5.0–5.5	5.24,5.24,5.25,5.24	$100.0^{+0.0}_{-2.3}$	$95.2^{+0.4}_{-0.4}$	$93.7^{+1.7}_{-2.0}$	$97.6^{+0.4}_{-0.4}$	$86.3^{+1.8}_{-2.9}$
	5.5–6.0	5.74,5.74,5.74,5.74	$100.0^{+0.0}_{-2.4}$	$95.7^{+0.4}_{-0.4}$	$94.8^{+1.7}_{-2.0}$	$99.0^{+0.2}_{-0.2}$	$89.0^{+1.8}_{-3.0}$
	6.0–7.0	6.47,6.46,6.48,6.47	$97.8^{+2.2}_{-3.1}$	$95.4^{+0.3}_{-0.3}$	$96.2^{+1.3}_{-1.6}$	$99.2^{+0.2}_{-0.2}$	$88.1^{+2.5}_{-3.2}$
	7.0–8.0	7.46,7.47,7.46,7.48	$99.4^{+0.6}_{-3.7}$	$95.2^{+0.4}_{-0.4}$	$96.7^{+1.4}_{-1.9}$	$99.3^{+0.2}_{-0.3}$	$90.0^{+1.7}_{-4.0}$
	8.0–10.0	8.88,8.86,8.89,8.86	$100.0^{+0.0}_{-3.3}$	$95.9^{+0.3}_{-0.4}$	$95.1^{+1.6}_{-2.1}$	$99.5^{+0.2}_{-0.2}$	$89.8^{+1.8}_{-3.7}$
	10.0–15.0	11.79,11.91,11.89,11.91	$98.7^{+1.3}_{-4.0}$	$97.4^{+0.4}_{-0.4}$	$97.1^{+1.3}_{-1.7}$	$99.6^{+0.1}_{-0.2}$	$92.1^{+2.0}_{-4.1}$
	15.0–20.0	16.99,17.05,16.87,17.01	$84.3^{+6.5}_{-6.3}$	$97.4^{+0.6}_{-0.7}$	$100.0^{+0.0}_{-1.4}$	$99.3^{+0.3}_{-0.3}$	$80.7^{+6.3}_{-6.2}$
	20.0–100.0	26.47,26.73,26.39,26.77	$100.0^{+0.0}_{-4.9}$	$97.2^{+1.0}_{-1.1}$	$100.0^{+0.0}_{-3.5}$	$99.6^{+0.4}_{-0.8}$	$95.9^{+1.4}_{-6.0}$
$1.0 < \|\eta\| < 1.2$	3.5–4.0	3.90,3.90,3.89,3.90	$99.2^{+0.8}_{-6.1}$	$93.6^{+0.6}_{-0.6}$	$73.5^{+4.6}_{-5.4}$	$77.9^{+1.4}_{-1.4}$	$52.6^{+3.5}_{-5.2}$
	4.0–4.5	4.23,4.24,4.24,4.24	$93.0^{+3.8}_{-3.6}$	$93.6^{+0.4}_{-0.4}$	$85.2^{+2.3}_{-2.4}$	$88.8^{+0.7}_{-0.7}$	$65.2^{+3.3}_{-3.2}$
	4.5–5.0	4.73,4.74,4.72,4.75	$96.7^{+3.3}_{-3.5}$	$93.4^{+0.4}_{-0.4}$	$90.4^{+2.0}_{-2.3}$	$94.8^{+0.5}_{-0.5}$	$76.6^{+3.2}_{-3.5}$
	5.0–5.5	5.24,5.24,5.24,5.24	$95.9^{+4.1}_{-4.1}$	$93.8^{+0.4}_{-0.4}$	$90.5^{+2.1}_{-2.4}$	$97.6^{+0.4}_{-0.4}$	$78.7^{+3.9}_{-4.1}$
	5.5–6.0	5.74,5.74,5.74,5.74	$94.8^{+4.4}_{-4.2}$	$93.6^{+0.5}_{-0.5}$	$86.4^{+2.7}_{-3.1}$	$98.0^{+0.4}_{-0.4}$	$74.4^{+4.3}_{-4.3}$
	6.0–7.0	6.46,6.46,6.51,6.45	$99.1^{+0.9}_{-3.8}$	$94.7^{+0.4}_{-0.4}$	$94.0^{+1.8}_{-1.8}$	$98.6^{+0.3}_{-0.3}$	$86.2^{+2.0}_{-3.8}$
	7.0–8.0	7.47,7.47,7.48,7.47	$91.3^{+0.0}_{-0.0}$	$95.4^{+0.5}_{-0.5}$	$98.3^{+0.9}_{-1.5}$	$99.3^{+0.3}_{-0.3}$	$84.1^{+1.3}_{-1.6}$
	8.0–10.0	8.87,8.87,8.94,8.87	$98.6^{+1.4}_{-4.5}$	$96.1^{+0.4}_{-0.4}$	$97.2^{+1.2}_{-1.8}$	$98.8^{+0.3}_{-0.3}$	$90.2^{+2.0}_{-4.6}$
	10.0–15.0	11.83,11.85,11.84,11.87	$100.0^{+0.0}_{-2.7}$	$96.3^{+0.4}_{-0.5}$	$100.0^{+0.0}_{-0.5}$	$98.8^{+0.3}_{-0.3}$	$94.2^{+1.1}_{-2.8}$
	15.0–20.0	16.97,17.04,16.83,17.03	$100.0^{+0.0}_{-3.2}$	$95.2^{+1.0}_{-1.1}$	$100.0^{+0.0}_{-1.8}$	$99.5^{+0.4}_{-0.5}$	$93.8^{+1.4}_{-3.8}$
	20.0–100.0	26.18,26.17,24.68,26.51	$100.0^{+0.0}_{-9.1}$	$97.9^{+1.0}_{-1.1}$	$100.0^{+0.0}_{-7.5}$	$100.0^{+0.0}_{-0.1}$	$96.9^{+1.4}_{-11.5}$

Continued on next page

Continued from previous page

$1.2 < \|\eta\| < 1.4$	2.5–3.0	2.97,2.96,2.95,2.97	$100.0^{+0.0}_{-7.7}$	$94.3^{+2.5}_{-2.8}$	$100.0^{+0.0}_{-8.2}$	$92.7^{+2.8}_{-3.7}$	$86.6^{+3.6}_{-10.7}$
	3.0–3.5	3.29,3.30,3.31,3.30	$31.7^{+16.7}_{-16.7}$	$95.4^{+0.4}_{-0.4}$	$91.6^{+2.4}_{-2.6}$	$95.0^{+0.6}_{-0.6}$	$26.0^{+13.8}_{-13.8}$
	3.5–4.0	3.75,3.76,3.76,3.75	$98.3^{+1.7}_{-3.4}$	$96.2^{+0.3}_{-0.3}$	$94.0^{+2.8}_{-2.8}$	$96.1^{+0.3}_{-0.3}$	$84.6^{+3.1}_{-4.0}$
	4.0–4.5	4.23,4.24,4.24,4.24	$96.7^{+3.3}_{-4.3}$	$96.5^{+0.3}_{-0.3}$	$96.8^{+1.4}_{-1.7}$	$97.4^{+0.3}_{-0.3}$	$87.2^{+3.4}_{-4.3}$
	4.5–5.0	4.74,4.74,4.74,4.74	$95.7^{+3.6}_{-3.5}$	$96.3^{+0.3}_{-0.3}$	$96.5^{+2.2}_{-5.9}$	$98.6^{+0.3}_{-0.4}$	$86.8^{+4.0}_{-6.3}$
	5.0–5.5	5.24,5.24,5.22,5.24	$100.0^{+0.0}_{-1.3}$	$96.5^{+0.4}_{-0.4}$	$94.8^{+1.7}_{-2.1}$	$98.3^{+0.3}_{-0.3}$	$89.0^{+1.9}_{-2.5}$
	5.5–6.0	5.74,5.74,5.73,5.74	$100.0^{+0.0}_{-1.8}$	$96.6^{+0.4}_{-0.4}$	$100.0^{+0.0}_{-0.8}$	$99.5^{+0.3}_{-0.3}$	$95.1^{+1.1}_{-2.2}$
	6.0–7.0	6.46,6.45,6.48,6.45	$100.0^{+0.0}_{-3.5}$	$96.8^{+0.4}_{-0.4}$	$97.4^{+1.5}_{-1.5}$	$98.9^{+0.2}_{-0.3}$	$92.3^{+1.8}_{-3.7}$
	7.0–8.0	7.46,7.46,7.49,7.46	$100.0^{+0.0}_{-4.4}$	$96.5^{+0.4}_{-0.4}$	$99.0^{+0.7}_{-0.7}$	$99.1^{+0.3}_{-0.3}$	$93.7^{+1.3}_{-4.4}$
	8.0–10.0	8.87,8.87,8.89,8.88	$91.6^{+4.5}_{-4.5}$	$97.2^{+0.4}_{-0.4}$	$100.0^{+0.0}_{-0.0}$	$99.3^{+0.3}_{-0.3}$	$87.6^{+4.4}_{-4.4}$
	10.0–15.0	11.86,11.87,12.02,11.92	$100.0^{+0.0}_{-3.3}$	$97.3^{+0.4}_{-0.4}$	$100.0^{+0.0}_{-0.7}$	$98.6^{+0.3}_{-0.4}$	$94.9^{+1.1}_{-3.4}$
	15.0–20.0	16.88,17.04,16.55,17.08	$94.6^{+5.4}_{-14.0}$	$97.4^{+0.8}_{-0.8}$	$100.0^{+0.0}_{-3.4}$	$98.3^{+0.9}_{-1.2}$	$89.6^{+5.4}_{-13.7}$
	20.0–100.0	26.28,26.03,25.70,26.26	$100.0^{+0.0}_{-10.6}$	$97.9^{+1.0}_{-1.1}$	$100.0^{+0.0}_{-3.1}$	$98.8^{+1.0}_{-1.1}$	$95.7^{+1.7}_{-10.7}$
$1.4 < \|\eta\| < 1.6$	2.0–2.5	2.31,2.40,2.34,2.39	$83.2^{+7.3}_{-6.4}$	$96.6^{+0.9}_{-1.0}$	$20.5^{+3.4}_{-3.2}$	$77.6^{+2.6}_{-2.7}$	$12.7^{+2.4}_{-2.2}$
	2.5–3.0	2.75,2.79,2.76,2.79	$95.5^{+4.2}_{-4.2}$	$97.2^{+0.3}_{-0.3}$	$59.5^{+5.7}_{-5.7}$	$90.7^{+0.6}_{-0.6}$	$49.6^{+5.2}_{-5.2}$
	3.0–3.5	3.23,3.24,3.24,3.25	$85.0^{+5.6}_{-5.6}$	$97.0^{+0.2}_{-0.3}$	$88.0^{+1.8}_{-1.9}$	$96.4^{+0.3}_{-0.4}$	$69.3^{+4.9}_{-4.9}$
	3.5–4.0	3.73,3.74,3.74,3.74	$100.0^{+0.0}_{-3.0}$	$97.2^{+0.3}_{-0.3}$	$92.6^{+1.5}_{-1.6}$	$97.9^{+0.3}_{-0.3}$	$87.3^{+1.7}_{-3.2}$
	4.0–4.5	4.23,4.24,4.23,4.24	$98.9^{+1.1}_{-4.4}$	$97.2^{+0.3}_{-0.3}$	$96.5^{+1.1}_{-1.4}$	$98.6^{+0.3}_{-0.3}$	$90.5^{+1.7}_{-4.3}$
	4.5–5.0	4.74,4.74,4.75,4.74	$94.5^{+5.0}_{-4.7}$	$97.4^{+0.3}_{-0.3}$	$97.5^{+1.1}_{-1.5}$	$98.3^{+0.3}_{-0.3}$	$87.4^{+4.8}_{-4.6}$
	5.0–5.5	5.24,5.24,5.25,5.24	$100.0^{+0.0}_{-1.1}$	$97.6^{+0.3}_{-0.4}$	$97.6^{+1.1}_{-1.1}$	$98.8^{+0.3}_{-0.3}$	$93.2^{+1.5}_{-1.8}$
	5.5–6.0	5.74,5.74,5.74,5.75	$93.9^{+4.5}_{-4.3}$	$97.8^{+1.0}_{-1.2}$	$97.5^{+1.7}_{-1.7}$	$99.1^{+0.2}_{-0.3}$	$87.9^{+4.7}_{-4.6}$
	6.0–7.0	6.47,6.45,6.49,6.47	$91.8^{+0.0}_{-0.0}$	$97.4^{+0.4}_{-0.4}$	$97.8^{+1.0}_{-1.5}$	$99.5^{+0.2}_{-0.2}$	$86.2^{+1.3}_{-1.6}$
	7.0–8.0	7.47,7.46,7.51,7.47	$92.2^{+5.8}_{-5.3}$	$97.8^{+0.4}_{-0.5}$	$98.9^{+0.2}_{-0.2}$	$99.8^{+0.2}_{-0.3}$	$88.1^{+5.6}_{-5.2}$
	8.0–10.0	8.84,8.87,8.90,8.87	$100.0^{+0.0}_{-2.8}$	$97.9^{+0.4}_{-0.4}$	$100.0^{+0.0}_{-0.5}$	$99.5^{+0.3}_{-0.3}$	$96.5^{+1.1}_{-2.9}$
	10.0–15.0	11.93,11.84,11.95,11.87	$100.0^{+0.0}_{-1.5}$	$98.2^{+0.4}_{-0.5}$	$97.5^{+2.5}_{-3.3}$	$99.3^{+0.3}_{-0.3}$	$94.1^{+2.6}_{-3.6}$
	15.0–20.0	16.88,17.01,16.67,16.99	$94.5^{+5.5}_{-13.3}$	$98.5^{+0.6}_{-0.8}$	$100.0^{+0.0}_{-4.1}$	$98.6^{+0.6}_{-1.0}$	$90.9^{+5.4}_{-13.4}$
	20.0–100.0	27.10,25.93,25.80,26.24	$96.4^{+3.6}_{-16.2}$	$99.7^{+0.3}_{-1.6}$	$100.0^{+0.0}_{-5.1}$	$100.0^{+0.0}_{-0.3}$	$95.1^{+3.7}_{-16.8}$

Continued on next page

Continued from previous page

$1.6 < \|\eta\| < 2.1$	2.0–2.5	2.23,2.29,2.24,2.29	$96.9^{+3.1}_{-3.6}$	$98.3^{+0.2}_{-0.2}$	$33.2^{+1.5}_{-1.5}$	$86.6^{+0.6}_{-0.6}$	$27.1^{+1.6}_{-1.6}$
	2.5–3.0	2.72,2.75,2.73,2.75	$95.1^{+3.3}_{-3.2}$	$98.2^{+0.2}_{-0.2}$	$58.6^{+2.9}_{-2.9}$	$93.3^{+0.3}_{-0.3}$	$50.5^{+3.1}_{-2.5}$
	3.0–3.5	3.23,3.24,3.24,3.24	$100.0^{+0.0}_{-1.8}$	$98.4^{+0.2}_{-0.2}$	$78.1^{+1.7}_{-1.8}$	$97.2^{+0.2}_{-0.2}$	$73.9^{+1.8}_{-2.3}$
	3.5–4.0	3.73,3.74,3.74,3.74	$96.0^{+3.5}_{-3.3}$	$98.5^{+0.2}_{-0.2}$	$82.7^{+1.8}_{-1.8}$	$98.7^{+0.2}_{-0.2}$	$76.3^{+3.3}_{-3.3}$
	4.0–4.5	4.23,4.24,4.24,4.24	$100.0^{+0.0}_{-7.2}$	$98.2^{+0.2}_{-0.2}$	$92.5^{+1.3}_{-1.4}$	$99.2^{+0.2}_{-0.2}$	$89.2^{+1.6}_{-6.7}$
	4.5–5.0	4.74,4.74,4.74,4.74	$100.0^{+0.0}_{-5.5}$	$98.4^{+0.2}_{-0.2}$	$93.3^{+1.4}_{-1.4}$	$99.3^{+0.2}_{-0.2}$	$90.3^{+1.6}_{-5.2}$
	5.0–5.5	5.23,5.24,5.23,5.25	$95.8^{+4.2}_{-4.6}$	$98.4^{+0.3}_{-0.3}$	$91.9^{+2.2}_{-2.3}$	$99.6^{+0.2}_{-0.2}$	$85.5^{+4.3}_{-4.7}$
	5.5–6.0	5.73,5.74,5.73,5.74	$100.0^{+0.0}_{-3.6}$	$98.5^{+0.2}_{-0.3}$	$94.0^{+1.6}_{-2.0}$	$99.3^{+0.2}_{-0.2}$	$91.1^{+1.8}_{-3.9}$
	6.0–7.0	6.45,6.46,6.46,6.46	$100.0^{+0.0}_{-1.4}$	$98.6^{+0.2}_{-0.2}$	$91.5^{+1.9}_{-1.9}$	$99.6^{+0.1}_{-0.1}$	$89.0^{+2.1}_{-2.4}$
	7.0–8.0	7.47,7.46,7.46,7.47	$100.0^{+0.0}_{-1.8}$	$98.4^{+0.3}_{-0.3}$	$92.5^{+2.8}_{-2.9}$	$99.5^{+0.2}_{-0.2}$	$89.7^{+2.8}_{-3.4}$
	8.0–10.0	8.87,8.86,8.84,8.86	$100.0^{+0.0}_{-4.8}$	$98.0^{+0.3}_{-0.3}$	$96.5^{+1.5}_{-1.6}$	$99.4^{+0.2}_{-0.2}$	$93.1^{+1.8}_{-4.9}$
	10.0–15.0	11.86,11.85,11.88,11.86	$86.8^{+6.0}_{-5.5}$	$98.7^{+0.3}_{-0.3}$	$95.2^{+1.6}_{-2.2}$	$99.5^{+0.2}_{-0.2}$	$80.4^{+5.8}_{-5.5}$
	15.0–20.0	16.95,16.92,17.24,16.83	$100.0^{+0.0}_{-9.5}$	$98.8^{+0.6}_{-0.7}$	$91.6^{+4.6}_{-7.3}$	$99.5^{+0.3}_{-0.3}$	$89.1^{+4.6}_{-11.1}$
	20.0–100.0	27.01,24.95,29.29,25.36	$100.0^{+0.0}_{-15.0}$	$100.0^{+0.0}_{-0.3}$	$100.0^{+0.0}_{-16.1}$	$97.8^{+1.4}_{-1.1}$	$96.8^{+1.7}_{-21.3}$
$2.1 < \|\eta\| < 2.4$	2.0–2.5	2.22,2.26,2.24,2.26	$79.8^{+5.6}_{-5.1}$	$92.9^{+0.7}_{-0.7}$	$59.8^{+2.9}_{-2.9}$	$90.8^{+0.9}_{-0.9}$	$39.8^{+3.5}_{-3.2}$
	2.5–3.0	2.72,2.75,2.73,2.75	$95.4^{+4.6}_{-6.9}$	$90.6^{+0.7}_{-0.7}$	$74.8^{+5.0}_{-3.4}$	$96.8^{+0.6}_{-0.7}$	$61.9^{+5.2}_{-5.4}$
	3.0–3.5	3.22,3.24,3.23,3.24	$94.7^{+5.3}_{-6.5}$	$90.0^{+0.8}_{-0.8}$	$84.0^{+6.3}_{-6.3}$	$98.1^{+0.5}_{-0.5}$	$69.6^{+6.6}_{-7.1}$
	3.5–4.0	3.73,3.74,3.73,3.74	$100.0^{+0.0}_{-13.0}$	$90.5^{+0.8}_{-0.8}$	$85.7^{+4.2}_{-4.4}$	$97.7^{+0.5}_{-0.6}$	$74.9^{+3.9}_{-10.5}$
	4.0–4.5	4.23,4.24,4.24,4.24	$93.5^{+6.5}_{-8.0}$	$90.4^{+0.9}_{-0.9}$	$80.8^{+4.3}_{-4.3}$	$99.5^{+0.4}_{-0.3}$	$67.3^{+6.0}_{-6.8}$
	4.5–5.0	4.74,4.73,4.73,4.73	$93.9^{+6.0}_{-0.0}$	$89.7^{+1.6}_{-1.1}$	$71.8^{+5.3}_{-5.7}$	$99.4^{+0.3}_{-0.3}$	$59.5^{+4.5}_{-4.8}$
	5.0–5.5	5.23,5.24,5.24,5.24	$84.7^{+11.1}_{-9.1}$	$89.3^{+1.2}_{-1.3}$	$87.5^{+3.8}_{-5.0}$	$99.7^{+0.2}_{-0.3}$	$65.3^{+9.1}_{-8.0}$
	5.5–6.0	5.72,5.74,5.74,5.74	$87.2^{+0.0}_{-0.0}$	$91.3^{+1.3}_{-1.4}$	$72.8^{+6.6}_{-7.9}$	$99.4^{+0.3}_{-0.4}$	$57.1^{+5.3}_{-6.3}$
	6.0–7.0	6.46,6.46,6.49,6.46	$100.0^{+0.0}_{-6.2}$	$90.2^{+1.4}_{-1.4}$	$84.0^{+3.8}_{-4.3}$	$99.3^{+0.7}_{-1.1}$	$74.5^{+3.7}_{-6.2}$
	7.0–8.0	7.47,7.44,7.37,7.45	$78.6^{+9.2}_{-8.2}$	$88.6^{+1.7}_{-1.8}$	$81.1^{+7.4}_{-7.4}$	$100.0^{+0.0}_{-0.2}$	$56.0^{+8.4}_{-7.9}$
	8.0–10.0	8.87,8.82,8.66,8.82	$86.5^{+0.0}_{-0.0}$	$92.5^{+1.9}_{-2.0}$	$69.1^{+8.2}_{-9.2}$	$99.3^{+0.3}_{-0.3}$	$54.3^{+6.6}_{-7.4}$
	10.0–15.0	11.78,11.74,11.49,11.73	$100.0^{+0.0}_{-22.5}$	$92.1^{+2.0}_{-3.5}$	$100.0^{+0.0}_{-22.2}$	$98.9^{+0.6}_{-0.6}$	$90.2^{+2.2}_{-28.7}$
	15.0–20.0	17.01,16.97,18.67,16.87	$91.6^{+8.4}_{-36.4}$	$88.2^{+4.8}_{-3.8}$	$100.0^{+0.0}_{-18.0}$	$100.0^{+0.0}_{-0.3}$	$80.0^{+8.6}_{-35.1}$
	20.0–100.0	26.41,24.19,21.93,24.18	$100.0^{+0.0}_{-20.0}$	$86.0^{+7.9}_{-12.7}$	$100.0^{+0.0}_{-22.1}$	$100.0^{+0.0}_{-0.9}$	$85.2^{+7.8}_{-28.4}$

Table B.2: MC based single muon efficiencies applying *tracker80* cuts and using the `L1_DoubleMu0_HighQ` seed for the L1·L2 efficiency.

	p_T [GeV/c]	$\langle p_T \rangle$ [GeV/c]	$\varepsilon_{\text{MuonID}}$ [%]	$\varepsilon_{\text{MuonQual}}$ [%]	$\varepsilon_{L1\cdot L2}$ [%]	ε_{L3} [%]	ε_{μ} [%]
$\lvert\eta\rvert < 0.2$	3.5–4.0	3.90,3.91,3.90,3.91	$91.1^{+0.2}_{-0.2}$	$96.1^{+0.2}_{-0.2}$	$72.5^{+0.5}_{-0.5}$	$65.5^{+1.0}_{-1.0}$	$41.2^{+0.8}_{-0.8}$
	4.0–4.5	4.25,4.27,4.25,4.27	$95.5^{+0.1}_{-0.1}$	$95.0^{+0.1}_{-0.1}$	$82.9^{+0.3}_{-0.3}$	$76.0^{+0.4}_{-0.4}$	$56.6^{+0.7}_{-0.7}$
	4.5–5.0	4.75,4.75,4.75,4.75	$97.9^{+0.1}_{-0.1}$	$95.0^{+0.1}_{-0.1}$	$91.7^{+0.2}_{-0.2}$	$86.0^{+0.3}_{-0.3}$	$72.6^{+0.8}_{-0.8}$
	5.0–5.5	5.25,5.25,5.25,5.25	$98.6^{+0.1}_{-0.1}$	$95.3^{+0.1}_{-0.1}$	$94.9^{+0.2}_{-0.2}$	$93.0^{+0.2}_{-0.2}$	$82.1^{+0.9}_{-0.9}$
	5.5–6.0	5.75,5.75,5.75,5.75	$98.9^{+0.1}_{-0.1}$	$95.3^{+0.1}_{-0.1}$	$96.9^{+0.1}_{-0.1}$	$98.4^{+0.1}_{-0.1}$	$89.0^{+0.9}_{-0.9}$
	6.0–7.0	6.49,6.49,6.49,6.50	$99.1^{+0.0}_{-0.0}$	$95.6^{+0.1}_{-0.1}$	$98.2^{+0.1}_{-0.1}$	$99.8^{+0.0}_{-0.0}$	$92.0^{+0.9}_{-0.9}$
	7.0–8.0	7.49,7.50,7.50,7.50	$99.3^{+0.0}_{-0.0}$	$95.7^{+0.1}_{-0.1}$	$98.5^{+0.1}_{-0.1}$	$100.0^{+0.0}_{-0.0}$	$92.6^{+0.9}_{-0.9}$
	8.0–10.0	8.97,8.97,8.97,8.98	$99.3^{+0.0}_{-0.0}$	$95.9^{+0.1}_{-0.1}$	$98.7^{+0.0}_{-0.0}$	$100.0^{+0.0}_{-0.0}$	$93.0^{+0.9}_{-0.9}$
	10.0–15.0	12.32,12.35,12.33,12.37	$99.3^{+0.0}_{-0.0}$	$96.0^{+0.0}_{-0.0}$	$98.7^{+0.0}_{-0.0}$	$100.0^{+0.0}_{-0.0}$	$93.1^{+0.9}_{-0.9}$
	15.0–20.0	17.33,17.37,17.33,17.37	$99.3^{+0.0}_{-0.0}$	$96.3^{+0.0}_{-0.0}$	$98.7^{+0.0}_{-0.0}$	$99.9^{+0.0}_{-0.0}$	$93.4^{+0.9}_{-0.9}$
	20.0–100.0	27.37,28.09,27.26,27.94	$99.4^{+0.0}_{-0.0}$	$96.4^{+0.0}_{-0.0}$	$98.8^{+0.0}_{-0.0}$	$99.9^{+0.0}_{-0.0}$	$93.7^{+0.9}_{-0.9}$
$0.2 < \lvert\eta\rvert < 0.3$	3.5–4.0	3.90,3.91,3.90,3.91	$71.1^{+0.5}_{-0.5}$	$95.6^{+0.5}_{-0.5}$	$45.2^{+1.0}_{-1.0}$	$67.7^{+1.8}_{-1.9}$	$20.6^{+0.8}_{-0.8}$
	4.0–4.5	4.25,4.27,4.25,4.28	$84.6^{+0.3}_{-0.3}$	$95.4^{+0.2}_{-0.2}$	$63.8^{+0.5}_{-0.5}$	$80.8^{+0.7}_{-0.7}$	$41.2^{+0.7}_{-0.7}$
	4.5–5.0	4.75,4.76,4.75,4.76	$92.8^{+0.2}_{-0.2}$	$95.4^{+0.2}_{-0.2}$	$74.3^{+0.5}_{-0.5}$	$89.6^{+0.4}_{-0.4}$	$58.3^{+0.8}_{-0.8}$
	5.0–5.5	5.25,5.25,5.25,5.25	$96.8^{+0.1}_{-0.1}$	$95.8^{+0.2}_{-0.2}$	$82.9^{+0.4}_{-0.4}$	$95.5^{+0.3}_{-0.3}$	$72.6^{+0.9}_{-0.9}$
	5.5–6.0	5.75,5.75,5.75,5.75	$98.0^{+0.1}_{-0.1}$	$95.8^{+0.2}_{-0.2}$	$86.3^{+0.4}_{-0.4}$	$98.5^{+0.1}_{-0.2}$	$79.0^{+0.9}_{-0.9}$
	6.0–7.0	6.49,6.50,6.50,6.50	$98.5^{+0.1}_{-0.1}$	$96.0^{+0.1}_{-0.1}$	$88.4^{+0.3}_{-0.3}$	$99.8^{+0.0}_{-0.0}$	$82.6^{+0.9}_{-0.9}$
	7.0–8.0	7.49,7.50,7.49,7.50	$98.7^{+0.1}_{-0.1}$	$96.2^{+0.1}_{-0.1}$	$90.2^{+0.3}_{-0.3}$	$100.0^{+0.0}_{-0.0}$	$84.7^{+0.9}_{-0.9}$
	8.0–10.0	8.98,8.98,8.98,8.99	$98.8^{+0.0}_{-0.0}$	$96.2^{+0.7}_{-0.5}$	$90.8^{+0.2}_{-0.2}$	$99.9^{+0.0}_{-0.0}$	$85.4^{+1.1}_{-1.0}$
	10.0–15.0	12.33,12.37,12.32,12.37	$99.0^{+0.0}_{-0.0}$	$96.6^{+0.1}_{-0.1}$	$90.5^{+0.1}_{-0.1}$	$100.0^{+0.0}_{-0.0}$	$85.7^{+0.9}_{-0.9}$
	15.0–20.0	17.32,17.36,17.32,17.37	$99.0^{+0.0}_{-0.0}$	$96.9^{+0.1}_{-0.1}$	$90.3^{+0.2}_{-0.2}$	$99.9^{+0.0}_{-0.0}$	$85.7^{+0.9}_{-0.9}$
	20.0–100.0	27.29,28.06,27.26,27.99	$99.1^{+0.0}_{-0.0}$	$97.0^{+0.0}_{-0.0}$	$90.4^{+0.1}_{-0.1}$	$99.9^{+0.0}_{-0.0}$	$86.0^{+0.9}_{-0.9}$

Continued on next page

Continued from previous page

$0.3 < \|\eta\| < 0.6$	3.5–4.0	3.90,3.90,3.90,3.90,3.91	$92.5^{+0.2}_{-0.2}$	$96.0^{+0.2}_{-0.2}$	$78.4^{+0.4}_{-0.4}$	$53.6^{+0.7}_{-0.7}$	$36.9^{+0.6}_{-0.6}$
	4.0–4.5	4.25,4.26,4.25,4.26	$95.8^{+0.1}_{-0.1}$	$95.7^{+0.1}_{-0.1}$	$89.3^{+0.2}_{-0.2}$	$72.7^{+0.3}_{-0.3}$	$58.8^{+0.7}_{-0.7}$
	4.5–5.0	4.75,4.75,4.75,4.75	$97.9^{+0.1}_{-0.1}$	$95.6^{+0.2}_{-0.2}$	$93.8^{+0.1}_{-0.1}$	$87.8^{+0.2}_{-0.2}$	$76.3^{+0.8}_{-0.8}$
	5.0–5.5	5.25,5.25,5.25,5.25	$98.7^{+0.0}_{-0.0}$	$95.9^{+0.1}_{-0.1}$	$96.5^{+0.1}_{-0.1}$	$97.3^{+0.1}_{-0.1}$	$88.0^{+0.9}_{-0.9}$
	5.5–6.0	5.75,5.75,5.75,5.75	$99.0^{+0.0}_{-0.0}$	$96.1^{+0.1}_{-0.1}$	$97.5^{+0.1}_{-0.1}$	$99.6^{+0.0}_{-0.0}$	$91.5^{+0.9}_{-0.9}$
	6.0–7.0	6.49,6.50,6.50,6.50	$99.1^{+0.0}_{-0.0}$	$96.4^{+0.1}_{-0.1}$	$98.3^{+0.1}_{-0.1}$	$99.9^{+0.0}_{-0.0}$	$92.9^{+0.9}_{-0.9}$
	7.0–8.0	7.49,7.49,7.49,7.50	$99.3^{+0.0}_{-0.0}$	$96.4^{+0.1}_{-0.1}$	$98.9^{+0.0}_{-0.0}$	$100.0^{+0.0}_{-0.0}$	$93.7^{+0.9}_{-0.9}$
	8.0–10.0	8.97,8.97,8.98,8.98	$99.3^{+0.0}_{-0.1}$	$96.8^{+0.0}_{-0.0}$	$99.1^{+0.0}_{-0.0}$	$100.0^{+0.0}_{-0.0}$	$94.2^{+1.0}_{-1.0}$
	10.0–15.0	12.33,12.36,12.35,12.38	$99.3^{+0.0}_{-0.0}$	$97.0^{+0.0}_{-0.0}$	$99.1^{+0.0}_{-0.0}$	$100.0^{+0.0}_{-0.0}$	$94.4^{+1.0}_{-1.0}$
	15.0–20.0	17.33,17.36,17.33,17.37	$99.3^{+0.0}_{-0.0}$	$97.2^{+0.0}_{-0.0}$	$99.0^{+0.0}_{-0.0}$	$100.0^{+0.0}_{-0.0}$	$94.6^{+1.0}_{-1.0}$
	20.0–100.0	27.40,28.13,27.30,27.98	$99.3^{+0.0}_{-0.0}$	$97.5^{+0.0}_{-0.0}$	$99.0^{+0.0}_{-0.0}$	$99.9^{+0.0}_{-0.0}$	$94.8^{+1.0}_{-1.0}$
$0.6 < \|\eta\| < 0.8$	3.5–4.0	3.90,3.90,3.90,3.90	$90.1^{+0.2}_{-0.2}$	$96.1^{+0.2}_{-0.2}$	$71.2^{+0.6}_{-0.6}$	$65.5^{+0.8}_{-0.8}$	$40.0^{+0.7}_{-0.7}$
	4.0–4.5	4.25,4.26,4.25,4.26	$94.7^{+0.1}_{-0.1}$	$95.7^{+0.1}_{-0.1}$	$85.8^{+0.3}_{-0.3}$	$81.6^{+0.3}_{-0.3}$	$62.8^{+0.7}_{-0.7}$
	4.5–5.0	4.75,4.75,4.75,4.75	$97.5^{+0.1}_{-0.1}$	$95.7^{+0.1}_{-0.1}$	$92.7^{+0.5}_{-0.5}$	$93.4^{+0.2}_{-0.2}$	$79.9^{+0.9}_{-0.9}$
	5.0–5.5	5.25,5.25,5.25,5.25	$98.5^{+0.1}_{-0.1}$	$96.0^{+0.1}_{-0.1}$	$95.8^{+0.2}_{-0.2}$	$99.1^{+0.1}_{-0.1}$	$88.9^{+0.9}_{-0.9}$
	5.5–6.0	5.75,5.75,5.75,5.75	$98.9^{+0.1}_{-0.1}$	$96.1^{+0.1}_{-0.1}$	$96.7^{+0.2}_{-0.2}$	$99.8^{+0.0}_{-0.0}$	$90.8^{+0.9}_{-0.9}$
	6.0–7.0	6.49,6.50,6.50,6.50	$99.2^{+0.0}_{-0.0}$	$96.3^{+0.1}_{-0.1}$	$97.5^{+0.1}_{-0.1}$	$99.9^{+0.0}_{-0.0}$	$92.1^{+0.9}_{-0.9}$
	7.0–8.0	7.49,7.50,7.50,7.50	$99.2^{+0.0}_{-0.0}$	$96.6^{+0.1}_{-0.1}$	$98.2^{+0.1}_{-0.1}$	$100.0^{+0.0}_{-0.0}$	$93.1^{+1.0}_{-0.9}$
	8.0–10.0	8.97,8.98,8.98,8.98	$99.2^{+0.0}_{-0.0}$	$96.8^{+0.1}_{-0.1}$	$98.5^{+0.1}_{-0.1}$	$100.0^{+0.0}_{-0.0}$	$93.7^{+1.0}_{-1.0}$
	10.0–15.0	12.32,12.35,12.33,12.37	$99.3^{+0.0}_{-0.0}$	$97.1^{+0.2}_{-0.1}$	$99.0^{+0.0}_{-0.0}$	$100.0^{+0.0}_{-0.0}$	$94.4^{+1.0}_{-1.0}$
	15.0–20.0	17.33,17.36,17.34,17.37	$99.4^{+0.0}_{-0.0}$	$97.3^{+0.0}_{-0.0}$	$99.2^{+0.0}_{-0.0}$	$99.9^{+0.0}_{-0.0}$	$94.9^{+1.0}_{-1.0}$
	20.0–100.0	27.41,28.08,27.34,27.97	$99.3^{+0.0}_{-0.0}$	$97.4^{+0.0}_{-0.0}$	$99.3^{+0.0}_{-0.0}$	$99.9^{+0.0}_{-0.0}$	$95.1^{+1.0}_{-1.0}$

Continued on next page

Continued from previous page

$0.8 < \|\eta\| < 1.0$	3.5–4.0	3.90,3.90,3.90,3.91	$92.6^{+0.2}_{-0.2}$	$96.2^{+0.2}_{-0.2}$	$72.6^{+0.6}_{-0.6}$	$72.0^{+0.7}_{-0.7}$	$46.1^{+0.8}_{-0.8}$
	4.0–4.5	4.25,4.26,4.25,4.26	$96.3^{+0.1}_{-0.1}$	$95.3^{+0.1}_{-0.1}$	$86.4^{+0.3}_{-0.3}$	$85.3^{+0.3}_{-0.3}$	$66.9^{+0.8}_{-0.8}$
	4.5–5.0	4.75,4.75,4.75,4.75	$98.0^{+0.1}_{-0.1}$	$95.0^{+0.1}_{-0.1}$	$93.9^{+0.2}_{-0.2}$	$96.0^{+0.2}_{-0.2}$	$83.1^{+0.9}_{-0.9}$
	5.0–5.5	5.25,5.25,5.25,5.25	$98.4^{+0.1}_{-0.1}$	$95.5^{+0.1}_{-0.1}$	$95.7^{+0.2}_{-0.2}$	$98.7^{+0.1}_{-0.1}$	$87.9^{+0.9}_{-0.9}$
	5.5–6.0	5.75,5.75,5.75,5.75	$98.8^{+0.1}_{-0.1}$	$95.8^{+0.1}_{-0.1}$	$96.6^{+0.1}_{-0.1}$	$99.5^{+0.1}_{-0.1}$	$90.1^{+0.9}_{-0.9}$
	6.0–7.0	6.49,6.49,6.49,6.50	$99.0^{+0.0}_{-0.0}$	$95.7^{+0.1}_{-0.1}$	$96.9^{+0.1}_{-0.1}$	$99.8^{+0.0}_{-0.0}$	$90.8^{+0.9}_{-0.9}$
	7.0–8.0	7.49,7.49,7.50,7.50	$99.0^{+0.0}_{-0.0}$	$96.1^{+0.1}_{-0.1}$	$97.0^{+0.1}_{-0.1}$	$99.9^{+0.0}_{-0.0}$	$91.3^{+0.9}_{-0.9}$
	8.0–10.0	8.97,8.97,8.98,8.98	$99.1^{+0.0}_{-0.0}$	$96.3^{+0.1}_{-0.1}$	$96.8^{+0.1}_{-0.1}$	$99.9^{+0.0}_{-0.0}$	$91.5^{+0.9}_{-0.9}$
	10.0–15.0	12.33,12.35,12.35,12.38	$99.3^{+0.0}_{-0.0}$	$96.8^{+0.0}_{-0.0}$	$96.6^{+0.1}_{-0.1}$	$100.0^{+0.0}_{-0.0}$	$91.9^{+0.9}_{-0.9}$
	15.0–20.0	17.34,17.36,17.34,17.37	$99.3^{+0.0}_{-0.0}$	$97.1^{+0.0}_{-0.0}$	$96.3^{+0.1}_{-0.1}$	$100.0^{+0.0}_{-0.0}$	$91.8^{+0.9}_{-0.9}$
	20.0–100.0	27.43,28.09,27.35,27.97	$99.3^{+0.0}_{-0.0}$	$97.3^{+0.0}_{-0.0}$	$96.4^{+0.1}_{-0.1}$	$99.9^{+0.0}_{-0.0}$	$92.2^{+0.9}_{-0.9}$
$1.0 < \|\eta\| < 1.2$	3.5–4.0	3.90,3.90,3.90,3.91	$89.7^{+0.3}_{-0.3}$	$95.0^{+0.0}_{-0.0}$	$67.0^{+0.7}_{-0.7}$	$75.1^{+1.0}_{-1.0}$	$42.5^{+0.8}_{-0.8}$
	4.0–4.5	4.25,4.27,4.25,4.27	$94.4^{+0.1}_{-0.1}$	$95.0^{+0.2}_{-0.2}$	$81.8^{+0.3}_{-0.3}$	$87.6^{+0.4}_{-0.4}$	$63.6^{+0.8}_{-0.8}$
	4.5–5.0	4.75,4.76,4.75,4.76	$96.5^{+0.1}_{-0.1}$	$95.1^{+0.2}_{-0.2}$	$91.3^{+0.3}_{-0.3}$	$95.7^{+0.2}_{-0.2}$	$79.4^{+0.9}_{-0.9}$
	5.0–5.5	5.25,5.25,5.25,5.25	$97.7^{+0.1}_{-0.1}$	$95.2^{+0.1}_{-0.1}$	$94.8^{+0.2}_{-0.2}$	$98.6^{+0.1}_{-0.1}$	$86.2^{+0.9}_{-0.9}$
	5.5–6.0	5.75,5.75,5.75,5.75	$98.2^{+0.1}_{-0.1}$	$95.5^{+0.1}_{-0.1}$	$96.2^{+0.2}_{-0.2}$	$99.4^{+0.1}_{-0.1}$	$88.8^{+0.9}_{-0.9}$
	6.0–7.0	6.50,6.50,6.50,6.50	$98.8^{+0.0}_{-0.1}$	$95.8^{+0.1}_{-0.1}$	$97.6^{+0.1}_{-0.1}$	$99.8^{+0.0}_{-0.0}$	$91.2^{+0.9}_{-0.9}$
	7.0–8.0	7.49,7.50,7.50,7.50	$99.1^{+0.0}_{-0.0}$	$95.9^{+0.6}_{-0.4}$	$98.3^{+0.1}_{-0.1}$	$99.9^{+0.0}_{-0.0}$	$92.4^{+1.1}_{-1.0}$
	8.0–10.0	8.98,8.99,8.99,8.99	$99.2^{+0.0}_{-0.0}$	$96.4^{+0.1}_{-0.1}$	$98.9^{+0.0}_{-0.0}$	$99.9^{+0.0}_{-0.0}$	$93.6^{+0.9}_{-0.9}$
	10.0–15.0	12.35,12.37,12.37,12.39	$99.3^{+0.0}_{-0.0}$	$96.8^{+0.0}_{-0.0}$	$99.2^{+0.2}_{-0.2}$	$100.0^{+0.0}_{-0.0}$	$94.4^{+1.0}_{-1.0}$
	15.0–20.0	17.34,17.36,17.35,17.37	$99.4^{+0.0}_{-0.0}$	$97.2^{+0.0}_{-0.0}$	$99.3^{+0.0}_{-0.0}$	$99.9^{+0.0}_{-0.0}$	$94.9^{+1.0}_{-1.0}$
	20.0–100.0	27.43,27.90,27.35,27.79	$99.4^{+0.0}_{-0.0}$	$97.2^{+0.0}_{-0.0}$	$99.3^{+0.1}_{-0.0}$	$99.9^{+0.0}_{-0.0}$	$94.9^{+1.0}_{-1.0}$

Continued on next page

Continued from previous page

$1.2 < \lvert\eta\rvert < 1.4$	2.5–3.0	2.97,2.96,2.97,2.97	$95.3^{+1.4}_{-1.7}$	$97.4^{+1.6}_{-1.6}$	$78.9^{+4.3}_{-4.8}$	$93.3^{+2.8}_{-3.7}$	$67.6^{+4.5}_{-5.2}$
	3.0–3.5	3.31,3.31,3.31,3.32	$96.1^{+0.2}_{-0.3}$	$97.2^{+0.2}_{-0.3}$	$88.1^{+0.6}_{-0.6}$	$97.2^{+0.3}_{-0.3}$	$79.1^{+1.0}_{-1.0}$
	3.5–4.0	3.77,3.77,3.77,3.77	$95.3^{+0.2}_{-0.2}$	$96.6^{+0.2}_{-0.2}$	$88.5^{+0.4}_{-0.4}$	$98.0^{+0.2}_{-0.2}$	$79.1^{+0.9}_{-0.9}$
	4.0–4.5	4.25,4.25,4.25,4.25	$96.4^{+0.1}_{-0.1}$	$96.8^{+0.5}_{-0.5}$	$93.1^{+0.3}_{-0.3}$	$99.3^{+0.1}_{-0.1}$	$85.4^{+1.0}_{-1.0}$
	4.5–5.0	4.75,4.75,4.75,4.75	$97.2^{+0.1}_{-0.1}$	$96.9^{+0.1}_{-0.1}$	$96.0^{+0.2}_{-0.2}$	$99.7^{+0.0}_{-0.1}$	$89.2^{+0.9}_{-0.9}$
	5.0–5.5	5.25,5.25,5.25,5.25	$97.8^{+0.1}_{-0.1}$	$96.7^{+0.1}_{-0.1}$	$96.8^{+0.2}_{-0.2}$	$99.7^{+0.1}_{-0.1}$	$90.3^{+0.9}_{-0.9}$
	5.5–6.0	5.75,5.75,5.75,5.75	$98.3^{+0.1}_{-0.1}$	$96.8^{+0.1}_{-0.1}$	$97.4^{+0.2}_{-0.2}$	$99.9^{+0.0}_{-0.0}$	$91.6^{+1.0}_{-1.0}$
	6.0–7.0	6.49,6.49,6.50,6.49	$98.6^{+0.1}_{-0.1}$	$96.9^{+0.1}_{-0.1}$	$98.3^{+0.1}_{-0.1}$	$99.9^{+0.0}_{-0.0}$	$92.8^{+1.0}_{-1.0}$
	7.0–8.0	7.49,7.50,7.50,7.50	$98.8^{+0.3}_{-0.3}$	$96.9^{+0.1}_{-0.1}$	$98.7^{+0.1}_{-0.1}$	$99.9^{+0.0}_{-0.0}$	$93.4^{+1.0}_{-1.0}$
	8.0–10.0	8.97,8.98,8.98,8.98	$99.1^{+0.0}_{-0.0}$	$97.0^{+0.1}_{-0.1}$	$99.2^{+0.1}_{-0.1}$	$99.9^{+0.0}_{-0.0}$	$94.3^{+1.0}_{-1.0}$
	10.0–15.0	12.33,12.35,12.35,12.37	$99.3^{+0.2}_{-0.2}$	$97.2^{+0.1}_{-0.1}$	$99.4^{+0.0}_{-0.0}$	$99.9^{+0.0}_{-0.0}$	$94.8^{+1.0}_{-1.0}$
	15.0–20.0	17.34,17.34,17.34,17.35	$99.4^{+0.0}_{-0.0}$	$97.4^{+0.1}_{-0.1}$	$99.5^{+0.0}_{-0.0}$	$99.9^{+0.0}_{-0.0}$	$95.3^{+1.0}_{-1.0}$
	20.0–100.0	27.46,27.93,27.36,27.78	$99.5^{+0.0}_{-0.0}$	$97.5^{+0.0}_{-0.0}$	$99.6^{+0.0}_{-0.0}$	$99.9^{+0.0}_{-0.0}$	$95.6^{+1.0}_{-1.0}$
$1.4 < \lvert\eta\rvert < 1.6$	2.0–2.5	2.34,2.41,2.34,2.41	$91.7^{+0.5}_{-0.6}$	$96.2^{+1.2}_{-1.1}$	$24.1^{+1.2}_{-1.2}$	$90.4^{+2.2}_{-2.5}$	$19.1^{+1.1}_{-1.1}$
	2.5–3.0	2.78,2.81,2.78,2.81	$93.9^{+0.3}_{-0.3}$	$97.1^{+0.2}_{-0.3}$	$61.2^{+0.8}_{-0.8}$	$95.7^{+0.4}_{-0.4}$	$52.9^{+0.9}_{-0.9}$
	3.0–3.5	3.25,3.25,3.25,3.25	$96.1^{+0.2}_{-0.2}$	$96.7^{+0.2}_{-0.2}$	$83.2^{+0.5}_{-0.5}$	$99.3^{+0.1}_{-0.1}$	$76.0^{+0.9}_{-0.9}$
	3.5–4.0	3.74,3.75,3.75,3.75	$97.8^{+0.1}_{-0.2}$	$97.1^{+0.2}_{-0.2}$	$92.0^{+0.4}_{-0.4}$	$99.5^{+0.1}_{-0.1}$	$86.1^{+1.0}_{-1.0}$
	4.0–4.5	4.24,4.24,4.24,4.24	$98.4^{+0.1}_{-0.1}$	$96.8^{+0.2}_{-0.2}$	$94.7^{+0.3}_{-0.4}$	$99.7^{+0.1}_{-0.1}$	$89.0^{+1.0}_{-1.0}$
	4.5–5.0	4.74,4.74,4.74,4.74	$98.7^{+0.1}_{-0.2}$	$97.0^{+0.2}_{-0.2}$	$96.7^{+0.3}_{-0.3}$	$99.6^{+0.1}_{-0.1}$	$91.3^{+1.0}_{-1.0}$
	5.0–5.5	5.24,5.24,5.24,5.24	$99.1^{+0.1}_{-0.1}$	$96.6^{+0.2}_{-0.2}$	$97.9^{+0.3}_{-0.3}$	$99.8^{+0.1}_{-0.1}$	$92.6^{+1.0}_{-1.0}$
	5.5–6.0	5.75,5.74,5.75,5.75	$99.0^{+0.1}_{-0.1}$	$96.9^{+0.3}_{-0.3}$	$98.2^{+0.3}_{-0.3}$	$99.9^{+0.0}_{-0.0}$	$93.2^{+1.0}_{-1.0}$
	6.0–7.0	6.47,6.47,6.47,6.47	$99.0^{+0.1}_{-0.1}$	$96.4^{+0.2}_{-0.2}$	$98.4^{+0.2}_{-0.2}$	$99.9^{+0.0}_{-0.1}$	$92.8^{+1.0}_{-1.0}$
	7.0–8.0	7.47,7.47,7.47,7.47	$99.2^{+0.1}_{-0.1}$	$96.7^{+0.3}_{-0.3}$	$98.4^{+0.2}_{-0.2}$	$99.8^{+0.1}_{-0.1}$	$93.3^{+1.0}_{-1.0}$
	8.0–10.0	8.87,8.87,8.87,8.87	$99.3^{+0.1}_{-0.1}$	$96.9^{+0.2}_{-0.2}$	$98.8^{+0.2}_{-0.2}$	$99.9^{+0.1}_{-0.1}$	$94.0^{+1.0}_{-1.0}$
	10.0–15.0	11.28,11.28,11.30,11.29	$99.6^{+0.1}_{-0.1}$	$96.8^{+0.3}_{-0.3}$	$99.5^{+0.2}_{-0.2}$	$100.0^{+0.0}_{-0.0}$	$94.9^{+1.0}_{-1.0}$
	15.0–20.0	15.02,15.02,15.01,15.01	$100.0^{+0.0}_{-5.5}$	$100.0^{+0.0}_{-5.5}$	$100.0^{+0.0}_{-22.1}$	$100.0^{+0.0}_{-8.2}$	$99.0^{+1.0}_{-24.6}$

APPENDIX C

ρ FACTOR

Figure C.1 and C.2 exhibits the ρ factor for $\Upsilon(1S)$ and the J/ψ as a function of ϕ_{HX}. The ρ factor in the CS and PX frames can be found in Ref. [61].

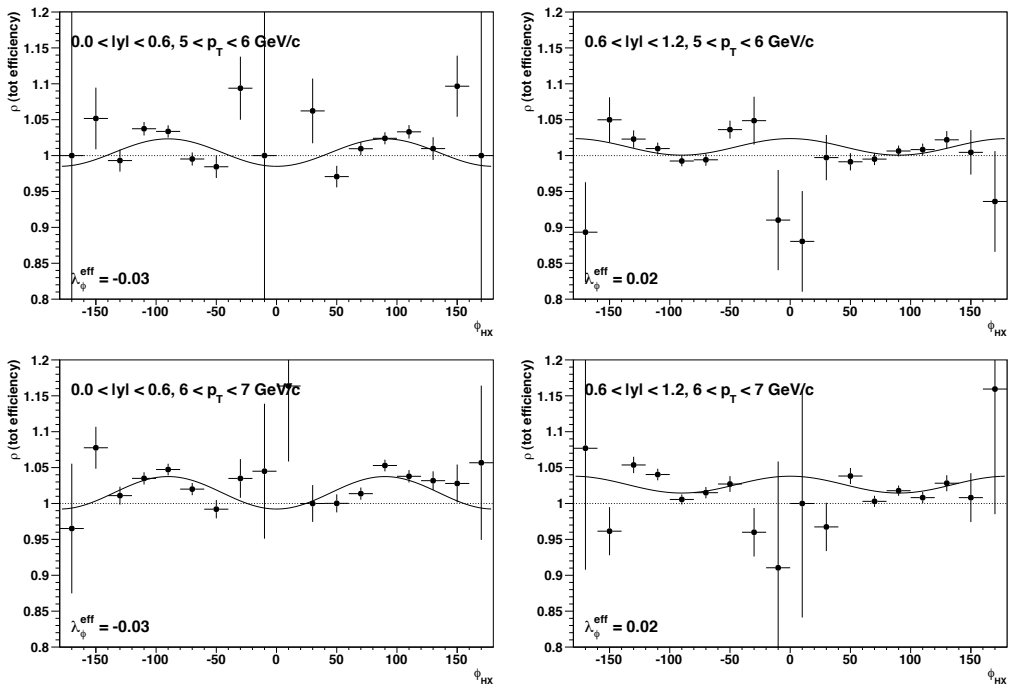

Figure C.1: ρ factor for the $\Upsilon(1S)$ as a function of ϕ, calculated in the HX frame using the `HLT_Dimuon5_Upsilon_Barrel` trigger path. The left panel shows the ρ factor at mid-rapidity ($|y| < 0.6$), the right side at $0.6 < |y| < 1.2$.

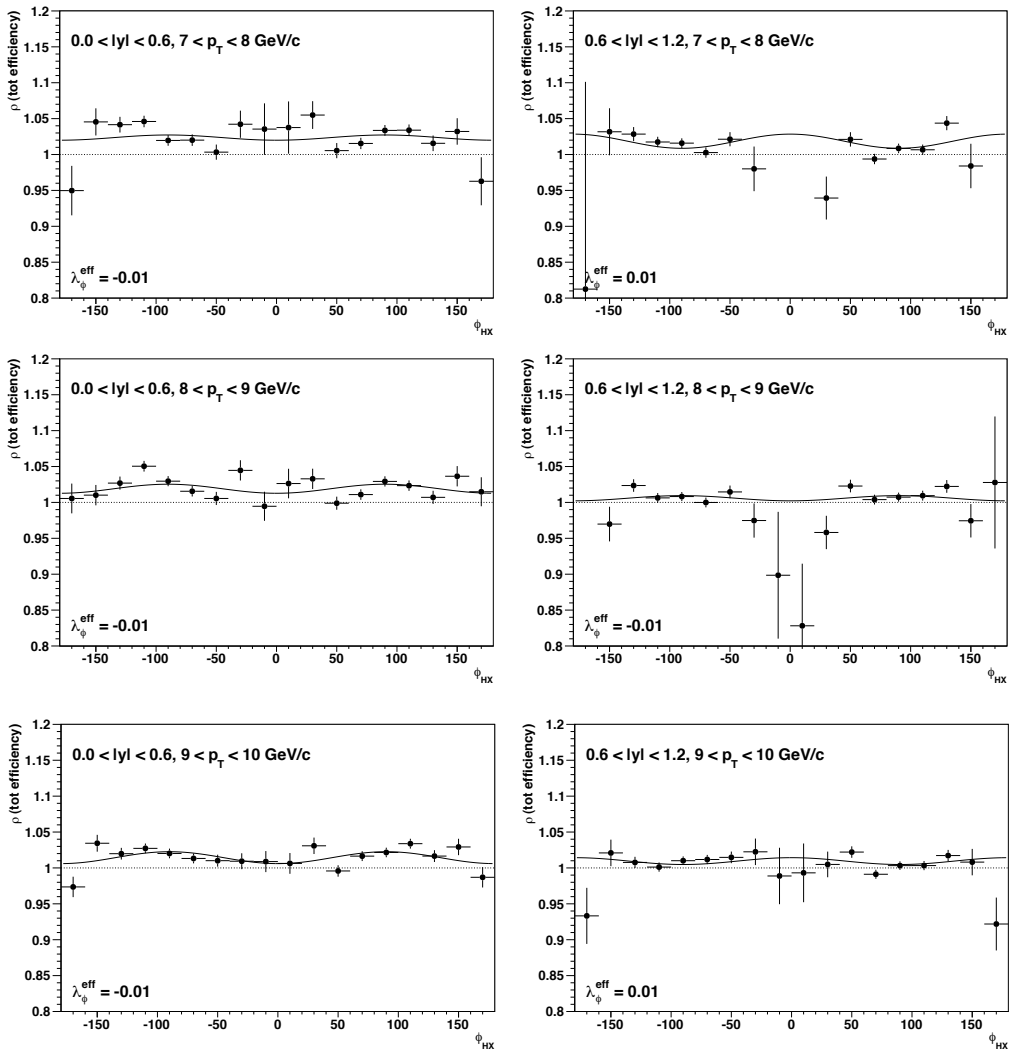

Figure C.1: ϕ_{HX} dependence of the ρ factor for the $\Upsilon(1S)$ (cont.)

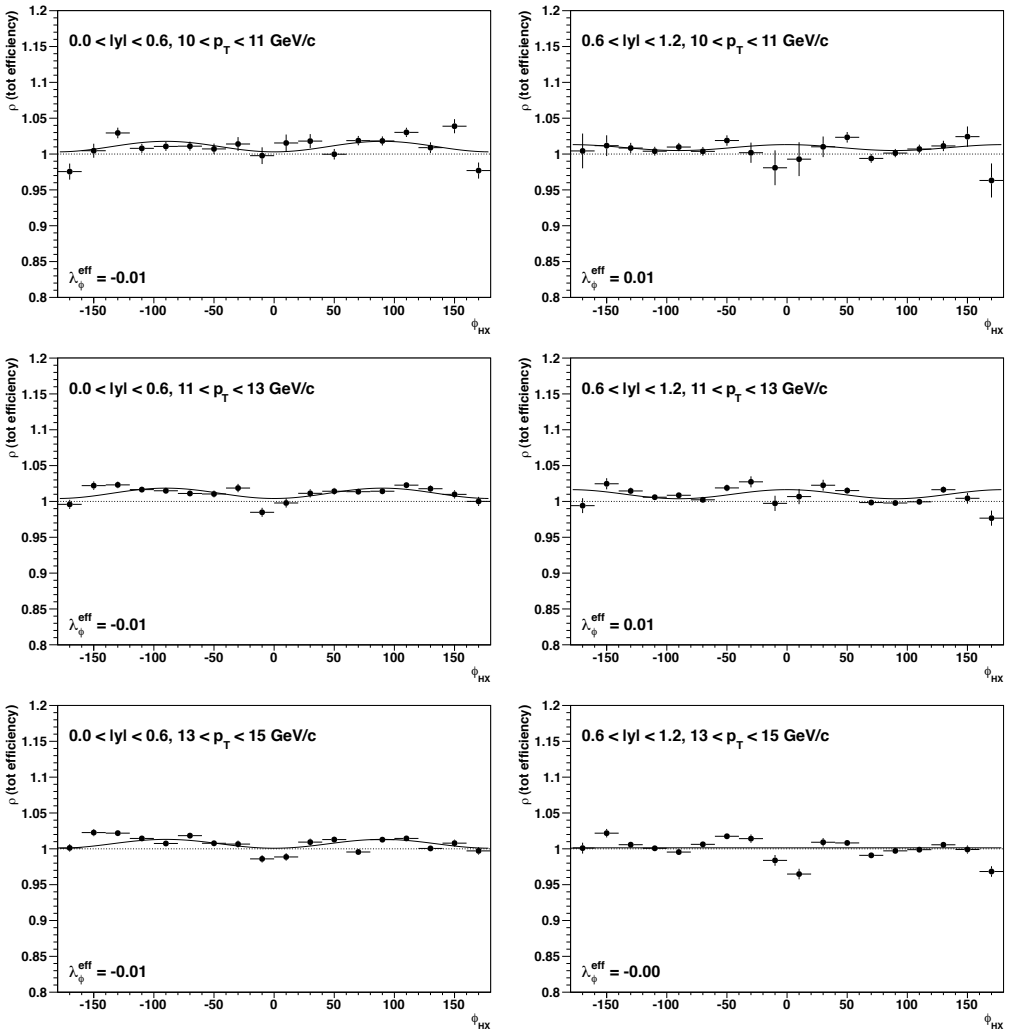

Figure C.1: ϕ_{HX} dependence of the ρ factor for the $\Upsilon(1S)$ (cont.)

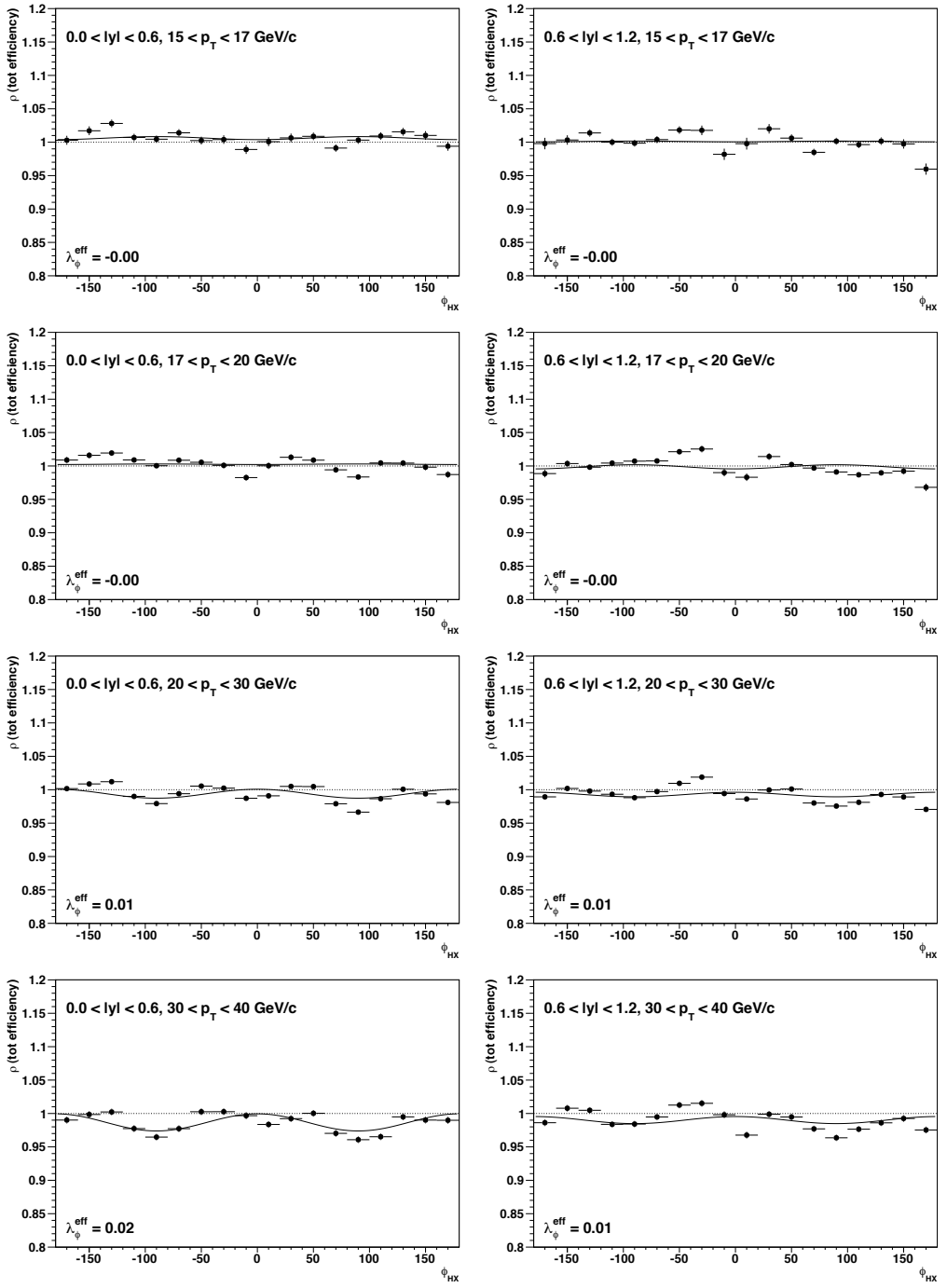

Figure C.1: ϕ_{HX} dependence of the ρ factor for the $\Upsilon(1S)$ (cont.)

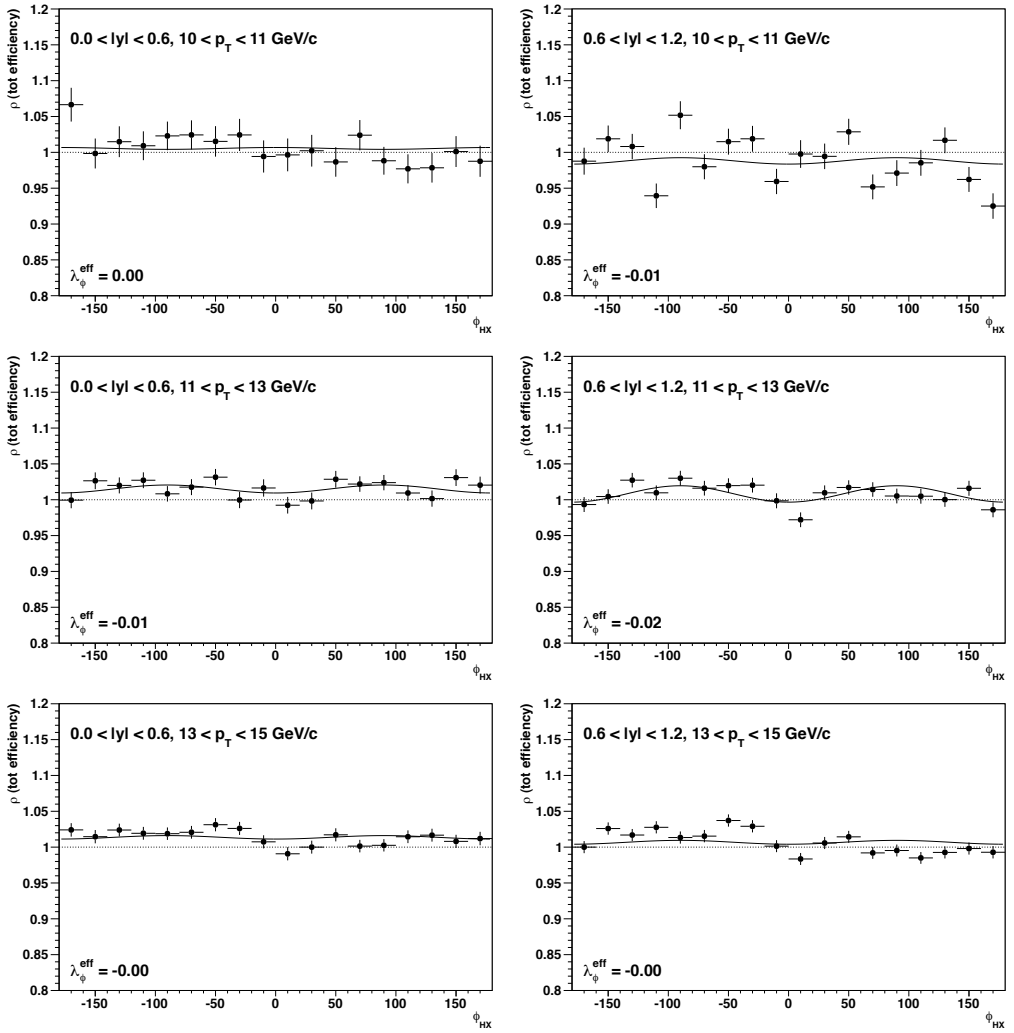

Figure C.2: ρ factor for the J/ψ as a function of ϕ, calculated in the HX frame using the `HLT_Dimuon10_Jpsi_Barrel` trigger path. The left panel shows the ρ factor at mid-rapidity ($|y| < 0.6$), the right side at $0.6 < |y| < 1.2$.

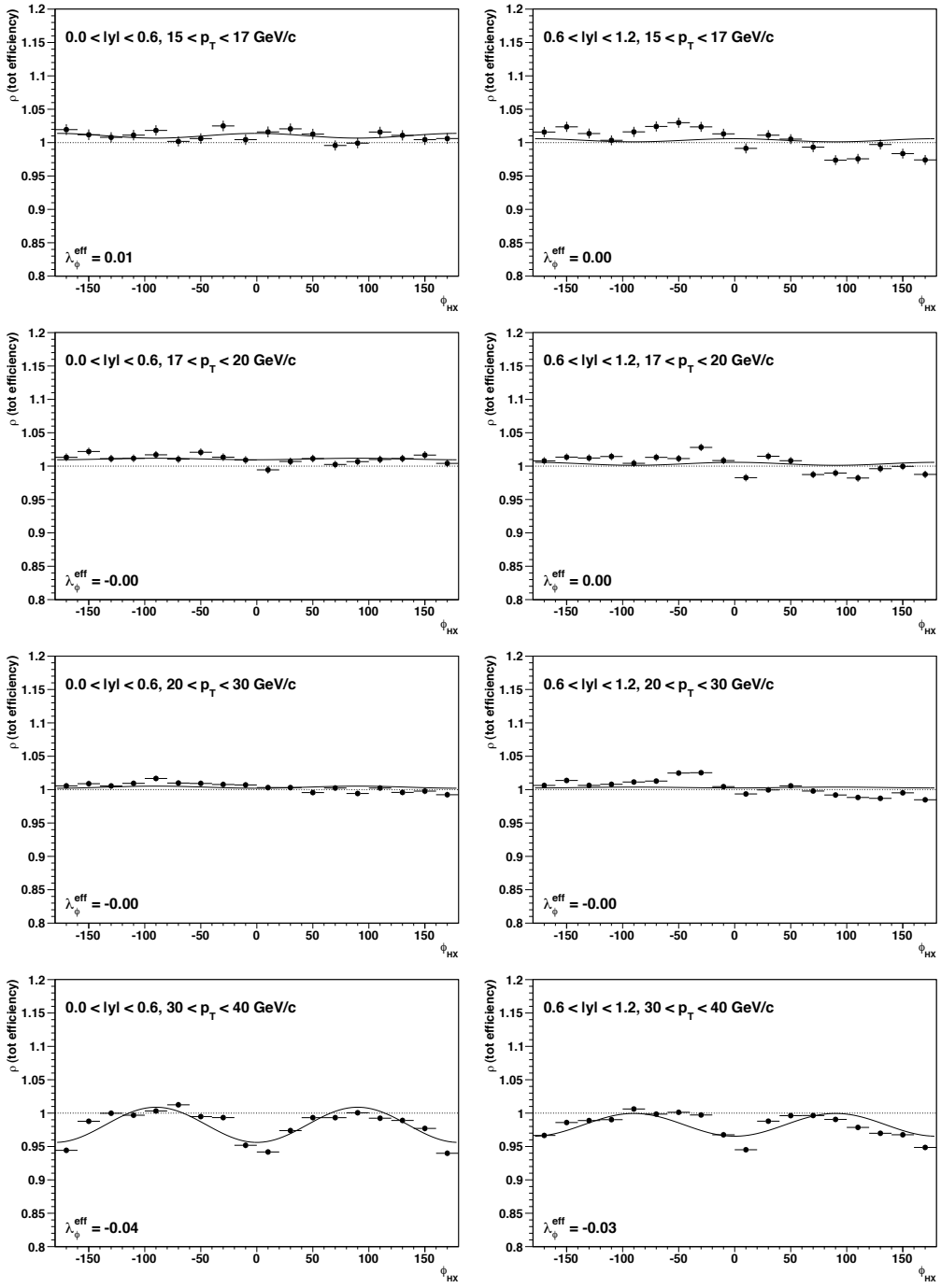

Figure C.2: ϕ_{HX} dependence of the ρ factor for the J/ψ (cont.)

Bibliography

[1] L. Evans, P. Bryant (editors). LHC Machine. *J. Instrum.*, 3:S08001, 2008.

[2] LHC - The Guide. *CERN Brochure*, 2009.

[3] CERN Accelerator Complex. http://public.web.cern.ch/public/en/research/-AccelComplex-en.html, (January 30, 2012).

[4] http://public.web.cern.ch/public/en/LHC/LHCExperiments-en.html, (January 30, 2012).

[5] Overall view of LHC experiments. http://cdsweb.cern.ch/record/841555, (January 30, 2012).

[6] A. De Roeck (editor). *CMS Physics - Technical Design Report, Volume II: Physics Performance.* CERN, 2006.

[7] R. Brout, F. Englert. Broken symmetry and the mass of gauge vector mesons. *Phys. Rev. Lett.*, 13, 1964.

[8] P.W. Higgs. Broken symmetries, massless particles and gauge fields. *Phys. Lett.*, 12, 1964.

[9] ATLAS and CMS experiments present higgs search status. http://press.web.cern.ch/press/pressreleases/releases2011/PR25.11E.html, (February 5, 2012).

[10] LHC-b collaboration. Measurement of the CP-violating phase ϕ_s in the decay $B_s \to \mathrm{J}/\psi \ + \phi$. 2011.

[11] H. Miyazawa. Baryon Number Changing Currents. *Prog. Theor. Phys.*, 36 (6), 1966.

[12] Towards a superforce. http://public.web.cern.ch/public/en/Science/Superforce-en.html, (February 5, 2012).

[13] D. Acosta (editor). *CMS Physics - Technical Design Report Volume I: Detector Performance and Software.* CERN, 2006.

[14] Dark secrets of the universe. http://public.web.cern.ch/public/en/Science/-Dark-en.html, (February 5, 2012).

[15] http://map.gsfc.nasa.gov/media/060916/index.html, (February 25, 2012).

[16] Antimatter detectives. http://public.web.cern.ch/public/en/Science/Antimatter-en.html, (February 5, 2012).

[17] ATLAS Collaboration. Observation of a Centrality-Dependent Dijet Asymmetry in Lead-Lead Collisions at $\sqrt{s_{\mathrm{NN}}} = 2.76$ TeV with the ATLAS Detector at the LHC. *Phys. Rev. Lett.*, 105, 2010.

[18] CMS Collaboration. Observation and studies of jet quenching in PbPb collisions at $\sqrt{s_{NN}} = 2.76$ TeV. *Phys. Rev. C*, 84, 2011.

[19] Secret dimensions. http://public.web.cern.ch/public/en/Science/Dimensions-en.html, (February 5, 2012).

[20] CMS Detector Overview. http://cmsinfo.web.cern.ch/cmsinfo/Detector/-FullDetector/index.html, (February 9, 2012).

[21] CMS Collaboration. The CMS experiment at the CERN LHC. *J. Instrum.*, 3(08), 2008.

[22] https://twiki.cern.ch/twiki/bin/view/CMSPublic/SWGuideMuonHLT, (January 30, 2012).

[23] A. Rao. 2011 proton collisions come to an end. http://cms.web.cern.ch/-news/2011-proton-collisions-come-end, (January 30, 2012).

[24] https://twiki.cern.ch/twiki/bin/view/CMSPublic/LumiPublicResults2010, (February 9, 2012).

[25] R. T. Garcia. Strategy for 2012. *LHC Performance Workshop: "Chamonix 2012"*, 2012.

[26] J.J. Aubert, et.al. Experimental Observation of a Heavy Particle J. *Phys. Rev. Lett.*, 33, 1974.

[27] J.-E. Augustin, et.al. Discovery of a Narrow Resonance in e^+e^- Annihilation. *Phys. Rev. Lett.*, 33, 1974.

[28] K. Nakamura et al. (Particle Data Group). *J. Phys. G*, 37, 2010.

[29] P. Faccioli, C. Lourenço, J. Seixas, H. Wöhri. Study of ψ' and χ_c decays as feed-down sources of J/ψ hadro-production. *JHEP*, 0810:004, 2008.

[30] P. Faccioli, C. Lourenço, J. Seixas, H. Wöhri. Determination of χ_c and χ_b polarizations from dilepton angular distributions in radiative decays. *Phys. Rev. D*, 83, 2011.

[31] P. Faccioli, C. Lourenço, J. Seixas, H. Wöhri. Towards the experimental clarification of quarkonium polarization. *Eur. Phys. J. C*, 69, 2010.

[32] E. Braaten, T.C. Yuan. Gluon Fragmentation into Heavy Quarkonium. *Phys. Rev. Lett.*, 71, 1993.

[33] P. Faccioli, J. Seixas. A new procedure for the extraction of angular distribution parameters in dilepton vector meson decays. *CMS AN AN-11-535 (internal note, unpublished)*, 2011.

[34] P. Faccioli, C. Lourenço, J. Seixas, H. Wöhri. Rotation-invariant observables in parity-violating decays of vector particles to fermion pairs. *Phys. Rev. D*, 82, 2010.

[35] FNAL E866/NuSea Collaboration. J/ψ Polarization in 800-GeV p-Cu Interactions. *Phys. Rev. Lett.*, 91, 2003.

[36] CDF Collaboration. Measurement of J/ψ and ψ(2S) polarization in $p\bar{p}$ collisions at $\sqrt{s} = 1.8$ TeV. *Phys. Rev. Lett.*, 85:2886–2891, 2000.

[37] HERA-B Collaboration. Angular distributions of leptons from J/ψ's produced in 920 GeV fixed-target proton-nucleus collisions. *Eur. Phys. J. C*, 60, 2009.

[38] CDF Collaboration. Polarizations of J/ψ and ψ(2S) Mesons Produced in $p\bar{p}$ Collisions at $\sqrt{s} = 1.96$ TeV. *Phys. Rev. Lett.*, 99:132001, 2007.

[39] P. Faccioli, C. Lourenço, J. Seixas, H. Wöhri. *J/ψ* Polarization from Fixed-Target to Collider Energies. *Phys. Rev. Lett.*, 102, 2009.

[40] P. Faccioli. Understanding quarkonium polarziation. *EP Seminar, CERN*, 2010.

[41] J.P. Lansberg. J/ψ production at $\sqrt{s} = 1.96$ and 7 TeV: Color-Singlet Model, NNLO* and polarisation. *arXiv:1107.0292v1[hep-ph]*, 2011.

[42] N. Brambilla et al. (QWG Collaboration). Heavy Quarkonium Physics. *CERN Yellow Report 2005-005.*

[43] P. Faccioli, C. Lourenço, J. Seixas. New approach to quarkonium polarization studies. *Phys.Rev.*, D81, 2010.

[44] P. Faccioli, C. Lourenço, J. Seixas, H. Wöhri. J/ψ polarization measurements revisited. *CERN-PH-EP/2008-xxx (unpublished)*, 2008.

[45] CDF Collaboration. Measurements of Angular Distributions of Muons From Υ Meson Decays in $p\bar{p}$ Collisions at $\sqrt{s} = 1.96$ TeV. 2011.

[46] M. Jones. Upsilon Decay Angular Distribution Analysis. http://www-cdf.fnal.gov/physics/new/bottom/110929.blessed-Ypolarization/index.-html. (February 17, 2012).

[47] ALICE Collaboration. J/Ψ polarization in pp collisions at $\sqrt(s) = 7$ TeV. 2011.

[48] Private Communication from P. Faccioli.

[49] W.-K. Tung C.S. Lam. Systematic approach to inclusive lepton pair production in hadronic collisions. *Phys. Rev. D*, 18, 1978.

[50] J. Seixas. Polarization measurements at the LHC. *Workshop Quarkonium production: Probing QCD at the LHC, Vienna*, 2011.

[51] B.L. Ioffe. Charmonium polarization in e^+e^- and heavy ion collisions. *Phys.Part.Nucl.*, 35, 2004.

[52] W.K. Hastings. Monte Carlo Sampling Methods Using Markov Chains and Their Applications. *Biometrika*, 57(01), 1970.

[53] N. Adam, et al. Generic Tag and Probe Tool for Measuring Efficiency at CMS with Early Data. *CMS AN-2009/111 (internal note, unpublished)*, 2009.

[54] G. Petrucciani, et. al. Documentation for TagProbeFitTreeProducer. https://twiki.cern.ch/twiki/bin/view/CMSPublic/SWGuideTagProbeFitTreeProducer, (January 30, 2012).

[55] Z. Gecse, et. al. Documentation for TagProbeFitTreeAnalyzer. https://twiki.cern.ch/twiki/bin/view/CMSPublic/SWGuideTagProbeFitTreeAnalyzer, (January 30, 2012).

[56] CMS collaboration. Measurement of Tracking Efficiency. *CMS-PAS-TRK-10-002*, 2010.

[57] I. Mikulec. Global Muon Trigger Changes. https://twiki.cern.ch/twiki/bin/viewauth/CMS/GlobalMuonTriggerChanges, (February 1, 2012).

[58] H. Wöhri, I. Krätschmer, J. Wang, L. Zhang. T&P single muon efficiencies for low p_T dimuon triggers in 2011. *CMS AN AN-11-417 (internal note, unpublished)*, 2011.

[59] H. Wöhri, I. Krätschmer, et. al. T&P fitter scripts. https://espace.cern.ch/cms-quarkonia/tnp/TP%20fitter/Home.aspx, (January 30, 2012).

[60] H. Wöhri, I. Krätschmer, et al. Low p_T Muon and Dimuon Efficiencies. *CMS AN AN-12-088 (internal note, unpublished)*, 2012.

[61] H. Wöhri, et.al. MC Closure test concerning efficiencies. https://espace.cern.ch/cms-quarkonia/onia-polarization/MC%20Closure/Home.aspx, (February 1, 2012).

[62] L. Guiducci. L1 Muon Configuration Changes. https://twiki.cern.ch/twiki/bin/viewauth/CMS/L1MuonTriggerChanges, (February 1, 2012).

Acronyms

ALICE A Large Ion Collider Experiment . . . 3
APD Avalanche PhotoDiode . . . 16
ASIC Application Specific Integrated Circuit . . . 19
ATLAS A Toroidal LHC ApparatuS . . . 3
BNL Brookhaven National Laboratory . . . 23
BSM Beyond the Standard Model . . . 7
CDF Collider Detector at Fermilab . . . 29
CERN European Organization for Nuclear Research, in French Organisation Européenne pour la Recherche Nucléaire . . . 3
CMS Compact Muon Solenoid . . . 1
CS Collins-Soper . . . 26
CSC Cathode Strip Chamber . . . 16
CSM Color Singlet Model . . . 29
DCA Distance of Closest Approach . . . 78
DT Drift Tube . . . 16
E866 Experiment 866 . . . 29
ECAL Electromagnetic CALorimeter . . . 11
FPGA Field Programmable Gate Array . . . 19
GJ Gottfried-Jackson . . . 27
GMT Global Muon Trigger . . . 19
GT Global Trigger . . . 19
HCAL Hadron CALorimeter . . . 11
HERA Hadron Elektron Ring Anlage
HLT High Level Trigger . . . 18
HX Helicity . . . 27
L1 Level 1 . . . 18

List of Figures

List of Tables